Chair of Materials Science and Testing of Polymers

Doctoral Thesis

Investigation of fretting behaviors of sealing materials

Chao Wang, M.Sc.

May 2020

When I let go of what I am, I become what I might be.

- Lao Tzu (Chinese philosopher)

AFFIDAVIT

I declare on oath that I wrote this thesis independently, did not use other than the specified sources and aids, and did not otherwise use any unauthorized aids.

I declare that I have read, understood, and complied with the guidelines of the senate of the Montanuniversität Leoben for "Good Scientific Practice".

Furthermore, I declare that the electronic and printed version of the submitted thesis are identical, both, formally and with regard to content.

Date 02.03.2020

Signature Author
Chao, Wang

Acknowledgement

Abstract

Fretting is a common failure, which can be found in many machines where vibration is present. Since the 1980s, a number of studies have investigated the fretting behavior of metals thoroughly. However, for polymers, especially sealing materials, their fretting behavior is still not completely understood. Due to their unique material properties, the methods, which were developed for metals, cannot be applied directly to polymers. In this thesis, a new test method with a corresponding analysis approach was developed for thermoplastic polyurethane (TPU). New calculations for the coefficient of friction (COF) in late cycles of the gross slip regime were introduced, which took the surface damage and the dynamic influence of the test system into consideration. Additionally, the influence of contact conditions (i.e. normal load and displacement amplitude) on fretting behavior was examined. Five different TPUs were tested and their fretting behaviors were compared. To connect sliding performance with fretting behavior, sliding tests were conducted using a component-like (ring on disc) set-up on a precision rotary tribometer. Due to the different test methods and wear mechanisms, the COF in the fretting and ring on disc tests cannot be compared; however, it can be concluded that the material with better tribological properties presents the improved fretting behavior.

Because alternating tangential stress superimposed with normal stress can lead to the generation of microcracks on the surface of TPUs, fretting can cause a severe reduction in fatigue life. However, the question remains: how does the material's fatigue properties correlate with its tribological performance? To understand this correlation, the fatigue (dumbbell, faint waist pure shear) and tribological (ball on disc, ring on disc) properties of filled and unfilled TPUs were characterized through various test configurations. Two wear models were verified for the tribological tests. One model predicts wear volume based on adhesive and fatigue wear mechanism, while the other one calculates the abrasive and fatigue wear volume by taking the surface roughness of the counter surface and surface energy into account.

The stick-slip effect, which is due to the contact transition between static friction and kinetic friction, was observed in fretting tests. The real contact area controls the tangential force release at the interface, and thus, dictates the alternating friction force. Therefore, it is necessary to obtain the contact area change for a better understanding of this physical process. In-situ techniques were employed to observe the real contact area during the stick-slip movement. In these tests, stick and slip regions were observed within the stick phase. By using machine learning, the movement of the stick region was analyzed. The correlation between friction force and the stick and slip regions in the stick phase was introduced using the mathematical model. Additionally, instead of using smooth samples, turned samples were used in this thesis, which represent the real surfaces of end products.

Material failure, especially in industrial factories, often originates at the surface due to wear, fatigue, or corrosion. To decrease the frequency of part replacements/repairs, industries have shifted their focused towards increasing the lifespan of materials through improved surface properties. As a result, the last thirty years has shown a growing interest in tribology, the study of surface and contact mechanics, among mechanical engineers. For example, applying coatings is becoming a more popular approach to improve the tribological properties of bulk materials. In this thesis, the application of composite coatings on sealing materials under emergency running was studied. Composites with varying ratios of diamond-like carbon (DLC) a hard coating, and molybdenum disulfide (MoS_2), a soft coating were investigated. Four common sealing materials, FKM, HNBR, NBR, and TPU, were coated using the magnetron sputtering method. Chemical (X-ray photoelectron spectroscopy, XPS) and physical (thickness, surface energy, microstructure) methods were applied to characterize the coatings. Tribological tests were performed at first in model tests under dry and starved lubrication conditions. Subsequently, the best and worst coating of each substrate was verified in component-like tests. There is no universal coating that is optimal for all substrates. The topography and rigidity of substrates are essential factors for the selection of coatings.

Kurzfassung

Fretting ist ein häufiger Fehler, der bei vielen Maschinen vorkommt, bei denen Vibrationen auftreten. Seit den 1980er Jahren haben eine Menge Studien das Frettingverhalten von Metallen gründlich untersucht. Bei Polymeren, insbesondere Dichtungswerkstoffen, ist ihr Frettingverhalten jedoch noch nicht vollständig verstanden. Aufgrund ihrer einzigartigen Werkstoffeigenschaften können die für Metalle entwickelten Methoden nicht direkt auf Polymere angewendet werden. In dieser Arbeit wurden neue Test- und Analysemethoden für thermoplastisches Polyurethan (TPU) entwickelt. Es wurde eine neue Berechnung des Reibungskoeffizienten (COF) für späte Zyklen im Gross Slip Regime eingeführt, bei der die Oberflächenbeschädigung und der dynamische Einfluss des Prüfsystems berücksichtigt wurden. Außerdem wurde der Einfluss der Kontaktbedingungen, nämlich der normalen Last, der Verschiebungsamplitude, auf das Frettingverhalten untersucht. Zusätzlich wurden fünf verschiedene TPUs hinsichtlich des Frettingverhalten verglichen. Um das Gleitverhalten mit dem tribologischen Verhalten zu vergleichen, wurden Gleittests mit einem komponenten-ähnlichen (Ring-Scheibe) Aufbau mit einem präzisen Rotationstribometer durchgeführt. Aufgrund der unterschiedlichen Testmethoden und Verschleißmechanismen sind die COF-Werte bei Fretting- und Ring-Scheibe-Tests nicht vergleichbar. Das Material mit den besten tribologischen Gleiteigenschaften weist jedoch auch das beste Frettingverhalten auf.

Wechselnde tangentiale Spannungen mit überlagerten normalen Spannungen können zu Mikrorissen auf der Oberfläche führen. Fretting kann die Lebensdauer erheblich verkürzen. Wie korrelieren die Ermüdungseigenschaften des Materials mit seiner tribologischen Eigenschaften? Um diesen Zusammenhang zu verstehen, wurden gefüllte und ungefüllte TPU untersucht. Verschiedene Testkonfigurationen wurden angewendet, um die Ermüdungs- (Hantel, Faint Waist Pure Shear) und tribologischen Eigenschaften (Kugel-Scheibe, Ring-Scheibe) zu charakterisieren. Für die tribologischen Tests wurden zwei Verschleißmodelle verifiziert. Ein Modell prognostiziert das Verschleißvolumen basierend auf dem Adhäsion- und Ermüdungsverschleißmechanismus,

während das andere das Volumen des Abrasive- und des Ermüdungsverschleißes unter Berücksichtigung der Oberflächenrauheit der Gegenfläche und der Oberflächenenergie berechnet.

Der Stick-Slip-Effekt wurde in Frettingversuchen beobachtet. Stick-Slip Bewegung ist eine Folge des Kontaktübergangs zwischen Haftreibung und kinetischer Reibung. Die reale Kontaktfläche steuert die Auslösung der tangentialen Kraft an der Grenzfläche. Somit ist es der entscheidende Faktor für den Wechsel der Reibungskraft. Daher ist es notwendig, die Kontaktflächenänderung zu beobachten, um diesen physikalischen Prozess besser zu verstehen. Die In-situ Techniken wurden verwendet, um die reale Kontaktfläche während der Stick-Slip Bewegung zu beobachten. Der Stick- und Slip Bereich wurden innerhalb der Stickphase beobachtet. Durch maschinelles Lernen wurde die Bewegung des Stickbereichs analysiert. Die Korrelation zwischen der Reibungskraft und dem Stick- und Slip Bereich in der Stickphase wurde unter Verwendung des mathematischen Modells eingeführt. Anstatt glatte Proben zu verwenden, wurden in dieser Arbeit gedrehte Proben verwendet, die die realen Oberflächen von Endprodukten darstellen.

Die Bedeutung der Oberfläche im Maschinenbau, insbesondere der Tribologie, wurde in den letzten dreißig Jahren erkannt. Tribologische Ausfälle entstehen an der Oberfläche durch Verschleiß, Ermüdung oder Korrosion. Mit der Entwicklung der Beschichtungstechnologie werden Beschichtungen zu einem praktischen Ansatz zur Verbesserung der tribologischen Eigenschaften von Schüttgütern. In dieser Arbeit wurde das Potenzial von Beschichtungen, insbesondere Hybrid-Beschichtungen, auf Dichtungsmaterialien, insbesondere unter Notlaufbedingungen, untersucht. „Diamond-like carbon" (DLC) kann als harte Beschichtung angesehen werden, während Molybdändisulfid (MoS_2) eine weiche Beschichtung ist. Sowohl die beiden Materialien als auch deren Komposite mit verschiedenen DLC/MoS_2-Verhältnissen wurden untersucht. Vier übliche Dichtungsmaterialien, nämlich FKM, HNBR, NBR und TPU, wurden unter Verwendung des Magnetron-Sputter-Verfahrens beschichtet. Zur Charakterisierung der Beschichtungen wurden chemische (Röntgenphotoelektronenspektroskopie, XPS), physikalische (Dicke, Oberflächen-energie, Mikrostrukturen) Methoden angewendet. Tribologische Untersuchungen wurden zunächst in Modellversuchen unter Trocken- und Mangelschmierbedingungen durchgeführt. Anschließend wurde die beste und schlechteste Beschichtung jedes Substrats in bauteilähnlichen Tests überprüft. Es gibt keine universelle Beschichtung, die für alle Substrate optimal ist. Die Topografie und Steifigkeit des Substrats sind wesentliche Einflussfaktoren für die Auswahl der Beschichtungen.

Scientific highlights

The present work extends the state of science by the following points:

1. A test method was developed for thermoplastic elastomers. Apart from the analysis of various wear mechanisms and their influence on fretting behavior, a new method was introduced to calculate the coefficient of friction in the gross slip regime, which takes the surface damage and the dynamic influence of the test system into consideration.

2. Five types of thermoplastic polyurethanes (TPU) were investigated in terms of their fretting behaviors. The tribological performance was characterized with sliding tests. Based on the wear scar analysis, the wear processes were revealed for the three fretting regimes respectively. At large amplitude, the scars vary considerably, while at small amplitude, their differences are difficult to identify. +

3. The correlation between tribological and fatigue properties was investigated. The impact of fillers on physical and mechanical properties of TPUs was studied with tensile tests and dynamic mechanical analysis (DMA). Two wear models were applied to correlate fatigue and tribological properties.

4. The stick-slip behavior of an elastomer was investigated using the in-situ technique. The real contact area was calculated from in situ videos, which were thresholded using Otsu's method for defining the contact area. During the stick phase, stick and slip regions were observed, and their alternation was investigated. The movement of the stick region was analyzed using machine learning. The influence of sliding velocity on stick-slip behaviors was studied over a range of speeds from 1 µm/s to 100 µm/s. The correlation between the real contact area and friction force provided a better understanding of the stick-slip process. A critical velocity was found, which is the transition from "micro" stick-slip to "macro" stick-slip.

5. The potential of hybrid coatings on elastomers was approved in terms of tribological performance. Pure diamond-like carbon (DLC), a hard coating, and molybdenum disulfide (MoS_2), a soft coating, as well as composite coatings of these two materials were deposited on four elastomeric substrates utilizing the magnetron sputtering method. The coatings were characterized by physical, chemical, and tribological tests. Various coatings were tested in model and component-like tests. Based on the material properties and surface structures of substrate, a better tribological performance was achieved for each elastomer through coating.

Contents

CONTENTS

Part I: Introduction and background

1. Introduction

Seals are small material components designed to prevent leakage, contain pressure, or exclude contamination. They can be found in a variety of applications, ranging from domestic appliances such as water faucets and pressure cookers to large vehicles such as automobiles and space shuttle. Despite the ubiquitous use of seals, their importance is often underestimated. With the growth and expansion of technology, there is a greater demand on seals, in particular dynamic seals, which can tolerate a variable environment such as steadily rising temperatures, pressures, and sliding speeds. A failure of a seal may lead to a fatal catastrophe of the corresponding instrument. The shocking disaster of the Challenger space shuttle can be traced back to the failure of an O-ring, which was incapable of preventing leakage due to the low temperature at night before launch [1,2].

Fretting occurs between two contacting surfaces that are reciprocating at small amplitudes for a large number of cycles. It may occur in any assembly of engineering components if a source of vibration is present. For seals in dynamic applications, fretting is one of the most common types of failure. Researchers have dedicated considerable effort into understanding the fretting behavior of metallic materials; however, the fretting behavior of polymeric sealing materials has not been deeply explored. Due to the unique material properties of metals, the fretting behavior of polymers may result from different mechanisms. In addition, the viscoelasticity and temperature-dependent properties make the study of polymers more complicated than metals. Therefore, new tests, as well as analysis methods, are needed.

Fretting occurs after a large number of cycles of alternating stresses, fretting fatigue becomes pronounced, leading to a reduction in fatigue life. Fretting wear is the loss of material due to fretting. The wear debris generated are often retained within the contact area because of the small amplitude movement. In sealing applications, fretting can lead to loss of clearance. The fretting behavior can be affected by many factors. Besides amplitude, frequency and cycle number, the contact temperature can be crucial, especially for polymeric seals. The sealing material itself is also decisive in the fretting behavior. Its visco-elastic property impacts the contact condition and subsequently the seals performance. The bulk fatigue properties, which are associated with crack initiation, determine the degree of fatigue [3,4]. Considering the significance of fretting on the lifespan of polymers, there is an urgent need to understand the correlation between the tribological performance and the bulk fatigue properties. Also, few studies have examined the effects of fillers

on the performance of sealing materials. To clarify these correlations, fatigue and tribological tests should be conducted separately.

The stick-slip effect can be identified not only in fretting tests, but also in the running condition of seals, especially at low speeds. Stick-slip can cause disturbing vibrations or noise, which can disrupt vibration-sensitive applications. The real contact area is of great importance for stick-slip movements because it controls the tangential force release. Many researchers have used smooth samples to investigate this phenomenon; however, the experimental samples had different surface features from the end products. Therefore, there is a need to utilize samples with similar surfaces as machined seals to study this physical process. In addition, in situ techniques facilitate the observation of the contact area during stick-slip movements. However, the conventional video post-processing method is not able to obtain the movement of the stick region during the stick phase, which plays a crucial role in understanding the correlation between stick-slip and friction force. Hence, an alternative approach is necessary to accomplish this task.

Coatings have been used to enhance the tribological properties of metals for a long time; however, there have been only a few experiments of applying coatings to polymers, especially soft elastomers. In contrast to single material coatings, composite coatings combine the advantages of its components. This thesis takes steps towards determining if sealing materials also benefit from composite components. There remains a need to verify this approach to improve the tribological performance of sealing materials.

Overall, fretting is only one of the failure mechanisms of seals. Often, failure results from a cumulative effect of several failure mechanisms. Therefore, to improve the performance of seals, apart from mechanical properties of sealing materials, other factors, such as manufacturing and installation, must be taken into consideration.

2. State of the art

2.1 Sealing materials

Mechanical seals are of great importance in industry. They can be found in a wide range of applications, from domestic equipment to aircraft gas turbines [5]. They prevent leakage of machines; however, zero leakage is theoretically impossible. Attempting to avoid leakage entirely can lead to high seal costs if slight leakage can be tolerated [6]. Seals prevent contaminants from entering the internal parts of a machine, which can have catastrophic consequences on the machine system. Contaminants accelerate the wear process of a sealing edge which would cause severe leakage of the sealed fluid that can ultimately lead to environmental pollution [7]. However, with the development of technology, the speed of the mechanical system is increasing, and the pressure is getting higher. Thus, the demand for sealing materials is increasing [8].

Among the many sealing materials, this work focuses on the thermoplastic polyurethane (TPU), which is a fully thermoplastic elastomer. Due to these unique properties, TPU compensates for the material gap between rubbers and thermoplastics. TPU is a linear segmented block copolymer consisting of hard (isocyanates and chain extenders) and soft (polyol) segments [9]. By varying the ratio and types of these segments, TPU has exceptional flexible properties, which makes it an ideal polymer in a wide range of applications. Because of its high strength and excellent abrasion and tearing resistance, TPU is becoming a more popular choice for mechanical seals. As a sealing material, TPU was investigated in different aspects, including i.e. nanostructure [10], tribological properties [11], fatigue properties [12] and other aspects [13–15].
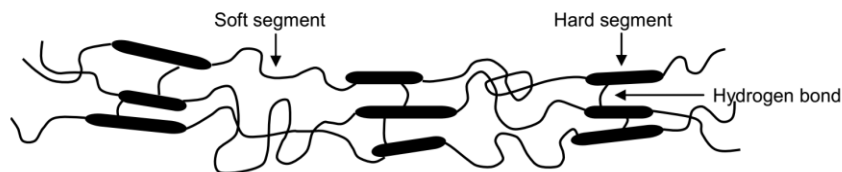
Fig. 1: Schematic structure of TPU composed of hard and soft segments [13].

Fluoroelastomers (FKM) were introduced in 1957 by the company DuPont [16]. They are commonly used as sealing materials in severe environments that require resistance to high temperatures (up to 200°C) or chemicals and oils [17]. Fig. 3 shows a comparison of a retained sealing force of four common sealing materials at 150°C. After 10000 hours, FKM still has more than 80% of the original sealing force. With increasing mechanical demands and more stringent

regulations, FKM is becoming more popular in industry [16]. Additionally, because of its high compressive strength, FKM is extensively used in O-rings and gaskets.

Fig. 2: Chemical structure of FKM [16].
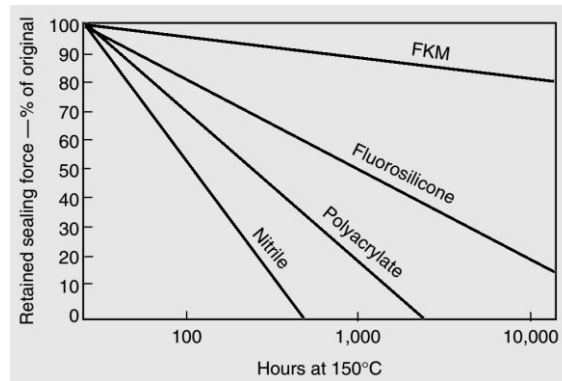
Fig. 3: Comparison of retained sealing force of common sealing materials [16].

Nitrile rubber (NBR) (Fig. 4) is one of the dominant material in rubber products [18]. It is widely used as general-purpose sealing material, with excellent mechanical, wear properties, and resistance to most mineral-based oils and greases [5]. Depending on its acrylonitrile content, NBR has a wide range of properties making it suitable for a number of applications.
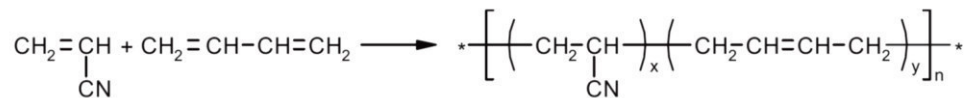
Fig. 4: Structure of NBR [19].

Through a hydrogenation process, NBR is processed into HNBR, which has an improved chemical and temperature resistance. Because of its high strength and fluid resistance, it fulfills the demands of the gas and oil industry, chemical industry, and diesel engines [5].

2.2 Tribology of elastomeric sealing material

2.2.1 Mechanisms of friction and wear of elastomer

Two friction mechanisms are primarily responsible for the friction between elastomers and hard surfaces: adhesion and deformation [20–22].
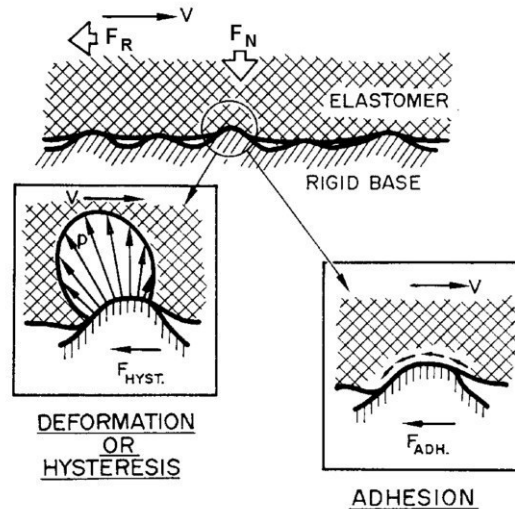
Fig. 5: Two main parts of elastomer friction: adhesion and deformation [22].

Adhesion involves the making and breaking of molecular bonds between the interfacing surfaces [23–28]. The low elasticity of elastomers leads to large deformation under normal stress, which results in energy loss associated with internal damping effects within a viscoelastic body. The lost dynamic energy is transformed into thermal energy. Depending upon the material properties, under unlubricated conditions, adhesion is generally the dominant source of friction [29–31]. The contribution of deformation/hysteresis to friction is deemed negligible. However, under lubricated conditions, the degree of adhesion is significantly reduced, and hysteresis remains nearly constant. Thus, hysteresis plays an essential role under lubricated conditions. At the microscale, as shown in Fig. 6, asperities on the countersurface exert pulsating forces onto the sliding elastomer. As a consequence, energy is dissipated into the elastomer in the form of internal friction [32].
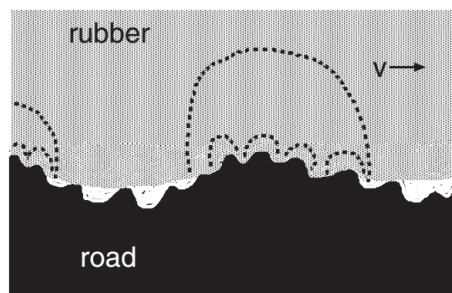
Fig. 6: Hysteretic friction of a rubber block on a rough road surface [32].

Schallamach made considerable progress in the understanding of rubber friction behavior. He observed the contact area of a hard material sliding against a rubber surface and found the "wave of detachment", which is known as "Schallamach waves" [33]. Fukahori et al. further explored the formation of Schallamach waves using experimental observations and finite element analysis [34].

5

The results of those experiments explained the mechanism of the initiation and propagation of the wave of detachment. First, the stress distribution at the contact zone with different coefficients of friction (COF) was simulated. It was found that the maximum tensile stress always appeared at the trailing edge of contact. Thus, the maximum tensile stress is responsible for the initiation of the meniscus, and the stick-slip motion is responsible for the propagation of the waves.
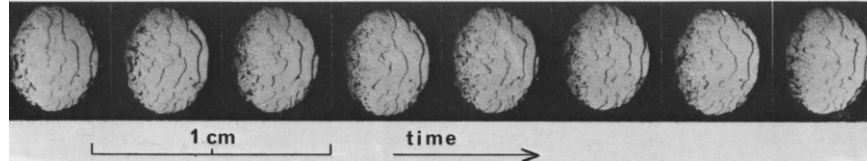

Fig. 7: Schallamach waves on rubber, sliding speed at 0.43 mm/s, 32 fps [33].

In the study of Johnson et al. [35], it was revealed that the area of contact between a rigid sphere and a flat rubber surface was larger than the value estimated from the Hertzian contact theory. The authors of that work proposed that the molecular attraction of van der Waals forces acting between the sphere and rubber surface increases the contact area.

Abrasive, adhesive and fatigue wear are the three main wear mechanisms for elastomers [24]. Abrasive wear is caused by hard particles or sharp asperities of a hard countersurface tearing the sliding surface of the elastomer [36]. It was found that rubber abrasion is composed of two kinds of periodic motions, stick-slip motion and micro vibration [37–39].

Adhesive wear occurs when two surfaces are brought together and then are separated, either normally or tangentially [40]. Various theories have been developed to explain this phenomenon [25,41]. Molecular-kinetic theories are one of the most comprehensive theories that describe adhesion as a thermally activated molecular stick-slip process [42,43].

Fatigue wear causes crack formation at the surface of a sliding elastomer due to repeated alternating stresses, which results in progressive fracture [31]. It is characterized by the accumulation of irreversible changes that lead to the generation and further development of cracks. The loss of material from solid surfaces due to frictional fatigue is referred to as fatigue wear. Cracks can form at or below the stressed surface.

Hausberger et al. investigated the adhesive- and deformation- contribution to the friction and wear behavior of TPUs [44]. He found that the ratio between the two frictional mechanisms is strongly influenced by the load, surface roughness, viscoelastic material behavior, and ambient conditions. Based on the in-situ observation and failure analysis, Grün et al. developed a functional tribological material model of TPU, which describes the formation of wear [45]. As shown in Fig. 8, in the first stage, the contact area is small, which results in high local adhesive bonding. Further movement

severely lengthens the surface feature initiating crack formation and propagation, which is characteristic of stage 2. In the third stage, the propagation of cracks removes surface material that begins to roll between the two surfaces due to the tangential movement. Finally, with further movement, the material becomes separated from the sample [45].
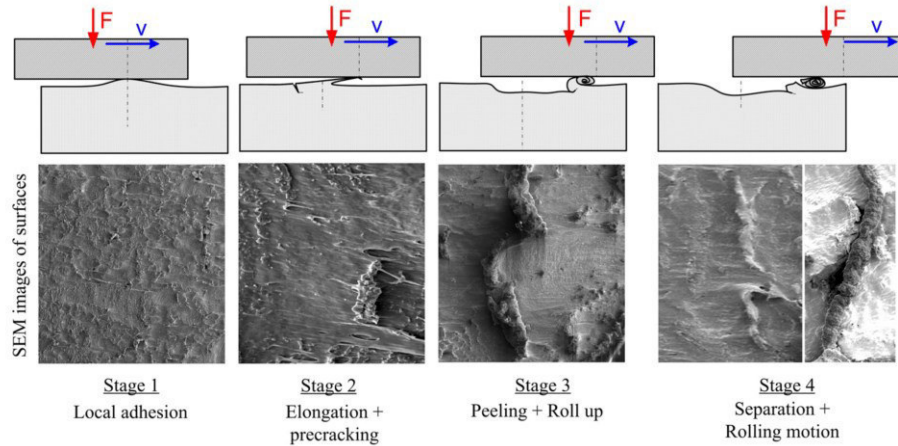
Fig. 8: Functional tribological material model of TPU [45].

In practice, a combination of three forms of wear occurs, and it is difficult to separate the contribution of each mechanism to the overall wear [22].

2.2.2 Influential factors

Tribological phenomena are complex physical processes that are related to a number of factors. The fact that friction and wear are essentially dynamic processes results in the interdependence between experiment and theory in tribology [46,47]. For sliding tests between an elastomer and a metal surface, the following main factors may impact the tribological behavior significantly:

– Surface roughness
– Sliding velocity
– Normal load
– Material properties
– Temperature

Surface roughness

Surface roughness is an important aspect of tribology. Due to the much lower surface stiffness of elastomers compared to metals, the roughness of the countersurface has a significant effect on the elastomer's sliding behavior. Persson investigated the contact between a rubber and a hard surface in sliding tests [48]. As shown in Fig. 9, he found that rubber can fill in the long wavelength

roughness. However, the microroughness, small-sized "cavities," are still unoccupied [48]. In addition, due to the high local contact pressure at the peak of large positive asperities, the "micro cavities" are more easily filled than the large negative valleys. Therefore, the small "cavities" also contribute to the sliding friction.
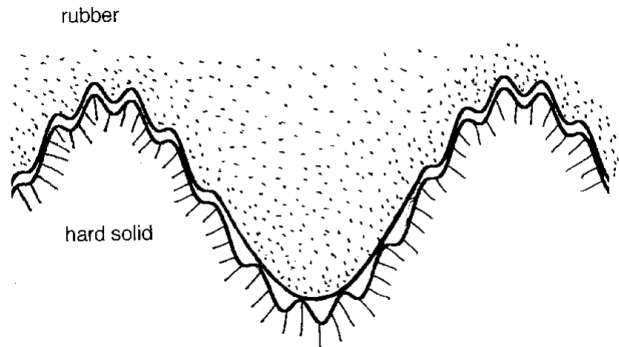
Fig. 9: Counter surface shows roughness in two length scale. Rubber is able to fill the "waviness" in long-wavelength, but, it is not able to fill the microroughness [48].

A strong correlation between tribological properties and the roughness of the countersurface has been provided by a number of studies [49–59]. A general thinking about surface roughness is that, the smoother the countersurface, the lower the wear rate and friction. However, that is not correct. As we know, a rough countersurface leads to high abrasive wear and vice versa. However, a lower roughness may lead to an increase in adhesive wear and fatigue wear. Dowson found an optimum countersurface roughness, which generates a minimum wear rate under dry condition (Fig. 10) [58]. During the wear process, the polymer properties of the surface layer, which is relevant to fatigue properties, may be changed drastically during sliding [60]. With a roughness (Ra) between 0.1 µm and 1 µm, fatigue cracks perpendicular to the sliding direction were observed on worn POM pins, which indicate that fatigue wear is the dominant wear mechanisms [61]. In addition, static friction of elastomers against a rough countersurface is higher than a relatively smooth surface [56]. The surface roughness affects the formation and modification of transfer film during sliding. The running-in phase is longer when the material slides over a smoother countersurface [56].
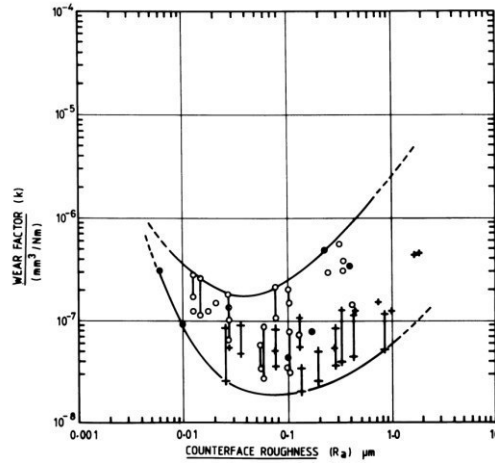
Fig. 10: Wear factor as a function of countersurface roughness (Ra) under dry condition [58].

For seals, surface roughness is an important factor that influences the rate of leakage [62]. For radial lip seals, its performance is dependent on the roughness. However, the actual mechanisms of roughness induced leakage are still not well understood [63,64]. Due to the viscoelasticity of elastomers, the real contact area increases continuously as the elastomer is pressed with a constant force against a rough surface [32]. Accordingly, the average space between the surfaces decreases with increasing time. This effect is beneficial for sealing applications.

Sliding velocity

The sliding velocity shows a strong influence on the tribological performance of the polymer by influencing the interface temperature [53,65,66]. At high sliding speeds, when the interfacial temperature is close to the softening point of the polymer, the wear rate increases rapidly, and friction decreases slightly [53]. At low temperatures, no significant dependence can be identified.
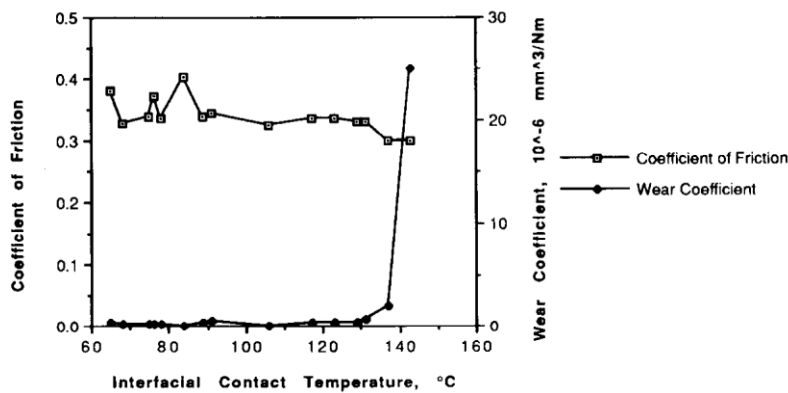
Fig. 11: Friction and wear coefficient of UHMWPE sliding against a counterface with a roughness of 0.13-0.14 μm vs interfacial contact temperature [53].

Normal load

Normal load influences not only the contact pressure but also the friction and wear mechanisms. The quantitative increase in normal load can result in a qualitative change. With increasing load, the asperities on the countersurface penetrate deeper into the polymer surface, leading to higher abrasive wear [67]. Generally, higher loads lead to higher energy dissipation, which result in a temperature rise. Consequently, the storage modulus of polymers decreases. With high loads, the increased thermal energy can cause an abrupt increase in wear rate, which can be attributed to softening or melting of the sliding polymer surface [65,67].

Material properties and temperature

The viscoelastic nature of elastomers is demonstrated in sliding friction through hysteresis friction. A number of theories have attempted to explain hysteresis friction in various aspects [29,30]. The sliding velocity and topography of a countersurface are the decisive factors of the applied excitation frequency. Grosch found that the velocity of maximum friction agrees excellently with the frequencies at which the maximum loss modulus occurs [20]. As shown in Fig. 12, all four rubbers follow this rule very well.
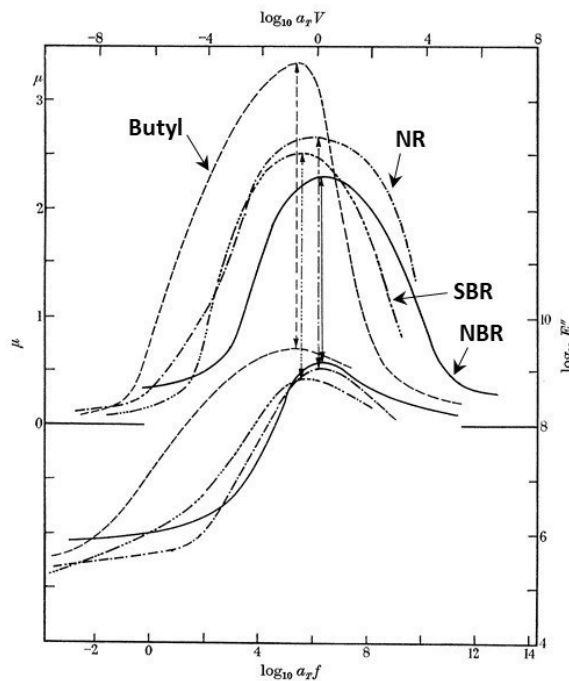
Fig. 12: Comparison of the master curve of the coefficient of friction (above) and loss modulus (below) of four rubbers [20].

The mechanical properties of polymers are susceptible to temperature. In dry sliding, due to their poor thermal conductivity and low specific heat, the interfacial temperature can increase quickly.

Correspondingly, the real contact area increases with increasing temperature. Based on the WLF shift, the different friction properties of a tire can be classified to certain frequency regions [68]. As shown in Fig. 13, with increasing temperature, the dominant friction mechanisms change from adhesive friction to hysteresis friction. At high frequency, e.g. in case of wet-braking friction, the material is dominant by maximum energy loss. For tires, they are deformed cyclically due to the rolling motion. However, this frequency is much lower than the frequency of surface vibration during wet braking. According to the time-temperature superposition, the material should have similar properties at high temperature as at low frequency. Hence, the high temperature in Fig. 13 represents rolling resistance.
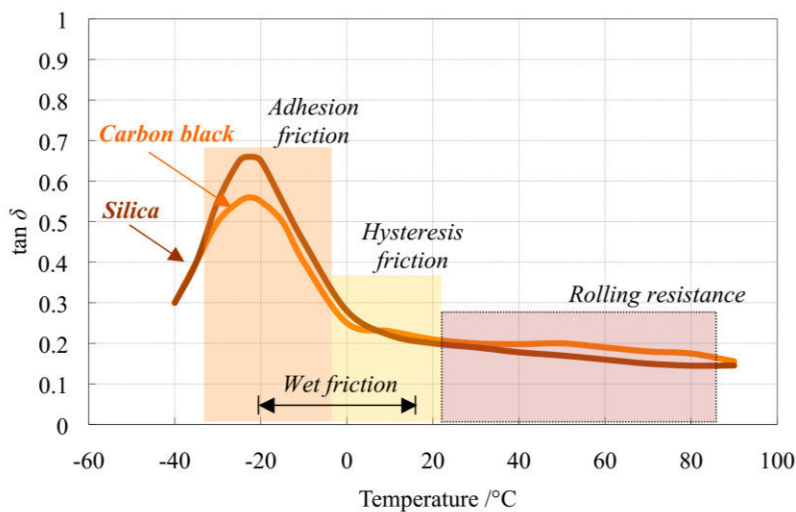
Fig. 13: Schematic relationship between loss modulus and temperature using WLF shift [68].

2.3 Fretting of polymers

Fretting occurs between two contacting surfaces that are reciprocating sliding at small amplitude for a large number of cycles. For seals in dynamic applications, fretting is one of the most common types of failure [69]. Since 1950, fretting was thoroughly investigated for metal-metal contact [70]. Different methods were developed to characterize fretting behavior. A classical approach is the load–displacement fretting map [71], which divides the fretting map into three regimes, namely partial slip regime (PSR), mixed fretting regime (MFR), and gross slip regime (GSR). Later, Vincent et al. developed the running condition fretting maps (RCFM) that describe the fretting behavior through the whole test [72,73]. As shown in Fig. 14, in PSR, the middle area is the stick region, and slip occurs only in the area of the outer ring. In MFR, the stick region shrinks to a point in the middle, whereas in GSR, no stick region exists. However, there is no clear criterion to divide these three regimes precisely.
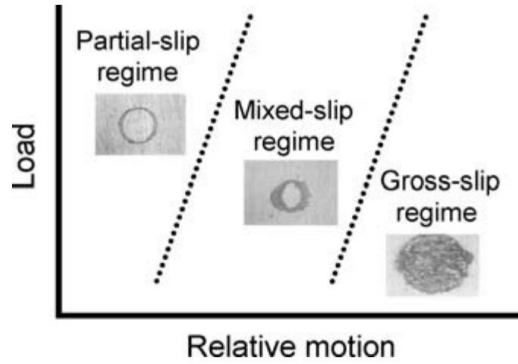
Fig. 14: Running condition fretting map (RCFM) [74].

Based on the methods developed for metals, research has focused on various polymers over the past two decades, including PMMA [75–77], PEEK [78], PTFE [78,79], PA11 [80], PC [77,81,82], thermoplastic elastomer [83], and NBR [84]. Due to the comparatively high compliance of polymer, the displacement amplitude required to cause fretting is usually larger for polymers than for metals [77]. Stick-slip motion was also identified under fretting condition [74,85,86]. The fretting regime can be characterized by the phase difference between friction force and relative displacement. In Fig. 15, the relationship between friction force and relative slip is shown. If the phase difference is close to 90°, then the fretting regime is in gross slip regime. When the phase difference is close to 0°, then it is mixed or partial slip regime [74].
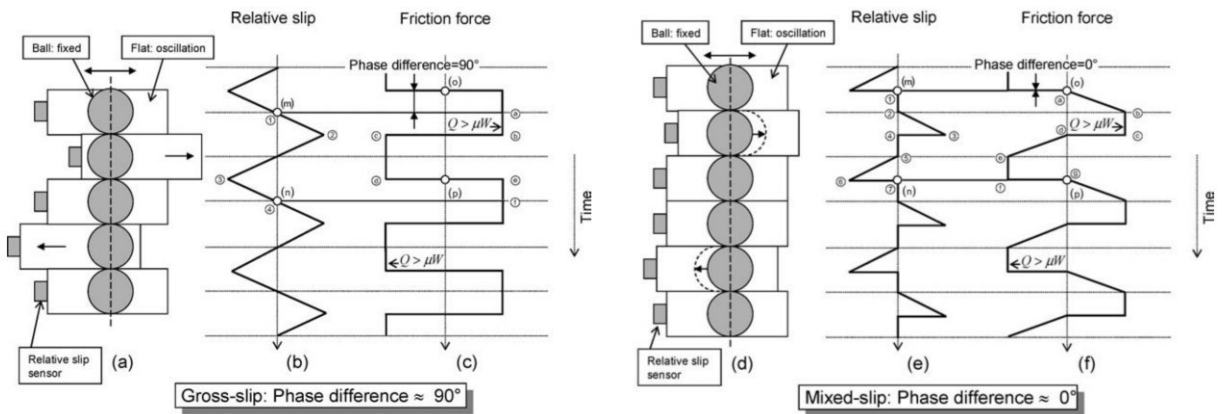
Fig. 15: Relationship between friction force and relative slip in fretting:
(a, b, c) gross-slip, (d, e, f) mixed-slip or partial-slip

2.4 Stick-slip behavior of elastomer

Stick-slip is generally a dynamic cyclic process where two mating surfaces oscillate between a stick phase and a slip phase [87]. It is a widely observed phenomenon, ranging from the atomic to macroscopic scale, and from delicate instrumentation to daily life. In the stick phase, the two

surfaces stick together, and no relative motion occurs at the interface. In the slip phase, finite relative motion occurs (Fig. 16). Stick-slip motion in seals can degrade performance significantly, cause vibration and damages, such as cracks and wear [88]. Stick-slip problems can be caused by insufficient lubrication at low speeds and high pressures, e.g., the running-in phase.
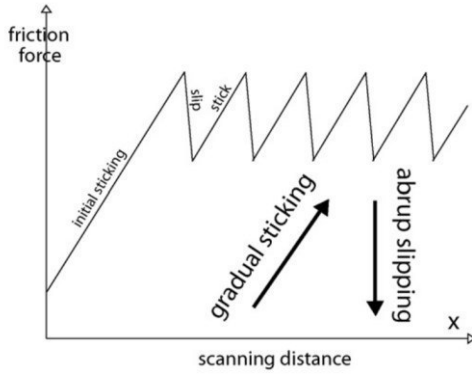
Fig. 16: Typical stick-slip behavior [89].
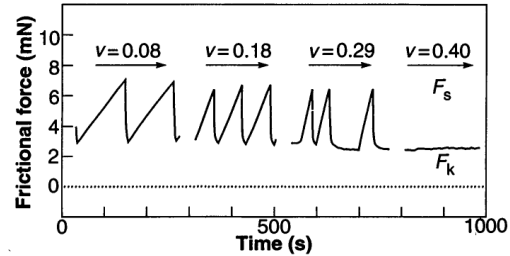
Fig. 17: Relationship between stick-slip behavior and sliding speed [90].

Bengisu et al. investigated the dynamic of friction and the effect of surface roughness on stick-slip behavior utilizing mathematical models [91]. The group found that friction depends on both the interface properties of the surfaces and on the dynamic response of the system. For polymers, material properties such as tensile strength, modulus, and surface energy influence the stick-slip behavior [92]. They investigated PMMA, PC, PTFE, and PVC and found that stick-slip behavior frequency is more dependent on the polar part of surface energy rather than the cohesive strength of polymers. The deformation and stick-slip behavior show a distinct relationship [93]. With a larger deformation, the stick-slip behavior is more obvious, the fluctuation amplitudes and COF are higher. There is a critical speed in which if the sliding speed exceeds this speed, the stick-slip phenomenon will vanish [90,94,95].

Liao et al. studied the stick-slip friction of reciprocating O-ring seals using acoustic emission techniques [96]. In that investigation, it was found that both the AE RMS voltage and the friction coefficient vary with the stroke length are consistent.

2.5   In-situ tribology

The tribological phenomenon is a result of two contacting surfaces in relative motion. Asperities are irregularly shaped protuberances that exist on all engineering surfaces [97]. Hence, when two surfaces come into contact, deformation of asperities occurs prior to other parts. Between the buried surfaces, the real contact area cannot be observed and thus the physical processes at the interface remains unknown. To gain a deeper understanding of the interaction, in situ observation

is of great interest for tribological analysis. In situ tribology method provides detailed measurements of the surface of the sample within the environment, but without any contact [98]. The surface topography, e.g., transfer film and wear particles, can be observed thoroughly between contacts. It enables a correlation between measured friction and normal force with observed surface topography alteration. In situ observation can be conducted at different scales, with optical observation at the macro- and microscales [45,98–103], scanning electron microscope (SEM) at the microscale [104], and transmission electron microscopy (TEM) at the nanoscale [105–110]. As shown in Fig. 18, optical in situ observation can be performed through a transparent countersurface from above, below or side. However, for such approaches, some compromises have to be made, e.g., material and geometry of the countersurface and test environment [98]. For example, a transparent countersurface is necessary for optical observation; however, these materials are in most cases not the countersurface used in practical applications.
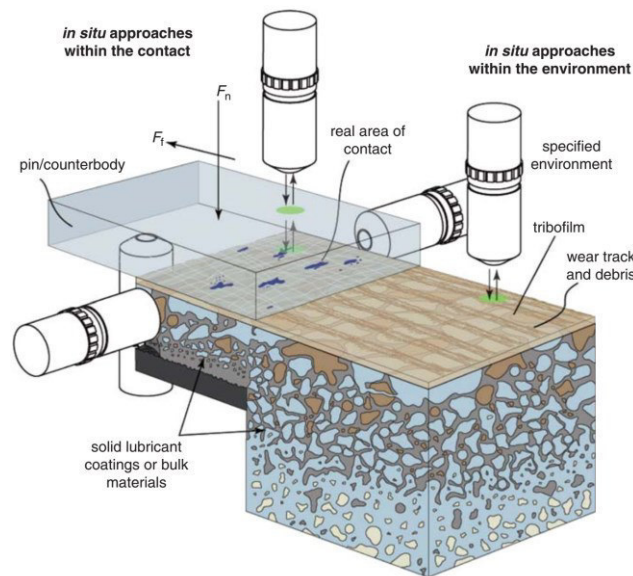
Fig. 18: Different optical in situ approaches in tribological studies [98].

Using the in situ technique, various polymers sliding against glass were tribologically studied. By testing resin sliding against glass, it was found that at high contact pressures, the wear rate was higher and the debris was larger, which facilitated the transformation of the motion from sliding to rolling [111]. The dynamic viscoelastic process of friction is divided into four stages: adhesion stage, transition stage between the adhering and sliding, full slip stage and recovery stage. Krick et al. studied a hemispherical NBR sliding against glass using an optical micro tribometer [99]. As shown in Fig. 19, there is a nearly linear increase in the contact area with increasing force over the range of tests, which indicates the average pressure of the real contact area is nearly constant. Sahli et al. investigated the evolution of real contact area under shear and the value of static

friction of cross-linked polydimethylsiloxane (PDMS) [112]. That study found that the real contact area is proportional to the normal load. Furthermore, the real contact area decreases under shear stress, decreasing up to 30% prior to macroscopic sliding.
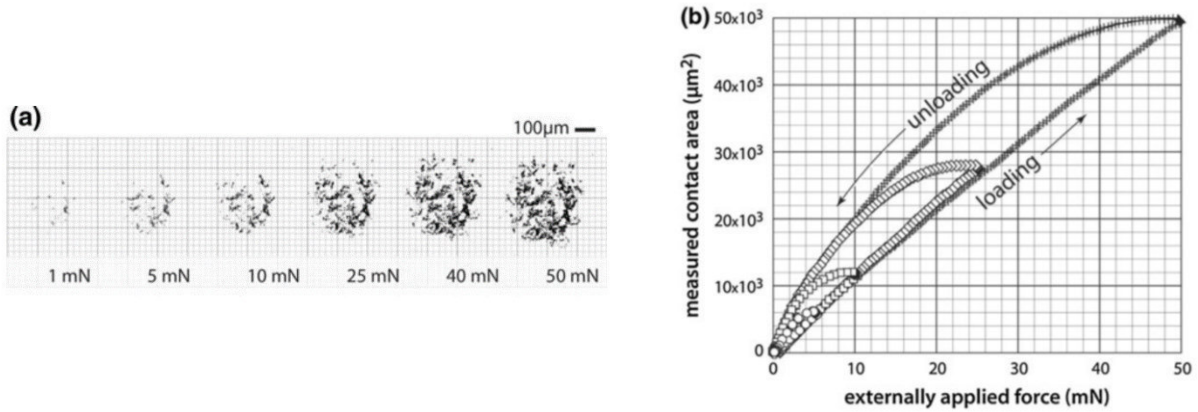
Fig. 19: Real contact area versus applied normal load. (a) contact area images for loads of 1, 5, 10, 25, 40, and 50 mN; (b) contact area plotted against applied normal load.

Within the real contact area, stick and slip regions were identified (Fig. 20). They have a significant influence on frictional behavior, especially the stick-slip behavior. To map the stick and slip regions in the real contact area, analysis was performed using particle image velocimetry (PIV), which uses the real contact points as chase markers for the interference images [101].
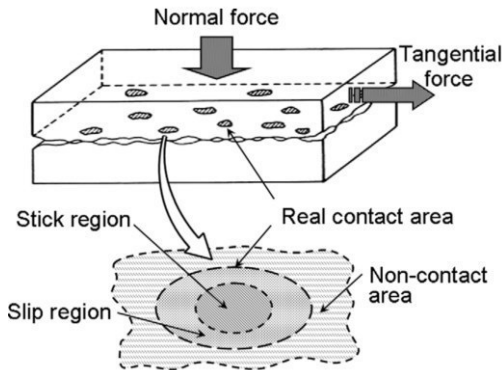
Fig. 20: Stick and slip region within the real contact area [101].
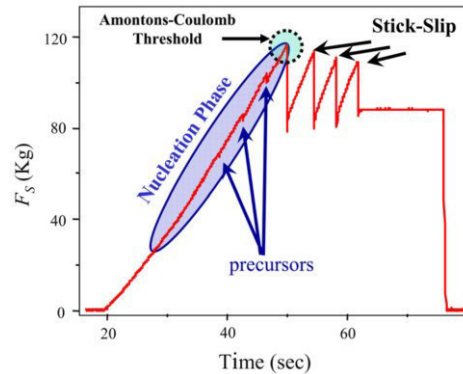
Fig. 21: Loading curve of a sliding stick-slip test [113].

In the sliding tests with PMMA block against PMMA block, small drops (1-2% of the mean value of friction force) were identified, which occurred before the shear force reached the maximum static friction force (Fig. 21) [113]. It was determined that the rapid fracture process and shear cracks are responsible for these cracklike precursor events [114]. Bennewitz et al. observed this

phenomenon by PDMS/glass tests and explained this with compressive strain, which progressed in the form of step-like increases [115].

2.6 Coatings on polymer

Tribology is a science of contacting surfaces in relative motion. Friction and wear processes occur at the interface. Coatings are used in tribology to prevent the surfaces from direct contact. Generally, coatings can be classified as either soft or hard [116]. Soft coatings, including polymers (e.g., PTFE, PI), soft metals (e.g., lead, indium), and lamellar solids (e.g., graphite and molybdenum disulfide (MoS_2)), provide excellent shearing characteristics and thus result in a reduction of friction. Hard coatings (e.g., diamond-like carbon (DLC), titanium nitride (TiN)) can improve protection against wear and present low wear rates.

Coating design can be optimized with the understanding of the mechanisms of friction and wear at different scales [117,118]. At the microscale, researches focus on asperity contacts, fracture, deformation, formation of transfer film and debris, and roughness influence [117]. Fig. 22 shows the essential properties in the five aspects of a coating system. Any change of a parameter may lead to a significant alteration of tribological performance. Therefore, it is challenging to define a general rule for choosing an optimal coating.
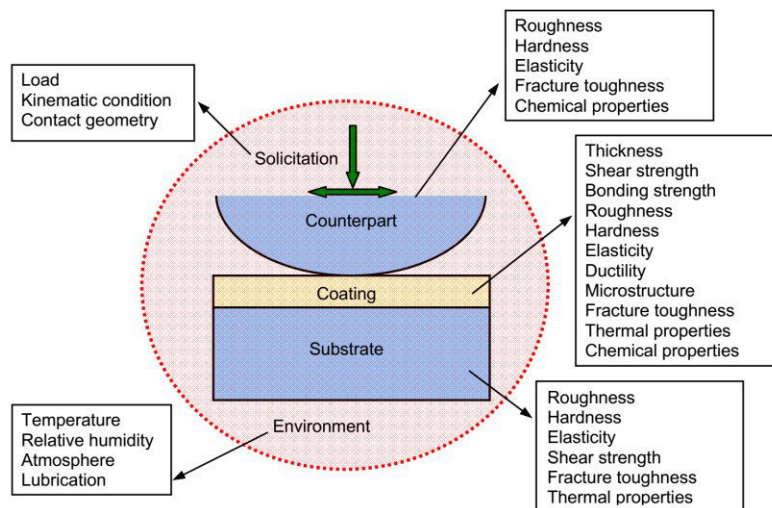
Fig. 22: Important properties from the perspective of tribology in different zones of the coated surface [119].

Since 2000, Nakahigashi and Takikawa et al. tried to increase the properties of O-rings by depositing DLC film on various rubbers, e.g., EPDM and FKM [120–122]. Later, researchers studied this subject thoroughly in terms of deposition methods [123–128], the microstructure of DLC film [129,130], physical and chemical characterization [125,131], substrates effects [132],

15

and tribological experiments [129,133]. The coefficient of friction decreased on NBR [134–136], HNBR [123,125,130,134,137], ACM [137–140], FKM [133,137,141], TPU [142], PDMS [143] with a DLC coating [134].
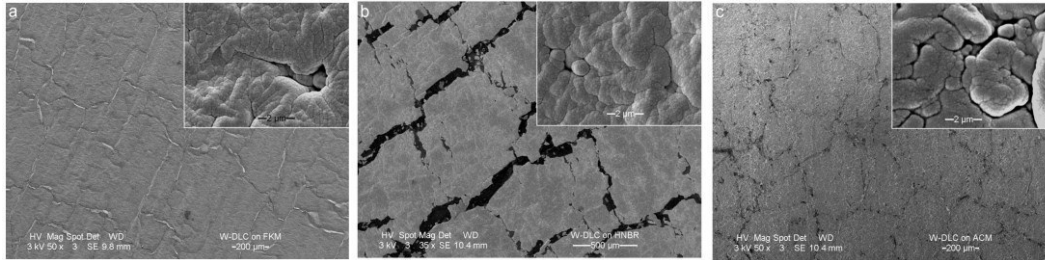
Fig. 23: Surface morphology of W-DLC coated (a) FKM; (b) HNBR; (c) ACM [137].

The coefficient of thermal expansion has a significant influence on the surface morphology of various rubbers. As can be seen in Fig. 23, the random crack networks opening is much larger on HNBR than on FKM and ACM. In addition, surface roughness can affect the coating morphology. A rougher substrate surface facilitates the shadowing effect, and thus more defects nucleate and grow in a coating [137].

For a coating system, the adhesion strength between the substrate and coating is of great importance. A low adhesion strength leads to fewer cracks but larger openings (Fig. 24a, c), while the adhesion is strong, initiation and opening of cracks are the only mechanisms responsible for releasing the stress applied on the whole system (Fig. 24b, d) [131]. As a consequence, the density of the crack network affects the flexibility and ultimately tribological properties of the coating system. Lower density of crack networks have a higher coefficient of friction [131]. This can be attributed to the larger segments of DLC film being more susceptible to breaking under normal and tangential stresses than smaller segments. Consequently, this can result in the formation of wear debris [131].
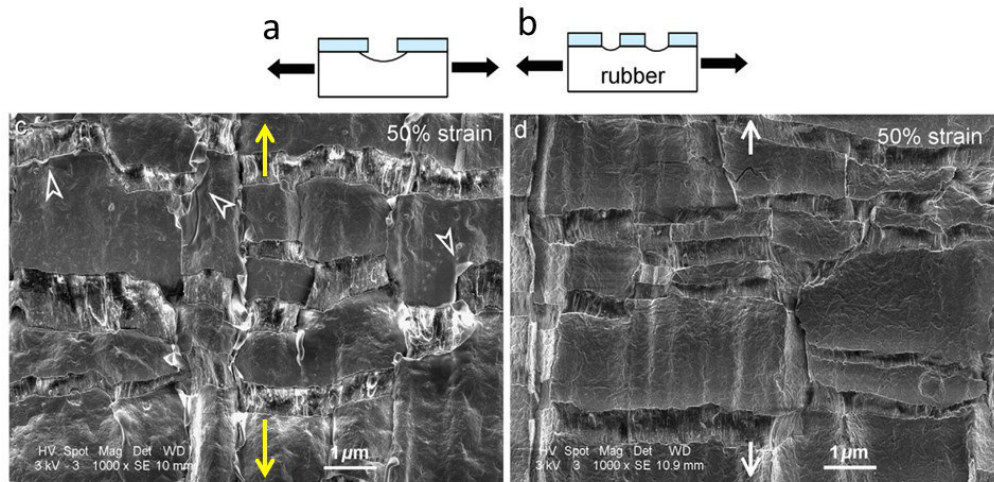
Fig. 24: Schematic sketch of the deformation of DLC film coated HNBR with (a) strong adhesion; (b) weak adhesion under tension. (c) Crack patterns of DLC film on HNBR, plasma cleaned for 20 mins; (d) for 40 mins and stretched to 50% strain along the direction indicated by yellow arrow [131].

References

[1]   Redesigning the space shuttles solid rocket motor seals. Sealing Technology 1996;1996(26):10–2. https://doi.org/10.1016/S1350-4789(96)80170-X.

[2]   Dalal SR, Fowlkes EB, Hoadley B. Risk Analysis of the Space Shuttle: Pre- Challenger Prediction of Failure. Journal of the American Statistical Association 1989;84(408):945–57. https://doi.org/10.1080/01621459.1989.10478858.

[3]   Szolwinski MP, Farris TN. Mechanics of fretting fatigue crack formation. Wear 1996;198(1-2):93–107. https://doi.org/10.1016/0043-1648(96)06937-2.

[4]   Dubourg MC, Chateauminois A, Villechaise B. In situ analysis and modeling of crack initiation and propagation within model fretting contacts using polymer materials. Tribology International 2003;36(2):109–19. https://doi.org/10.1016/S0301-679X(02)00137-8.

[5]   Flitney RK. Seals and sealing handbook. Amsterdam, Boston, Heidelberg: BH Butterworth-Heinemann an imprint of Elsevier; 2014.

[6]   Horve LA. Shaft seals for dynamic applications. New York, N.Y.: Dekker; 1996.

[7]   Hirabayashi H, Yukimasa T, Uchino K. Effect of Foreign Matters on Sealing Characteristics of Oil Seals. In: SAE Technical Paper Series. SAE International400 Commonwealth Drive, Warrendale, PA, United States; 1977.

[8]   Chandrasekaran VC. Rubber seals for fluid and hydraulic systems. Amsterdam: William Andrew; 2010.

[9]   Drobny JG. Handbook of thermoplastic elastomers. 2nd ed. Oxford, UK: William Andrew Publishing; 2014.

[10]   Zeinolebadi A. In-situ Small-Angle X-ray Scattering Investigation of Transient Nanostructure of Multi-phase Polymer Materials Under Mechanical Deformation. Berlin, Heidelberg: Springer Berlin Heidelberg; 2013.

[11]   Pinedo B, Hadfield M, Tzanakis I, Conte M, Anand M. Thermal analysis and tribological investigation on TPU and NBR elastomers applied to sealing applications. Tribology International 2018;127:24–36. https://doi.org/10.1016/j.triboint.2018.05.032.

[12]   Marcello Conte, Guido Belforte, Luigi Mazza. Accelerated life tests on piston seals for pneumatic cylinders. In: Ciulli E, editor. Proceedings of the 2nd European Conference on Tribology ECOTRIB 2009 ; Pisa, Italy, June 7 - 10, 2009. Pisa: Ed. Ets; 2009.

[13] El-Sonbati AZ. Thermoplastic elastomers. Rijeka, Croatia: InTech; 2012.

[14] Hieber J. Polyurethane for Special Sealing Applications and a Comparison to Rubber. International Polymer Science and Technology 2010;37(10):1–4. https://doi.org/10.1177/0307174X1003701001.

[15] Papatheodorou T (ed.). Friction and wear of piston rod sealings of filled PTFE compounds and TPU materials as a function of the piston rod surface. Gesellschaft fuer Tribologie e.V. (GfT); 2000.

[16] Klingender RC. Handbook of specialty elastomers. Boca Raton: CRC Press/Taylor & Francis; 2008.

[17] Hofmann W. Rubber technology handbook. Hanser Publishers. Distributed in the USA by Oxford University Press; 1989.

[18] Röthemeyer F, Sommer F. Kautschuk Technologie. München: Carl Hanser Verlag GmbH & Co. KG; 2013.

[19] Fritz Röthemeyer FS. Kautschuktechnologie: Werkstoffe - Verarbeitung - Produkte. München: Carl Hanser Verlag; 2013.

[20] Grosch KA. The Relation between the Friction and Visco-Elastic Properties of Rubber. Proceedings of the Royal Society A: Mathematical, Physical and Engineering Sciences 1963;274(1356):21–39. https://doi.org/10.1098/rspa.1963.0112.

[21] Persson BNJ. On the theory of rubber friction. Surface Science 1998;401(3):445–54. https://doi.org/10.1016/S0039-6028(98)00051-X.

[22] Moore DF. The friction and lubrication of elastomers. 1st ed. Oxford, New York: Pergamon Press; 1972.

[23] Zeng H. Polymer adhesion, friction, and lubrication; 2013.

[24] Myshkin NK, Petrokovets MI, Kovalev AV. Tribology of polymers: Adhesion, friction, wear, and mass-transfer. Tribology International 2005;38(11-12):910–21. https://doi.org/10.1016/j.triboint.2005.07.016.

[25] Moore DF, Geyer W. A review of adhesion theories for elastomers. Wear 1972;22(2):113–41. https://doi.org/10.1016/0043-1648(72)90271-2.

[26] Johnson KL. Adhesion and friction between a smooth elastic spherical asperity and a plane surface. Proceedings of the Royal Society A: Mathematical, Physical and Engineering Sciences 1997;453(1956):163–79. https://doi.org/10.1098/rspa.1997.0010.

[27] Maeda N, Chen N, Tirrell M, Israelachvili JN. Adhesion and friction mechanisms of polymer-on-polymer surfaces. Science 2002;297(5580):379–82. https://doi.org/10.1126/science.1072378.

[28] Belyi VA, Sviridyonok AI, Smurugov VA, Nevzorov VV. Adhesive Wear of Polymers. J. Lub. Tech. 1977;99(4):396. https://doi.org/10.1115/1.3453232.

[29] Moore DF, Geyer W. A review of hysteresis theories for elastomers. Wear 1974;30(1):1–34. https://doi.org/10.1016/0043-1648(74)90055-6.

[30] Heinrich G. Hysteresis Friction of Sliding Rubbers on Rough and Fractal Surfaces. Rubber Chemistry and Technology 1997;70(1):1–14. https://doi.org/10.5254/1.3538415.

[31] Zhang S-W. Tribology of elastomers. 1st ed. Amsterdam: Elsevier; 2004.

[32] Persson BNJ, Albohr O, Tartaglino U, Volokitin AI, Tosatti E. On the nature of surface roughness with application to contact mechanics, sealing, rubber friction and adhesion. J Phys Condens Matter 2005;17(1):R1-R62. https://doi.org/10.1088/0953-8984/17/1/R01.

[33] Schallamach A. How does rubber slide? Wear 1971;17(4):301–12. https://doi.org/10.1016/0043-1648(71)90033-0.

[34] Fukahori Y, Gabriel P, Busfield JJC. How does rubber truly slide between Schallamach waves and stick–slip motion? Wear 2010;269(11-12):854–66. https://doi.org/10.1016/j.wear.2010.08.016.

[35] Johnson KL, Kendall K, Roberts AD. Surface Energy and the Contact of Elastic Solids. Proceedings of the Royal Society A: Mathematical, Physical and Engineering Sciences 1971;324(1558):301–13. https://doi.org/10.1098/rspa.1971.0141.

[36] Zum Gahr K-H. Microstructure and wear of materials. Amsterdam, Oxford: Elsevier; 1987.

[37] Fukahori Y, Yamazaki H. Mechanism of rubber abrasion. Part I: Abrasion pattern formation in natural rubber vulcanizate. Wear 1994;171(1-2):195–202. https://doi.org/10.1016/0043-1648(94)90362-X.

[38] Fukahori Y, Yamazaki H. Mechanism of rubber abrasion part 3: How is friction linked to fracture in rubber abrasion? Wear 1995;188(1-2):19–26. https://doi.org/10.1016/0043-1648(94)06571-3.

[39] Fukahori Y, Yamazaki H. Mechanism of rubber abrasion. Wear 1994;178(1-2):109–16. https://doi.org/10.1016/0043-1648(94)90135-X.

[40] Rabinowicz E. Friction and wear of materials. 2nd ed. New York u.a.: Wiley; 1995.

[41] Arnell R d., Davies PB, Halling J, Whomes TL. Tribology: Principles and Design Applications. London, s.l.: Macmillan Education UK; 1991.

[42] Schallamach A. A theory of dynamic rubber friction. Wear 1963;6(5):375–82. https://doi.org/10.1016/0043-1648(63)90206-0.

[43] Bartenev GM, Lavrent'ev VV (eds.). Friction and wear of polymers. Amsterdam u.a.: Elesvier; Elsevier; 1981.

[44] Hausberger A, Major Z, Theiler G, Gradt T. Observation of the adhesive- and deformation-contribution to the friction and wear behaviour of thermoplastic polyurethanes. Wear 2018;412-413:14–22. https://doi.org/10.1016/j.wear.2018.07.006.

[45] Grün F, Sailer W, Gódor I. Visualization of the processes taking place in the contact zone with in-situ tribometry. Tribology International 2012;48:44–53. https://doi.org/10.1016/j.triboint.2011.03.026.

[46] Stachowiak GW, Batchelor AW, Stachowiak GB. Experimental methods in tribology. 1st ed. Amsterdam u.a.: Elsevier; 2004.

[47] Buckley DH. Surface effects in adhesion, friction, wear, and lubrication. Amsterdam, New York, New York: Elsevier Scientific Pub. Co; 2010.

[48] Persson BNJ. Theory of rubber friction and contact mechanics. The Journal of Chemical Physics 2001;115(8):3840–61. https://doi.org/10.1063/1.1388626.

[49] Bellow DG, Viswanath NS. An analysis of the wear of polymers. Wear 1993;162-164:1048–53. https://doi.org/10.1016/0043-1648(93)90121-2.

[50] Birkett A, Lancaster JK. Counterface effects on the wear of a composite dry-bearing liner. Wear 1986;110(3-4):345–57. https://doi.org/10.1016/0043-1648(86)90108-0.

[51] Ovaert TC, Cheng HS. Counterface topographical effects on the wear of polyetheretherketone and a polyetheretherketone-carbon fiber composite. Wear 1991;150(1-2):275–87. https://doi.org/10.1016/0043-1648(91)90323-M.

[52] Elliott DM, Fisher J, Clark DT. Effect of counterface surface roughness and its evolution on the wear and friction of PEEK and PEEK-bonded carbon fibre composites on stainless steel. Wear 1998;217(2):288–96. https://doi.org/10.1016/S0043-1648(98)00148-3.

[53] Barrett TS, Stachowiak GW, Batchelor AW. Effect of roughness and sliding speed on the wear and friction of ultra-high molecular weight polyethylene. Wear 1992;153(2):331–50. https://doi.org/10.1016/0043-1648(92)90174-7.

[54] Santner E, Klaffke D, Meine K, Polaczyk C, Spaltmann D. Effects of friction on topography and vice versa. Wear 2006;261(1):101–6. https://doi.org/10.1016/j.wear.2005.09.028.

[55] Friedrich K, Karger-Kocsis J, Lu Z. Effects of steel counterface roughness and temperature on the friction and wear of PE(E)K composites under dry sliding conditions. Wear 1991;148(2):235–47. https://doi.org/10.1016/0043-1648(91)90287-5.

[56] Mofidi M, Prakash B. Influence of counterface topography on sliding friction and wear of some elastomers under dry sliding conditions. Proceedings of the Institution of Mechanical Engineers, Part J: Journal of Engineering Tribology 2008;222(5):667–73. https://doi.org/10.1243/13506501JET392.

[57] Gabriel P, Thomas AG, Busfield JJC. Influence of interface geometry on rubber friction. Wear 2010;268(5-6):747–50. https://doi.org/10.1016/j.wear.2009.11.019.

[58] Dowson D, Diab MME-H, Gillis BJ, Atkinson JR. Influence of Counterface Topography on the Wear of Ultra High Molecular Weight Polyethylene Under Wet or Dry Conditions. In: Lee L-H, editor. Polymer Wear and Its Control. Washington, D.C.: American Chemical Society; 1985, p. 171–187.

[59] Sedlaček M, Podgornik B, Vižintin J. Influence of surface preparation on roughness parameters, friction and wear. Wear 2009;266(3-4):482–7. https://doi.org/10.1016/j.wear.2008.04.017.

[60] Hollander AE, Lancaster JK. An application of topographical analysis to the wear of polymers. Wear 1973;25(2):155–70. https://doi.org/10.1016/0043-1648(73)90068-9.

[61] Murat Aksulu and Mehmet Palabiyik (ed.). Effect of Counterface Roughness on the Wear of Polyoximethylene and Polypropylene; 2008.

[62] Thomas TR. Rough surfaces. 2nd ed. London: Imperial College Press; 1999.

[63] van Bavel PGM, Ruijl TAM, van Leeuwen HJ, Muijderman EA. Upstream Pumping of Radial Lip Seals by Tangentially Deforming, Rough Seal Surfaces. J. Tribol. 1996;118(2):266. https://doi.org/10.1115/1.2831295.

[64] Horve L. The Correlation of Rotary Shaft Radial Lip Seal Service Reliability and Pumping Ability to Wear Track Roughness and Microasperity Formation. In: SAE Technical Paper Series. SAE International400 Commonwealth Drive, Warrendale, PA, United States; 1991.

[65] Zhang G, Zhang C, Nardin P, Li W-Y, Liao H, Coddet C. Effects of sliding velocity and applied load on the tribological mechanism of amorphous poly-ether–ether–ketone (PEEK). Tribology International 2008;41(2):79–86. https://doi.org/10.1016/j.triboint.2007.05.002.

[66] Abdelbary A. Wear of polymers and composites. Oxford: Woodhead Publishing; 2015.

[67] Larson MG, Timpe SJ. Effect of Load and Temperature on the Tribological Characteristics of a Steel Pin on Polyoxymethylene Disk Interface. J. Tribol. 2017;139(5):51603. https://doi.org/10.1115/1.4035341.

[68] Gabriel P. Investigation and modelling of rubber friction. London: Queen Mary University of London; 2010.

[69] Sealing sense. Pumps & Systems 2004;November:20–1.

[70] Feng I‑M, Rightmire BG. An experimental study of fretting. ARCHIVE: Proceedings of the Institution of Mechanical Engineers 1847-1982 (vols 1-196) 1956;170(1956):1055‑64. https://doi.org/10.1243/PIME_PROC_1956_170_089_02.

[71] Vingsbo O, Söderberg S. On fretting maps. Wear 1988;126(2):131–47. https://doi.org/10.1016/0043-1648(88)90134-2.

[72] Vincent, L, Berthier, Y, Godet, M. Testing Methods in Fretting Fatigue: A Critical Appraisal. In: Attia HM, editor. Standardization of fretting fatigue test methods and equipment. Philadelphia Pa; 1992, p. 33–48.

[73] Zhou ZR, Nakazawa K, Zhu MH, Maruyama N, Kapsa P, Vincent L. Progress in fretting maps. Tribology International 2006;39(10):1068–73. https://doi.org/10.1016/j.triboint.2006.02.001.

[74] Jeong S-H, Yong S-J, Lee Y-Z. Friction and Wear Characteristics Due to Stick-Slip under Fretting Conditions. Tribology Transactions 2007;50(4):564–72. https://doi.org/10.1080/10402000701691076.

[75] Briscoe BJ, Chateauminois A, Lindley TC, Parsonage D. Fretting wear behaviour of polymethylmethacrylate under linear motions and torsional contact conditions. Tribology International 1998;31(11):701–11.

[76] Chateauminois A. Analysis of Fretting Damage in Polymers by Means of Fretting Maps. In: Elliott CB, Hoeppner DW, Chandrasekaran V, editors. Fretting fatigue: Current technology and practices. West Conshohocken, Pa: ASTM International; 2000.

[77] Dahmani N, Vincent L, Vannes B, Berthier Y, Godet M. Velocity accommodation in polymer fretting. Wear 1992;158(1-2):15–28.

[78] Wang Q, Wang Y, Wang H, Fan N, Yan F. Experimental investigation on tribological behavior of several polymer materials under reciprocating sliding and fretting wear conditions. Tribology International 2016;104:73–82.

[79] Stott FH, Bethune B, Higham PA. Fretting-induced damage between contacting steel-polymer surfaces. Tribology International 1977;10(4):211–5. https://doi.org/10.1016/0301-679X(77)90022-6.

[80] Rajesh JJ, Bijwe J. Influence of fillers on the low amplitude oscillating wear behaviour of polyamide 11. Wear 2004;256(1-2):1–8.

[81] Higham PA, Stott FH, Bethune B. The influence of polymer composition on the wear of the metal surface during fretting of steel on polymer. Wear 1978;47(1):71–80. https://doi.org/10.1016/0043-1648(78)90204-1.

[82] Higham PA, Bethune B, Stott FH. Changes in the surface morphology of polycarbonate induced by fretting. J Mater Sci 1977;12(12):2503–10. https://doi.org/10.1007/BF00553937.

[83] Major Z, Isasi M, Schwarz T. Characterization of the Fracture and Fatigue Behavior of Thermoplastic Elastomer Materials. KEM 2009;417-418:789–92. https://doi.org/10.4028/www.scientific.net/KEM.417-418.789.

[84] Shen M-x, Peng X-d, Meng X-k, Zheng J-p, Zhu M-h. Fretting wear behavior of acrylonitrile–butadiene rubber (NBR) for mechanical seal applications. Tribology International 2016;93:419–28.

[85] Banerjee N, Hills DA. Analysis of stick–slip and contact-edge behaviour in a simplified fretting fatigue test. The Journal of Strain Analysis for Engineering Design 2006;41(3):183–92. https://doi.org/10.1243/03093247JSA83.

[86] Jeong SH, Yong SJ, Ahn TS, Lee YZ. Influence of Stick-Slip Behavior on Friction and Wear under Fretting Conditions. KEM 2006;326-328:1189–92. https://doi.org/10.4028/www.scientific.net/KEM.326-328.1189.

[87] Robert M. Gresham. Slip-stick: What's it all about? Tribology & Lubrication Technology 2011;06:32–3.

[88] Alan Hitchcox. Reduce Vibration and Avoid Stiction in Seals; Available from: https://www.hydraulicspneumatics.com/hydraulic-fluids/reduce-vibration-and-avoid-stiction-seals.

[89] Landolsi F, Sun Y, Lu H, Ghorbel FH, Lou J. Regular and reverse nanoscale stick-slip behavior: Modeling and experiments. Applied Surface Science 2010;256(8):2577–82. https://doi.org/10.1016/j.apsusc.2009.10.107.

[90] Yoshizawa H, McGuiggan P, Israelachvili J. Identification of a second dynamic state during stick-slip motion. Science 1993;259(5099):1305–8. https://doi.org/10.1126/science.259.5099.1305.

[91] Bengisu MT, Akay A. Stick–slip oscillations: Dynamics of friction and surface roughness. The Journal of the Acoustical Society of America 1999;105(1):194–205. https://doi.org/10.1121/1.424580.

[92] Park JS, Lee SM, Joo BS, Jang H. The effect of material properties on the stick–slip behavior of polymers: A case study with PMMA, PC, PTFE, and PVC. Wear 2017;378-379:11–6. https://doi.org/10.1016/j.wear.2017.01.097.

[93] Dong C, Yuan C, Bai X, Qin H, Yan X. Investigating relationship between deformation behaviours and stick-slip phenomena of polymer material. Wear 2017;376-377:1333–8. https://doi.org/10.1016/j.wear.2017.01.061.

[94] Robbins MO, Thompson PA. Critical velocity of stick-slip motion. Science 1991;253(5022):916. https://doi.org/10.1126/science.253.5022.916.

[95] Berman AD, Ducker WA, Israelachvili JN. Origin and Characterization of Different Stick−Slip Friction Mechanisms †. Langmuir 1996;12(19):4559–63. https://doi.org/10.1021/la950896z.

[96] Liao C, Suo S, Wang Y, Huang W, Liu Y. Study on Stick–Slip Friction of Reciprocating O-Ring Seals Using Acoustic Emission Techniques. Tribology Transactions 2012;55(1):43–51. https://doi.org/10.1080/10402004.2011.626145.

[97] J. A. Greenwood and J. B. P. Williamson. Contact of nominally flat surfaces. Proc. R. Soc. Lond. A 1966;295(1442):300–19. https://doi.org/10.1098/rspa.1966.0242.

[98] Sawyer WG, Wahl KJ. Accessing Inaccessible Interfaces: In Situ Approaches to Materials Tribology. MRS Bull. 2008;33(12):1145–50. https://doi.org/10.1557/mrs2008.244.

[99] Krick BA, Vail JR, Persson BNJ, Sawyer WG. Optical In Situ Micro Tribometer for Analysis of Real Contact Area for Contact Mechanics, Adhesion, and Sliding Experiments. Tribol Lett 2012;45(1):185–94. https://doi.org/10.1007/s11249-011-9870-y.

[100] Wahl KJ, Sawyer WG. Observing Interfacial Sliding Processes in Solid–Solid Contacts. MRS Bull. 2008;33(12):1159–67. https://doi.org/10.1557/mrs2008.246.

[101] Eguchi M, Shibamiya T, Yamamoto T. Measurement of real contact area and analysis of stick/slip region. Tribology International 2009;42(11-12):1781–91. https://doi.org/10.1016/j.triboint.2009.04.046.

[102] Schulze KD, Bennett AI, Marshall S, Rowe KG, Dunn AC. Real Area of Contact in a Soft Transparent Interface by Particle Exclusion Microscopy. J. Tribol 2016;138(4):41404. https://doi.org/10.1115/1.4032822.

[103] Viswanathan K, Mahato A, Yeung H, Chandrasekar S. Surface phenomena revealed by in situ imaging: Studies from adhesion, wear and cutting. Surf. Topogr.: Metrol. Prop. 2017;5(1):14002. https://doi.org/10.1088/2051-672X/aa612a.

[104] Murarash B, Varenberg M. Tribometer for In Situ Scanning Electron Microscopy of Microstructured Contacts. Tribol Lett 2011;41(2):319–23. https://doi.org/10.1007/s11249-010-9717-y.

[105] Bennewitz R, Dickinson JT. Fundamental Studies of Nanometer-Scale Wear Mechanisms. MRS Bull. 2008;33(12):1174–80. https://doi.org/10.1557/mrs2008.248.

[106] Hÿtch MJ, Minor AM. Observing and measuring strain in nanostructures and devices with transmission electron microscopy. MRS Bull. 2014;39(02):138–46. https://doi.org/10.1557/mrs.2014.4.

[107]   Gammer C, Kacher J, Czarnik C, Warren OL, Ciston J, Minor AM. Local and transient nanoscale strain mapping during in situ deformation. Appl. Phys. Lett. 2016;109(8):81906. https://doi.org/10.1063/1.4961683.

[108]   Ferreira PJ, Mitsuishi K, Stach EA. In Situ Transmission Electron Microscopy. MRS Bull. 2008;33(02):83–90. https://doi.org/10.1557/mrs2008.20.

[109]   Marks LD, Warren OL, Minor AM, Merkle AP. Tribology in Full View. MRS Bull. 2008;33(12):1168–73. https://doi.org/10.1557/mrs2008.247.

[110]   Taheri ML, Stach EA, Arslan I, Crozier PA, Kabius BC, LaGrange T et al. Current status and future directions for in situ transmission electron microscopy. Ultramicroscopy 2016;170:86–95. https://doi.org/10.1016/j.ultramic.2016.08.007.

[111]   Feng C, Zhang D, Chen K, Guo Y, Hao T. Research on in-situ microscopic observation of dynamic contact and reciprocating sliding friction of GM-3 lining interface. Tribology International 2017;115:179–90. https://doi.org/10.1016/j.triboint.2017.05.023.

[112]   Sahli R, Pallares G, Ducottet C, Ben Ali IE, Akhrass S al, Guibert M et al. Evolution of real contact area under shear and the value of static friction of soft materials. Proc Natl Acad Sci U S A 2018;115(3):471–6. https://doi.org/10.1073/pnas.1706434115.

[113]   Rubinstein SM, Cohen G, Fineberg J. Visualizing stick–slip: experimental observations of processes governing the nucleation of frictional sliding. J. Phys. D: Appl. Phys. 2009;42(21):214016. https://doi.org/10.1088/0022-3727/42/21/214016.

[114]   Rubinstein SM, Cohen G, Fineberg J. Cracklike Processes within Frictional Motion: Is Slow Frictional Sliding Really a Slow Process? MRS Bull. 2008;33(12):1181–9. https://doi.org/10.1557/mrs2008.249.

[115]   Bennewitz R, David J, Lannoy C-F de, Drevniok B, Hubbard-Davis P, Miura T et al. Dynamic strain measurements in a sliding microstructured contact. J Phys Condens Matter 2008;20(1):15004. https://doi.org/10.1088/0953-8984/20/01/015004.

[116]   Holmberg K, Matthews A. Coatings tribology: Properties, mechanisms, techniques and applications in surface engineering. 2nd ed. Amsterdam u.a.: Elsevier; 2009.

[117]   Matthews A, Franklin S, Holmberg K. Tribological coatings: contact mechanisms and selection. J. Phys. D: Appl. Phys. 2007;40(18):5463–75. https://doi.org/10.1088/0022-3727/40/18/S07.

[118]   Menezes PL, Ingole SP, Nosonovsky M, Kailas SV, Lovell MR (eds.). Tribology for scientists and engineers: From basics to advanced concepts. New York: Springer; 2013.

[119]   Dabing LUO. Selection of Coatings for Tribological Applications [Dissertation]. Lyon: École Centrale de Lyon; 2009.

[120]   Takikawa H, Miyakawa N, Minamisawa S, Sakakibara T. Fabrication of diamond-like carbon film on rubber by T-shape filtered-arc-deposition under the influence of various ambient gases. Thin Solid Films 2004;457(1):143–50. https://doi.org/10.1016/j.tsf.2003.12.029.

[121]   Takikawa H, Miyakawa N, Toshifuji J, Minamisawa S, Matsushita T, Takemura K et al. Preparation of Elastic DLC Film on Rubber by T-shape Filtered Arc Deposition. IEEJ Trans. FM 2003;123(8):738–43. https://doi.org/10.1541/ieejfms.123.738.

[122]   T. Nakahigashi, K. Miyake, Y. Murkami. Application of DLC Coating to Rubber and Polymer Materials. Journal of Japanese Society of Tribologists 2002;47.

[123]   Pei YT, Bui XL, Hosson JTM de. Flexible protective diamond-like carbon film on rubber. Scripta Materialia 2010;63(6):649–52. https://doi.org/10.1016/j.scriptamat.2010.05.036.

[124]   Bui XL, Pei YT, Hosson JTM de. Magnetron reactively sputtered Ti-DLC coatings on HNBR rubber: The influence of substrate bias. Surface and Coatings Technology 2008;202(20):4939–44. https://doi.org/10.1016/j.surfcoat.2008.04.078.

[125]   Bui XL, Pei YT, Mulder EDG, Hosson JTM de. Adhesion improvement of hydrogenated diamond-like carbon thin films by pre-deposition plasma treatment of rubber substrate. Surface and Coatings Technology 2009;203(14):1964–70. https://doi.org/10.1016/j.surfcoat.2009.01.027.

[126]   Thirumalai S, Hausberger A, Lackner JM, Waldhauser W, Schwarz T. Anode layer source plasma-assisted hybrid deposition and characterization of diamond-like carbon coatings deposited on flexible substrates. Thin Solid Films 2018;655:54–61. https://doi.org/10.1016/j.tsf.2018.04.012.

[127]   Miyakawa N, Minamisawa S, Takikawa H, Sakakibara T. Physical–chemical hybrid deposition of DLC film on rubber by T-shape filtered-arc-deposition. Vacuum 2004;73(3-4):611–7. https://doi.org/10.1016/j.vacuum.2003.12.079.

[128]   Martinez-Martinez D, Hosson JTM de. On the deposition and properties of DLC protective coatings on elastomers: A critical review. Surface and Coatings Technology 2014;258:677–90. https://doi.org/10.1016/j.surfcoat.2014.08.016.

[129]   van der Pal JP, Martinez-Martinez D, Pei YT, Rudolf P, Hosson JTM de. Microstructure and tribological performance of diamond-like carbon films deposited on hydrogenated rubber. Thin Solid Films 2012;524:218–23. https://doi.org/10.1016/j.tsf.2012.10.005.

[130]   Pei YT, Martinez-Martinez D, van der Pal JP, Bui XL, Zhou XB, Hosson JTM de. Flexible diamond-like carbon films on rubber: Friction and the effect of viscoelastic deformation of rubber substrates. Acta Materialia 2012;60(20):7216–25. https://doi.org/10.1016/j.actamat.2012.09.031.

[131]   Pei YT, Bui XL, Hosson JTM de. Deposition and characterization of hydrogenated diamond-like carbon thin films on rubber seals. Thin Solid Films 2010;518(21):S42-S45. https://doi.org/10.1016/j.tsf.2010.03.018.

[132]   Thirumalai S, Hausberger A, Lackner JM, Waldhauser W, Schwarz T. Effect of the type of elastomeric substrate on the microstructural, surface and tribological characteristics of diamond-like carbon (DLC) coatings. Surface and Coatings Technology 2016;302:244–54. https://doi.org/10.1016/j.surfcoat.2016.06.021.

[133]   Pei YT, Bui XL, Zhou XB, Hosson JTM de. Tribological behavior of W-DLC coated rubber seals. Surface and Coatings Technology 2008;202(9):1869–75. https://doi.org/10.1016/j.surfcoat.2007.08.013.

[134]   Martínez L, Nevshupa R, Álvarez L, Huttel Y, Méndez J, Román E et al. Application of diamond-like carbon coatings to elastomers frictional surfaces. Tribology International 2009;42(4):584–90. https://doi.org/10.1016/j.triboint.2008.06.016.

[135]   Lubwama M, Corcoran B, Sayers K, Kirabira JB, Sebbit A, McDonnell KA et al. Adhesion and composite micro-hardness of DLC and Si-DLC films deposited on nitrile rubber. Surface and Coatings Technology 2012;206(23):4881–6. https://doi.org/10.1016/j.surfcoat.2012.05.079.

[136]   Pei YT, Eivani AR, Zaharia T, Kazantzis AV, van de Sanden MCM, Hosson JTM de. High throughput deposition of hydrogenated amorphous carbon coatings on rubber with expanding thermal plasma. Surface and Coatings Technology 2014;245:74–83. https://doi.org/10.1016/j.surfcoat.2014.02.043.

[137]   Pei YT, Bui XL, Zhou XB, Hosson JTM de. Microstructure and tribological behavior of tungsten-containing diamondlike carbon coated rubbers. Journal of Vacuum Science & Technology A: Vacuum, Surfaces, and Films 2008;26(4):1085–92. https://doi.org/10.1116/1.2889443.

[138]   Martinez-Martinez D, Schenkel M, Pei YT, Hosson JTM de. Microstructural and frictional control of diamond-like carbon films deposited on acrylic rubber by plasma assisted chemical vapor deposition. Thin Solid Films 2011;519(7):2213–7. https://doi.org/10.1016/j.tsf.2010.11.006.

[139]   Martinez-Martinez D, Schenkel M, Pei YT, Sánchez-López JC, Hosson JTM de. Microstructure and chemical bonding of DLC films deposited on ACM rubber by PACVD. Surface and Coatings Technology 2011;205:S75-S78. https://doi.org/10.1016/j.surfcoat.2011.02.067.

[140]   Martinez-Martinez D, van der Pal JP, Pei YT, Hosson JTM de. Performance of diamond-like carbon-protected rubber under cyclic friction. I. Influence of substrate viscoelasticity on the depth evolution. Journal of Applied Physics 2011;110(12):124906. https://doi.org/10.1063/1.3665443.

[141]   Masami I, Haruho M, Tatsuya M, Junho C. Low temperature Si-DLC coatings on fluoro rubber by a bipolar pulse type PBII system. Surface and Coatings Technology 2011;206(5):999–1002. https://doi.org/10.1016/j.surfcoat.2011.04.011.

[142]   Lackner JM, Major R, Major L, Schöberl T, Waldhauser W. RF deposition of soft hydrogenated amorphous carbon coatings for adhesive interfaces on highly elastic polymer materials. Surface and Coatings Technology 2009;203(16):2243–8. https://doi.org/10.1016/j.surfcoat.2009.02.012.

[143]   Nagashima S, Hasebe T, Tsuya D, Horikoshi T, Ochiai M, Tanigawa S et al. Controlled formation of wrinkled diamond-like carbon (DLC) film on grooved poly(dimethylsiloxane) substrate. Diamond and Related Materials 2012;22:48–51. https://doi.org/10.1016/j.diamond.2011.12.013.

Part II: Structure and collection of papers

1. Structure and content

Vibration is a common phenomenon in machines, which can be found in almost every aspect of our daily life, from the washing machine to automotive vehicles to industrial machinery. The seals in these machines, experience small amplitude reciprocating movements due to the vibration of the system. For a large number of cycles, fretting behavior can be observed in seals, which can lead to a failure of seals and ultimately the machinery system.

Fretting is one of the most common failures for seals in dynamic applications. With the advancement of technology, the demand for seals is increasing. Even though considerable research has been conducted on the fretting behavior of metals, there is still little understanding of this behavior in polymers, in particular, sealing materials. Due to the viscoelastic material properties and low elasticity modulus of elastomers, the experimental method of studying fretting behavior of metals, which were developed in the last decades, cannot be directly applied to elastomers. In addition, to understand the fretting behavior of elastomers, the dynamic mechanical properties, tribological properties, and fatigue properties, etc., must all be taken into consideration. Therefore, there is a critical need to investigate the fretting behavior of sealing materials with a newly developed method.

Fretting is a multidisciplinary theme, which includes contact mechanics, tribology, fatigue and physical phenomenon (e.g., stick-slip motion). In this work, several topics, which can be identified in the fretting behavior of elastomers, are studied separately. Therefore, the following topics were thoroughly studied in this work:

- **Fretting behavior of elastomers**: development of a fretting test method for elastomers; analysis based on material properties; hysteresis behavior; fractographic and wear mechanism; new method to calculate the coefficient of friction; comparison of the fretting behavior of different TPUs.
- **Correlation between fatigue and tribological properties of TPU**: validation of two analytical models of wear for unfilled and filled TPUs; fatigue tests with dumbbell and faint-waist-pure-shear tests; considering the asperities on countersurface in one of the models; abrasive, adhesive and fatigue wear mechanism.
- **Stick-slip behavior using the in-situ technique:** observation of the real contact area during sliding and creep tests; a correlation between friction and

real contact area; the influence of sliding velocity on stick-slip behavior; analysis of the stick region during stick phase using machine learning; alteration of stick-slip behavior with cycles.

- **Coatings on elastomers:** optimization of the tribological properties of elastomers using coatings; deposition of DLC and MoS_2 and combined coatings of MoS_2 and DLC on four sealing materials; tribological model and component-like tests under dry and lubricated conditions; analysis of the friction and wear mechanism; selection of the best coating for each material.

In this study, TPU was chosen for most of the experiments. In the fretting tests, five different TPUs were investigated. Furthermore, the effect of fillers on the fatigue and tribological properties of TPU were studied. For the stick-slip sliding tests, five elastomers were investigated. However, due to the limited space, only the behavior of FKM was reported in the paper. To get a general application potential of coatings on sealing materials, four elastomers were investigated.

In this section, a collection of five papers, regarding the topics mentioned above, was introduced. The topics of the papers, the name of the scientific journals and publishing re are listed below. The original papers with their formats from each journal are listed in the fourth part of this section.

- **Paper 1:** An investigation of fretting behavior of thermoplastic polyurethane for mechanical seal application. (**Polymer Testing**, Elsevier)

- **Paper 2:** Fretting behavior of thermoplastic polyurethanes. (**Lubricants**, MDPI)

- **Paper 3:** Correlation between tribological behavior and fatigue properties of filled and unfilled TPU. (**Lubricants**, MDPI)

- **Paper 4:** Precise correlation of friction force and contact area during stick-slip by in situ microscopy with microtribometry in an elastomer-glass contact.

    (**Tribology International**, Elsevier)

- **Paper 5:** The Potential of Tribological Application of DLC/MoS_2 Coated Sealing Materials.

    (**Coatings**, MDPI)

2. Outline of papers

Although fretting is a common failure in seals, few studies have been done to investigate the fretting behavior of sealing materials. Significant research has been conducted to study the fretting behavior of metals; however, the conclusions developed for metals cannot be applied directly to elastomers and thermoplastic elastomers. Elastomers have a much lower elasticity modulus than metals, and their mechanical properties depend strongly on the dynamic conditions. The other significant difference is the temperature dependence of the properties of polymers. Because of their viscoelasticity and temperature-dependence, polymers exhibit starkly different fretting behavior from metals. For elastomers, the test conditions, wear mechanism, calculation of the coefficient of friction, and other analysis must be studied and newly defined.

In **Paper 1**, a method of characterization of the fretting behavior of TPU was introduced. The method includes the experimental tests and analysis of the results. In the experimental part, new test parameters were defined based on the pretests. According to the transition criterion, a calculation was performed to guaranty that the tests performed fall under the definition of fretting. The criterion is based on the oscillatory amplitude, Hertzian radius of contact, and set a transition line between fretting and sliding. To study the influence of normal loads and displacement amplitudes on fretting behavior, four different displacement amplitudes (0.1 mm, 0.25 mm, 0.5 mm, 1.0 mm) and three normal loads (20 N, 28 N, 48 N) were applied. The total number of cycles was 8×10^5 because the fretting phenomena can only be observed after $10^4 - 10^5$ cycles. In addition, several tests were repeated and ran until some given cycles, in which their hysteresis form changed significantly. Using this method, the development of the wear scar can be carefully studied and correlated to the hysteresis. All three fretting regimes were identified. Based on the two-dimensional tangential force–displacement (F_t–D) curve and three-dimensional hysteresis, the change in tangential force with cycles was analyzed. The analysis of the wear scar was performed with an optical microscopy and a scanning electron microscopy (SEM). For partial slip regime (PSR) and mixed fretting regime (MFR), the diameter of the whole contact area and stick region were measured, and their coefficients of friction were calculated based on the wear scar. For gross slip regime (GSR), due to its large wear scar, the topography of the wear scar and the mass of the test system cannot be neglected. In the end, the running condition fretting map (RCFM) was presented. Even though no accurate border among the three regimes can be defined, the map shows how the test parameters influence the fretting behavior. The newly developed method can also be used to test other elastomers and thermoplastic elastomers.

Using the method developed in **Paper 1**, five different TPUs were compared with respect to their fretting behavior. The results were presented in **Paper 2**. The dynamic mechanical properties of materials were characterized using dynamic mechanical analysis (DMA). To study the difference in the thermal properties of the materials, thermal conductivity was measured. The chemical structures were characterized with a Fourier-transform infrared spectroscopy (FTIR). As we know, temperature dictates the properties of polymers. However, due to the limited space near the contact area, the specimen temperature is difficult to measure. Therefore, an indirect method was applied, the temperature of the counterpart was measured using an infrared sensor with a resolution of 0.1 K. Dissipated energy was calculated for each test and presented approximately how temperature changed during the tests. In addition, to compare the sliding performance and fretting behavior of the five TPUs, tribological tests were conducted using a component-like (ring on disc) configuration. However, due to the different test methods and wear mechanisms, the COF from tribological and fretting tests are not comparable. Wear scars and counterparts were analyzed using microscopy. It was found, in PSR, materials were adherent to the counterpart, which can be attributed to the large stick region and the cyclic shear stress. Compared to PSR, the amount of adherent material is less in MFR. In GSR, slight abrasive wear and third body wear were identified. TPU_4 shows the best tribological performance and the best fretting behavior.

Fretting is a long-term physical process, in which fatigue plays an essential role. Generally, seals are designed for long service life in machines. Their functions, e.g., avoiding leakage and excellent tribological performance, should be guaranteed during the service life. Therefore, the fatigue properties and their relations with tribological properties were investigated. In **Paper 3**, two analytical wear models were verified for filled and unfilled TPUs. Fatigue properties and crack growth rate were characterized with dumbbell and faint waist pure shear tests, respectively. The influence of temperature on fatigue properties was identified at 23°C and 80°C. To compare the tribological properties, various tests were conducted using different experimental configurations. SEM was applied to analyze the fracture and worn surfaces after fatigue and tribological tests, respectively. Dynamic mechanical analysis (DMA) was conducted in temperature sweep mode, which was correlated with the fatigue performance at 23°C and 80°C. The Panda model describes abrasive and fatigue wear mechanisms, which are consequences of plastic and elastic deformation of materials, respectively. The asperities on the countersurface are assumed to be rigid, and their heights follow a probability distribution. Each asperity has the same spherical tip, and its radius is the average measured radius of the whole surface. This model is modified by introducing a factor for abrasive wear. In tribological tests, a transfer film was generated after the space among the asperities were filled. Thus, polymeric samples did not slide against the same

countersurface as at the beginning. A correction factor, which is based on each tribological test, helps to reflect the real wear process. The Atkins model was developed for adhesive wear and fatigue wear mechanisms. It aims to correlate the tribological performance with crack growth. The comparisons of the experimental results and analytical wear models show that the Panda model is better for rough countersurfaces, while the Atkins model is more suitable for smooth countersurfaces.

Paper 4 focuses on the stick-slip behavior of elastomers, which is observed in the fretting tests. In addition to fretting behavior, stick-slip motion is also a common phenomenon that can be observed in our daily life. For seals, stick-slip causes vibrations that lead to crack initiation and wear. Insufficient lubrication at low speeds and high pressures can induce stick-slip. To understand the stick-slip motion, the real contact area is of great importance. Using the in-situ technique, the real contact area was observed during the sliding tests. Otsu's method was applied to threshold the video and define the contact area. In the stick phase, the specimen moved with the countersurface until the tangential force reached a maximum. However, partial slip was observed in the outer part of the contact area. Machine learning was employed to analyze the stick region. By using the coordinates obtained from manually marking the stick region in about 300 single frames, a convolutional neural network (CNN) was trained to predict the stick region of the remaining 61000 images accurately. The results show a good correlation between the movement of the stick region and the change in friction force. The contact area changed within the stick phase, and it decreased from the outer area. Prior to slip, only the middle region was still adherent on the countersurface. The size of the stick region was calculated through subtraction of two frames, which was adjusted according to the movement of the countersurface at that time. The overlapped region is the stick region. The stick area decreased from the beginning to the end of the stick phase. In the beginning, due to the low elasticity of FKM, the whole contact area moved with the countersurface. Therefore, no slip took place. With further movement, the tangential force increased with increasing deformation of the sample. Consequently, part of the adhesive bonds began to break, and these areas transformed into the slip region. The stick process was analyzed using differential equations, which includes a stick term and a slip term. In addition, the influence of sliding speeds on stick-slip behavior was studied. In the low-speed regime (between 1 µm/s and 5 µm/s), a critical sliding speed was identified as a transition between "micro" and "macro" stick-slip. It differs from the critical speed in literature, which describes a transition between stick-slip and sliding motion. The change in the stick region and whole contact region with cycles were studied. Depending on the sliding velocity, stick-slip behavior disappeared gradually after a certain number of cycles. Creep tests were performed to study the change in contact area with time. Due

to the viscoelasticity of the material, the creep effect was observed in sliding tests. The contact area increased with cycles. The frequencies of stick-slip behavior and change in contact area were analyzed with Fast Fourier Transition (FFT). It showed a strong correlation between friction force and contact area. This study on the sliding behavior of the viscoelastic sealing material will be of value to understanding its friction and stick-slip behavior.

To improve the tribological performance of sealing materials, several coatings were investigated. Coatings improve the surface properties by controlling friction and wear without changing the substrate material. In **Paper 5**, both hard and soft coatings were investigated on four sealing materials, including FKM, NBR, HNBR, and TPU. Due to its high hardness and low coefficient of friction, diamond-like carbon (DLC) was studied as the hard coating on elastomers. DLC film was coated with C_2H_2 and Ar, and thus it existed in the form of a-c: H film. Molybdenum disulfide (MoS_2) allows two bodies to slide against each other with low friction, which can be attributed to its lamellar structure and consequently a reduction of adhesive resistance and excellent shear characteristics. Besides pure DLC and MoS_2, composite coatings of these two materials with various DLC/ MoS_2 ratios were investigated in terms of their tribological performance. To improve the adhesion of the coatings, a pre-treatment process was carried out before deposition. The pulsed DC magnetron sputtering method was applied for deposition. To avoid the thermal influence of substrates, the pre-treatment and deposition processes were performed under constant ambient temperature (23°C). The deposited coatings were chemically, physically, and mechanically characterized. X-ray photoelectron spectroscopy (XPS) was employed to check the chemical compositions. Thickness and surface roughness were characterized to check their quality. In addition, the coefficient of thermal expansion and thermal conductivity were measured to analyze the differences in thermal properties of four substrates. Microscopic analysis was conducted before and after the coating process. The different material properties, in particular, elasticity and viscosity, affect the material behavior in the molding process and ultimately their surface microstructure. Even though all substrates show similar structures at the macroscale, an entirely different structure was identified at the microscale. The coating roughness was influenced by the substrate properties and the composition of the coating. Scaly microstructures were observed on the DLC coated samples, while the MoS_2 coatings appeared to be much finer and more adaptable to the substrate roughness. For the hybrid coatings, MoS_2 lowered the average coating hardness. Due to the low wettability of FKM, the coatings on it were porous and loose. Model tests were conducted using the ball on disc setup under dry and lubricated conditions. Under the lubricated condition, the adhesion part of friction was decreased significantly. Thus, the difference of COF among various coatings was not evident as they were in dry tests. Based on the tribological

performance in model tests, the best coating for each substrate material was chosen and verified in the component-like (ring on disc) experiments. Overall, the concept to improve the tribological performance of rubbers, especially under starved lubrication condition, was verified. It was found that there is no single coating is the optimal one for all substrates. Depending on the substrate properties, the best coating can be selected individually. Soft coatings like MoS_2 showed the best tribological performance for rubbers with low rigidity, while hard coatings are better for rubbers with high rigidity. Hybrid coatings are the best choice for rubbers with medium stiffness.

3. Outlook

The scope of the thesis was, to a certain extent, subject to the availability of materials provided by industrial partners. The sealing materials studied in this thesis were TPU, HNBR, NBR, and FKM. Only TPUs were characterized in fretting tests. It is suggested to test the other types of sealing materials using the developed fretting test method. It would also be beneficial if the surface temperature of samples can be measured during fretting tests. It will enable an exact correlation between material properties and fretting behavior. With a smaller interval of displacement amplitude, clear transitions can be identified between partial slip, mixed fretting, and gross slip regimes in the Running Condition Fretting Map (RCFM).

The wear models verified in Paper 2 possess several limitations, because they do not reflect the environment of real situations. For example, all of the surface asperities in the experiments have a spherical tip and their heights follow a probability distribution, which would not be found in a real-world environment. Additionally, the transfer films generated during the sliding tests were not taken into consideration. The two models describe adhesive and abrasive wear separately. A model that considers all of the wear mechanisms is needed.

The stick-slip effect was observed in fretting tests. To understand the physical process, sliding tests were conducted with turned samples. The movement of the stick region in the stick phase was analyzed utilizing machine learning. However, the size of the stick region was not characterized. The size of the stick region has an essential meaning in tangential force. It is suggested to characterize the size of the stick region and correlate with the tangential force. Additionally, it is beneficial to employ an optical observing system with a higher frame rate (higher than 20 FPS). The reason for this is that the slip phase occurs merely in a few milliseconds. To capture the slip moments, cameras with a higher frame rate is necessary.

The improved performance of mechanical seals with coatings was verified. DLC and MoS_2 were chosen as the hard and soft coatings in this thesis, respectively. However, many other coating materials should also be investigated. The combinations of different materials may present a better performance than individually. The deposition method can influence the coating performance significantly. The best deposition process enables a homogenous composite distribution in the coating, excellent adhesion with the substrate and consequently, long service life.

Overall, fretting is only one of the many factors that can lead to the failure of polymeric seals. Failure is a consequence of many factors and mechanisms. To guarantee better performance of

mechanical seals, other forms of failure, e.g., incorrect starting procedure, fitting errors, and incorrect setting, should also be considered.

4. Collection of papers

Paper 1: An Investigation of Fretting Behavior of Thermoplastic Polyurethane for Mechanical Seal Application

C. Wang[1], A. Hausberger[1], M. Berer[1], G. Pinter[2], F. Grün[3], T. Schwarz[4]

[1] Polymer Competence Center Leoben GmbH, Leoben, Austria

[2] Chair of Materials Science and Testing of Polymers, Montanuniversität Leoben, Leoben, Austria

[3] Chair of Mechanical Engineering, Montanuniversität Leoben, Leoben, Austria

[4] SKF Sealing Solutions Austria GmbH, Judenburg, Austria

Authors and relevant contributions to this publication:

- C. Wang: Application and implementation of fretting method, experimental testing, data evaluation, preparation of the publication
- A. Hausberger: Conceptualization, discussion of experimental data, review the publication
- M. Berer: Program for energy calculation, review the publication
- G. Pinter: Review the publication
- F. Grün: Review the publication
- T. Schwarz: Specimen production, Review the publication

Material Behaviour

An investigation of fretting behavior of thermoplastic polyurethane for mechanical seal application

C. Wang[a,*], A. Hausberger[a], M. Berer[a], G. Pinter[b], F. Grün[c], T. Schwarz[d]

[a] Polymer Competence Center Leoben GmbH, Leoben, Austria
[b] Chair of Materials Science and Testing of Polymers, Montanuniversität Leoben, Leoben, Austria
[c] Chair of Mechanical Engineering, Montanuniversität Leoben, Leoben, Austria
[d] SKF Sealing Solutions Austria GmbH, Judenburg, Austria

ARTICLE INFO

ABSTRACT

For seals in dynamic applications, fretting is one of the most common types of failure. In this study, the fretting behavior of thermoplastic polyurethane (TPU) was investigated. The hysteresis behavior, wear scar and coefficient of friction were analyzed in detail. Various wear mechanisms and their influences on the fretting behavior were examined. A new method was introduced to calculate the coefficient of friction for late cycles in gross slip regime. It takes the surface damage and the dynamic influence of the test system into consideration. Besides, the dependency of fretting behavior on displacement amplitudes, normal loads were investigated.

1. Introduction

TPU is an elastomer, which is fully thermoplastic. Hence, it offers elasticity and also processing flexibility at the same time. These unique properties make TPU an ideal polymer in a large variety of applications and markets. These range from footwear, mobile electronic devices to the automotive industry, and seals. The latter are subjected to investigations in the industry. In spite of the vital importance for the industrial applications, there is still lack of scientific studies of seals [1].

Fretting occurs between two contacting surfaces that are reciprocating sliding in short amplitude for a large number of cycles. For seals in dynamic applications, fretting is one of the most common types of failure. Plenty of effort has been done on fretting in metallic materials. Christiner et al. [2] have developed a calculation model that allows an assessment of the fretting fatigue endurance limit. Instead of the classical normal load – displacement fretting map approach, Fourvy et al. [3] have developed a new method to quantify the fretting damage, which is based on the normalized representations. Varenberg et al. [4] have introduced a slip index to determine the different fretting regimes. In addition, the crack initiation for fretting fatigue was also widely investigated. Kubiak et al. [5] have studied the influence of roughness of the contact interfaces on fretting behavior, and they mentioned the importance of the initial surface roughness on the coefficient of friction at the transition from partial slip to the gross slip regime. Some research has focused on polymers during the past two decades. Briscoe et al. [6] have studied the fretting wear behavior of polymethylmethacrylate

(PMMA) under linear and torsional motions by using an in-situ method. It reveals the effect of contact kinematics on debris accumulation and elimination. Chateauminois et al. [7] have investigated the fretting wear behavior of epoxy and PMMA by using fretting maps and finite element method (FEM) simulation. Recently, Tan et al. [8] have studied the fretting behaviors of several unfilled thermoplastics and pointed out the correlation of fretting wear amount and glass transition temperature (T_g), melting point (T_m) and dielectric constant (ε). Shen et al. [9] have studied the fretting behaviors of Nitrile Butadiene Rubber (NBR) and analyzed the relation among fretting wear behavior, the coefficient of friction, wear mechanisms, displacement amplitude, and normal load. Wang et al. [10] have compared the fretting behavior of six polymers. However, for thermoplastic elastomer, there is an urgent need to reveal its fretting behavior and damage mechanisms.

In this research, the fretting behavior of TPU was experimentally investigated by varying the displacement amplitudes and normal loads between the contact surfaces. Moreover, the fretting hysteresis, wear scar, and coefficient of friction were analyzed in detail. The study aims to shed light on the fretting behavior and damage mechanisms of thermoplastic elastomer-to-metal contact.

2. Experimental details

2.1. Material and specimen

The TPU specimens used in this study were produced by injection

---

Table 1
Material properties of the TPU used in this study.

Material	Density [g/cm3]	Hardness	Dynamic Mechanical Analysis			
		Shore-D	Frequency	E' [MPa]	E″ [MPa]	Tan δ
TPU	1.192	47	10 Hz	93.8	12.3	0.131

E': storage Modulus.
E″: loss Modulus.

molding at SKF Sealing Solutions Austria GmbH. Before the tests, they were cut into 36 mm × 22 mm plates with a thickness of 6.2 mm. For the basic mechanical characterization, the hardness was measured using Shore-D method, and the dynamic mechanical properties were analyzed by using Dynamic Mechanical Analysis (DMA) by means of temperature scan method (EPLEXOR 100 N, NETZSCH GABO Instruments GmbH, Germany). The DMA values at 25 °C and other properties of the material are given in Table 1.

2.2. Test setup and methods

In this research, the fretting behavior of TPU was experimentally investigated by varying displacement amplitudes and normal loads acting on the contact surfaces. As counterpart commercial stainless steel balls (1.4301 steel, polished, unhardened, $\phi = 15$ mm, Ra = 0.05 μm, HSI-Solutions GmbH, Austria) were used.

The fretting tests were performed on a servo-hydraulic MTS 858 Horizontal (MTS Systems Corporation, USA) with a self-made setup (Fig. 1a). The top view of this fretting wear test setup is illustrated in Fig. 1b.

The whole setup was conducted by a hydraulic system, which was regulated by a digital servo controller. The specimen holder was connected to the hydraulic system through a load cell. Thus the tangential force (F_t) could be measured. Two specimens, come at each side, were fixed on the specimen holder by lids. The counterparts, which were fixed on cylinders, pressed on the specimens through holes on these lids. The normal loads (F_n) were measured by one load cell on each side. The normal loads, specimens, and counterparts for both sides were identical. Thus an unbalanced running condition for the servo-hydraulic system can be avoided.

There are three fretting regimes, namely partial slip regime (PSR), mixed fretting regime (MFR), and gross slip regime (GSR) [11–13]. In PSR, the middle area of the contact sticks to the counterpart. Hence, there is no relative motion in the middle area. Partial slip occurs only on the edge part. Due to the large displacement in GSR, the whole contact area slips over counterpart. MFR is a transition regime, in which only the middle point sticks to the counterpart, the majority of the area slips.

The test parameters are listed in Table 2. In order to cover the three fretting regimes, namely partial slip regime (PSR), mixed fretting regime (MFR), and gross slip regime (GSR) [11,12], the displacement amplitudes (D) range from ± 0.1 mm to ± 1.0 mm. Due to the

comparatively high compliance of polymer, the displacement amplitude required to cause fretting is usually larger for polymers than for metals. For the latter, the amplitude is approximately 10–50 μm [14]. Because of their elasticity, the displacement amplitudes for thermoplastic elastomers were expected to be above those for normal glass polymers. According to the transition criteria, which was proposed by Fouvry et al. [13], when the ratio of D (oscillatory amplitude) to a (Hertzian radius of contact), D/a < 1, it is still fretting. For the test with 1 mm amplitude and 28 N load, the radius of the Hertzian contact radius (a) is 1.062. Hence, the ratio of D/a is 0.942, still smaller than 1. So, it is still fretting, but almost reached the limit.

Three different load levels were used to investigate the dependence of TPUs' fretting behavior on normal loads. The tests were carried out in the displacement controlled mode with a sinusoidal signal and one fixed frequency. The total number of cycles was 8×10^5, because the fretting phenomena can be observed only after 10^4 - 10^5 cycles [15]. Several tests were repeated and ran until some given cycles, in which their hystereses form changed greatly. By means of this method, the alteration process of the wear scar can be investigated and correlated to their hystereses.

All the experiments were performed at a temperature of 23 ± 2 °C and under a relative humidity of 50 ± 10%. The wear scars were characterized by a scanning electron microscope (SEM, VEGA-II, TESCAN, Czech Republic). The quantification of the wear scars was conducted with an optical microscope (InfiniteFocus, Alicona Imaging GmbH, Austria).

3. Results & discussion

In the following part, results were discussed for each fretting regime separately. On the basis of the fretting maps, which were introduced by Vinsbo and Söderberg [11], the fretting hysteresis (3D) and F_t-D curves (2D) will be discussed. They provide valuable information about the running conditions of the contact surfaces [12]. From Fig. 1b it is noticed that the tangential force includes not only the friction force but also a force F_a, which is responsible for the acceleration of the specimens and specimen holder (Eq. (1)).

$$F_t = F_{t,\ measured} - F_a = F_{t,\ measured} - m*a \tag{1}$$

Where m – mass, including specimen holder, lids and specimens, a – acceleration.

The tangential force (F_t) for partial slip and mixed fretting regimes was already compensated using Eq. (1). In order to observe the change of the tangential force more clearly, the hystereses are projected on the cycle – tangential force plane (green) in Figs. 2–10.

With the combination of hystereses and SEM micrographs, the wear scars were analyzed and correlated with fretting hystereses to disclose the damage mechanism. Due to the various sizes of debris, different magnifications had to be used for SEM micrographs. For partial slip and mixed fretting regimes, the width of the inner (2c, stick region) and outer ring (2a, slip region) was characterized with a three-dimensional micro coordinate microscope and showed here in the SEM micrographs.
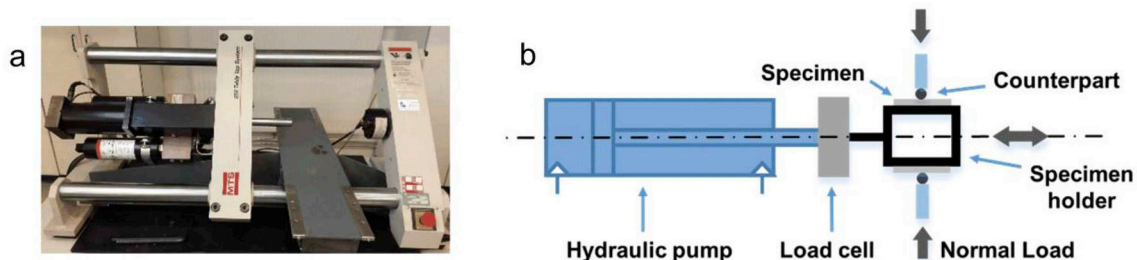

Fig. 1. a) MTS 858 horizontal test system; b) Schematic diagram of fretting wear test setup.

Table 2
Test parameters selected for the fretting tests.

Displacement amplitudes (D, mm)	Normal loads (F_n, N)	Frequency (f, Hz)	Total number of cycles (N, -)
± 0.1, ± 0.25, ± 0.5, ± 1.0	20, 28, 48	10	8×10^5

The total dissipated energy, which was mainly transformed into heat during the test, was calculated by using a Matlab script. Besides, the coefficients of friction were calculated for partial slip and gross slip regimes separately. In the end, the running condition fretting map was generated for TPU.

3.1. Hysteresis & wear scar analysis

3.1.1. Partial slip regime (PSR)

In partial slip regime, two comparisons were carried out from three different tests. The first comparison shows the influence of normal load on fretting behavior, while the second one reveals the impact of displacement amplitude on fretting behavior. As shown in Fig. 2, during the first 4×10^3 cycles the fretting hysteresis was consistent and the maximum tangential force kept at approximately 24 N. However, after 4×10^3 cycles the $F_t – D$ curves changed from a parallelogram to a more linear shape. This indicates that the morphology of the surface, in particular at the edge of the stick region, began to be damaged gradually. After 2×10^4 cycles, the form of the hysteresis kept unchanged.

In the partial slip regime an annular ring was formed, which separated the central area from the rest of the polymer sample (Fig. 3a). The middle area is a stick region (2a) and at the edge of the ring the material underwent micro slip. As shown in Fig. 3b, several pieces of debris are delaminated from the surface. However, the stripe-like debris were generated in the upper area (Fig. 3c) and transferred on the counterpart. As indicated in Fig. 2, after approximately 5×10^3 cycles, obvious changes can be identified in the fretting hysteresis. It should be noted that the relation between tangential force and displacement depends on the state of the two surfaces and their contact conditions. That means that during the first 5×10^3 cycles very small debris was generated from the surface at the edge of the ring. After approximately 5×10^3 cycles the affected surface morphology changed in a way that the debris did not break into small pieces anymore, instead they were rolled into long stripes under the reciprocating micro slips. A similar phenomenon was also be found in some previous studies [16,17]. Surface fatigue wear was found on both sides (Fig. 3d). It was caused by the repeated

stresses [18]. The lower arrow in Fig. 3d shows the wear scar, where the debris was removed.

Compared with the test with 28 N normal load, the changes are more obvious for the test with 48 N normal load (Fig. 4). They began at a similar cycle number (after approximately 3×10^4 cycles). The hysteresis first kept its shape, but the maximum tangential force tended to grow (above 60 N).

Generally, the contact area increases with increasing normal load, so the inner and outer diameters of the ring became larger (Fig. 5a). However, the c/a ratio stays at the similar level in partial slip regime (Fig. 17). The stick region of the sample with 48 N normal load was slightly larger. However, its scar depth is slightly smaller. With 48 N normal load, the deformation is larger than under 28 N. At the right edge small debris were found, which were rolled because of the reciprocating micro slip (Fig. 5b). In the top area, similar wear scar was observed, whereas in the stick region no change is visible after the test (Fig. 5c). From Fig. 5a it is also evident that less material was removed from the surface and less debris was gathered at the edges in comparison with Fig. 3a.

When the displacement amplitude was increased to ± 0.25 mm, the tangential force was almost constant from D = −0.2 mm to D = 0.2 mm in the first 10^3 cycles (Fig. 6). It was similar to the test with ± 0.1 mm displacement amplitude. However, it began to change a bit earlier after approximately 2.5×10^3 cycles and remained unchanged at circa 3×10^4 cycles. The maximum tangential force was 78 N.

As the displacement amplitude increases from 0.1 mm to 0.25 mm, the diameter of the outer ring (2a) becomes larger, whereas the stick region (2c) decreases. The c/a ratio decreases from 0.88 (by D = ± 0.1 mm, F_n = 28 N) to 0.58 (by D = ± 0.25 mm, F_n = 28 N). It is noticeable that the sample shows a butterfly-like wear scar. Large pieces of debris were generated around the inner edge (Fig. 7a). In Fig. 7b the debris looks similar to the one observed in Fig. 3c. However, in this case the debris particles left on the surface is much larger. It is assumed that during the test, several small stripe-like debris were rolled into a large piece of debris. Small pieces of debris were generated due to the shear force on right and left areas (Fig. 7d). In Fig. 7c, connections between debris and stick region can be observed. They were rolled together at first and then pressed on the substrate. With increasing cycles, this butterfly-like scar was created.

3.1.2. Mixed fretting regime

The results of a test conducted in the mixed fretting regime are shown in Fig. 8, the tangential force increased slightly in the first 1×10^3 cycles. From 10^3 to 10^4 cycles the tangential force doubled. It
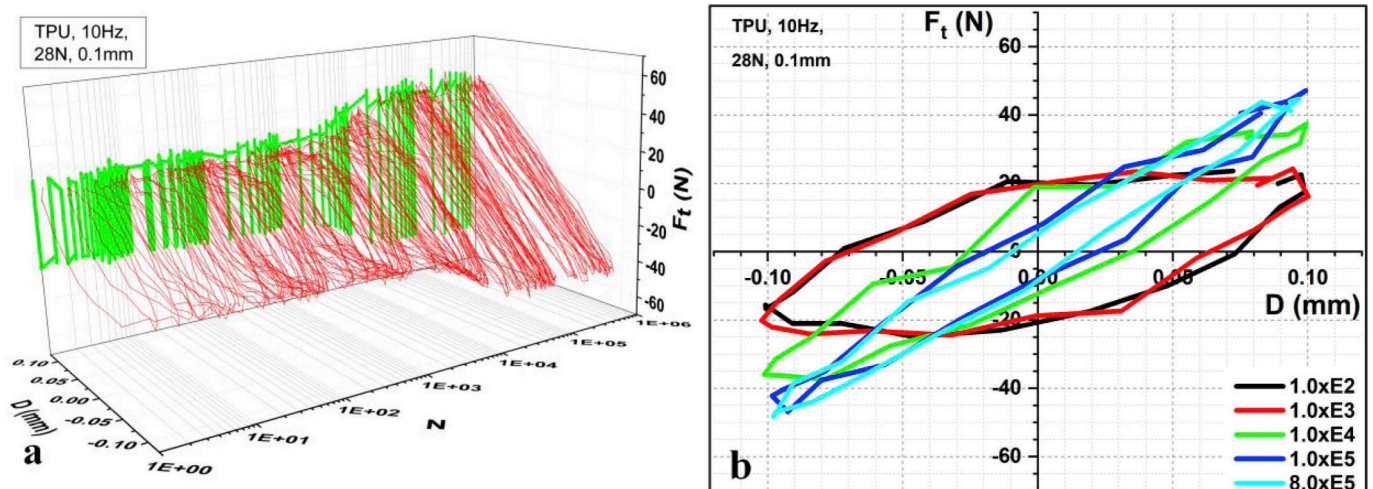

Fig. 2. Material response during the test in PSR (F_n = 28 N, D = ± 0.1 mm, f = 10 Hz, N = 8×10^5): a) Fretting hysteresis; b) F_t-D curve.
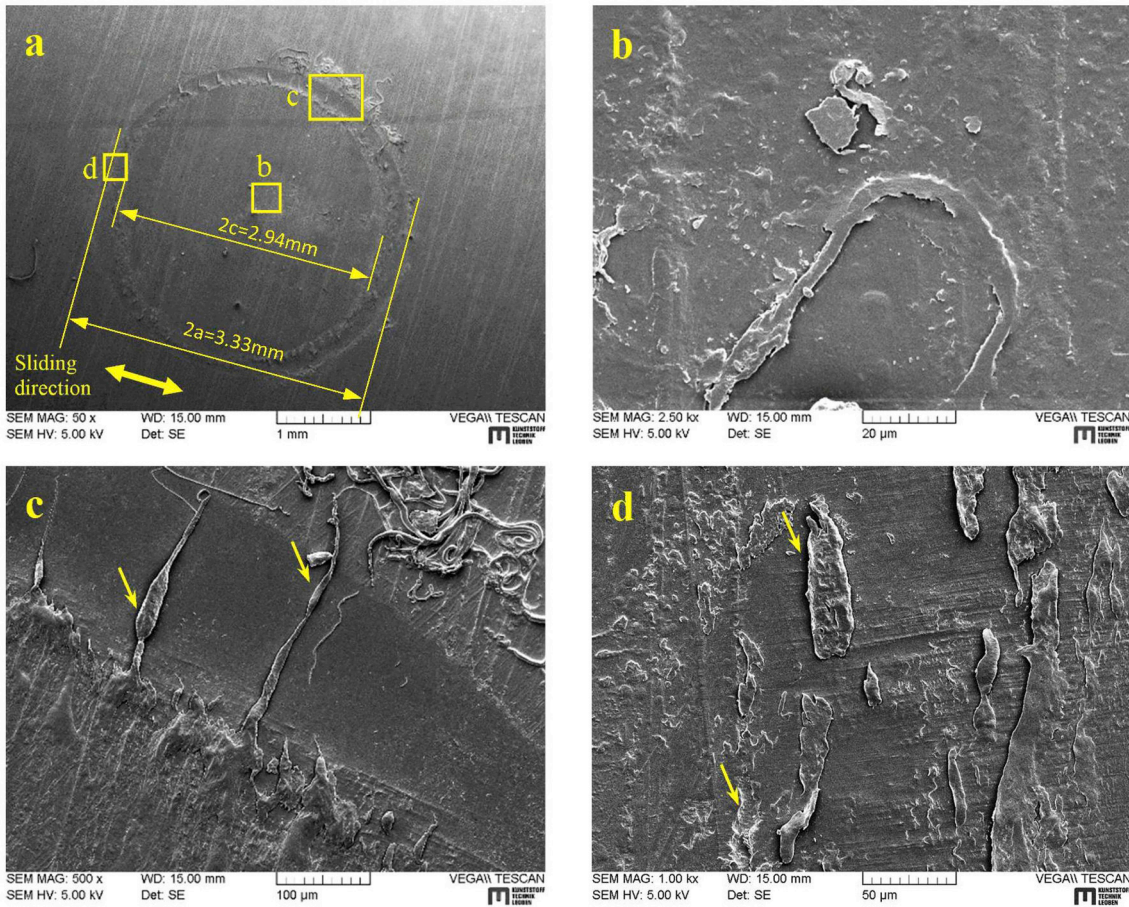
Fig. 3. SEM micrographs of wear scar determined for the following parameters: F_n = 28 N, D = ± 0.1 mm, f = 10 Hz, N = 8 × 10⁵. Related areas are marked and shown with larger magnifications.

should be noted that the tangential force decreased gradually from 109 N to 95 N between 2 × 10⁴ and 10⁵ cycles. However, it increased again since 10⁵ cycle. As shown in Fig. 9, for this regime cracks are visible in the stick region. Cracks can reduce the slip displacement [19], which is expected to be responsible for the interim decrease of the tangential force. Moreover, the elimination of small cracks due to material loss [15,19] and the filling of large cracks with small wear debris [20] let the tangential force rise again after 10⁵ cycles.

With the increase of the displacement amplitude to ± 0.5 mm, the wear width (2a) of the damage scar was enlarged to over 5 mm. Meanwhile, the stick region (2c) shrunk (Fig. 9a). In the latter region due to the repeated shear stress, cracks were nucleated below and on the surface. With the further repeated stress cycles, cracks were extended and propagated [18]. Cracks below the surface led to fatigue wear, while the cracks on the surface propagated perpendicularly to the sliding direction (Fig. 9b). Moreover, wave formation was observed on
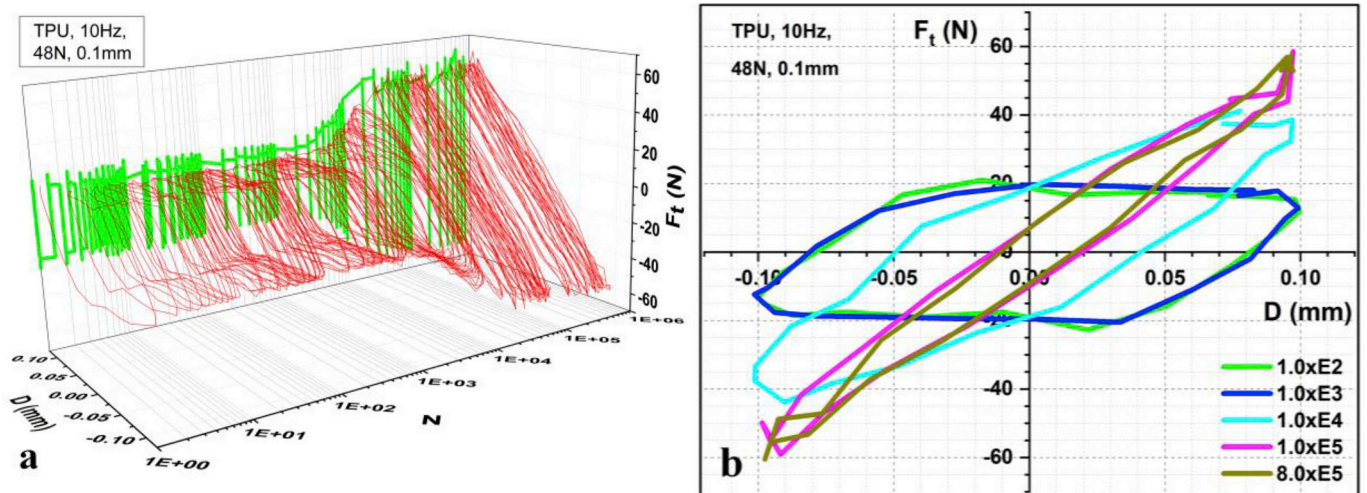

Fig. 4. Material response during the test in PSR (F_n = 48 N, D = ± 0.1 mm, f = 10 Hz, N = 8 × 10⁵): a) Fretting hysteresis; b) F_t-D curve.

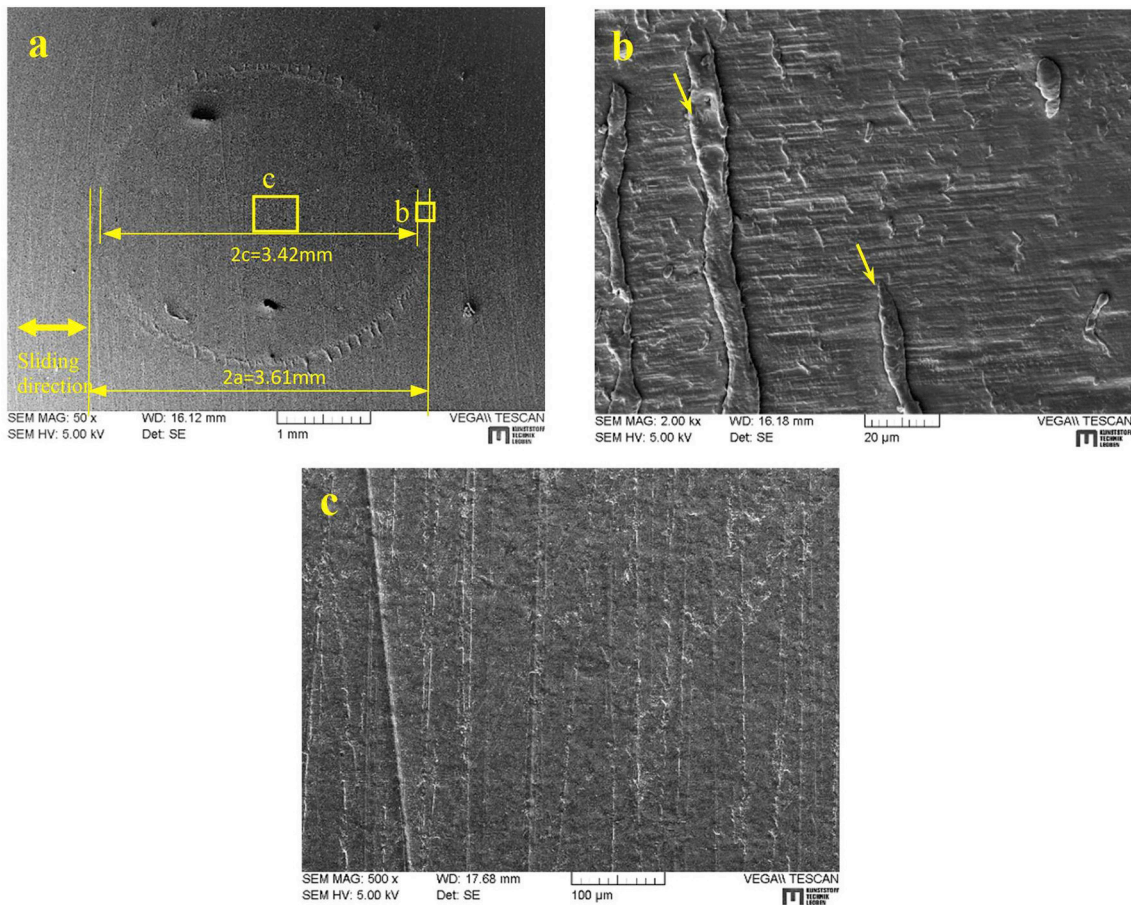**Fig. 5.** SEM micrographs of wear scar determined for the following parameters: F_n = 48 N, D = ± 0.1 mm, f = 10 Hz, N = 8 × 10^5. Related areas are marked and shown with larger magnifications.

the worn surface (Fig. 9c and d), which can be attributed to additional fatigue mechanisms [21,22]. At the beginning, which is called incubation period by Vincent [19], "Schallamach waves" [22–24] were formed due to the shear stress. With further cyclic sliding motions, the waves were rolled into larger debris until they were moved away from the surface. In Fig. 9d, a large piece of debris can be observed.

3.1.3. Gross slip regime

Different to the tests in partial slip and mixed fretting regimes, which show a stable phase of tangential force after the increasing phase, the tests in gross slip regime showed a stepwise increasing tendency of tangential force with the number of, from 10^2 to 10^3 cycles the tangential force increased slightly. After 10^3 cycles the tangential force increased until $7 × 10^3$ cycle and then kept almost constant until 10^4 cycle. Subsequently, the tangential force increased again before it
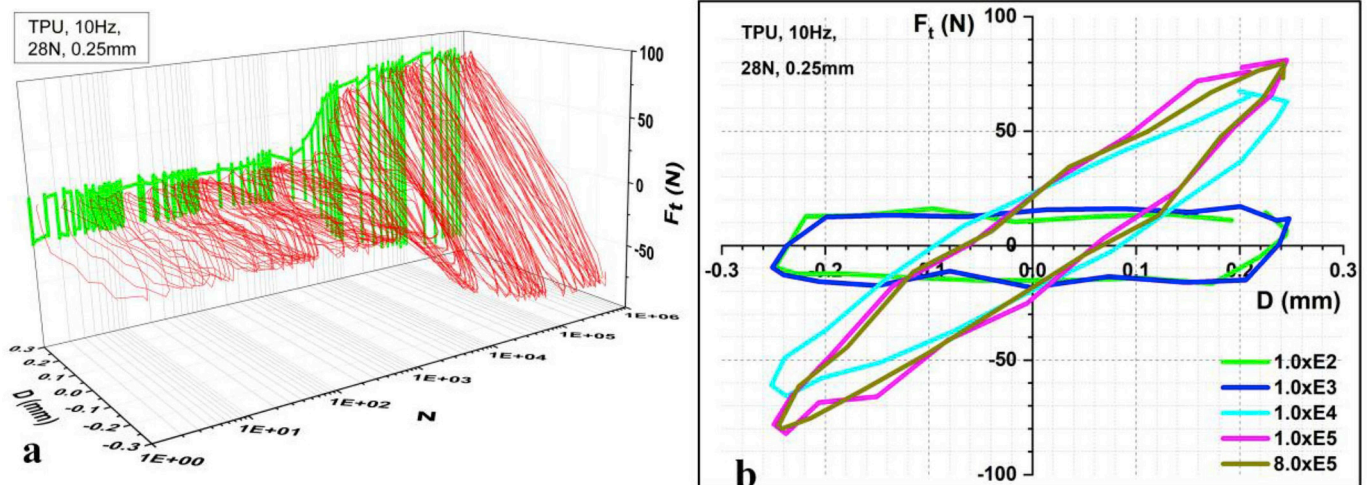

Fig. 6. Material response during the test in PSR (F_n = 28 N, D = ± 0.25 mm, f = 10 Hz, N = 8 × 10^5): a) Fretting hysteresis; b) F_t-D curve.

Fig. 7. SEM micrographs of wear scar determined for the following parameters: $F_n = 28$ N, D = ± 0.25 mm, f = 10 Hz, N = 8 × 10^5. Related areas are marked and shown with larger magnifications.

reached a relatively stable phase, which was from 2 × 10^4 to 7 × 10^4 cycles. Afterward, the tangential force increased rapidly. This can be attributed to the contact conditions. After the incubation period, microcracks were generated. With increasing cycles more wear debris will be created, so that the contact geometry changed continuously.

In gross slip regime, there is no stick region between the two contacting surfaces. This means that the elasticity of TPU is not high

enough to deform with the counterpart when it slides over. After 8 × 10^5 cycles, small waves were observed in the middle area (Fig. 11b). Meanwhile, much larger waves can be identified in the right and left areas in Fig. 11c and d. These waves were generated due to the great shear stresses. In Fig. 10 it can be seen that the maximum tangential force appeared at approximately D = ± 0.75 mm. This correlates very well with the position of the large waves. The large waves

Fig. 8. Material response during the test in MFR ($F_n = 28$ N, D = ± 0.5 mm, f = 10 Hz, N = 8 × 10^5): a) Fretting hysteresis; b) F_t -D curve.
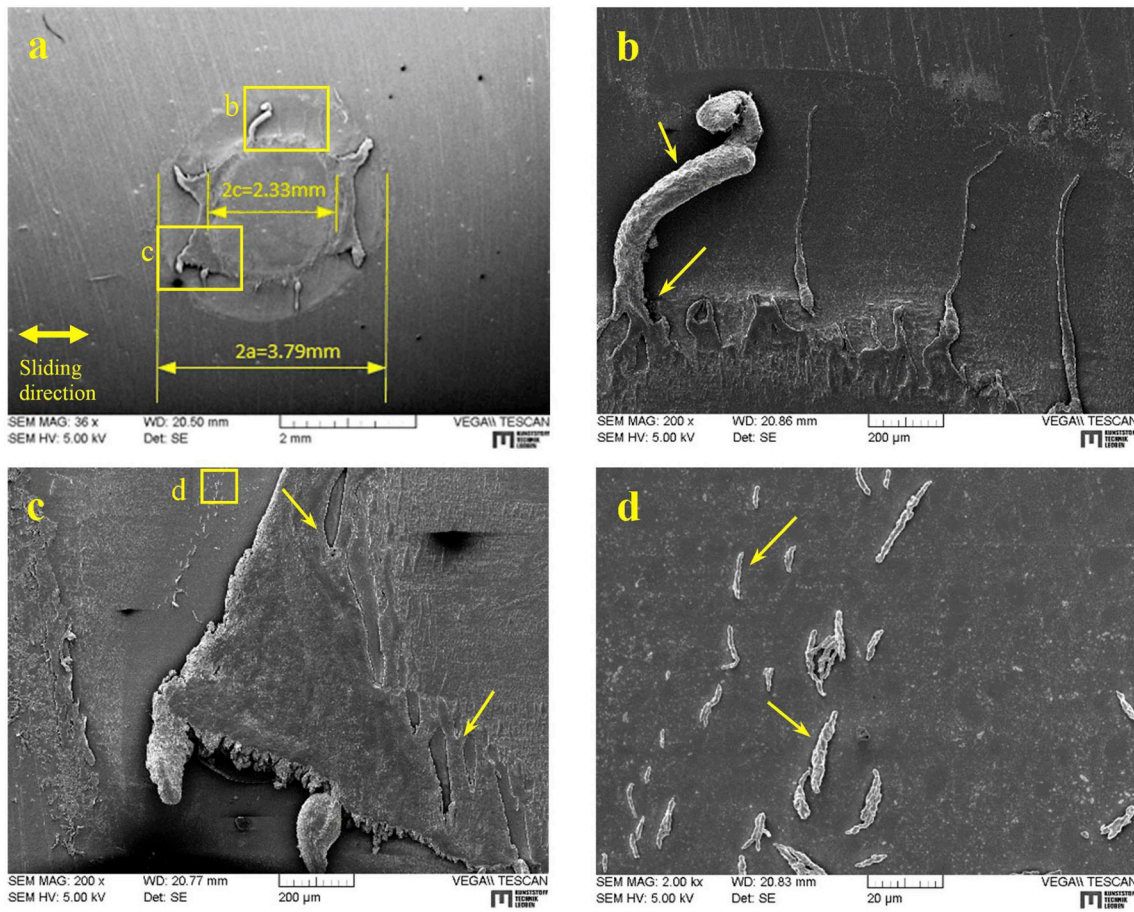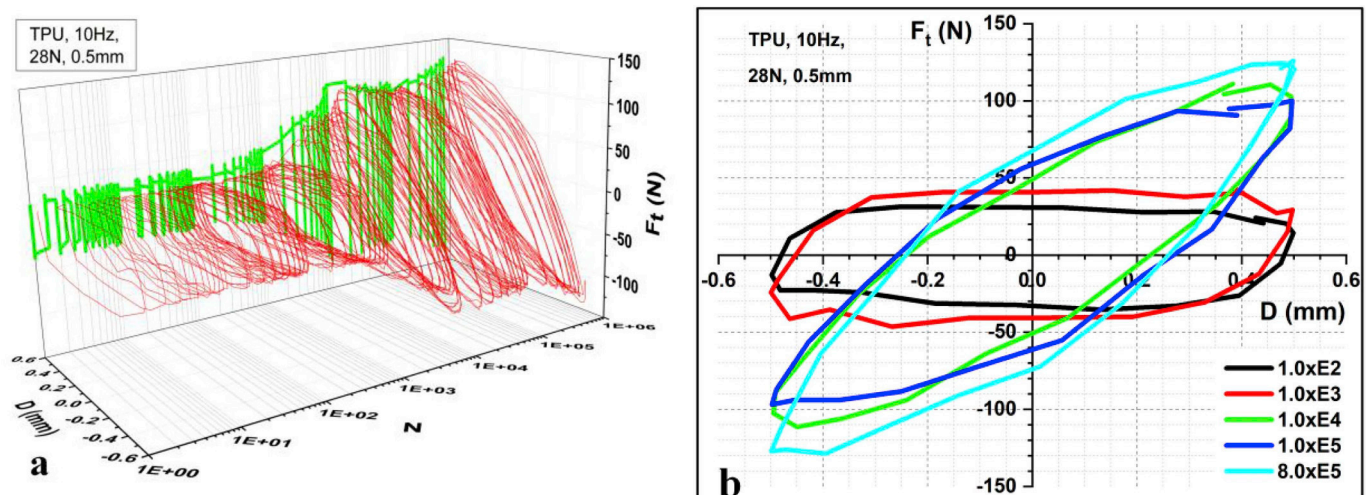
Fig. 9. SEM micrographs of wear scar determined for the following parameters: $F_n = 28\,N$, $D = \pm 0.5\,mm$, $f = 10\,Hz$, $N = 8 \times 10^5$. Related areas are marked and shown with larger magnifications.

locate at approximately 75% of the horizontal radius from the center. Also, this phenomenon is in good agreement with previous studies [25,26]. In addition, as evident from Fig. 11d, the wave crest was partially rolled and torn away from the surface.

In addition, the topography of the surface after 10^4 cycles was also investigated. As shown in Fig. 12a, large cracks were nucleated and propagated perpendicularly to the sliding direction. According to Fig.10b, 10^4 cycles is the transitional phase, in which the hysteresis changed significantly. At 10^3 cycles the tangential force stayed at

around 25 N, and it was almost not dependent on the displacement. However, at 10^5 cycles, it was partially above 100 N, and the hysteresis form changed. At 10^4 cycles the maximum tangential force was almost constant, between the displacement of $+0.3\,mm$ to $-1.0\,mm$. Rolled debris was also observed in the middle area (Fig. 12b). Furthermore, with higher magnification microcracks can be identified (Fig. 12c). At the edge of the slip zone, flow-like waves were generated by shear stress.

Through the above comparisons, it can be concluded that in partial

Fig. 10. Material response during the test in GSR ($F_n = 28\,N$, $D = \pm 1.0\,mm$, $f = 10\,Hz$, $N = 8 \times 10^5$): a) Fretting hysteresis; b) F_t-D curve.
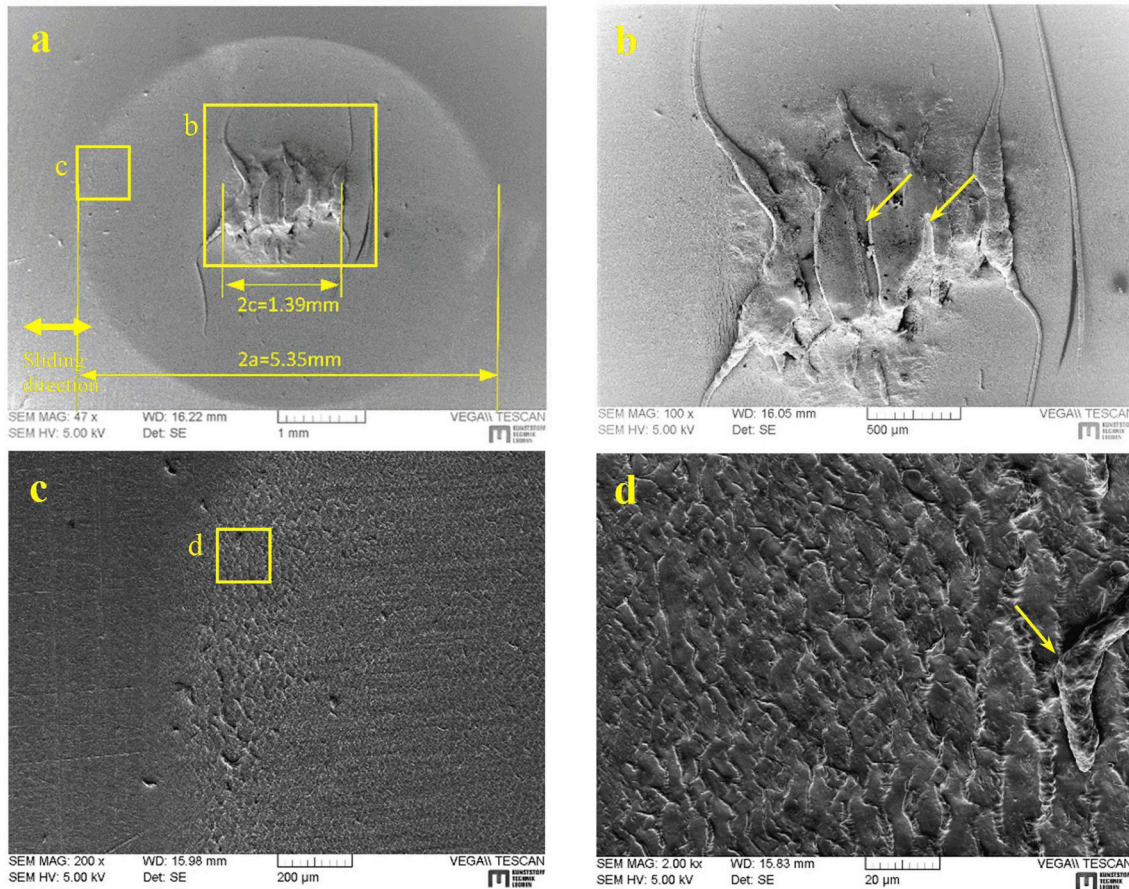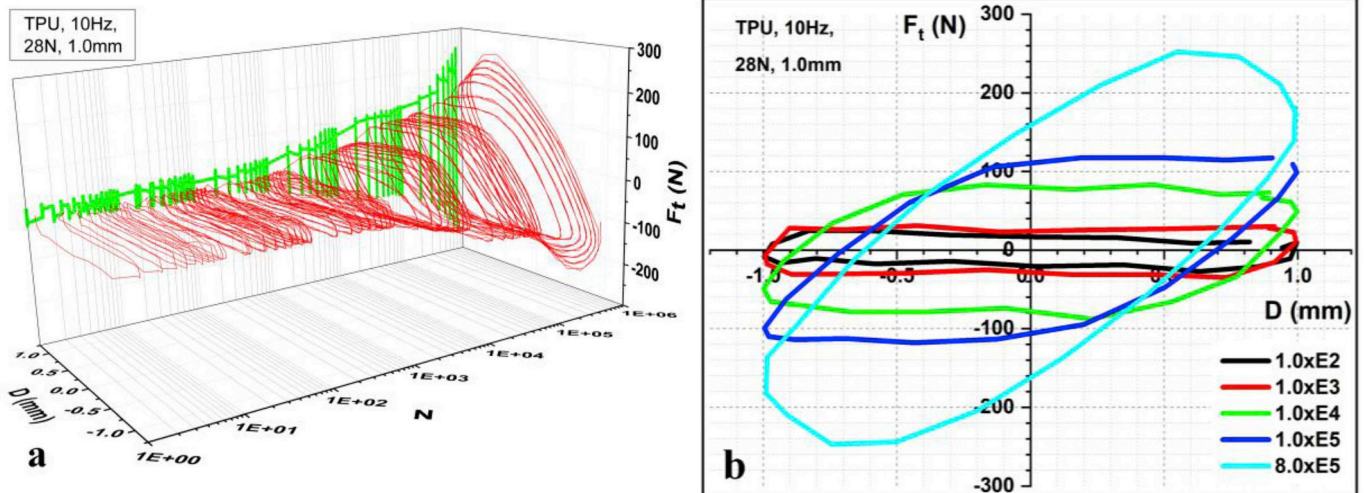
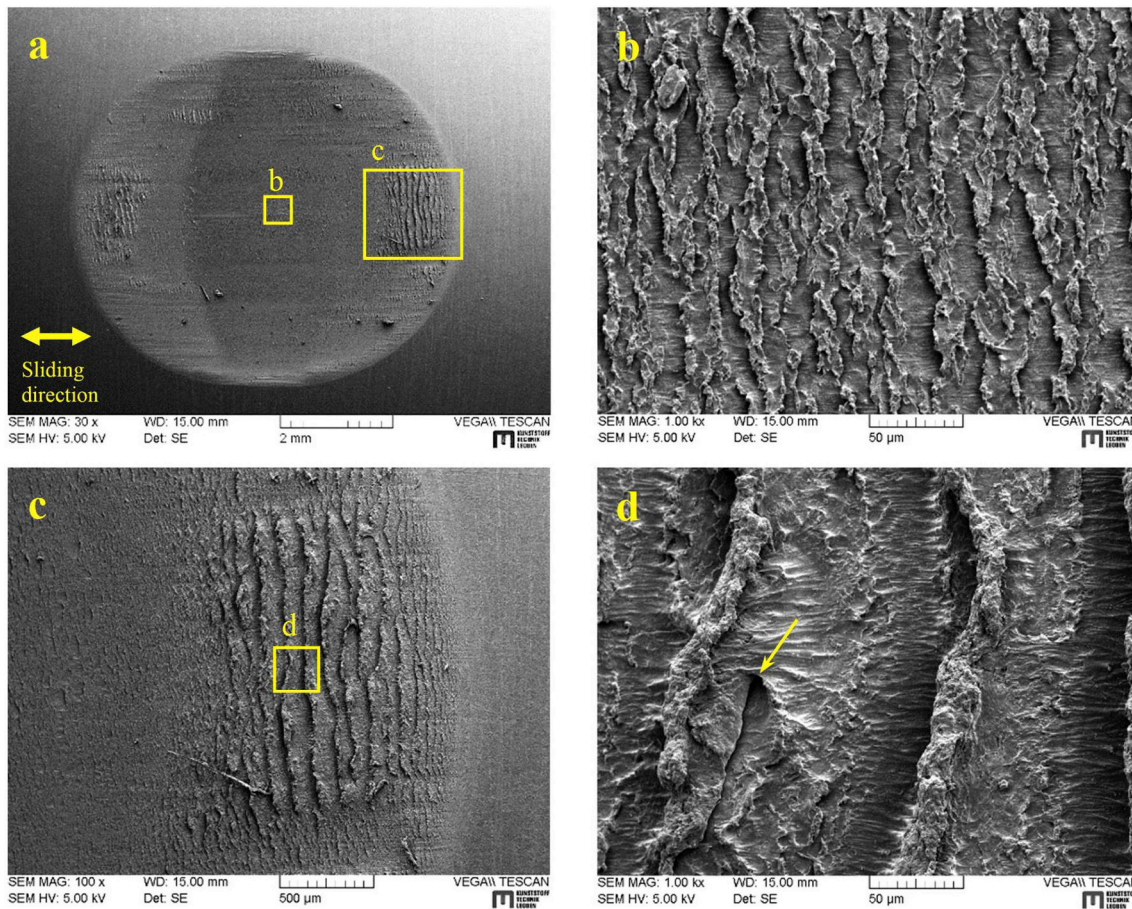**Fig. 11.** SEM micrographs of wear scar determined for the following parameters: $F_n = 28\,N$, $D = \pm 1.0\,mm$, $f = 10\,Hz$, $N = 8 \times 10^5$. Related areas are marked and shown with larger magnifications.

slip regime the tests with different normal loads were similar, in particular in the first 10^3 cycles. It is noticeable that the tangential force increased slightly with the normal load. In addition, in mixed fretting and gross slip regimes the incubation time for the formation of waves was shorter than in partial slip regime. Due to their greater tangential forces and larger displacements, the fretting hysteresis of mixed fretting and gross slip regimes changed earlier. The fretting behavior shows a strong dependence on the displacement amplitudes, which in fact also strongly influence the fretting regimes of the tests.

3.2. Observation of counterparts

The counterparts were observed under microscopy. Slight wear trace and elastomer transfer are identified. High material transfer is to observe, especially in the tests with high load (48 N) or high amplitude ($\pm 1.0\,mm$). The higher normal pressure combined with cyclic shear stress leads to a larger material transfer to the counterpart. In addition, under large amplitude, the tangential force and the dissipated energy is higher. Thus, relatively larger amount of material was transferred to the steel balls (Table 3).

3.3. Analysis of wear scar size

Fig. 13 shows the influence of normal load on the wear scar size. With increasing loads, both the outer and inner edges become larger. In addition, the diameter of contact area after Hertzian contact theory is shown.

As shown in Fig. 13, the diameter (d) of Hertzian contact area, which represents the contact size at the beginning of the fretting tests,

increases with a higher normal load. Also, as can be seen from the left figure, the outer edge of wear scar (2a), which is the last state of wear scar, increases with a higher amplitude. Hence, the last state (wear scar size, 2a) are proportional to both the start state (diameter of Hertzian contact area, d) and the test parameter (amplitude, D). In Fig. 14, their relation is shown, which is

$$2a = kDd$$

Where k is a constant. The outer edge (2a) is almost linear proportional to the results of amplitude multiply the diameter of Hertzian contact area.

3.4. Dissipated energy

The dissipated energy was calculated by integration of the $F_t - D$ curves over all cycles. It was determined for each test. As shown in Fig. 15, the dissipated energy depends strongly on the displacement amplitudes. The larger the displacement is, the more energy will be dissipated.

When the displacement amplitude is $\pm 0.1\,mm$ or $\pm 0.25\,mm$, all of the tests are in partial slip regime and the dissipated energies for the tests with same displacement and different normal loads are nearly the same. Hence, no noticeable dependence between dissipated energy and normal loads is observed in partial slip regime. However, when the displacement amplitude is $\pm 0.5\,mm$, the difference is more visible. The test with 48 N normal load consumed the minimal energy among the three tests. The dissipated energy for the tests with 20 N and 28 N normal loads are a bit higher. For an overview of the differences among fretting regimes and their corresponding test parameters please refer to Fig. 22. Whereas, the test with 48 N normal load is still in partial slip
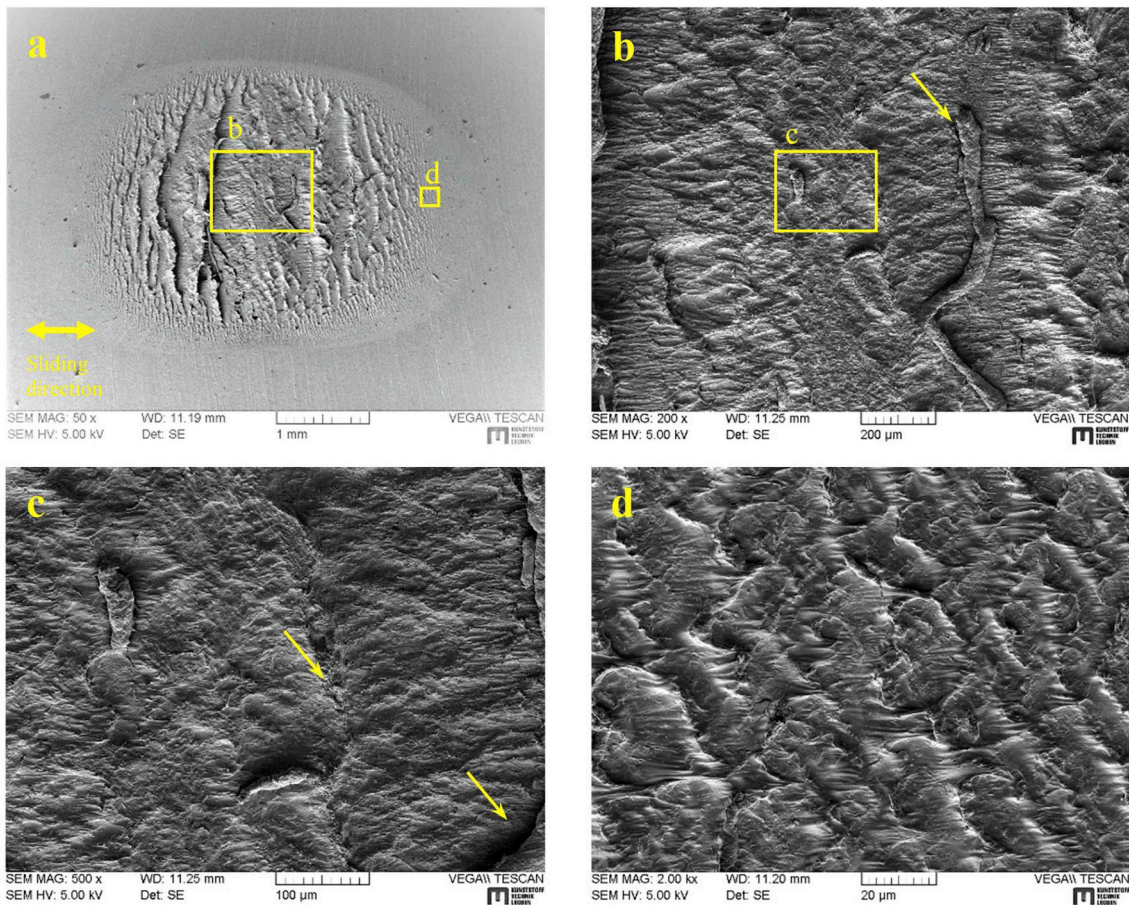
Fig. 12. SEM micrographs of wear scar determined for the following parameters: $F_n = 28\,N$, $D = \pm 1.0\,mm$, $f = 10\,Hz$, $N = 10^4$. Related areas are marked and shown with larger magnifications.

Table 3
Micrographics of counterparts after tests.

Amplitude (mm)	± 0.1		± 0.25	± 0.5	± 1.0
Load (N)	28	48	28	28	28
Graphic					

regime. In MFR more material was removed after tests comparing to PSR. Therefore, more energy was consumed.

For the tests with ± 1.0 mm displacement amplitude, a clear relationship between normal load and dissipated energy can be identified (all tests are in the gross slip regimes). The dissipated energy grows with increasing normal load. This correlates well with the wear volume (Fig. 19b). In gross slip regime, larger normal loads lead to more material loss. Hence, more energy is dissipated.

From Fig. 15, it can be concluded for the tested material in this study, when the dissipated energy is around 10^3 J, the test is in partial slip regime. 10^5 J is an approximate boundary between mixed fretting and gross slip regimes. The transition from PSR to MFR result in a dissipated energy between 10^3 to 10^5 J.

In addition, a proportional relation between wear volume and dissipated energy is identified. However, it is inconsistent with the results in Ref. [27], in which dissipated energy is linear proportional to wear volume of TiN coating. For the tests in this study, dissipated energy and wear volume shows a power law relation (Fig. 16).

3.5. Coefficient of friction

3.5.1. Partial slip and mixed fretting regimes

In the partial slip regime, the coefficient of friction (COF) cannot be calculated by using Coulomb's law, which was generally applied to calculate the COF for static and also kinetic friction. However, under partial slip conditions, micro slip occurred at the edge of the ring (radius = a) with a stick region in the middle (radius = c). Based on the work of Cattaneo and Mindlin, Johnson has introduced a method to calculate the COF for the partial slip in the contacts of spheres [28]. The "stick region" can be calculated with tangential force as follows:

$$\frac{c}{a} = \left(1 - \frac{F_t}{\mu F_n}\right)^{1/3}$$

(2)

Where a – radius of the outer ring;

c – radius of the inner ring;
F_t – tangential force;
F_n – normal load;
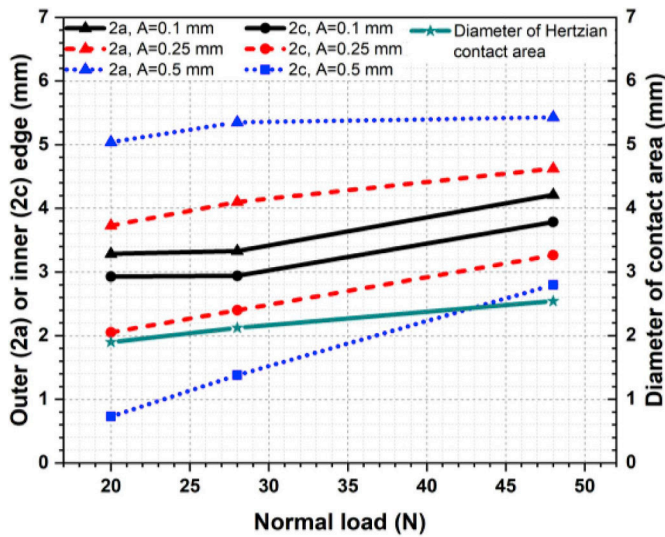μ- coefficient of friction in sliding region.

Fig. 13. Diameter of Hertzian contact area and wear scar size by different normal loads.
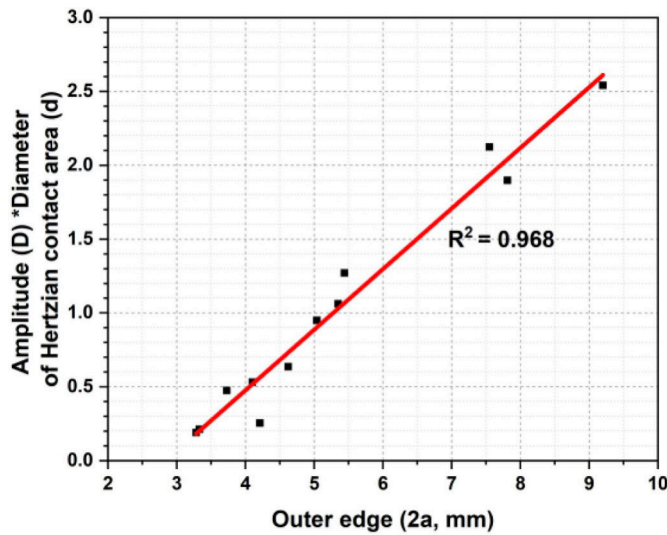

Fig. 15. The dissipated energy during the tests.

Fig. 14. Relation of outer edge, amplitude and diameter of Hertzian contact area.

Fig. 16. Relation of wear volume and dissipated energy.

From equation (1) we can get

$$\mu = \frac{1}{1 - \left(\frac{c}{a}\right)^3} \times \frac{F_t}{F_n}$$

(3)

In Fig. 14, the coefficients of friction, which were calculated by using equation (3) and the ratios of c/a for the tests in the partial slip and mixed fretting regimes are illustrated. From the figure, it can be seen that only for a displacement amplitude (D) of ± 0.1 mm the c/a ratio is approximately constant at a value of 0.9. This means that in partial slip regime, the c/a ratio stayed at a relatively constant value when the normal load increased. On the contrary, in mixed fretting regime (D = ± 0.5 mm) the c/a ratio grew with increasing normal loads. The comparison of the c/a ratios with three displacement amplitudes examined indicates that the greater the displacement amplitude is, the larger the c/a ratio with the normal load increases. In other words, the smaller the displacement is, the less dependence is the alteration of the morphology on normal load. In PSR and MFR, the COF decreased with increasing normal load. Nevertheless, this effect has a strong dependence on the different displacement amplitudes examined.
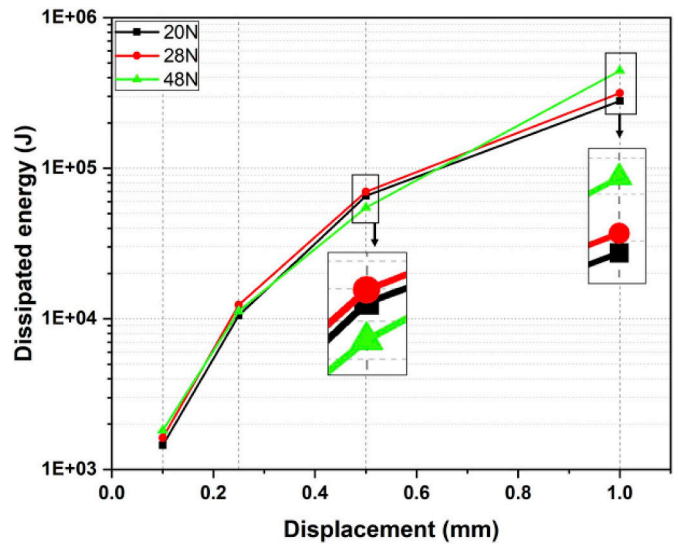

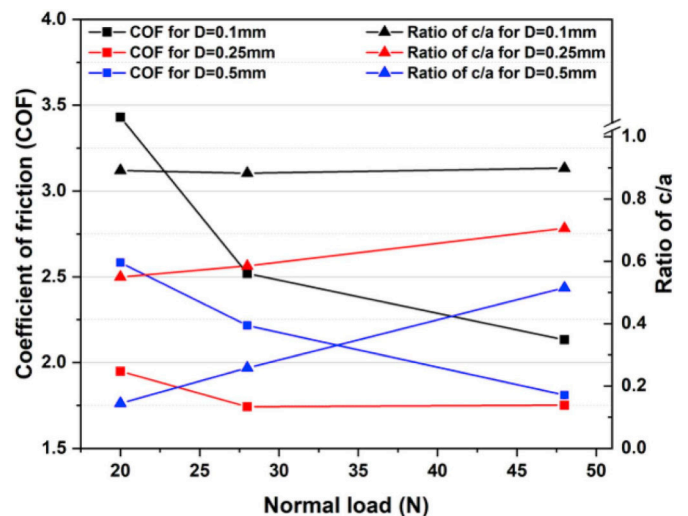**Fig. 17.** Comparison of the coefficients of friction and ratios of c/a in partial slip and mixed fretting regimes.
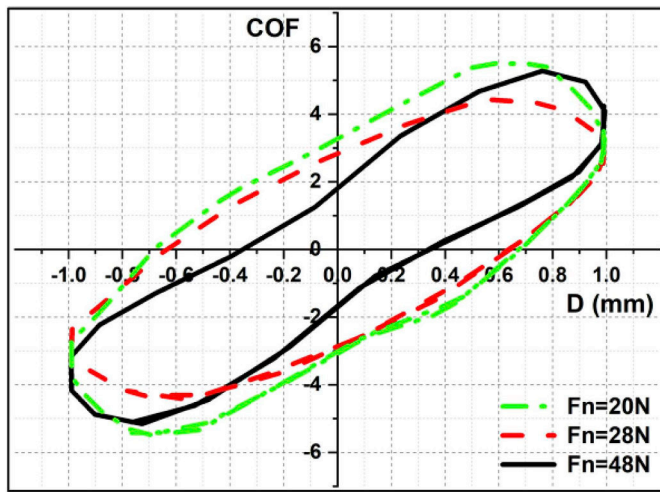
Fig. 18. Coefficient of friction (COF) as a function of the displacement (D) from the last cycle in gross slip regime with Eq. (4).

Noteworthy, the coefficient of friction decreased when the displacement amplitude increased from ± 0.1 mm to ± 0.25 mm. It increased, however, when the displacement increased further from ± 0.25 mm to ± 0.5 mm.

3.5.2. Gross slip regime

The coefficient of friction in gross slip regime was at first calculated with

$$\mu = \frac{F_t}{F_n} \tag{4}$$

which was widely applied in several studies [13,29–31]. In the coefficient of friction was calculated with the tangential force from the last cycle. The COF - D curves were elliptical for the normal load of 20 N and

28 N. With a normal load of 48 N, however, the shape of the curve changes in the middle area. Fig. 19 illustrates the profiles of the wear scars in gross slip regime under the three different normal loads examined. The wear depth and width increase with the normal load. Generally, for the 20 N and 48 N normal loads, asperities can be observed in the profiles in Fig. 19b, which implies that several wave-formed cracks were on both edges of the wear scars.

The Eq. (4) is, however, applicable for the gross slip regime. Only, when the surface is not damaged and the mass of the system can be neglected. These factors depend on the materials tested and construction of the test system, respectively. The large wear depth in Fig. 19 plays an essential role in the calculation of the COF. Moreover, for the test system used in this research, the specimen holder was connected to the load cell (Fig. 1b). Hence part of the tangential force measured was used to move the specimens and the specimen holder parts ($m = 1.536$ kg), which has to be included in the considerations.

To facilitate the analysis, three assumptions are made:

1. The contour of the wear scar is a part of a circle with a radius of a.
2. The surface of the wear scar is continuous and smooth.
3. No deformation occurs on substrate and no debris.

Fig. 20 shows the general situation in the wear scar, which is the basis for the calculation of the COF. Position A is the start position. When the specimen moves to position B, the force situation is illustrated in Fig. 20b. From this situation, the following forces in X- and Y-directions are deduced.

$$X: \; F_t(t) + F_{ax}(t) = N(t)*\sin(\alpha(t)) + F_f(t)*\cos(\alpha(t)) \tag{5}$$

$$Y: \; F_n(t) + F_f(t)*\sin(\alpha(t)) = N(t)*\cos(\alpha(t)) + F_{ay}(t) \tag{6}$$

$$F_{ax}(t) = ma_x(t) \tag{7}$$

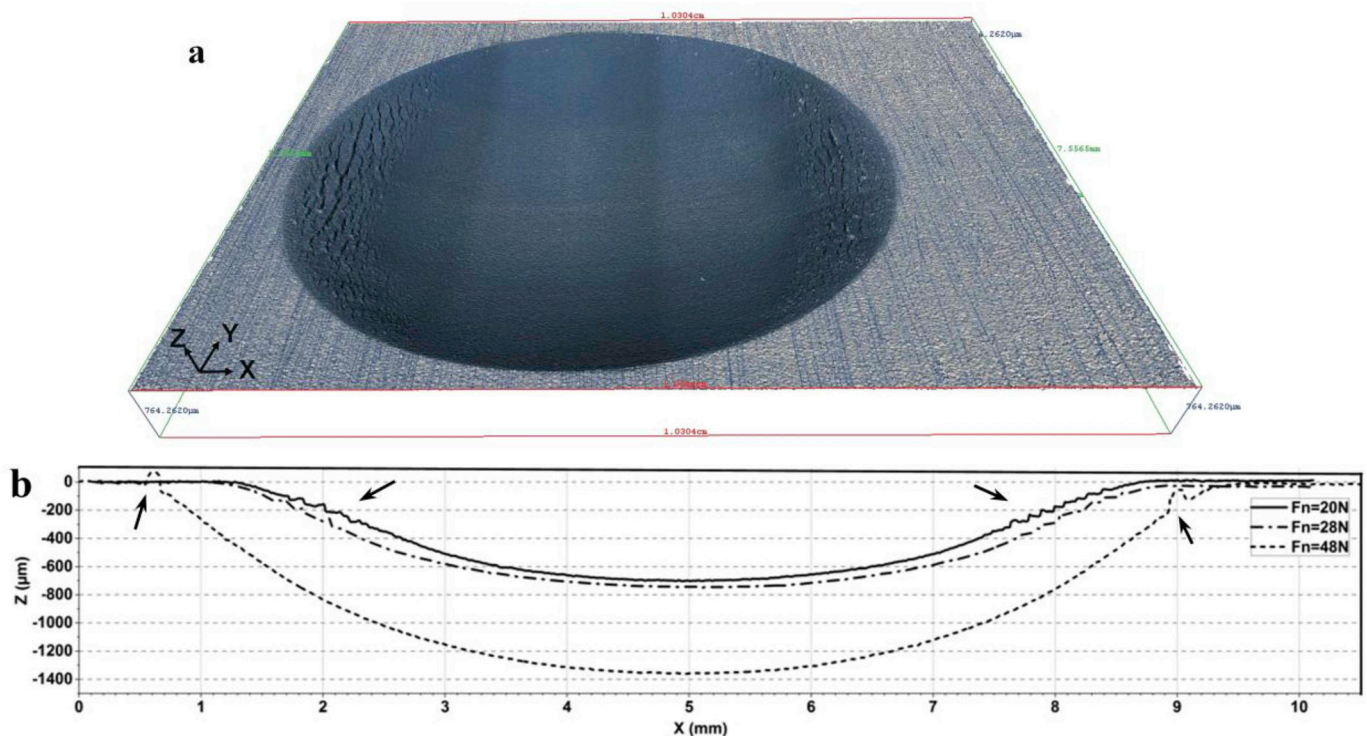$$F_{ay}(t) = ma_y(t) \tag{8}$$

Where $F_t(t)$ – tangential force;

Fig. 19. a). 3D/2D image of the wear scar (Fn = 20 N); b). Profiles of the wear scars in gross slip regime (D = ± 1.0 mm).
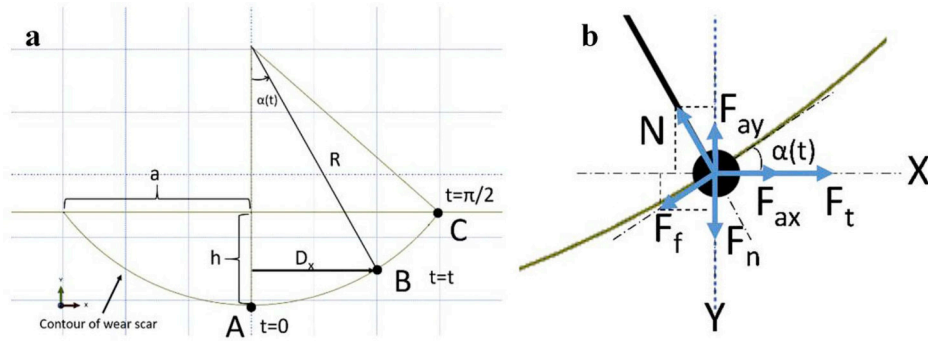
Fig. 20. a). Three different positions of counterpart; b). Force analysis of position B.
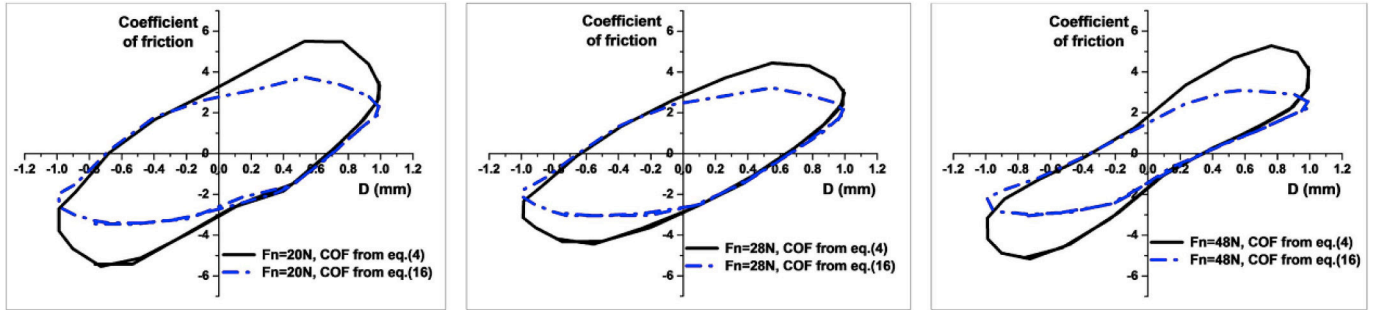

Fig. 21. Comparison of the coefficient of friction examined from Eqs. (4) and (16) for the gross slip regime.
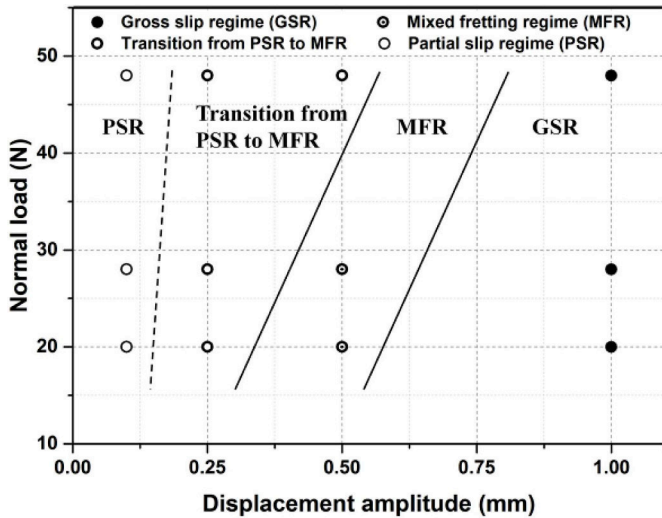
Fig. 22. Running condition fretting map (RCFM) of TPU samples.

F_{ax} (t), F_{ay} (t) – net force in X and Y-direction;
F_n (t) – normal load;
F_f (t) – friction force;
N (t) – support force of the surface.

Since the normal load (F_n) is constant, from equations (4)–(7) we can get

$\mu(t)$

$= \dfrac{F_{ax}(t)*\cos(\alpha(t)) + F_t(t)*\cos(\alpha(t)) - F_n*\sin(\alpha(t)) + F_{ay}(t)*\sin(\alpha(t))}{F_n*\cos(\alpha(t)) + F_{ax}(t)*\sin(\alpha(t)) + F_t(t)*\sin(\alpha(t)) - F_{ay}(t)*\cos(\alpha(t))}$

(9)

Because the displacement is applied as a sinusoidal wave, the displacement in x-direction is

$D_x(t) = D*\sin(\omega t)$

(10)

and the corresponding acceleration is

$a_x(t) = D_x^{'}(t) = -D\omega^{2}*\sin(\omega t)$

(11)

the displacement in y-direction is

$h_y(t) = h*\sin(2\omega t)$

(12)

What gives the acceleration as

$a_y(t) = h_y^{''}(t) = -4h\omega^{2}*\sin(2\omega t).$

(13)

The angular velocity of the control system is

$\omega = 2\pi f$

(14)

and the coefficient of friction is

$\mu(t) = \dfrac{F_f(t)}{N(t)}$

(15)

With these boundary conditions, Eq. (8) can be transferred to

$\mu(t) = \dfrac{\begin{aligned}-4\pi^2 f^2 mD*\sin(2\pi ft)*\cos(\alpha(t)) + F_t(t)*\cos(\alpha(t)) - F_n \\ *\sin(\alpha(t)) - 16\pi^2 f^2 mh*\sin(4\pi ft)*\sin(\alpha(t))\end{aligned}}{\begin{aligned}F_n*\cos(\alpha(t)) - 4\pi^2 f^2 mD*\sin(2\pi ft)*\sin(\alpha(t)) + F_t(t)*\sin(\alpha(t)) \\ + 16\pi^2 f^2 mh*\sin(4\pi ft)*\cos(\alpha(t))\end{aligned}}$

(16)

From Fig. 20a we get

$\alpha(t) = \arcsin\left(\dfrac{D_x}{R}\right) = \arcsin\left(\dfrac{D*\sin(2\pi ft)}{R}\right).$

(17)

R can be calculated by using the depth (h) and width (2a) of the wear scar, as shown in Fig. 20a,

$R^2 = a^2 + (R - h)^2.$

(18)

This gives

$R = \dfrac{h^2 + a^2}{2h}$

(19)

The COFs were recalculated for the last cycle of gross slip regime

using equation (16) and compared with the results of Eq. (4) (Fig. 21).

When taking the geometry of the wear scar and the acceleration of the test system into consideration, substantial differences are observed in the COF - D curves. Especially when the displacement is in the vicinity of D = ± 0.7 mm, where the maximum tangential force occurs. Overall, the hysteresis gets smaller with an increasing normal load. This means that the observed relation of the coefficient of friction and the normal load for the partial slip and mixed fretting regimes (Fig. 14), is also present in the gross slip regime. This is different to the result from Fig. 18, which were calculated with Eq. (4). Furthermore, as shown in Fig. 21, when the normal load increases, the form of the hysteresis becomes more parallelogrammic.

3.6. Running condition fretting map (RCFM)

Running condition fretting map represents the transition from one regime to the other approximately [32,33]. Based on the hysteresis and wear scar analysis, a running condition fretting map was generated for TPU. Fig. 22 shows that only the tests with ± 0.1 mm displacement amplitude, whose c/a ratios were approximately 0.9. As the amplitude increased to ± 0.25 mm, the c/a ratio reduced to 0.7 (48 N normal load) and 0.57 (20 and 28 N), respectively. These tests can be regarded as the transition phase between partial slip (PSR) and mixed fretting regimes (MFR). Moreover, the test with 48 N normal load and ± 0.5 mm displacement amplitude was found to belong to this area. In mixed fretting regime, the c/a ratio for the tests with ± 0.5 mm displacement amplitude and normal load 20 N and 28 N was 0.14 and 0.26, respectively. In order to find out the trend, how the test parameters influence the fretting behavior of TPU, no accurate borders can be acquired between the three regimes from the used parameters. However, the trends can be deduced from the tests. The larger the normal load is, the milder the surface gets damaged with the same displacement amplitude and frequency. Meanwhile, the larger the amplitude, the more material is removed from the surface under the same normal load and frequency.

4. Conclusion

In this study, the fretting behavior of thermoplastic polyurethane was investigated. Because of its high elasticity, the applied amplitudes are much larger than those in fretting tests on metals. The hystereses, wear scars and coefficients of friction were analyzed in detail.

1) Three kinds of fretting regimes were found. Their fretting hystereses were compared and related to the wear scars.
2) In partial slip and mixed fretting regimes, for the tests with the same displacement amplitude, the coefficient of friction decreases with increasing normal loads. For the tests with ± 0.1 mm displacement amplitude, its c/a ratio kept almost constant when the normal load increased. However, for the tests with ± 0.25 mm and ± 0.5 mm displacement amplitudes, their ratios of c/a increased with the normal loads. It increased faster for ± 0.5 mm displacement amplitude than for ± 0.25 mm.
3) A new method to calculate the coefficient of friction for the late cycles in gross slip regime was introduced, which takes the wear scar and acceleration of the test system into consideration.
4) The running condition fretting map was generated. It represents the fretting behavior in relation with normal load and displacement amplitude.
5) The larger the normal load was, the milder the surface got damaged with the same amplitude and frequency. Also, the larger the displacement amplitude was, the more material was removed from the surface for the same normal loads and frequency.

Further tests will be continued for different types of TPU. This test method can also be extended to test the fretting behavior of other elastomeric materials.

References

[1] G.K. Nikas, Eighty years of research on hydraulic reciprocating seals: review of tribological studies and related topics since the 1930s, Proc. IMechE 224 (1) (2010) 1–23.
[2] T. Christiner, J. Reiser, B. Maier, F. Grün, Calculation approach for the assessment of fretting, ATZ Worldw. 115 (12) (2013) 38–43.
[3] S. Fouvry, P. Kapsa, L. Vincent, A global methodology to quantify fretting damages, in: D.W. Hoeppner, S.E. Kinyon, Y. Mutoh (Eds.), Fretting Fatigue: Advances in Basic Understanding and Applications, ASTM International, West Conshohocken, Pa, 2003, pp. 17–32.
[4] M. Varenberg, I. Etsion, G. Halperin, Slip index: a new unified approach to fretting, Tribol. Lett. 17 (3) (2004) 569–573.
[5] K.J. Kubiak, T.W. Liskiewicz, T.G. Mathia, Surface morphology in engineering applications: influence of roughness on sliding and wear in dry fretting, Tribol. Int. 44 (11) (2011) 1427–1432.
[6] B.J. Briscoe, A. Chateauminois, T.C. Lindley, D. Parsonage, Fretting wear behaviour of polymethylmethacrylate under linear motions and torsional contact conditions, Tribol. Int. 31 (11) (1998) 701–711.
[7] A. Chateauminois, Analysis of fretting damage in polymers by means of fretting maps, Fretting Fatigue: Current Technology and Practices, ASTM International, West Conshohocken, Pa, 2000.
[8] Z.H. Tan, Q. Guo, Z.P. Zhao, H.B. Liu, L.X. Wang, Characteristics of fretting wear resistance for unfilled engineering thermoplastics, Wear 271 (9–10) (2011) 2269–2273.
[9] M.X. Shen, X.D. Peng, X.K. Meng, J.P. Zheng, M.H. Zhu, Fretting wear behavior of acrylonitrile–butadiene rubber (NBR) for mechanical seal applications, Tribol. Int. 93 (2016) 419–428.
[10] Q. Wang, Y. Wang, H. Wang, N. Fan, F. Yan, Experimental investigation on tribological behavior of several polymer materials under reciprocating sliding and fretting wear conditions, Tribol. Int. 104 (2016) 73–82.
[11] O. Vingsbo, S. Söderberg, On fretting maps, Wear 126 (2) (1988) 131–147.
[12] Z.R. Zhou, K. Nakazawa, M.H. Zhu, N. Maruyama, P. Kapsa, L. Vincent, Progress in fretting maps, Tribol. Int. 39 (10) (2006) 1068–1073.
[13] S. Fouvry, P. Kapsa, L. Vincent, Analysis of sliding behaviour for fretting loadings: determination of transition criteria, Wear 185 (1–2) (1995) 35–46.
[14] N. Dahmani, L. Vincent, B. Vannes, Y. Berthier, M. Godet, Velocity accommodation in polymer fretting, Wear 158 (1–2) (1992) 15–28.
[15] R.C. Bill, Fretting wear and fretting fatigue—how are they related? J. Lub. Tech. 105 (2) (1983) 230.
[16] F.H. Stott, B. Bethune, P.A. Higham, Fretting-induced damage between contacting steel-polymer surfaces, Tribol. Int. 10 (4) (1977) 211–215.
[17] P.A. Higham, B. Bethune, F.H. Stott, Changes in the surface morphology of polycarbonate induced by fretting, J. Mater. Sci. 12 (12) (1977) 2503–2510.
[18] N.P. Suh, The delamination theory of wear, Wear 25 (1) (1973) 111–124.
[19] L. Vincent, Materials and fretting, in: R.B. Waterhouse (Ed.), Fretting Fatigue: Papers Presented at the International Symposium on Fretting Fatigue, Held at the University of Sheffield, Mechanical Engineering Publ, London, 1994, pp. 323–337.
[20] B.P. Conner, A.L. Hutson, L. Chambon, Observations of fretting fatigue micro-damage of Ti–6Al–4V, Wear 255 (1–6) (2003) 259–268.
[21] R.C.L. da Silva, C.H. da Silva, J.T.N. Medeiros, Is there delamination wear in polyurethane? Wear 263 (7–12) (2007) 974–983.
[22] G.M. Bartenev, V.V. Lavrent'ev (Eds.), Friction and Wear of Polymers, Elsevier, Amsterdam u.a, 1981.
[23] A. Schallamach, How does rubber slide? Wear 17 (4) (1971) 301–312.
[24] M. Barquins, Sliding friction of rubber and Schallamach waves — a review, Mater. Sci. Eng. 73 (1985) 45–63.
[25] N. Noraphaiphipaksa, A. Manonukul, C. Kanchanomai, Y. Mutoh, Fretting-contact-induced crack opening/closure behaviour in fretting fatigue, Int. J. Fatig. 88 (2016) 185–196.
[26] J. Schijve (Ed.), Fatigue of Structures and Materials, Springer Netherlands, Dordrecht, 2009.

[27] M.Z. Huq, J.-P. Celis, Expressing wear rate in sliding contacts based on dissipated energy, Wear 252 (5–6) (2002) 375–383.

[28] K.L. Johnson, Contact Mechanics, first ed., Cambridge Univ. Press, Cambridge u.a, 1985.

[29] S. Fouvry, P. Kapsa, L. Vincent, Developments of fretting sliding criteria to quantify the local friction coefficient evolution under partial slip condition, Tribology for Energy Conservation, Proceedings of the 24th Leeds-Lyon Symposium on Tribology, Elsevier, 1998, pp. 161–172.

[30] J. Hintikka, A. Lehtovaara, C. Lönnqvist, Effect of start-up schemes and amplitude of tangential motion on friction behavior in fretting point contact, Tribol. Int. 44 (11) (2011) 1535–1543.

[31] D.R. Swalla, R.W. Neu, Influence of coefficient of friction on fretting fatigue crack nucleation prediction, Tribol. Int. 34 (7) (2001) 493–503.

[32] Z.R. Zhou, S. Fayeulle, L. Vincent, Cracking behaviour of various aluminium alloys during fretting wear, Wear 155 (2) (1992) 317–330.

[33] L. Vincent, Y. Berthier, M. Godet, Testing methods in fretting fatigue: a critical appraisal, Standardization of Fretting Fatigue Test Methods and Equipment, ASTM International, Philadelphia, 1992, pp. 33–48.

Paper 2: Fretting Behavior of Thermoplastic Polyurethanes

C. Wang[1], A. Hausberger[1], M. Berer[1], G. Pinter[2], F. Grün[3], T. Schwarz[4]

[1] Polymer Competence Center Leoben GmbH, Leoben, Austria

[2] Chair of Materials Science and Testing of Polymers, Montanuniversität Leoben, Leoben, Austria

[3] Chair of Mechanical Engineering, Montanuniversität Leoben, Leoben, Austria

[4] SKF Sealing Solutions Austria GmbH, Judenburg, Austria

Authors and relevant contributions to this publication:

- C. Wang: Application and implementation of fretting method, experimental testing, data evaluation, preparation of the publication
- A. Hausberger: Conceptualization, discussion of experimental data, review the publication
- M. Berer: Program for energy calculation, review the publication
- G. Pinter: Review the publication
- F. Grün: Review the publication
- T. Schwarz: Specimen production, Review the publication

Fretting Behavior of Thermoplastic Polyurethanes

Chao Wang [1] , **Andreas Hausberger** [1,*] , **Michael Berer** [1] , **Gerald Pinter** [2] , **Florian Grün** [3] **and Thomas Schwarz** [4]

1   Polymer Competence Center Leoben GmbH, 8700 Leoben, Austria
2   Materials Science and Testing of Polymers, Montanuniversität Leoben, 8700 Leoben, Austria
3   Mechanical Engineering, Montanuniversität Leoben, 8700 Leoben, Austria
4   SKF Sealing Solutions Austria GmbH, 8750 Judenburg, Austria
*   Correspondence: andreas.hausberger@pccl.at; Tel.: +43-3842-42962-36

check for updates

Abstract: Fretting tests were conducted with five different thermoplastic polyurethanes against a steel ball. Their fretting behaviors were investigated under various test parameters, such as normal load and displacement amplitude. In order to test the sliding performances, tribological tests were conducted using a ring-on-disc setup. The results show that their fretting behaviors can be related to the dynamic mechanical properties, which were characterized by dynamic mechanical analysis (DMA). The three fretting regimes were identified by means of hysteresis and wear scar analysis. In addition, investigations were carried out until the transition regimes occurred. Different wear processes were revealed for each of the three regimes. Differences were identified using dissipated energy. The profiles of wear scars and the counterparts were analyzed using a microscope. The coefficient of friction was calculated separately for the partial slip and gross slip regimes. In the mixed fretting regime, the coefficient of friction is almost at the same level among the five materials. In the partial slip regime, however, it can be distinguished. Temperature measurements were conducted on the counterparts during the tests. Overall, the material that showed the best tribological properties also performed the best in the fretting tests.

Keywords: fretting; wear; fatigue; coefficient of friction; TPU

1. Introduction

Thermoplastic polyurethane elastomers (TPUs) are multiblock copolymers with hard and soft segments. Due to their unique structure, they have high tensile strength and the ability to be processed with thermoplastic methods. These unique properties make TPUs useful in a great variety of applications. TPUs can be applied as a substitution for vulcanized rubber, for example [1]. Due to their excellent mechanical properties, seals made of TPU can maintain an effective dynamic sealing geometry at high pressure for extended periods [2]. The physical and tribological properties of TPUs have been extensively investigated by several researchers. Anisimov investigated the influence of chemical structure on the mechanical and abrasive properties of TPUs [3]. It was found that the hard segment is the determining structure for their properties. The mechanical properties of TPUs have been investigated in various aspects. Qi researched the stress–strain behavior of TPUs and a constitutive model was introduced, which can reflect their nonlinear, time-dependent, and softening behaviors [4]. Sui [5] provided one clarification for the physical deformation mechanisms of TPUs using in situ observation of the morphological changes during deformation and the finite element method. Da Silva discovered the delamination wear on TPUs [6]. Hausberger [7] studied the adhesive and deformation contribution to the friction and wear behaviors of TPUs. Elleuch [8] studied the tribological property of TPUs in sliding contact with indentation and friction tests. Martinez [9] characterized the wear

property of TPUs by means of sliding reciprocating tests using a long stroke tribometer. The effects of contact pressure and temperature alteration on tribological properties has been analyzed. Yahiaoui [10] found that the friction and wear of TPU–steel hybrids follow Coulomb and Archard's laws at room temperature, respectively. The dominant wear mechanisms are abrasive and adhesive wear.

For seals in dynamic applications, fretting is one of the most common types of failures [11]. Numerous studies have been conducted on the fretting behaviors of metals. The fretting behavior, fatigue properties, and damage mechanisms of thermoplastic elastomer-to-metal were discussed in our previous work [12,13]. However, the impact of material properties on their fretting behaviors is still not understood well. Besides, excellent sliding performance is one of the key characteristics that dynamic seals should have. Unanswered questions remain regarding whether a material which has an outstanding sliding performance also shows excellent resistance to fretting, and how these factors associate with each other.

In this research, five different TPUs were investigated with respect to their fretting behaviors. The test method was reported in previous work [12]. The differences among the five materials are discussed regarding various aspects. This study aims to reveal the correlation between the material properties of TPUs and their fretting behaviors. In addition, the sliding performance of each TPU was correlated with their fretting behaviors.

2. Experimental Details

2.1. Test Material

The TPU specimens were produced by injection molding at SKF Sealing Solutions Austria GmbH (Judenburg, Austria). Before the test, they were cut into 36×22 mm plates with a thickness of 6.2 mm. The hardness was measured using the Shore-D method according to DIN ISO 7619-1 and the dynamic mechanical properties were analyzed by means of dynamic mechanical analysis (DMA) with the temperature scan method at 25 °C (EPLEXOR 100 N, NETZSCH GABO Instruments, Ahlden, Germany). The DMA tests were conducted with tension geometry. Concerning the thermal influence of the samples, thermal conductivity was measured with a guarded heat flow meter (DTC 300, TA Instruments, New Castle, DE, USA) at 25 °C. The properties of the materials used are shown in Table 1. As counterparts, commercial stainless-steel balls (diameter = 15 mm, EN 1.4301, HRC 25–39, polished, unhardened, HSI-Solutions GmbH, Vienna, Austria) were employed. An optical microscope (Stereo Microscope SZX 12, Olympus, Tokyo, Japan) was used to analyze the wear scars of the counterparts.

Table 1. Material properties of the five thermoplastic polyurethane elastomers (TPUs).

Material	Density (g/cm³)	Hardness Shore-D	Thermal Conductivity (W/(m·K))	Dynamic Mechanical Analysis (10 Hz)		
				E′ [a] (MPa)	E″ [b] (MPa)	Tan δ
TPU_1	1.192	47	0.199	93.8	12.3	0.131
TPU_2	1.182	41	0.194	51.7	5.6	0.108
TPU_3	1.193	44	0.206	64.4	10.5	0.163
TPU_4	1.176	40	0.194	48.0	4.0	0.083
TPU_5	1.135	40	0.198	56.3	7.0	0.124

[a] storage modulus; [b] loss modulus.

The Fourier transformed infrared spectroscope (FTIR) was applied to characterize the chemical structures of the five used TPUs. As shown in Figure 1, all materials are similar polyester-based TPUs.
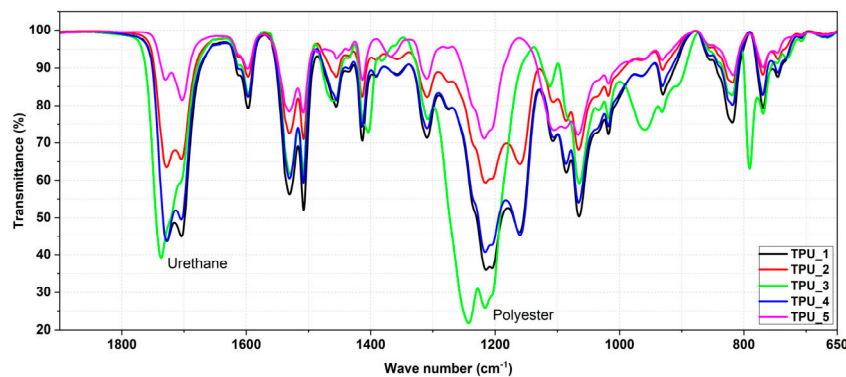
Figure 1. Absorption spectrum of the studied TPUs by FTIR: transmittance vs. wave number.

2.2. Fretting Test Setup and Procedures

Fretting tests were performed on a MTS 858 (MTS Systems Corporation, Eden Prairie, MN, USA) with an in-house design setup, which had been introduced in previous work [12]. Due to the small amplitudes and narrow space in the vicinity of the contact area, the specimen temperature in the contact area was challenging to measure. For that reason, an indirect method was applied in which the temperature of the counterpart was measured using an infrared sensor with a temperature resolution of 0.1 K (CTlaser LT, Optris GmbH, Berlin, Germany).

The applied parameters are listed in Table 2. In order to cover the three fretting regimes, namely partial slip, mixed fretting, and gross slip [14], the displacement amplitude ranges from 0.1 to 1.0 mm. Due to the high compliance of polymers, the displacement amplitudes for polymers are usually larger than for metals, which are approximately 10–50 μm [15]. Three normal loads and two frequencies were applied to investigate the dependency of the fretting behavior of TPUs on normal load and frequency. The total number of cycles was set to 8×10^5 cycles. Some cycles were chosen based on three-dimensional fretting hysteresis, in which the form changed substantially, so that the alteration process of wear scars could be investigated and correlated to fretting hysteresis.

Table 2. Test parameters for fretting.

Displacement Amplitude (mm)	Normal Load (N)	Frequency (Hz)	Number of Cycles
0.1, 0.25, 0.5, 1.0	20, 28, 48	10	8×10^5

All of the experiments were performed at 23 ± 2 °C with a relative humidity of 50 ± 10%. The wear scars were characterized by a scanning electron microscope (SEM) (Tescan VEGA-II, Brno, Czech Republic). Quantifications of the wear scars were conducted with a three-dimensional micro coordinate microscope (Alicona InfiniteFocus, Raaba, Austria).

2.3. Ring-on-Disc Tests

To compare the sliding performance with fretting behavior, tests were conducted using a component-like (ring-on-disc) setup on a precision rotary tribometer (TE-93, Phoenix Tribology Ltd., Kingsclere, UK). The setup and specimen geometry were introduced in [16]. All tests were conducted at 150 mm/s under a normal load of 1 MPa for 4 h. Each test was repeated four times. Ring-shaped counterparts of 34CrNiMo6 were used, with a roughness of 0.03 μm. After the tests, the surfaces of the specimen and counterparts were analyzed with a light microscope.

3. Results and Discussion

For the ring-on-disc tests, the coefficient of friction (COF) and wear rate were compared and discussed. The worn surfaces were analyzed and correlated with the COF and wear rate.

The fretting hysteresis and F_t-D curves are shown and compared with each other. With the help of the micrographics of wear scars, it is possible to understand the hysteresis change during the tests. Based on the geometry of the wear scars, the coefficients of friction are calculated for the partial slip and mixed fretting regimes. For the gross slip regime, a select calculation is used, which also takes the geometry of the wear scars and construction of the test system into consideration [12]. As reported in [17], the surface in the contact area changed continuously during the tests. The calculation of the COF is only based on the worn surface after the last cycle. Hence, the calculated COF can only represent the COF value at the last cycle.

3.1. Ring-on-Disc Tests

The results are shown in Figure 2. Compared with the other four materials, TPU_4 shows the best tribological performance. Both COF and wear rate values are significantly lower than for the other materials. Its COF is 0.61, around 40% lower than others, which is over 1. More importantly, nearly no wear debris was identified with TPU_4. Its wear rate is only 0.4 cm^3/Nm, making it 110-times lower than that of TPU_3. From the DMA results in Table 1, we can see that its low storage modulus and low loss factor indicate that TPU_4 is the softest and most elastic material among the five TPUs. Hence, its deformation contribution of friction is larger than in the other materials. As can be seen in [7], deformation contribution is the dominant contribution of friction for TPUs. In spite of this, TPU_4 shows the lowest COF and best wear resistance. It is worth mentioning that the COF shown here is the average COF throughout all of the tests. The wear debris, surface alteration, and temperature affect the COF significantly.
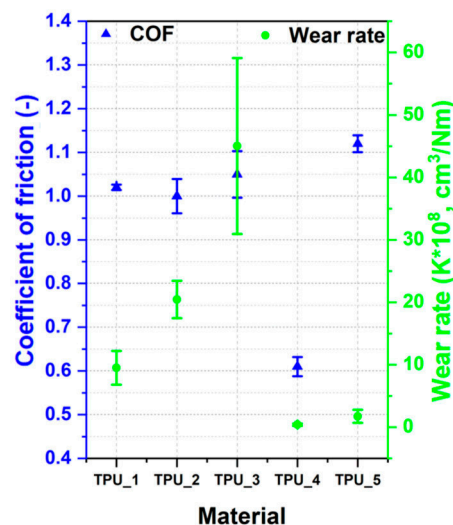
Figure 2. Results from tribological tests.

The difference in wear rate can also be identified from the wear scars. As shown in Figure 3, adhesive wear is the dominant wear mechanism for TPUs_1, 2, and 3. However, no noticeable wear can be identified on TPU_4. For TPU_5, its high COF leads to a higher temperature (over 100 °C) at the interface, which is about 70 °C for TPU_4. As a consequence, TPU_5 experienced a larger deformation, especially in the microtexture area on the surface.
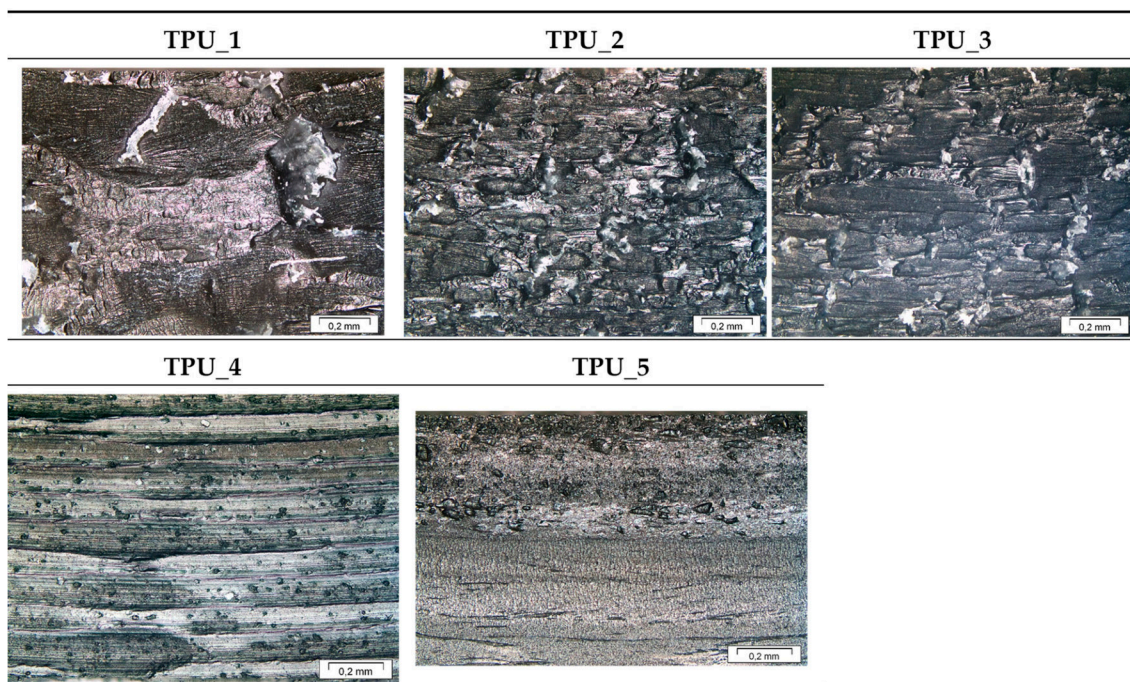
Figure 3. Micrographs of wear scars after tribological tests.

3.2. Fretting Tests

3.2.1. Fretting Hysteresis and Wear Scar Analysis

The hysteresis and F_t-D curves are discussed. TPU_1 was discussed in our previous work [12], but in order to compare it with the other TPUs, its results are also shown here.

Each material was observed with a light microscope. Additionally, several samples representing the typical wear tracks were chosen to have a more accurate scar analysis using scanning electron microscopy (SEM). The diameters of the inner (2c) and outer rings (2a) were characterized with a three-dimensional, micro-coordinate microscope (Figure 4), and are shown here in the SEM micrographs. It should be noted that TPU_5 is transparent, so the marks we made on the back of the samples as distinctions can be seen in the micrographs.
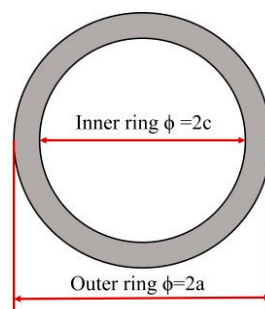
Figure 4. Inner and outer rings of the wear scar.

Partial Slip Regime

Figure 5 shows the hysteresis and F_t-D curves of the five TPUs. In order to observe the change of the tangential force more clearly, the hystereses are projected on the cycle-tangential force plane (green) in Figure 5. In the partial slip regime after approximately 10^5 cycles, the hystereses of all five TPUs are very similar. For TPUs_2, 3, and 4, their hystereses are almost linear, whereas for TPU_1 and TPU_5, they were parallelogrammical in the first 10^3 cycles and then gradually changed to linear.

Materials	3D	2D
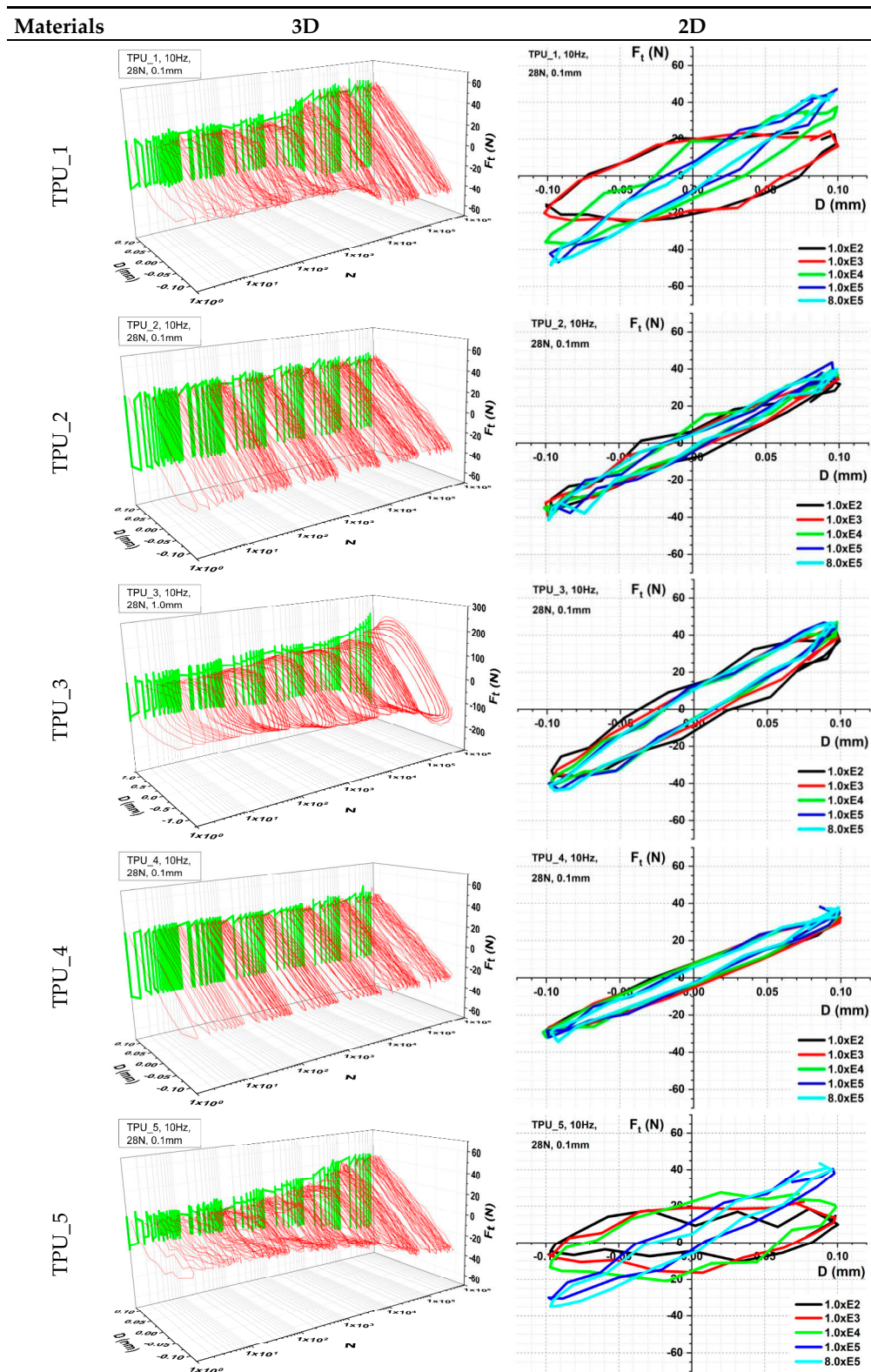
Figure 5. Hysteresis and F_t-D curves of the five TPUs in the partial slip regime.

In the partial slip regime, ring-like wear scars were generated. As illustrated in Figure 6, all five TPUs show similar wear scars. The middle area is the stick region, while a micro slip occurs at the edge of the ring.

Figure 6. Micrographs of wear scars of the five TPUs (D = 0.1 mm, F_n = 28 N).

The damage scar of TPU_1 with 0.1 mm displacement amplitude was outlined in our previous work [12]. The damage began with the drop of small debris from the ring area. As the test ran further, debris was rolled into stripe-like particles. This can be attributed to the small amplitude, which is not large enough to separate the particles from the surface.

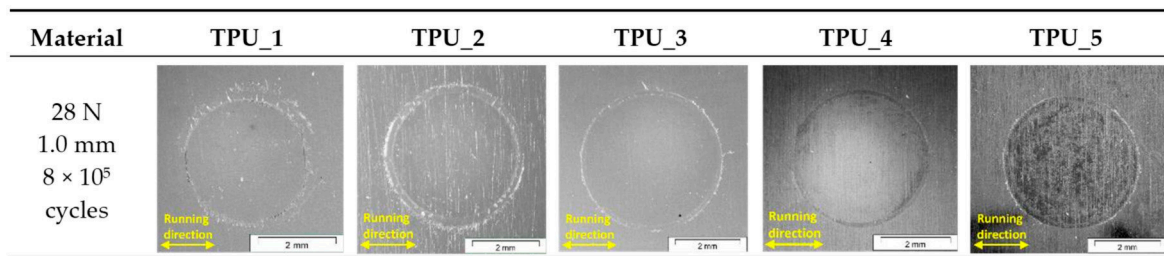Comparing Figures 6 and 7, it is evident that more debris was generated when the displacement amplitude increased from 0.1 to 0.25 mm. A butterfly-like scar can be identified on TPUs_1 and 2. The ring-like scar on TPUs_3, 4, and 5 with 0.25 mm displacement amplitude is larger than that with 0.1 mm. Small, stripe-like debris can also be observed in the top and bottom areas of the inner ring on TPU_1 and TPU_3, whereas on the other samples, these areas are much smoother.
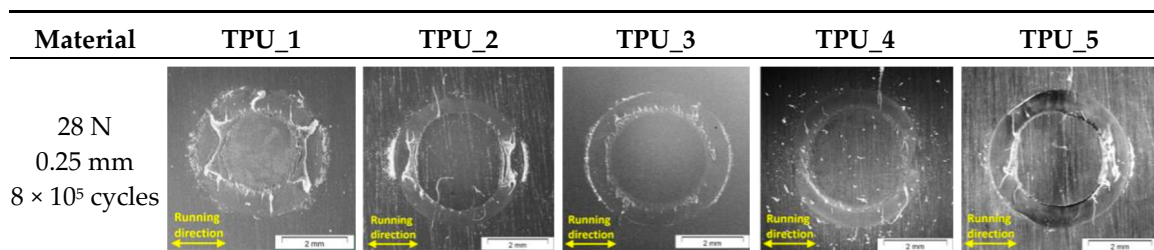

Figure 7. Micrographs of wear scars of the five TPUs (D = 0.25 mm, F_n = 28 N).

Figure 8 shows the wear scar of TPU_4 after 10^4 cycles. The test was conducted under 28 N normal load with 0.25 mm displacement amplitude. As shown in Figure 8a, small amounts of wear debris can be seen at the edge of the ring. Small wear particles were generated during the micro-slip. They can be identified in Figure 8c,d.

Mixed Fretting Regime

Compared to the hystereses in the partial slip regime, more alterations of the hystereses can be observed in the mixed fretting regime (Figure 9). Among the five TPUs, the hysteresis of TPU_1 changed differently, while the other TPUs behaved similarly in the mixed fretting regime. For TPU_1, the tangential force remained almost constant in the first 10^3 cycles when the samples were between −0.3 mm and +0.3 mm. As can be seen from the hysteresis, after approximately 10^3 cycles, its form began to change. The tangential force became larger with the increased displacement. It should be mentioned that the tangential force at the displacement (D) = ±0.5 mm reduced at first and then increased again when the cycle number increased from 10^4 to 10^6, whereas it increased continually at D = 0 mm. This phenomenon can be attributed to the wear generating process. As examined in [12], delamination wear and cracks can be found in the stick region after the test. After approximately 10^3 cycles, the damage began to appear on the edge of the ring. More wear debris was generated with increasing cycles because of the partial slip between the sample and the counterpart. Hence, the stick region became smaller and the tangential force at the maximum displacement decreased slightly. Due to the repeated shear stress, delamination and cracks can occur in the stick region. As a consequence, the tangential force can be altered.
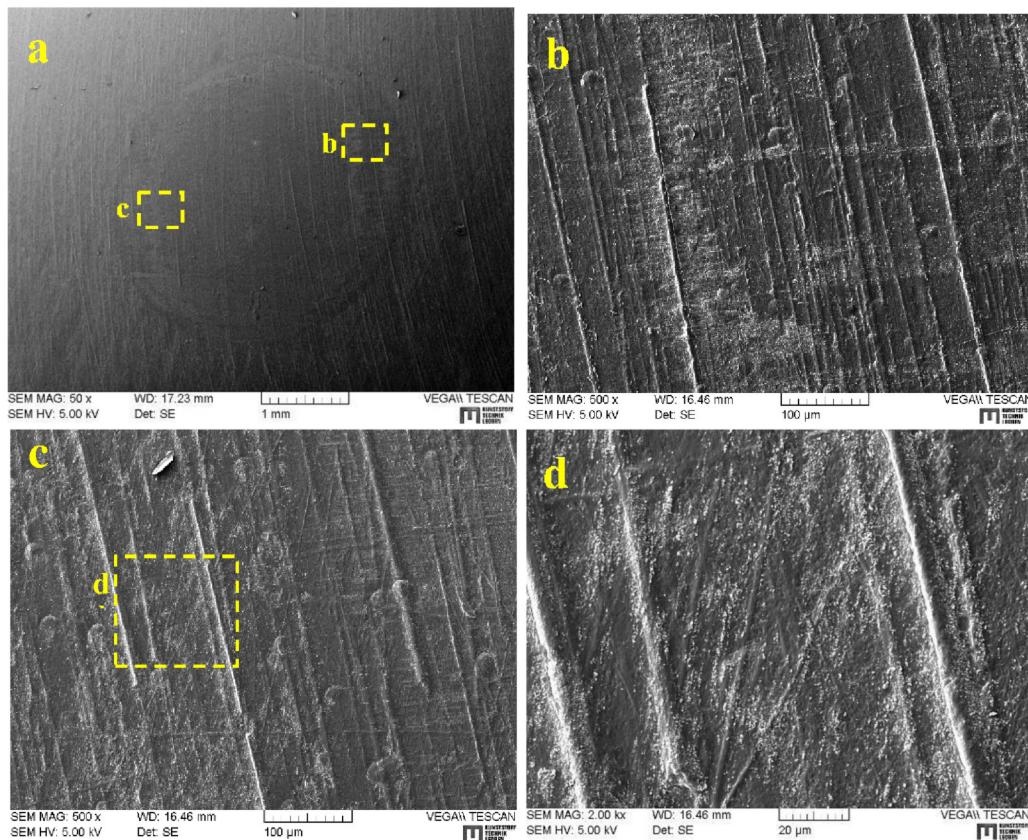
Figure 8. (**a**) SEM micrograph of wear scars determined for the following parameters: TPU_4, $F_n = 28$ N, D = 0.25 mm, f = 10 Hz, N = 10^4. Related areas are marked and shown with larger magnifications (**b**–**d**).

TPU_2 and TPU_3 show similar hystereses. From 10^2 to 10^3 cycles, the hysteresis narrows, which means the tangential force reduces at D = 0 mm and increases at D = ±0.5 mm. For TPU_4 this change occurred later, after 10^3 cycles. However, for TPU_5 the maximum tangential force becomes slightly smaller with the increasing number of cycles. From the 2×10^5 cycle, it begins to increase. It is also noticeable that the tangential force does not change linearly, but rather with an inflection point at approximately D = +0.15 mm for the movement from D = +0.5 to −0.5 mm, and vice versa. Due to the repeated shear stress, the left and right sides of the stick region can be folded (Figure 9). This can lead to an inflection in the tangential force.

The mixed fretting regime, as its name suggests, is the transition field between the partial slip and gross slip regimes. As seen in Figure 9, the stick regions are much smaller than those in the partial slip regimes. Due to its larger amplitude, the stick region becomes smaller with increasing cycle numbers. Butterfly-like wear scars can be identified distinctly on TPU_3. On both sides of the stick regions, folds can be observed on TPUs_2, 3, 4, and 5. As explained in [12], repeated normal and shear stresses induce cracks and delamination wear on TPU_1. Figure 10 shows the profiles of the wear scars. TPUs_1 and 5 have the smallest stick regions and the deepest scars in the slip regions. In the stick regions of TPU_2 and TPU_5, slight surface alteration can be observed on the edges. Especially on TPU_5, the deformation of the surface decreases from the edge to the middle (Figure 11). This can be explained by the shear stress distribution. For this circular contact under a steady normal force and an oscillating tangential load, the maximum shear stress is located at the edge of the stick region (Figure 12) [18].
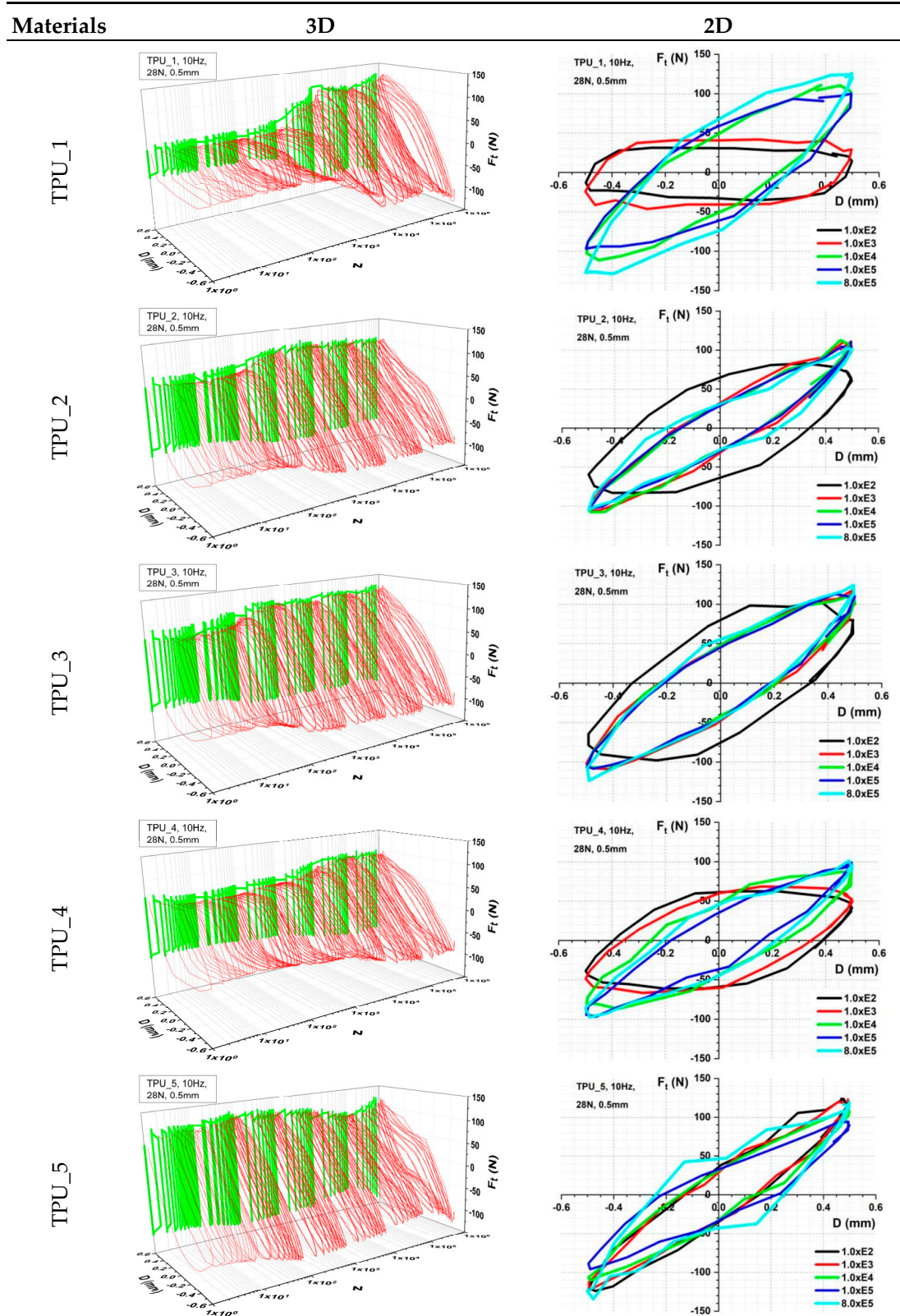
Materials	3D	2D
TPU_1		
TPU_2		
TPU_3		
TPU_4		
TPU_5		

Figure 9. Hystereses and F_t-D curves of the five TPUs in the mixed fretting regime.

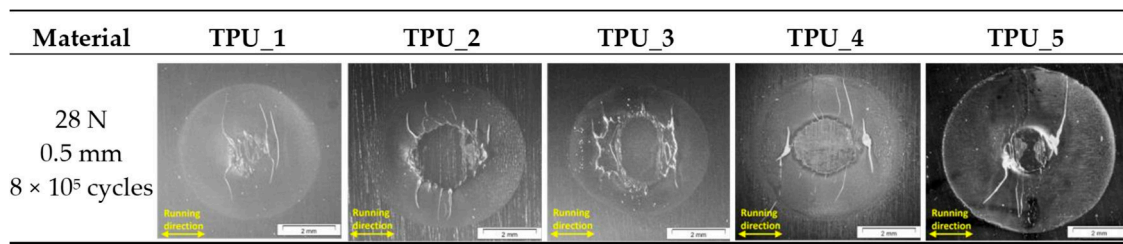| Material	TPU_1	TPU_2	TPU_3	TPU_4	TPU_5
28 N 0.5 mm 8×10^5 cycles					

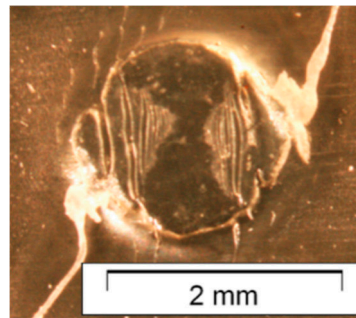**Figure 10.** Micrographs of wear scars of the five TPUs (D = 0.5 mm, F_n = 28 N).

Figure 11. Magnification of the stick region of TPU_5.
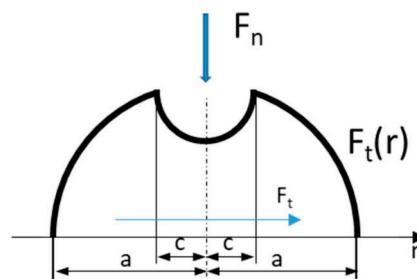
Figure 12. Shear stress distribution under a steady normal force and an oscillating tangential load of amplitude F_t [18].

The hysteresis of TPU_1 shows a distinct transitional phase by approximately 5×10^3 cycles (Figure 9). The wear scar after 5×10^3 cycles is shown in Figure 13. Rolled stripe-like debris can be observed around the stick region (Figure 13a). Similar but much smaller debris can also be found in the partial slip regions. Additionally, micro pitting is identified at the edge of the outer ring. Due to surface fatigue, micro pitting can occur after the incubation period in fretting tests [19,20]. At the edge of the inner ring, the rolled debris was pressed into the surface and flattened due to plastic deformation. The contact was changed to three-body contact, which can lead to debris formation, and hence an alteration in the hysteresis form. Due to the debris between the contact surfaces, the tangential force was reduced slightly. The alteration in the hysteresis form is in good agreement with the previous studies [21]. However, a similar steady phase after the alteration cannot be identified, similar to in Godet's experiments with steel alloys [21]. After a short steady phase, the tangential force began to increase because the surface morphology changed with the increasing number of cycles. Though the hardness of the debris is similar to the substrate, it can also affect the contact situation. The real contact area decreases, which leads to higher local contact stress and contact temperatures [22,23]. For polymers, all of these changes can affect the contact states, and thus accelerate the wear process. The profiles of wear scars show the depth of each scars (Figure 14).

Figure 13. (**a**) SEM micrograph of wear scars determined for the following parameters: F_n = 28N, D = 0.5 mm, f = 10 Hz, N = 5×10^3. Related areas are marked and shown with larger magnifications (**b–d**).
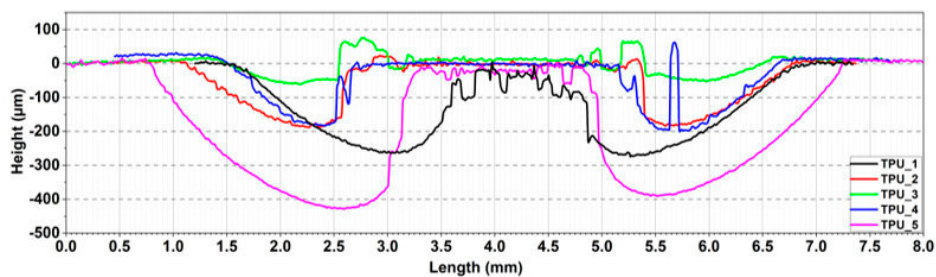
Figure 14. Profiles of wear scars of the five TPUs (D = 0.5 mm, F_n = 28 N, 8×10^5 cycles).

Compared to TPU_1, no apparent debris can be observed on TPU_4 after 5×10^3 cycles (Figure 15). However, delamination wear, which is attributed to cyclic shear and normal stresses [24,25], can be found in particular in the region where the maximum shear stress occurred, according to the hystereses in Figure 9.
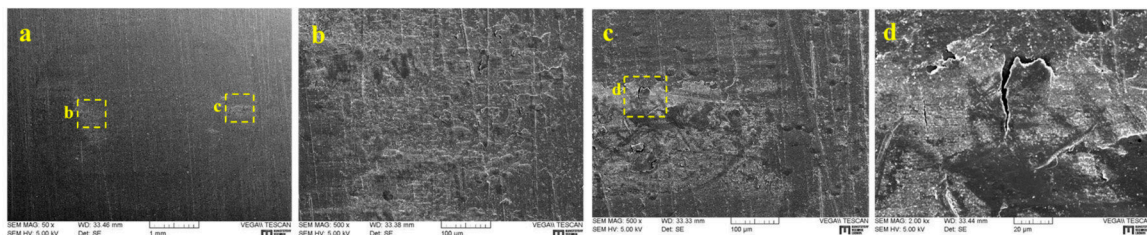
Figure 15. (**a**) SEM micrograph of wear scars determined for the following parameters: TPU_4, F_n = 28N, D = 0.5 mm, f = 10 Hz, N = 5×10^3. Related areas are marked and shown with larger magnifications (**b–d**).

According to the hystereses, the transitional phase occurred slightly later. Its wear scar after 5×10^4 cycles is shown in Figure 16. Various kinds of wear debris can be identified on the surface. On the whole, its debris is considerably larger than that of other materials. Larger block-like debris can be found on both sides, while stripe-like debris can be seen in the top and bottom regions. The stripe-like debris was rolled together due to the repeated movement, which was also observed using the in situ method [26]. Small stripe-like debris can be found in the middle area (Figure 16b,c), which was partially pressed into the surface (Figure 16d). Due to the larger block-like debris, the tangential force changed continuously. At the edge of the ring, layer-like debris can be found, which can be attributed to repeated stresses. Meanwhile, debris particles were observed at the edge of the outer ring, where according to the microstructures of the substrate, no contact occurs (Figure 16g,h). Therefore, the wear particles could be generated in the early phase and were removed at that point.
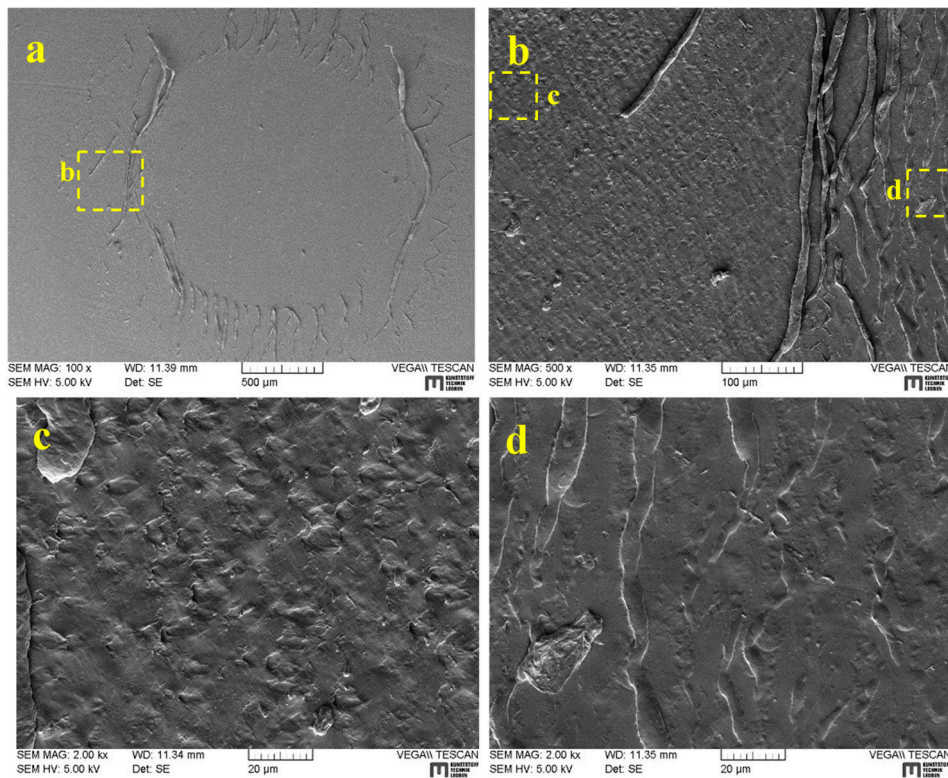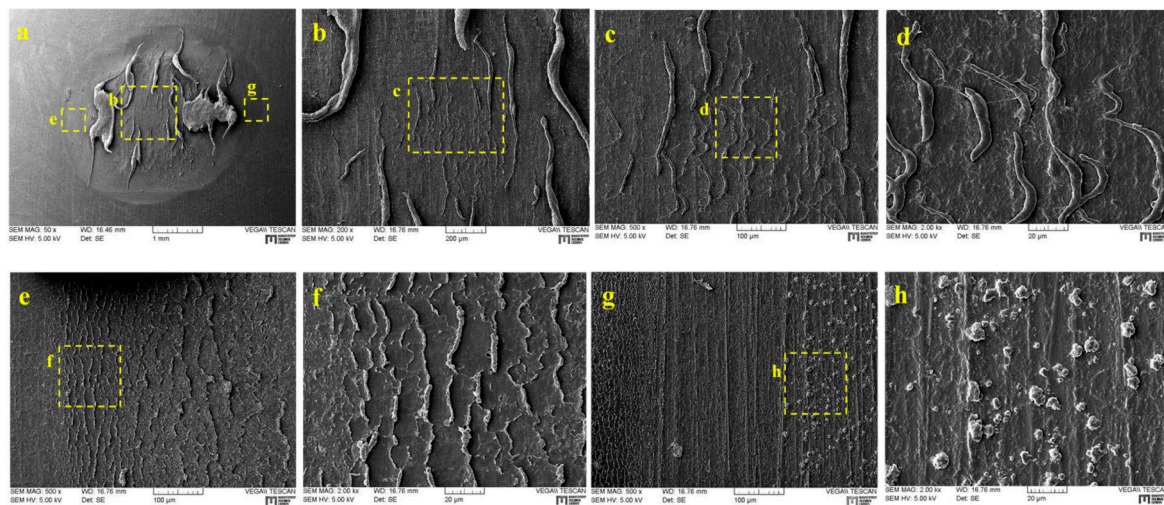

Figure 16. (**a**) SEM micrograph of wear scars determined for the following parameters: TPU_5, F_n = 28 N, D = 0.5 mm, f = 10 Hz, N = 5×10^4. Related areas are marked and shown with larger magnifications (**b**–**h**).

Gross Slip Regime

For the behaviors in the gross slip regime, each material shows its differences (Figure 17). For TPU_1, in the first 10^3 cycles, its tangential force remained almost constant with a slight increase during the movements, but still at a very low level of approximately 30 N, which is much smaller than other materials. The beginning behavior depends very much on the TPU surface. All surfaces were cleaned before the tests, even though their surfaces were slightly different. After 10^3 cycles its form began to change. When the sample moved from the furthest point (D = ±1.0 mm) to the central position (D = 0 mm), the tangential force reduced at first and then increased. After reaching the middle point, the tangential force remained almost constant until the furthest point. After approximately 2×10^5 cycles, the hysteresis form changed again. This was caused by severe wear, which altered the geometry of the sample.
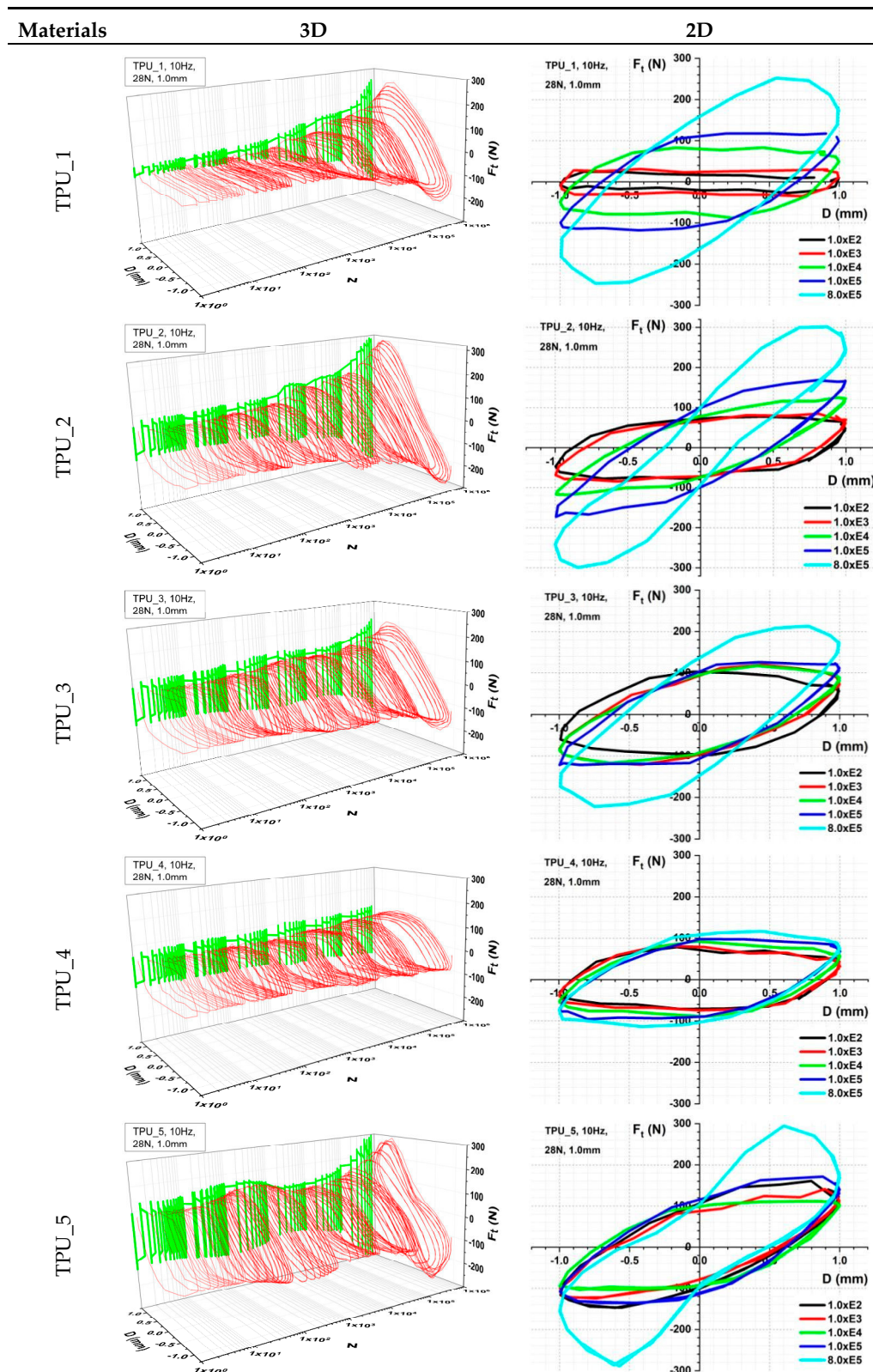
Figure 17. Hysteresis and F_t-D curves of the five TPUs in the gross slip regime.

TPU_2's tangential force increased gradually with the number of cycles and stayed in a similar form. From approximately 10^5 cycles, server wear was generated on both sides of the contact area (Figure 18). This explains the hysteresis form in the 8×10^5 cycle. In the middle area, the surface is

much smoother than other regions, so the tangential force changed when the sample moved in the central area.

Figure 18. Micrographs of wear scars of the five TPUs (D = 1.0 mm, Fn = 28 N).

For TPU_3, its tangential force increases slowly with the number of cycles until 10^5 cycles. Similar hysteresis to TPU_1 can be observed after 10^5 cycles. However, its maximum tangential force is slightly smaller than that of TPU_1.

The hysteresis of TPU_4 can be described with three parallelograms, the first of which describes the first 10^3 cycles. The second one shows the hysteresis from 10^5 cycles. Between 10^3 and 10^5, the hysteresis is illust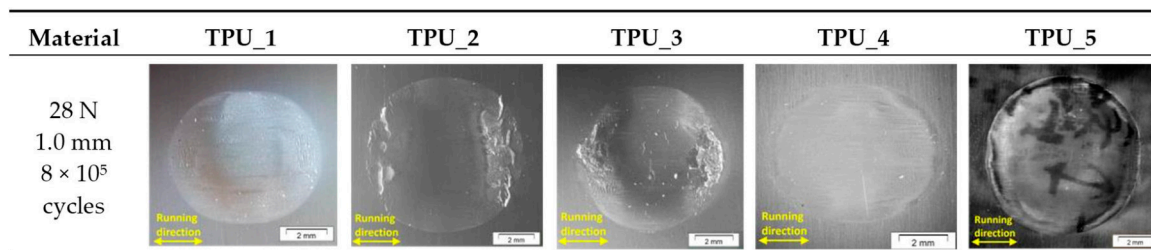rated with the third parallelogram, which can be treated as a transition phase. Both its height and width are between the first two parallelograms.

For TPU_5, its hysteresis looks very similar to the first 10^5 cycles. However, the maximum tangential force was not constant. It increased for the first 100 cycles and then decreased. From 5×10^3 cycles, it increased again. After 4×10^5 cycles, the tangential force grew faster after passing over the middle point.

In the gross slip regime, the counterpart slips over the contact area. As can be observed in Figure 18, the wear scars of TPU_1, 4, and 5 show a definite similarity, and materials were removed because of the slip movements. However, severe wear can be seen on both sides of the scars in TPUs_2 and 3. This phenomenon can also be identified in the hysteresis. The evidence points to the substantial likelihood that these two materials behaved differently under cyclic normal and shear stresses, in particular at a relatively high temperature, which is related to fatigue mechanisms. Additionally, this can also be initiated by third body wear; the liberated debris stays in the contact zone and acts as a third body, which can lead to an acceleration of the wear process.

In comparison to the mixed fretting regime, wear scars in the gross slip regime are considerably broader and deeper. Among the five materials, the most severe wear was identified in TPU_5, which corresponds to the mixed fretting regime. For TPU_5, rolled debris on the bottom of the wear scar facilitated the slip movement of the counterpart, which resulted in a reduction of tangential force in the middle area (Figure 17). TPU_4 shows the best wear resistance, which is consistent with the results in tribological tests. The scar depth of TPU_4 is about 500 μm, which is only one-third of the depth in TPU_5 and half of that in TPU_3 (Figure 19).
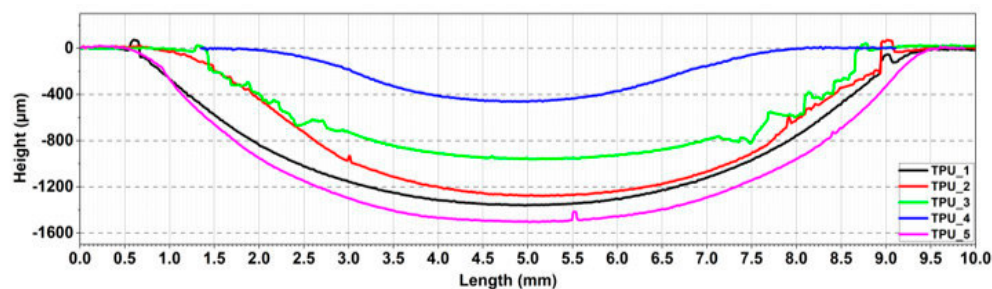

Figure 19. Profiles of wear scars of the five TPUs (D = 1.0 mm, F_n = 28 N, 8×10^5 cycles).

On both sides of the contact area, severe wear can be found on TPUs_2 and 3 after 8×10^5 cycles. Larger cracks can be observed in Figure 20d. At the end of the test, its tangential force increased to

over 300N on both sides (Figure 17). Flake-like sections can be identified in Figure 20b,d. On the one hand, the glass transition temperature increases with increasing frequency. Thus, the material becomes slightly more brittle under 10 Hz than in a static situation. On the other hand, due to the large amplitude, debris can be easily torn away from the surface. Small wave-like debris was found in the middle area, which was generated as a result of repeated shear stress (Figure 20e,f). This kind of debris was also found in TPU_1 [12]. Moreover, the smooth wave surface was observed in the topside region (Figure 20h), which looks different to Figure 20b. This can be ascribed to the contact state. In Figure 20a, due to the spherical counterpart, the normal and shear stresses in region g are considerably smaller than those in region b. Hence, cracks in region g are smaller. Small wave-like debris was rolled together into larger debris (Figure 20g) when the ball slid over the region. After this process, the surface, which was full of small wave-like debris, looked smooth. Microcracks are generated with further movement.

Figure 20. (**a**) SEM micrograph of wear scars determined for the following parameters: TPU_2, F_n = 28 N, D = 1.0 mm, f = 10 Hz, N = 8×10^5. Related areas are marked and shown with larger magnifications (**b**–**h**).

Compared with TPU_2, the wear on TPU_4 is not as severe. The tangential force of its last cycle, approximately 120N, is significantly smaller than that of the other materials. On the one hand, it is the softest material in both static and dynamic states (Table 1). On the other hand, no severe wear, such as was seen for TPU_2, can be found for TPU_4 (Figure 19). As shown in Figure 21a, wave-like debris can be found on both sides, whereas the middle region is relatively smooth but with a lot of stripe-like debris. As evident in Figure 21c,g, several grooves are visible, which can be attributed to third-body abrasive wear. Particles can also be found in Figure 21g. Generally, the abrasive material must be harder than the surface [27]. These particles can be wear particles from the counterpart or external contamination. Both matter types are harder than the substrate. The particles might be tiny at the beginning, however they can be wrapped up in TPU debris. Compared to the other materials, except for TPU_5, the height of the wave-like debris is much smaller, so the sides are smoother. In addition, due to its lower hardness, the waves seem to be flattened when the counterpart slides over them. Both of these phenomena facilitate the moment of the counterpart.
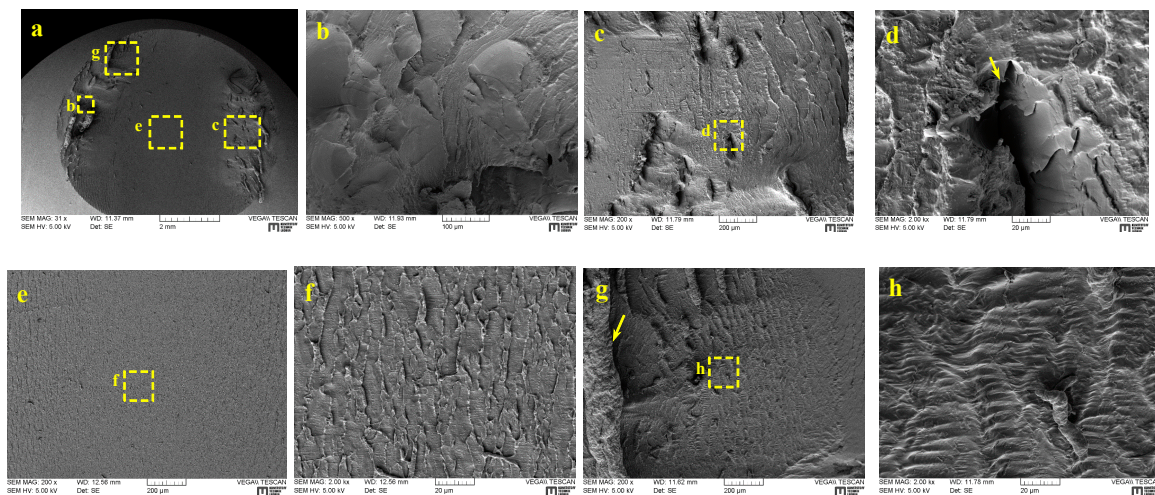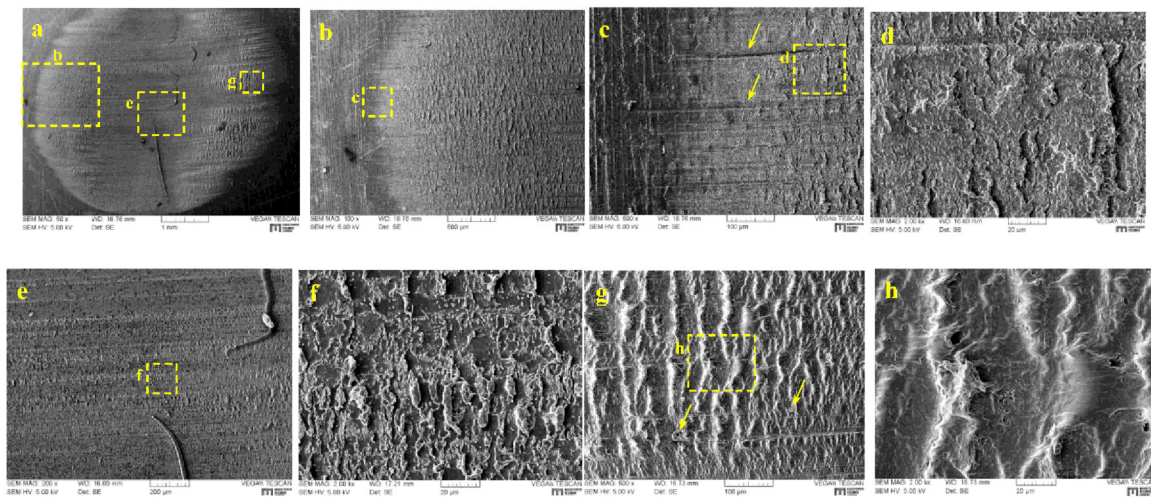
Figure 21. (**a**) SEM micrograph of wear scars determined for the following parameters: TPU_4, F_n = 28N, D = 1.0mm, f = 10 Hz, N = 8×10^5. Related areas are marked and shown with larger magnifications (**b–h**).

Consequently, the tangential force of TPU_4 remains almost constant or even reduces with the counterpart's movement from the middle to the side (Figure 17). The wear debris at the edge of the contact area and in the middle of the area is shown in Figure 21d,f, respectively. They look different from TPU_1 [12] and TPU_2. As shown in Figure 21d, owing to surface fatigue, the wear debris seems to be either delaminated from the surface or pressed into the surface. The debris clearly appears to be looser. The wear scars of the middle region can be affected by the interfacial debris, making the rolled wear debris look less neat than TPUs_1 and 2.

The wear scars of TPU_4 seem to be smoother than those of TPU_5. As shown in Figure 22b, a slight trough can be found on the surface. Images with high magnification for the trough are shown in Figure 22c,d. By using the method from our previous work [12], the friction force and normal force were calculated and are shown in Figure 23 with tangential force. As can be observed, the friction force is slightly smaller than the tangential force. The normal force is 28 N at D = 0 mm and increases with displacement. The maximal normal force reaches approximately 46 N at approximately D = 0.8–0.9 mm. In the reverse direction, the normal force decreases to 28 N. The trough could be the result of the coaction of small debris with large stripe-like debris under high normal load.

As shown in Figure 17 and discussed previously, the 10^4 cycle is the approximate transition field for all five TPUs in hysteresis. In order to investigate the alteration process of the wear scars and correlate the hysteresis with the wear scars, tests were conducted until 10^4 cycles. Figure 24 shows the micrographs of the wear scars. In TPUs_1, 2, and 5, similar wear scars can be observed on the surface after 10^4 cycles. Large cracks were nucleated and propagated perpendicular to the sliding direction, while on TPU_3 the cracks are focused in the middle area and both sides are relatively smooth. For TPU_4, its wear scars after 10^4 cycles look similar to those seen after 8×10^5 cycles in the mixed fretting regime. The middle area seems to be stuck on the counterpart. This can be ascribed to its distinctly lower storage modulus under 10 Hz load compared with the other materials. For this reason, TPU_4 can deform even under 1.0 mm displacement amplitude, so that no slip can occur between the middle area of the sample and the counterpart. Stripe-like wear debris can be seen on the surface, which was rolled because of the slip movements on both sides.

Figure 22. (**a**) SEM micrograph of wear scars determined for the following parameters: TPU_5, F_n = 28 N, D = 1.0 mm, f = 10 Hz, N = 8 × 10^5. Related areas are marked and shown with larger magnifications (**b**–**j**).
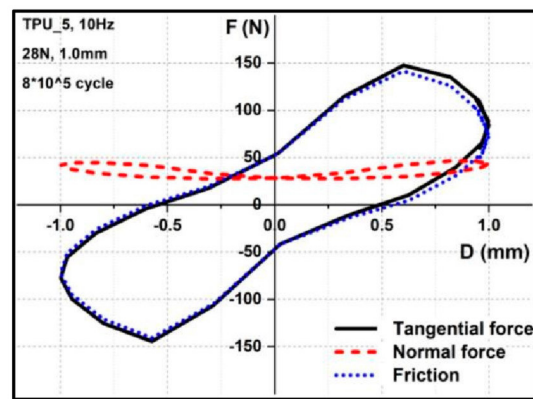
Figure 23. Tangential force, normal force, and friction at the 8 × 10^5 cycle of TPU_5 (28 N, 1.0 mm, 10 Hz).
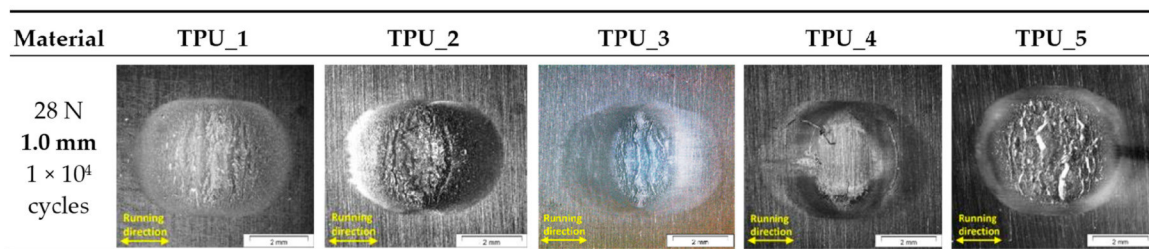
Figure 24. Micrographs of wear scars of the five TPUs (D = 1.0 mm, F_n = 28 N, 10^4 cycles).

Figure 25 shows the profiles of the wear scars after 10^4 cycles. Almost no change can be identified for TPU_4. However, severe wear can be observed in other materials to varying degrees. This reveals the formation process of the wear scars.
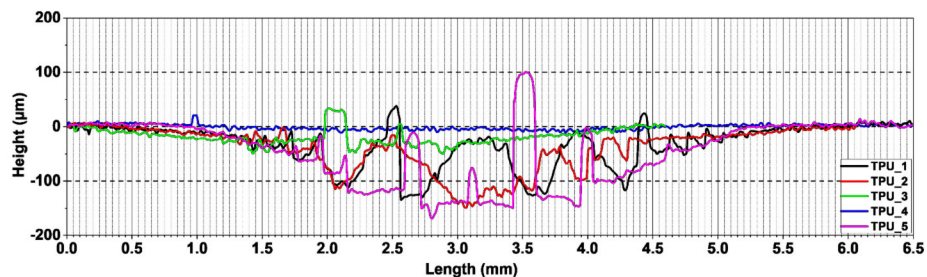
Figure 25. Profiles of wear scars of the five TPUs (D = 1.0 mm, F_n = 28 N, 10^4 cycles).

After 10^4 cycles, severe wear can be observed in the middle part of the contact area in TPU_3 (Figure 26a). Sizeable stripe-like debris was generated on both sides, which is perpendicular to the sliding direction. However, small debris can be found at the edge of the sliding area (Figure 26c,d). This debris was not rolled together as large debris and was partially removed to the edge and partially pressed on the surface (Figure 26d). In addition, abrasive wear can also be identified (Figure 26e). Meanwhile, flake-like debris is visible (Figure 26f), which can be attributed to surface fatigue. At the edge of the middle scar, the embryonic form of the sizeable stripe-like debris can be observed (Figure 26g). As shown in Figure 26h, because of the cracks, the debris was separated from the substrate and began to connect to form large pieces of debris. With further cycles, more debris would be rolled together.
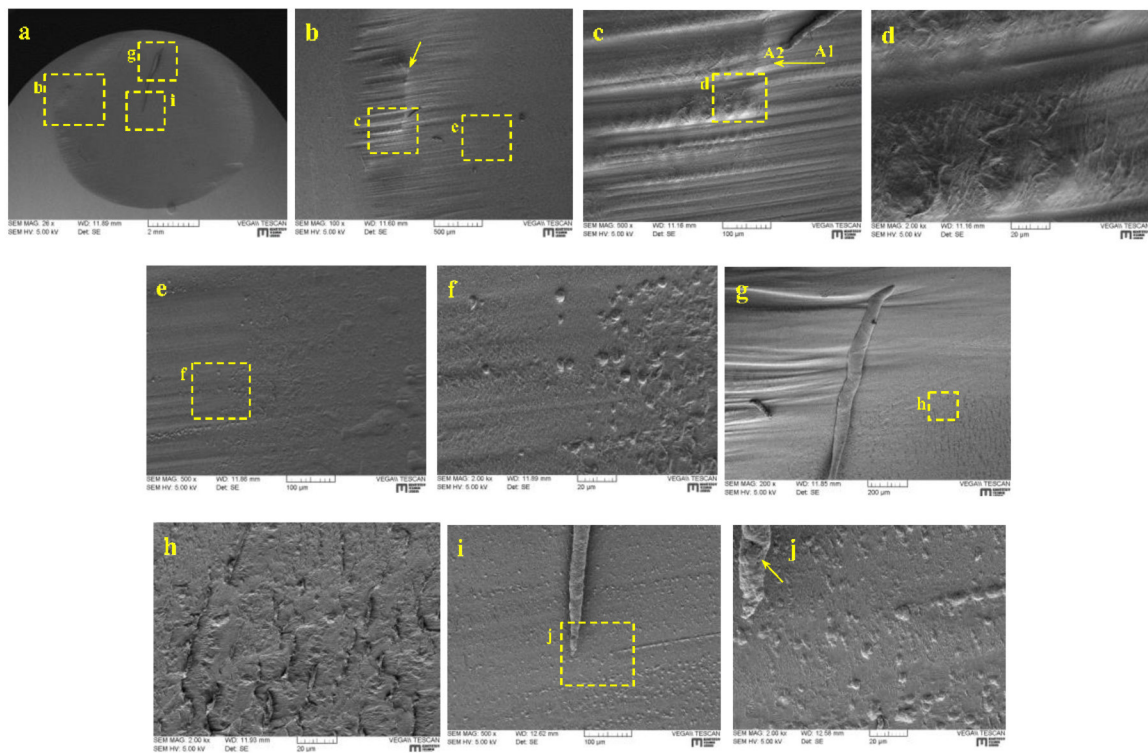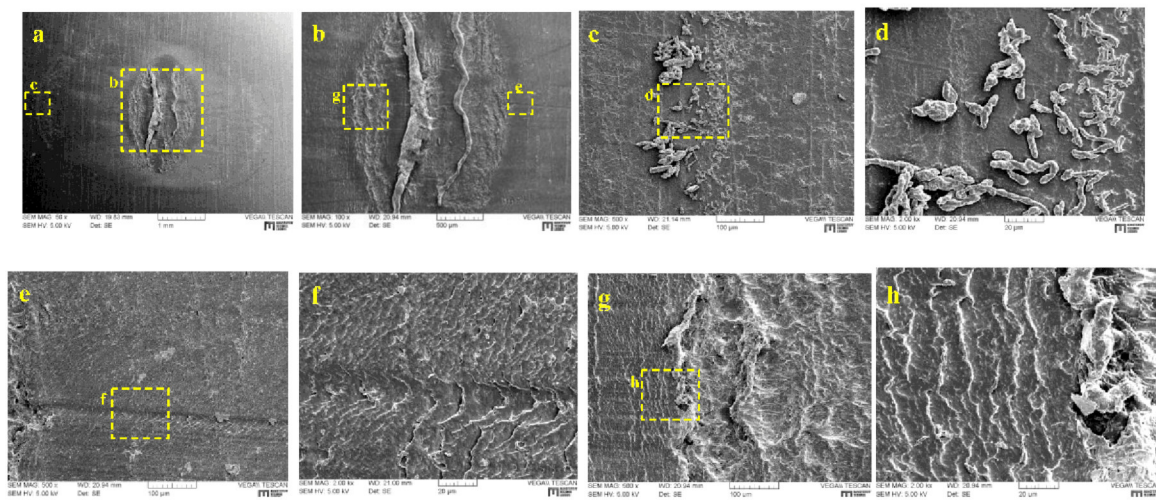

Figure 26. (**a**) SEM micrograph of wear scars determined for the following parameters: TPU_3, F_n = 28 N, D = 1.0 mm, f = 10 Hz, N = 10^4. Related areas are marked and shown with larger magnifications (**b**–**h**).

3.2.2. Counterpart

Besides the wear scars, the counterpart surfaces were also analyzed with a microscope. In Figure 27, the micrographics of counterparts are shown. The micrographics were taken with a ring illuminator. Two extreme examples, TPU_4 and TPU_5, were chosen. They represent the best and worst fretting behavior, respectively. In the partial slip regime (PSR), due to the large stick region and the cyclic shear stress, the materials adhered to the counterpart. This phenomenon can also be identified in the mixed fretting regime. However, the amount is less and size is smaller than in the partial slip regime. In the gross slip regime, slight abrasive wear scars can be observed on the

counterpart. For TPU_5, visible wear marks are found on the counterpart. It is evident that the wear debris, which is on the bottom of the wear scar (Figures 19 and 22), worked as a third body [21] in the interface. Under normal and shear stresses, it can be attached to the counterpart.
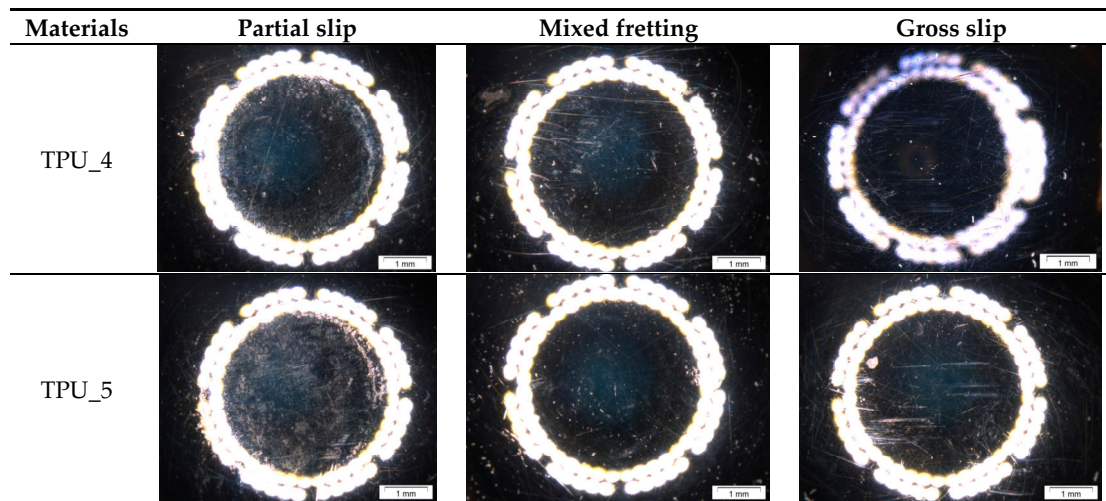
Figure 27. Micrographics of counterparts of TPU_4 and 5.

3.2.3. Dissipated Energy

Dissipated energy is an integration of the tangential force with the displacement for a full test. It is also the energy converted from kinetic energy to heat because of friction. As can be observed in Figure 28 with all four displacement amplitudes, TPU_1, 3, and 5 have dissipated more energy than TPU_2 and 4.
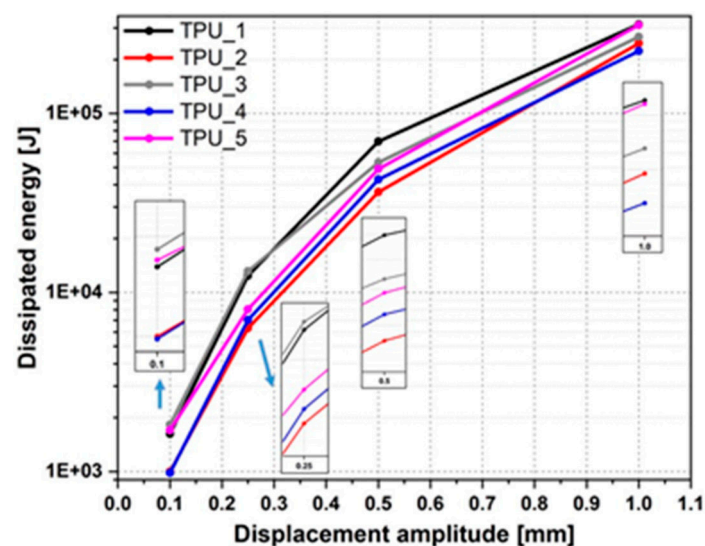
Figure 28. Dissipated energy during the fretting tests with four different displacement amplitudes.

Several factors can affect the dissipated energy. One crucial factor is the mechanical properties of the material under dynamic stresses, which can be determined by dynamic mechanical analysis tests. The other factor is the time during a fretting test when the contact surface begins to be worn. Once the contact surface is worn, the tangential force can be changed significantly. The thermal effect would also be considered as a significant influence factor for the dissipated energy. As we know, polymers are materials whose mechanical properties change dramatically with temperature. During the fretting test, the temperature of the contact area changes with dissipated energy. This can result in an alteration of

the mechanical properties of the TPU. Hence, the tangential force changes, conversely affecting the dissipated energy.

3.2.4. Temperature Development

The temperature was measured with infrared sensors. However, due to the narrow and small structure, there is not enough room to measure the in situ temperature in the contact area. As we know, steel is an excellent thermal conductor ($\lambda \approx 80$ W/(m·K)), which is around 400-times more effective than TPU (Table 1). For this reason, the temperature of the counterpart was measured. Generally, the temperature increases at the beginning of the test and after a while it becomes balanced. The rise in temperature can be roughly correlated to the dissipated energy. Nevertheless, the heat can also be taken away by debris, convection, and thermal radiation in the air. In the partial slip regime, the increase is smaller than 1 °C. In the mixed fretting and gross regimes, it is approximately 5 and 11 °C, respectively.

3.2.5. Coefficient of Friction

Partial Slip and Mixed Fretting Regimes

In the partial slip regime, the coefficient of friction (COF) cannot be calculated by using Coulomb's law, which is generally applied to calculate the COF for static and kinetic friction. However, under partial slip conditions, micro-slips occurred at the edge of the ring (radius = a) with a stick region in the middle (radius = c). In addition, in Coulomb's law, the dependence of the contact area is not considered. Based on the work of Cattaneo and Mindlin, Johnson introduced a method to calculate the COF of partial slip for contacts between spheres [24]. The stick region can be calculated through tangential force.

$$\frac{c}{a} = \left(1 - \frac{F_t}{\mu F_n}\right)^{1/3} \tag{1}$$

where *a* is the radius of the outer ring, c is the radius of the inner ring; F_t is the tangential force; and F_n is the normal load.

From Equation (1) we can get Equation (2):

$$\mu = \frac{1}{1 - \left(\frac{c}{a}\right)^3} \times \frac{F_t}{F_n} \tag{2}$$

In Figure 29, the coefficients of friction, which were calculated by using Equation (2) and the ratio of c/a for the tests in the partial slip and mixed fretting regimes, were illustrated. It should be emphasized that the coefficient of friction and the ratio of c/a, which have been discussed in this research, are merely for the final state of the tests. For this reason, there is no direct correlation between the coefficient of friction and dissipated energy.

When D = 0.1 mm, significant differences can be identified, as seen in Figure 29. For TPU_1, the COF is approximately 2.5, whereas for TPUs_3, 4, and 5 it is substantially higher than 4. As discussed in [12], debris was found in the middle region of the TPU_1 sample after the test, which was conducted with a normal 28 N load and 0.1 mm displacement amplitude. The debris was not generated in the stick region, but rather from the top area. It was accumulated outside the ring and fell onto the counterpart over time. This can affect the generation of wear debris in the slip region, which influences the calculation of COF. However, when the displacement amplitude increases to 0.25 mm or 0.5 mm, the frictional behaviors are approximate; their COFs are around 2. The ratio of c/a at D = 0.1 mm is approximately 0.9 among all five TPUs, whereas more substantial differences can be found when the displacement amplitude increases to 0.25 mm or 0.5 mm. As can be seen in Figure 7 and 10 some samples do not show the typical ring-like scars after tests, but rather show butterfly-like scars. This phenomenon affects the c-value, which acts upon the ratio of c/a and the coefficient of friction directly.
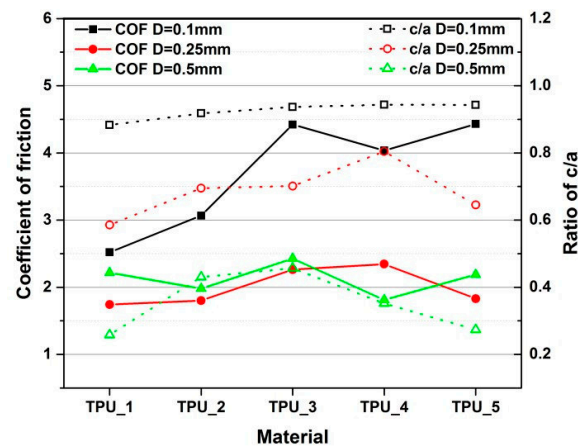
Figure 29. Comparison of coefficient of friction and c/a in partial slip and mixed fretting regimes (F_n = 28 N, N = 10^5).

Gross Slip Regime

The coefficient of friction in the gross slip regime was calculated based on the analysis of the force, wear scars, and acceleration of the samples, which were considered in previous work [12]. The COF displacement is shown in Figure 30. For the five TPUs, their COF can be classified into two categories. For TPUs_1, 4, and 5, their COF is approximately 3, and there is no obvious turning point on the curves. However, for TPU_2 and 3, distinct turning points can be observed, and their curves look similar to a parallelogram, which is composed of polylines. This can be traced back to the wear scar. As shown in Figure 18 and 24, severe wear can be found on both sides of the scars. Due to these phenomena, their COF changed significantly with the movement.
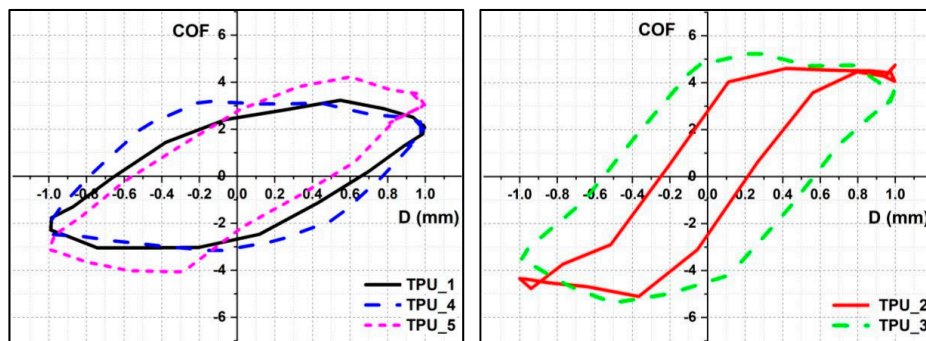
Figure 30. Comparison of the COF in the gross slip regime ((F_n = 28 N, N = 10^5).

3.2.6. Running Condition Fretting Map (RCFM)

Based on the hysteresis and wear scar analysis, a running condition fretting map could be obtained. This represents the transition from one zone to the other [28,29]. However, a clear boundary between MFR and GSR can only be achieved with a large number of experiments. In Figure 31 the normal force is plotted versus effective displacement, which should indicate a more accurate running condition fretting map. Due to different effective displacements, the location of points has a slight deviation. Overall, the three regimes of the five TPUs show no significant differences and can be described adequately with one RCFM.
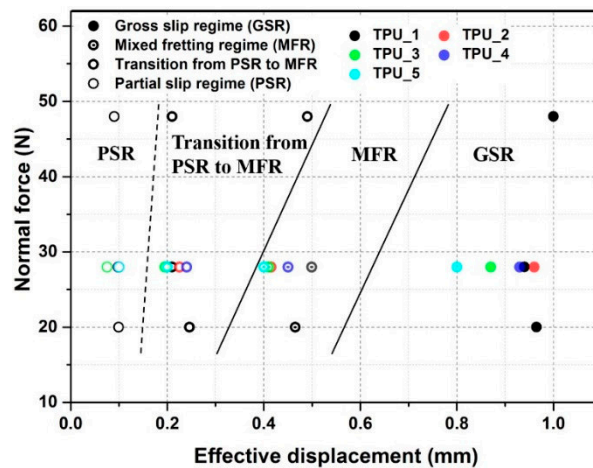
Figure 31. Running condition fretting map of TPUs.

4. Conclusions

Our prior study defined the method of investigation for the fretting behavior of polymeric materials [12]. It is notable that the fretting behavior of TPUs was related to the dynamic mechanical properties, which is different from metals. In this study, we have identified the differences in fretting behaviors among the five TPUs.

(1) Fretting tests were conducted for the five TPUs. In order to compare the fretting behavior and sliding performance, tribological tests were performed. The three fretting regimes were identified by using hysteresis and wear scar analysis.

(2) Based on the wear scar analysis, the wear processes were revealed for the three different regimes. However, this can depend on material properties and test parameters. In the partial slip regime, the scars seem to be quite similar, while with larger amplitude, the scars vary considerably among materials. In the mixed fretting regime, cracks and delamination could be identified, and in the gross slip regime, severe wear was observed.

(3) The dissipated energy also shows differences. Generally, TPUs_1, 3, and 5 have higher energy dissipation than the other two materials. This is induced by the differences in material properties and the moment at which the transition occurs.

(4) The coefficient of friction was calculated separately for the partial slip and gross slip regimes. They are correlated to the wear scar well. In the mixed fretting regime (D = 0.25 mm and 0.5 mm), the coefficient of friction is almost at the same level for the five materials. In the partial slip regime, however, it can be distinguished. The material properties and the contact conditions are responsible for this phenomenon.

(5) Due to the different test methods and wear mechanisms, the COF values in fretting and ring-on-disc tests are not comparable. However, TPU_4 shows the best tribological properties and the best fretting behavior.

In the future, attention should be paid to the in situ temperature in the contact area, which can have a significant effect on the material properties, especially for polymeric materials.

Mechanical Engineering and the Chair of Materials Science and Testing of Polymers, Montanuniversität Leoben, SKF Sealing Solutions, Austria GmbH.

Conflicts of Interest: The authors declare no conflict of interest.

References

1. Holden, G.; Kricheldorf, H.R.; Quirk, R.P. *Thermoplastic Elastomers*, 3rd ed.; Hanser: Munich, Germany, 2004; p. 36, ISBN 978-3-446-22375-2.
2. Flitney, R. *Seals and Sealing Handbook*, 6th ed.; Butterworth-Heinemann an Imprint of Elsevier: Amsterdam, The Netherlands, 2014; p. 397, ISBN 978-0-08-099416-1.
3. Anisimov, V.N.; Semenets, A.A.; Letunovskii, M.P.; Strakhov, V.V. Effect of Rigid Blocks on the Mechanical Characteristics and Abrasive Resistance of Polyurethanes. *Mater. Sci.* **2002**, *38*, 95–98. [CrossRef]
4. Qi, H.J.; Boyce, M.C. Stress–strain behavior of thermoplastic polyurethanes. *Mech. Mater.* **2005**, *37*, 817–839. [CrossRef]
5. Sui, T.; Baimpas, N.; Dolbnya, I.P.; Prisacariu, C.; Korsunsky, A.M. Multiple-length-scale deformation analysis in a thermoplastic polyurethane. *Nat. Commun.* **2015**, *6*, 6583. [CrossRef] [PubMed]
6. da Silva, R.C.L.; da Silva, C.H.; Medeiros, J.T.N. Is there delamination wear in polyurethane? *Wear* **2007**, *263*, 974–983. [CrossRef]
7. Hausberger, A.; Major, Z.; Theiler, G.; Gradt, T. Observation of the adhesive- and deformation- contribution to the friction and wear behaviour of thermoplastic polyurethanes. *Wear* **2018**, 14–22. [CrossRef]
8. Elleuch, R.; Elleuch, K.; Salah, B.; Zahouani, H. Tribological behavior of thermoplastic polyurethane elastomers. *Mater. Des.* **2007**, *28*, 824–830. [CrossRef]
9. Martínez, F.J.; Canales, M.; Alcalá, N.; Jiménez, M.A.; Yahiaoui, M.; Ural, A.G.; Paris, J.-Y.; Delbé, K.; Denape, J. Analysis of Wear Mechanism in TPU-Steel Contact Pair by Means of Long Stroke Tribometer Tests. In Proceedings of the LUBMAT '12, Bilbao, Spain, 6–8 June 2012.
10. Yahiaoui, M.; Denape, J.; Paris, J.-Y.; Ural, A.G.; Alcalá, N.; Martínez, F.J. Wear dynamics of a TPU/steel contact under reciprocal sliding. *Wear* **2014**, *315*, 103–114. [CrossRef]
11. *Sealing Sense*; Fluid Sealing Association; Pumps & Systems: Wayne, PA, USA, 2004.
12. Wang, C.; Hausberger, A.; Berer, M.; Pinter, G.; Grün, F.; Schwarz, T. An investigation of fretting behavior of thermoplastic polyurethane for mechanical seal application. *Polym. Test.* **2018**, *72*, 271–284. [CrossRef]
13. Wang, C.; Stiller, T.; Hausberger, A.; Pinter, G.; Grün, F.; Schwarz, T. Correlation of Tribological Behavior and Fatigue Properties of Filled and Unfilled TPUs. *Lubricants* **2019**, *7*, 60. [CrossRef]
14. Vingsbo, O.; Söderberg, S. On fretting maps. *Wear* **1988**, *126*, 131–147. [CrossRef]
15. Dahmani, N.; Vincent, L.; Vannes, B.; Berthier, Y.; Godet, M. Velocity accommodation in polymer fretting. *Wear* **1992**, *158*, 15–28. [CrossRef]
16. Hausberger, A.; Godor, I.; Grün, F.; Pinter, G.; Schwarz, T. Optimierung tribologischer Testmethoden für die Dichtungstechnik. In Proceedings of the ÖTG-Symposium, Leoben, Austria, 26 November 2014.
17. Chai, Y.S.; Argatov, I.I. Fretting wear accumulation in partial-slip circular Hertzian contact. *Mech. Res. Commun.* **2019**, *96*, 45–48. [CrossRef]
18. Johnson, K.L. *Contact Mechanics*; Cambridge University Press: Cambridge, UK, 1987; ISBN 9780521347969.
19. Bill, R.C. Fretting Wear and Fretting Fatigue—How Are They Related? *J. Lub. Tech.* **1983**, *105*, 230. [CrossRef]
20. Errichello, R.L. Morphology of Micropitting. *Gear Technol.* **2012**, *4*, 74–81.
21. Godet, M. Third-bodies in tribology. *Wear* **1990**, *136*, 29–45. [CrossRef]
22. Wu, H.-W.; Chen, Y.-Y. Effect of two-body and three-body microcontacts under dry friction on contact characteristics. *Proc. Inst. Mech. Eng.* **2017**, *232*, 706–719. [CrossRef]
23. Wu, H.-W.; Chen, Y.-Y.; Horng, J.-H. Contact temperature under three-body dry friction conditions. *Wear* **2015**, *330–331*, 85–92. [CrossRef]
24. Suh, N.P. An overview of the delamination theory of wear. *Wear* **1977**, *44*, 1–16. [CrossRef]
25. Suh, N.P. The delamination theory of wear. *Wear* **1973**, *25*, 111–124. [CrossRef]
26. Grün, F.; Sailer, W.; Gódor, I. Visualization of the processes taking place in the contact zone with in-situ tribometry. *Tribol. Int.* **2012**, *48*, 44–53. [CrossRef]
27. Rabinowicz, E. *Friction and Wear of Materials*, 2nd ed.; Wiley: New York, NY, USA, 1995; ISBN 9780471830849.

28. Zhou, Z.R.; Fayeulle, S.; Vincent, L. Cracking behaviour of various aluminium alloys during fretting wear. *Wear* **1992**, *155*, 317–330. [CrossRef]

29. Vincent, L.; Berthier, Y.; Godet, M. Testing Methods in Fretting Fatigue: A Critical Appraisal. In *Standardization of Fretting Fatigue Test Methods and Equipment*; Attia, H.M., Ed.; ASTM International: Philadelphia, PA, USA, 1992; pp. 33–48, ISBN 0-8031-1448-6.

Paper 3: Correlation of Tribological Behavior and Fatigue Properties of Filled and Unfilled TPUs

C. Wang[1], T. Stiller[1], A. Hausberger[1], G. Pinter[2], F. Grün[3], T. Schwarz[4]

[1] Polymer Competence Center Leoben GmbH, Leoben, Austria

[2] Chair of Materials Science and Testing of Polymers, Montanuniversität Leoben, Leoben, Austria

[3] Chair of Mechanical Engineering, Montanuniversität Leoben, Leoben, Austria

[4] SKF Sealing Solutions Austria GmbH, Judenburg, Austria

Authors and relevant contributions to this publication:

- C. Wang: Application and implementation of Panda model, experimental testing, data evaluation, preparation of the publication
- T. Stiller: Application and implementation of Atkins model, experimental testing, data evaluation, preparation of the publication
- A. Hausberger: Discussion of experimental data, review the publication
- G. Pinter: Review the publication
- F. Grün: Review the publication
- T. Schwarz: Specimen production, Review the publication

Correlation of Tribological Behavior and Fatigue Properties of Filled and Unfilled TPUs

Chao Wang [1,]* [ID]**, Tanja Stiller [1], Andreas Hausberger [1], Gerald Pinter [2], Florian Grün [3]** [ID] **and Thomas Schwarz [4]**

[1]   Polymer Competence Center Leoben GmbH, Roseggerstraße 12, 8700 Leoben, Austria
[2]   Chair of Materials Science and Testing of Polymers, Montanuniversität Leoben, 8700 Leoben, Austria
[3]   Chair of Mechanical Engineering, Montanuniversität Leoben, 8700 Leoben, Austria
[4]   SKF Sealing Solutions Austria GmbH, 8750 Judenburg, Austria
*   Correspondence: c.submission.w@gmail.com; Tel.: +43-3842-42962-85

check for updates

Abstract: For a long service time, fatigue has been a typical problem that mechanical sealing materials face. How does it relate to tribological performance? In this study, filled and unfilled thermoplastic polyurethanes (TPUs) were investigated. Dumbbell and faint wait pure shear (FWPS) specimens were used to characterize the fatigue properties and crack growth rate of TPUs, respectively. Additionally, to identify the impact of temperature on fatigue tests, the tests were conducted at room temperature and 80 °C. Different tribological tests were conducted to investigate their tribological properties. Fracture surfaces from fatigue tests and worn surfaces from tribological tests were analyzed using a scanning electron microscope (SEM). Two wear models were verified to correlate between fatigue and tribological properties; one of the models is better for rough counter surfaces, while the other is advantageous if the counter surface is smooth.

Keywords: fatigue; filler; TPU; tribology; crack

1. Introduction

Thermoplastic polyurethane (TPU) is an elastomer that is also fully thermoplastic. Due to these unique properties, TPU compensates for the material gap between rubbers and plastics. As a linear segmented block copolymer, TPU consists of hard and soft segments [1]. By varying the ratio and types of these segments, TPU can provide exceptional flexibility in its properties, making it an ideal polymer in many applications. With good strength, excellent abrasion, and tearing resistance, TPU has also been applied recently as a mechanical seal. When mixed with fillers, its properties can be enhanced [2]. Nguyen et al. [3] investigated the functionalized graphene sheet as a filler in TPU, showing that the TPU matrix was efficiently reinforced, especially in the temperature region above the soft segment melt. A multiwalled carbon nanotube-graphene hybrid as a filler in TPU was studied by Roy et al. [4]. More than 200% improvement of storage modulus in the rubber state can be achieved. Suresha [5] researched the friction and dry sliding wear of short glass fiber (SGF) reinforced TPU. He found that the coefficient of friction decreases with increasing SGF content in TPU, and 40 wt% of SGF in TPU shows the best tribological performance for a bearing application. Mineral fillers have also been investigated. Barick et al. [6] studied the effect of organoclay nanocomposites on TPU's thermal and dynamic mechanical properties and found that storage modulus, loss modulus, and glass transition temperature are significantly increased with increasing nanoclay content to 9 wt%. The effect of mica and aluminum trihydrate as fillers in TPU were studied by Pinto et al. [7]. With 20 phr of mica, the best reinforcement effect was achieved regarding tensile strength, whereas a high amount of aluminum trihydrate provides good flame resistance, but causes a pronounced decrease in tensile strength,

abrasion resistance, and hardness. However, few researchers have addressed the effect of fillers on fatigue or tribological properties in TPU.

In this work, we try to bridge this gap and present a possible correlation between fatigue and tribological properties for graphite-filled and unfilled TPUs. To characterize the basic mechanical properties, tensile tests and a dynamic mechanical analysis were performed. Notched dumbbell samples were applied to investigate the fatigue properties, and notched pure shear specimens were used to analyze the crack growth behavior. The tribological properties were studied through component-like tests. The influence of the load was determined by load ramp tests and the influence of counterpart roughness by different ground steel discs. Both fracture surfaces of fatigue tests and worn surfaces from tribological tests were analyzed with scanning electron microscopy (SEM).

2. Experimental Details

2.1. Material

The TPU specimens were produced by injection molding at SKF Sealing Solutions Austria GmbH. Two kinds of TPUs were studied, namely unfilled TPU (TPU_A) and graphite-filled TPU (TPU_B). The hardness was measured using the Shore D method, according to the standard DIN ISO 7619-1 [8]. The density was measured using a level balance (Mettler–Toledo, Columbus, OH, USA) using the buoyancy method—Archimedes' principle. The tensile tests were conducted with ISO 527-2 standard [9] test specimens (S2) with 200 mm/min on a Zwick Z010 (Zwick GmbH, Ulm, Germany). In order to get a wide range of temperature dependence of material properties, two temperatures (23 °C, 80 °C) were chosen for the tensile and fatigue tests. 23 °C is the room temperature and 80 °C is the average contact temperature in the tribological experiments. Due to the friction heat, the temperature in the contact interface increased significantly, while in the fatigue test the temperature increase was less than 5 °C. Therefore, the fatigue tests at 80 °C were conducted to obtain the fatigue behavior at a high temperature and a better understanding and correlation between fatigue and tribological properties. The dynamic mechanical properties were analyzed by means of dynamic mechanical analysis (DMA) utilizing the temperature scan method (EPLEXOR 100 N, NETZSCH GABO Instruments GmbH, Ahlden, Germany). Concerning the thermal influence on the samples, thermal conductivity was measured with a guarded heat flow meter (DTC 300, TA Instruments, New Castle, DE, USA) at 25 °C. Hardness measurements were repeated five times, and other experiments were repeated three times with similar results. The material properties are shown in Table 1.

Table 1. Material properties of the thermoplastic polyurethanes (TPUs) used in this study.

	Shore D	Density [g/cm³]	Thermal Conductivity [W/mK]	Dynamic Mechanical Analysis (2Hz)			
				Temperature [°C]	Storage Modulus [MPa]	Loss Modulus [MPa]	Loss Factor
TPU_A	46 ± 0.71	1.196 ± 0.001	0.209 ± 0.001	23	100.07 ± 6.87	17.68 ± 2.10	0.1763 ± 0.009
				80	42.08 ± 0.36	1.74 ± 0.09	0.0413 ± 0.0018
TPU_B	49 ± 1.58	1.225 ± 0.001	0.229 ± 0.001	23	110.97 ± 7.37	19.70 ± 2.37	0.1771 ± 0.0095
				80	47.57 ± 0.34	1.95 ± 0.10	0.0410 ± 0.0018

2.2. Wear Prediction Model

In this study, two wear models were applied to correlate the wear behavior and fatigue properties. The first model, developed by Panda [10], is based on abrasive and fatigue wear mechanisms. In Panda's model, the surface roughness of the counter surface is taken into consideration. It is possible to predict the influence of roughness on wear. The second model was developed by Atkins et al. [11]; it is based on the adhesive and fatigue wear mechanisms and is able to correlate the wear rate with the number of cycles until failure.

2.2.1. Panda's Model

Description of Model

In Panda's model, wear is partly due to the fatigue wear mechanism, which is purely caused by elastic contacts, while the other part is from the abrasive mechanism under plastic contacts [10,12]. The model is based on the micro-mechanistic deformation at the asperity scale. Therefore, it is assumed that the interface consists of an ideally smooth polymer surface and a random rough counter surface. The asperities on a rough surface are rigid and show a spherical tip; they follow a probability distribution. In addition, abrasive wear only results from plastic contacts of asperities, while only elastic contacts lead to fatigue wear [10]. The filler effect, specimen roughness, and thermal influence are beyond the scope of this model.

The abrasive wear can be described as

$$V_a \approx N_s \left(\frac{\pi^2 \mu H^2 \overline{R}^2 \sigma^4}{K_{IC}^2} \right) \int_{\Delta_2}^{\infty} (f_A)^3 \varnothing (h + \Delta) d\Delta \tag{1}$$

$$f_A = 2\Delta^{2/3} - \frac{\Delta_c}{\Delta^{\frac{1}{3}}} - \frac{2}{\lambda \Delta^{1/3}}, \ N_s = \eta A_s \tag{2}$$

where:

- N_S: Total number of asperities encountered during sliding;
- η: Average asperity density per unit area in μm^{-2};
- A_s: Total area covered during the tribological test in μm^2;
- μ: Coefficient of friction;
- H: Hardness in MPa, coverted from Shore D;
- $\overline{R}$: Average radius of curvature at asperity tip in μm;
- σ: Standard deviation of asperity heights in μm;
- K_{IC}: Fracture toughness MPa·m$^{0.5}$;
- h: Normalized mean separation in μm;
- Δ: Normalized deformation in μm;
- Δ_c: Critical normalized deformation;
- λ: $H\sigma/\gamma$ [13];
- γ: Surface energy per unit area J·m^{-2}.

The fatigue wear can be calculated with

$$V_f \approx N_s \left(\frac{1.5 C \Psi}{\pi} \right) \int_{\Delta_0}^{\Delta_1} V_{el}(f_F)^t \varnothing (h + \Delta) d\Delta \tag{3}$$

$$C = \frac{\pi \mu (4 + \nu)}{8} + (1 - 2\nu)/3, \ \Psi = \left(\frac{K}{H} \right) \sqrt{\sigma/R} \tag{4}$$

$$f_F = \sqrt{\Delta} - \sqrt{\Omega - \sqrt{\Delta}}, \ \Omega = (6\pi/\theta) \sqrt{R/\sigma} \tag{5}$$

The volume of deformation under elastic contact can be described as

$$V_{el} = \pi \{ \overline{R} \Delta^2 - (\Delta^3/3) \} \sigma^3, \ \Delta \leq \Delta_{el} \tag{6}$$

where:

- ν: Poisson's ratio;
- K: Combined Young's modulus of two surfaces in MPa;

- *t:* Fatigue ratio;

The total wear volume is a summary of both parts:

$$V \approx \alpha V_a + V_f \qquad (7)$$

where: α: Factor for abrasive wear.

    A factor was introduced for abrasive wear. It is assumed in the model that the ideal smooth polymer surface slides against a rough counter surface all through the tests. However, in real tribological tests, a transfer film is formed after the running-in phase [14–16]. Hence, the interface changes and the abrasive wear are not the dominant wear mechanisms. Especially for filled polymers, fillers can significantly affect the wear rate through the transfer film [14]. The factor α is defined as a ratio of the duration of the running-in phase and whole test duration, obtained from tribological tests.

Parameter Generation

    The hardness was measured with a Shore D hardness tester. The fracture toughness and fatigue ratio were obtained from dumbbell tests. In terms of surface parameters, the counter surfaces were characterized according to the standard [17] with a 3D optical microscope (InfiniteFocus, Alicona Imaging GmbH, Raaba, Austria). Based on the surface measurements, the surface parameters were calculated using MATLAB programs (ver. 2018b). The determination of surface energy was carried out in a self-developed contact angle device. The methods of Owens et al. [18], Rabel [19], and Kaelble [20] were employed to calculate the surface energy.

Experimental Deatils

    The fatigue tests were conducted with dumbbell specimens on a dynamic mechanical analyzer (ElectroForce 3450, TA Instruments, New Castle, DE, USA). The tests were carried out in the load-controlled mode with a sinusoidal signal. The frequency used was 3 Hz, which is a compromise of test duration and thermal influence. The specimen geometry is shown in Figure 1. In the middle of the specimen, a sharp circumferential initial notch (depth $\approx$ 1 mm) was introduced using a razor blade (thickness = 0.1 mm, tip radius <5 mm), which was mounted on a lathe. After the tests, the area of the fracture surfaces was measured with optical microscopy (Stereo Microscope SZX 12, Olympus, Tokyo, Japan). The calculation of the stress was based on the fracture surface measured. To investigate the influence of the temperature on the fatigue property of unfilled and filled TPUs, tests were conducted at room temperature (23 °C, 50% RH) and 80 °C.
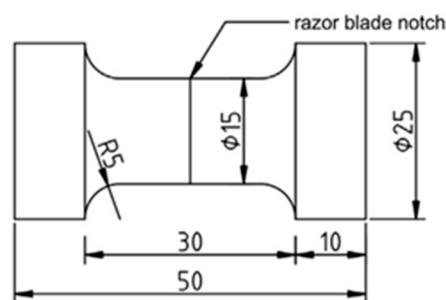
Figure 1. The geometry of a specimen used for fatigue [21].

    Distilled water and diiodomethane were applied as liquids to determine the polar and dispersive parts of the surface energy, respectively. For each measurement, a drop with 2.5 µL volume was used. Each measurement was repeated three times.

    A pin on disc configuration was used to investigate the influence of the counterpart roughness. The tests were conducted on a Universal Mechanical Tester (UMT-2, Bruker Nano Surfaces Division, Campell, CA, USA) with a rotating steel disc as the counterpart, made of 100Cr6 with a roughness

(R_a) of 0.3 μm or 0.03 μm. The roughness was characterized, according to the standard [17], with a 3D optical microscope (InfiniteFocus, Alicona Imaging GmbH, Raaba, Austria). The sample slid on a counter surface at 150 mm/s for 4 h. The total track length for each test was 2.16 km. All experiments were repeated three times with similar results.

2.2.2. Atkins Model

Based on a publication of Omar, Atkins, and Lancaster [9], the model aims to find a mathematical correlation of tribological values and fatigue values.

Description of Model

Atkins et al.'s [11] idea to correlate the wear and crack growth behaviors of the same material was revived and adapted for TPU [22]. Atkins investigated the correlation of different thermoplastics in a dry or wet state. The basic equation (Equation (1)) is the Paris–Erdogan law, which sets the correlation between the stress intensity factor and the crack growth rate. The Paris–Erdogan law is solved based on the cycle number. Atkins' idea was to correlate the wear rate with the inverse value of the number of cycles until failure, as demonstrated in Equation (9).

$$\frac{da}{dN} = A * K^n \tag{8}$$

$$Wear\ rate\ \propto\ \frac{1}{N_f}\ \propto A * \Delta\sigma^n * \sqrt{\pi^n} * a_0^{\frac{n}{2}-1} * \left(\frac{n}{2} - 1\right) \tag{9}$$

where:

- *a:* Crack length (a_0 initial crack length);
- *N:* Cycle number;
- *A:* Material constant;
- *K:* Stress intensity factor;
- *n:* Slope of the straight;
- *Δσ:* Difference in applied stress.

For the calculation of a theoretical wear rate, there is the need for some values, which can be calculated using the data from the experiments. N_f is the fatigue cycle number at which the specimen breaks. The value a_0 can be correlated to the wear particle thickness. For Equation (9), the stress intensity factor K is substituted by $\Delta\sigma(\pi a)^{1/2}$. All these assumptions were put in the Paris–Erdogan law, integrated, and then solved to the fatigue cycle number.

Since the model was made with polyethersulphone (PES) and polymethylmethacrylate (PMMA), it was tested with single edge notched specimens. Due to the elasticity of TPUs, it is not recommended that the same geometry be used, because of the deformation in front of the crack tip [23]. To use this geometry, a J-integral would be necessary to calculate the required values. Another way of calculating them is to use a pure shear specimen. This geometry allows the energy release rate to be substituted with the tearing energy [21]. Because of the proportionality of the energy release rate and stress intensity factor, including the E-modulus and Poisson's ratio, it is valid to substitute the stress intensity factor with

$$G = -\frac{dU}{dA} = -\frac{U}{t * (L - da)} = Wh_0 = T \tag{10}$$

where:

- *G:* Energy release rate in J/m^2;
- *U:* Energy required for crack growth (area under σ-ε curve) in J;
- *A:* Uncracked surface of specimen in mm^2;
- *t:* Thickness of specimen in mm;

- *L:* Initial length of uncracked area in mm;
- *a:* Crack length in mm;
- *W*: Work of cracking in N/mm^2;
- h_0: Constant height of the testing area in mm;
- *T:* Tearing energy in J/m^2.

The tearing energy *T* or energy release rate *G* describes the required energy to provoke an ongoing crack. *G* represents the released energy *U* by the newly-formed area *A*, which can be written as the thickness *t* of the specimen and the ongoing crack length *da*. For elastomers, the Paris–Erdogan law is valid for a stable crack growth region and can be written as Equation (11). For a calculated wear rate based on the mechanical fracture values, the tearing energy is calculated by the energy *U* divided by the remaining area of the surface. This term is put into the Paris–Erdogan law and solved after the crack length with the following, Equation (12).

$$\frac{da}{dN} = B * T^m \tag{11}$$

$$a_0 = L - \sqrt[m+1]{N * B * (m + 1) * \left(\frac{U}{t}\right)^m} \tag{12}$$

where:

- *B:* Material constant in mm/cycle;
- *m:* Slope of the straight [–];
- a_0: Initial crack length at which wear particles start to detach in mm.

To get a minimal crack length, the values were used after the first 1000 cycles. This crack length was taken to calculate a fatigue cycle number by solving the Paris–Erdogan law. An assumption here is a continually growing crack, which means it always cracks at the same length.

Parameter Generation

To set up the Atkins model, tribological and fracture mechanical tests were conducted to generate the necessary values.

Tribological Values

For the correlation, two different kinds of test setup were used; a Ring on Disc (RoD) with different load levels and a Pin on Disc (PoD) with different counterpart roughness. These investigations generated the necessary wear rate, which will be correlated with a calculated wear rate. These values are calculated with the weight loss, applied load, and test distance.

Crack Growth Tests

The necessary parameters can be measured from the crack growth tests, which provide all values to calculate an initial crack length. This crack length can be taken to calculate a fatigue cycle number if a crack is growing equidistantly. *L* and *t* are just geometrical values, *N* is the fatigue cycle number of a certain load level, and *B* and *m* are determined by the curves of the tearing energy over the crack growth rate. *U* is the integrated force displacement or stress-strain curve.

Experimental Details

Tribological Investigation

To determine the wear rates, a Universal Mechanical Tester (UMT-2) (Bruker Nano Surface Division, Campell, CA, USA) and a TE93 Precision Rotary Tribometer (Phoenix Tribology Ltd., Berkshire, England) were utilized. An investigation of roughness influence was performed on the UMT-2, whereas the load ramp tests were done on the TE93. For each test setup, the counterparts were made of 100Cr6 steel and the roughness was controlled according to [17].

The PoD tests were conducted with a rotating speed of 150 mm/s at a load of 1 MPa for 4 h, later shortened by UMT-2 rot. To compre between both test setups, the RoD tests were conducted at 150 mm/s and 4 h of testing. To gain some information about the influence of the load, two different load levels were chosen, namely 1 MPa and 1.5 MPa. These load ramp tests were developed by Jölly for TPU materials [24]. The results of the load ramp were shortened by TE LR. For lower loads, the filler cannot evolve its lubricating potential [25]. Therefore, higher loads were chosen.

Crack Growth Investigations

To investigate the crack growth behavior, pure shear tests were conducted. To ensure a horizontally growing crack, faint waist pure shear (FWPS) specimens were tested. When using these slightly curved specimens, Equation (3) ($Wh_0 = T$) is not valid. However, the thickness was assumed to be constant, thus justifying that it should only provide information on the conductibility and a possible trend. The geometry of an FWPS specimen is illustrated in Figure 2.
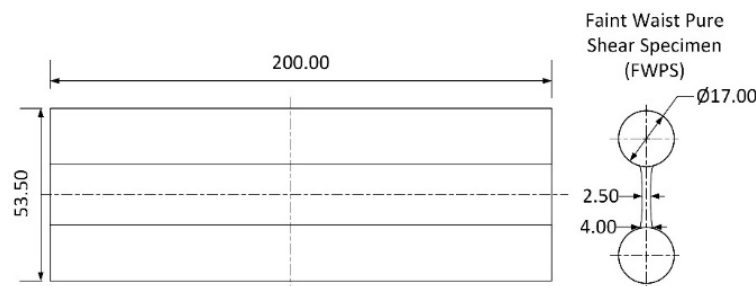
Figure 2. Geometry of a faint waist pure shear (FWPS) specimen for crack growth investigations.

The tests were conducted on an MTS 858 tabletop system (MTS Systems Corporation, Eden Prairie, MN, USA) and run in a load-controlled mode with a testing frequency of 3 Hz. The specimens were notched with a razor blade. The initial crack length was 25 mm, and the specimens were sprayed with a developer (Nord-test developer U89, Helling GmbH, Heidgraben, Germany) before testing for a higher contrast in photos, which facilitates the crack observability. To observe the crack growth, a camera system was employed, which took a picture every 1000 cycles. The crack growth was analyzed with a Tracker (version 5.0, comPADRE). The tests were performed with a stress ratio of 0.1 (F_{min}/F_{max}) at room temperature. These tests were conducted at an F_{max} of 2700 N and 3000 N. Lower loads took too long to crack, whereas higher loads led to too fast failure. The specimens were tested until they ripped completely apart in two halves, but for the evaluation only the first half of the cracking was considered, due to the undefined stress situation of a further cracked specimen [26,27].

3. Results & Discussion

Firstly, the results of the fatigue tests are discussed. The evaluation is based on the stress-cycle (S–N) curve, stress intensity factor, and dissipated energy. As one of the basic mechanical properties of materials, tensile tests at room temperature and 80 °C correlate well with fatigue tests. Secondly, crack growth tests are shown and correlated with the fatigue tests. The fracture surfaces show the crack growth processes. For tribological tests, the coefficient of friction (COF) and wear rate are discussed. The surfaces after the tests are analyzed and discussed.

3.1. Comparison of Two Materials

3.1.1. Fatigue Tests

Stress–Cycle (S–N) Curve

The S-N curve is shown in Figure 3. In order to achieve a better correlation with tensile tests, maximum stress σ_{max} is plotted as the *y*-axis (logarithmic) against the number of cycles to failure (logarithmic).

Figure 3. The stress–cycle (S–N) curve of the tested materials.

In this study, the cycles to failure follow a power law

$$N = \left(\frac{\sigma_a}{\sigma_0}\right)^k \tag{13}$$

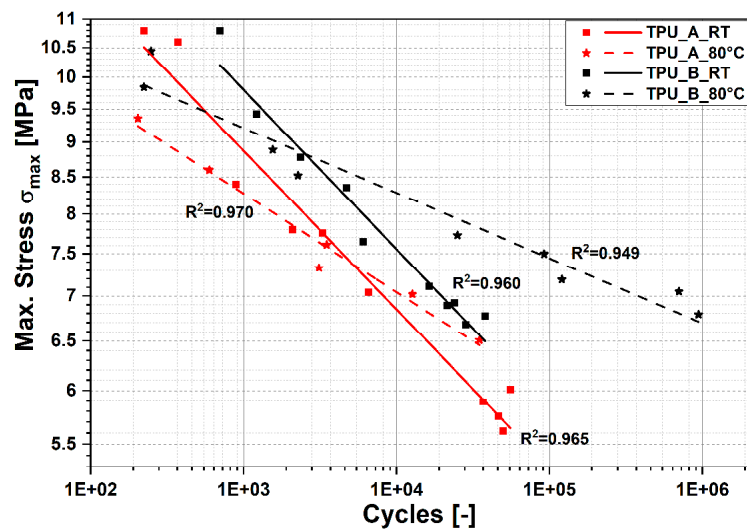where N is cycles to failure, σ_a is the maximum stress, and σ_0 and k are constant. As shown in Figure 3, the curves of both materials at room temperature are parallel, indicating that fillers in TPU_B are beneficial for these kinds of fatigue tests at room temperature. However, the reinforcement effect of the filler against fatigue is not because fillers strengthen the crack growth resistance of TPU_B, but rather because they increase the E-modulus. Under the same conditions, TPU_B experienced approximately double the time to fail as TPU_A.

For the tests at room temperature, at low load, the S–N curve corresponds very well with the stress-strain curve. There is evidence to indicate that in the S–N curve, the stresses at the same cycles to the failure can be traced back to the same strain in the tensile test. This implies that at the low load, the key factor that influences the cycles to failure is the strain. Even though TPU_B is filled, it has the same lifetime as TPU_A when the tests are conducted with the same strain. At the high load, due to the stronger nonlinearity of the tensile curve, the correspondence is not as good as at the low load. However, the trend can still be identified.

At elevated temperature, the slope of the curves becomes slight. There is a cross point of the curve at room temperature and 80 °C for each material. It indicates that, compared to the tests at room temperature, the fatigue properties of the two materials are more sensitive to the load at elevated temperature. The cross point for TPU_A is about 7.4 MPa, while for TPU_B it is 8.8 MPa. At cross points, the positive and negative effects of elevated temperature on fatigue properties balanced out. For both materials, when the maximum stress is higher than the cross-point stress, elevated temperature represents an adverse effect on the fatigue property. At lower stress, a high temperature brings advantages to fatigue properties.

Stress Intensity Factor

The stress intensity factor ΔK_I was calculated according to Benthem and Koiter [28]. Both materials show a linear trend at room temperature, while at elevated temperature the linear trend shows a more significant deviation compared to the trend at room temperature (Figure 4). In general, the trends correspond well with those in the S–N curve. This indicates that in the tests, the total maximum stress is more relevant to predict the lifetime of the samples.
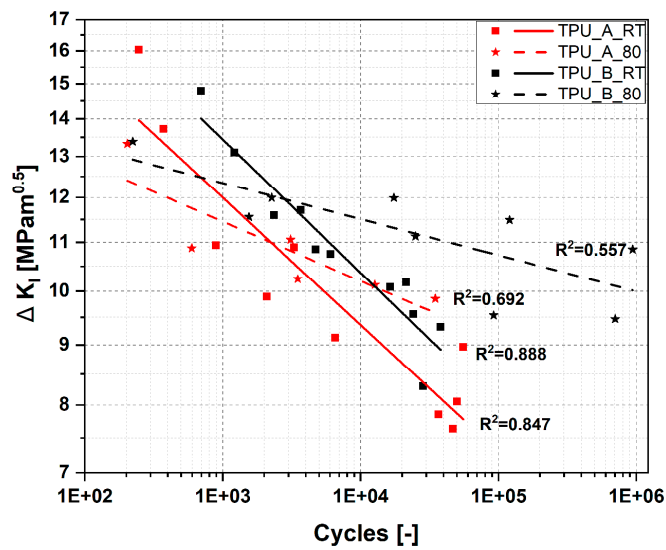
Figure 4. Stress intensity factor of the tested materials.

3.1.2. Crack Growth Tests

Tearing Energy Over Cycles

In Figure 5a, the tearing crack growth rate is plotted against the tearing energy. This kind of plotting provides information about the crack growth resistance by analyzing the slope of the graphs. A higher slope means a lower resistance against crack growth. It is visible that TPU_B has a lower crack growth rate than TPU_A, which can be traced back to the higher stiffness due to the filler. The high scattering of the values at the beginning of the curves is due to the barely recognizable crack growth in the evaluation of the pictures. After a certain crack length, the curves separate clearly.

(a)

Figure 5. *Cont.*

(b)
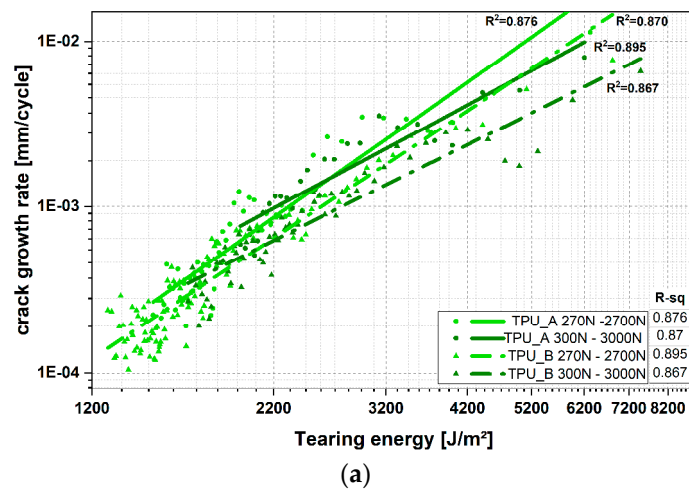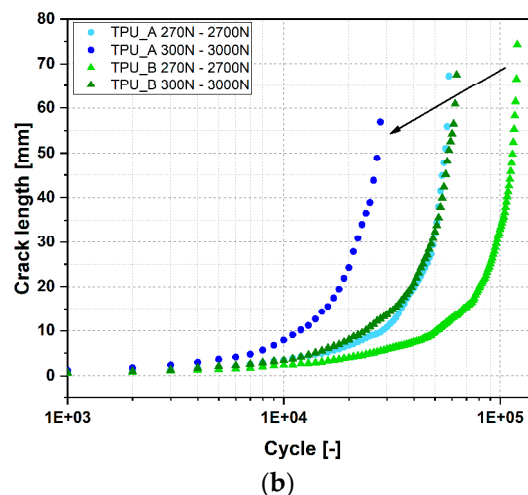
Figure 5. (**a**) Tearing energy plotted against the crack growth rate of unfilled TPU (TPU_A) and graphite-filled TPU (TPU_B) for 270–2700 N and 300–3000 N; (**b**) the average crack length after every 1000th cycle for the same loads.

The higher crack growth resistance is evident if the crack length is examined over the cycles, as shown in Figure 5b. In this plot it is visible that TPU_A continues to crack earlier than TPU_B. It is also visible that under tearing energy of approx. 2400 J/m^2, no significant separation can be observed. The values are not usable if the crack reaches the half-length of the specimen, since, theoretically, under those conditions, the shear is not pure shear anymore [27]. For the FWPS tests, the impact of temperature was studied by Schieppati et al. [29], which shows that a higher local strain leads to an increase in temperature at the crack tip.

3.1.3. Tribological Tests

For tribological tests, the real contact stress at the contact point is much higher than the nominal contact stress.

Load Ramp Tests

The results of load ramp tests are shown in Figure 6. The COF and average contact temperature are only calculated for each load ramp stage, while the weight loss is determined for all of the previously experienced stages. Generally, COF decreases with load increments, while a higher load leads to more weight losses. This result is in good agreement with Schallamach's research [30], which is based on the real contact area combined with Hertz's contact theory. When increasing normal load, more asperities come into contact. However, COF, which is mainly determined by the contact state between the two rubbing surfaces, is affected by many other factors, e.g., temperature, wear debris in between, material properties at elevated temperature, fillers, etc. The contact state changes continuously with cycles.

When the load is 0.5 MPa, both materials behave similarly, which indicates that at a low load, the beneficial effect of fillers cannot be manifested noticeably. As the tests run further to the next stage, COFs decrease rapidly; for TPU_A the reduction of COF is ca. 12%, while for TPU_B it is over 35%. The contact temperature of TPU_A increased from 82 °C to 115 °C, whereas the contact surface of TPU_B experienced a declining temperature from 91 °C to 62 °C as the load increased to 1 MPa. This can be attributed to two factors. One crucial point is that heat was generated by friction. Since the COF decreases significantly for TPU_B, the work, which was converted into thermal energy, reduced consequently. In addition, thermal energy can be taken away from the contact surface by wear debris. The wear volume increased considerably for TPU_B, while for TPU_A its wear volume remained almost unchanged. Thermal energy was accumulated to heat the whole system, including the sample,

counterpart, holders, drive shaft, etc. With increasing time, the system got heated and stayed in a relatively balanced state.
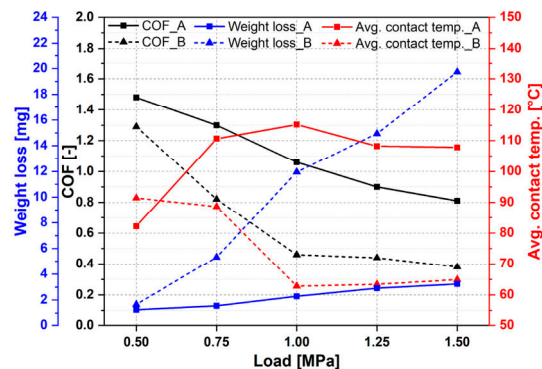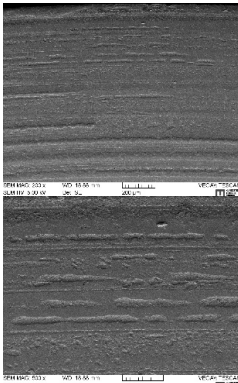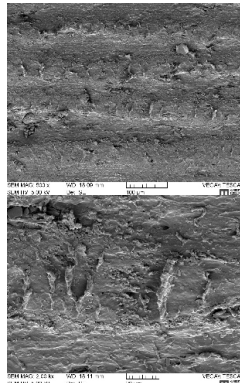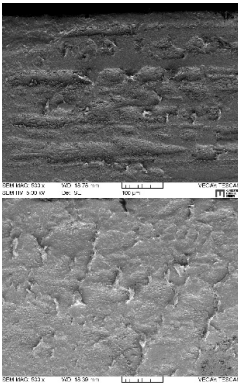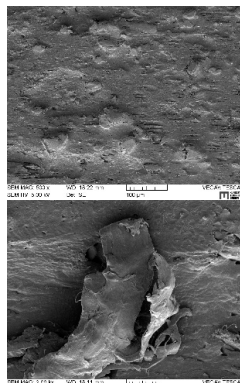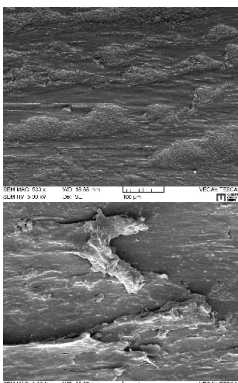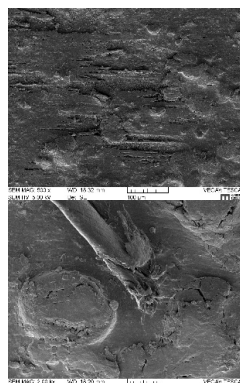
Figure 6. Results of load ramp tests of TPU_A and TPU_B.

Both COFs decreased when the load increased to 1 MPa. Significant weight loss was observed for TPU_B, while it stayed almost unchanged for TPU_A. For TPU_B, this load is an inflection point. After this stage, its COF and contact temperature kept stable, though its weight loss increased more or less proportionally to the load. For TPU_A, it seems that its contact temperature reaches a balance at this stage. It decreases at the next stage as a result of the reduction of COF. A slight increase in wear can be identified through 1.5 MPa.

Table 2 shows the worn surface of the load ramp tests of TPU_A and TPU_B. After the first stage (0.5 MPa), the texture from turning marks is still visible in the whole contact area. The peaks of the turning textures become relatively flat. The height difference between the peak and the middle of the groove, however, is still visible. By contrast, rolled worm-like debris can be observed on TPU_B, especially on the peaks of the turning textures. This phenomenon can also be found in [31,32]. This phenomenon occurred in the outer area of TPU_A at higher loads. Due to the effect of time and higher normal stress, after the second stage, the turning textures could still be identified, but the peaks were almost worn out. TPU_B experienced serve rolled wear so that the turning textures could not be observed after the tests. In some places, fillers were uncovered due to wear debris. Fillers were uncovered after the substrate polymer was "smeared", due to sliding movement. However, the filler system starts to show its effect. As can be seen in Figure 6, a significant change occurred for TPU_B under 1 MPa normal load. The COF and contact temperature decreased with an increase in wear volume. At this stage, a transfer film was generated. Thus, the interface changed from metal-TPU to graphite-graphite. The transfer film was not perfect and covered the whole contact area. After this stage, TPU_B reached a relatively stable stage. When increasing the normal load, its COF stayed at the same level. The wear volume, however, kept increasing. Under a higher normal load, adhesive wear dominated in TPU_A.

Table 2. Scanning electron microscope (SEM) micrographics of load ramp tests of TPU_A and TPU_B.

Pin on Disc Tests

To check the influence of counterpart roughness, the steel discs were prepared in a smooth (R_a = 0.03 µm) and a rough (R_a = 0.3 µm) way. Besides the roughness, all parameters are kept the same to have comparability between the two roughnesses without any other influences. In Figure 7, the coefficient of friction and wear rate for both roughnesses are shown. For TPU_B, due to the filler effect and stiffness, its average COF is lower than TPU_A for both roughnesses. Its higher stiffness facilitates a reduction of the deformation part of friction [33,34]. Higher wear rate was identified for both materials with a rough counter surface. However, probably due to the tribologically advantageous transfer film of TPU_B, its wear rate does not show a significant difference between rough and smooth counter surfaces. For TPU_A, its wear rate on the rough counter surface is higher than that with a smooth counter surface.
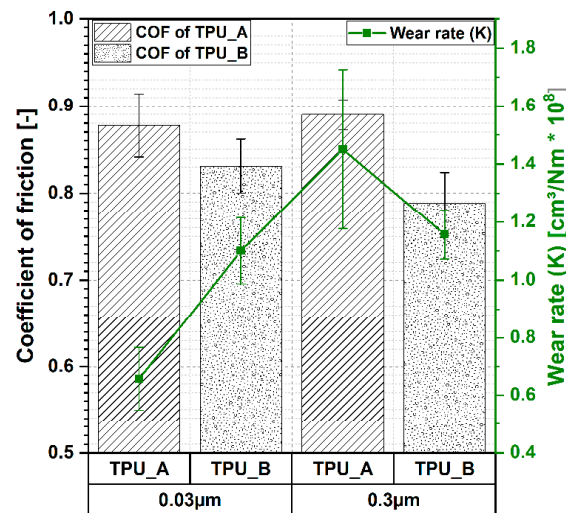
Figure 7. Coefficient of friction and wear rate (K) for TPU_A and TPU_B tested on different counterpart roughnesses.

3.2. Damage Analysis Proof

Since a comparison of different tests or dimensions needs proof, the damage of the surfaces should provide equivalency. If the appearance of the damage is comparable, it means the same failure process took place. In Table 3, all three mechanical tests with damage are summarized for both materials. The arrows indicate quite similar damage, which looks like waves for the mechanical fracture tests. This is caused by the cyclic loading, during which the material elongates relaxes relatively. Even though the tribological surface does not show such characteristic waves, it exhibits the same off ripping damage as for the fracture mechanical tests. The remaining part on the surface is immediately attached to the surface because of the contact with the counterpart, therefore no relaxing of the stripes is possible and no wave structures can be formed.

Table 3. Comparison of the damage equality of tribologically and mechanically fractured tested specimens.

3.3. Verifications of Two Models

3.3.1. Panda's Model

The roughness parameters of two counterparts are shown in Table 4. In addition, the material properties were obtained through different tests and are shown in Table 5.

Table 4. Roughness parameters of two counterparts.

Surfaces	σ (μm)	R (μm)	η (μm^{-2})	Sk	Ku	β_{Sk}	β_{Ku}
Rough ground	0.68	1.211	7.39×10^{-4}	0.06719	2.988	1.39	0.88
Smooth polished	0.26	2.28	7.60×10^{-4}	−0.215	3.367	1.99	0.96

- ς: Standard deviation of asperity heights;
- R: Average radius of curvature at asperity tip;
- η: Average asperity density per unit area;
- Sk: Skewness of asperity heights;
- Ku: Kurtosis of asperity heights;
- β_{Sk}: Weibull shape parameter from skewness;
- β_{Ku}: Weibull shape parameter from kurtosis.

Table 5. Material properties of TPU_A, TPU_B, and counterpart.

Materials	E (MPa)	H (MPa)	S_y (MPa)	ν	K_{IC} (MPa m$^{0.5}$)	t	γ (J m^{-2})	ρ (g/cm^3)	α Rough	α Smooth
TPU_A	17.2 ± 0.2	37.04 ± 0.57	10.5 ± 0.1	0.48	7.8	2.2	0.033 ± 0.001	1.196 ± 0.001	0.0694	0.1389
TPU_B	19.6 ± 0.3	41.27 ± 1.14	12 ± 0.2	0.48	8.9	2.0	0.037 ± 0.001	1.225 ± 0.001	0.0694	0.1042
100Cr6 steel	2.1×10^5	710	500	0.28	-	-	-	7.9		

- E: Young's modulus;
- H: Hardness, converted from Shore D [35];
- S_y: Yield strength; for TPU, the stress at 50% strain from tensile test was used.
- ν: Poisson's ratio;
- K_{IC}: Fracture toughness; the minimum values from dumbbell fatigue tests were used.
- t: Fatigue ratio; based on the empirical research.
- γ: Surface energy;
- ρ: Density;
- α: Factor of abrasive wear.

Based on the values in Table 4; Table 5 and our tribological tests under the same conditions, wear rates were calculated. As shown in Figure 8, TPU_B has a better wear resistance to both counterpart roughnesses than TPU_A. However, in the experiments, only when it runs against a rough counterpart is the predicted trend consistent with the experimental results. For tests with a smooth counter surface, the predicted value is lower than the experimental results. This can be attributed to adhesive wear, which is included in this model, but for a smooth counter surface, especially when the transfer film is formed, adhesion turns out to be one of the primary wear mechanisms [12]. With a transfer film in the interface, abrasive wear can be reduced significantly. Moreover, as the blue line shows in Figure 8, for the rough counterpart, abrasive wear contributes to more than 96% of the total wear volume. For the tests with a smooth counter surface, abrasive wear is still dominant, but fatigue wear is higher than that with a rough counter surface.
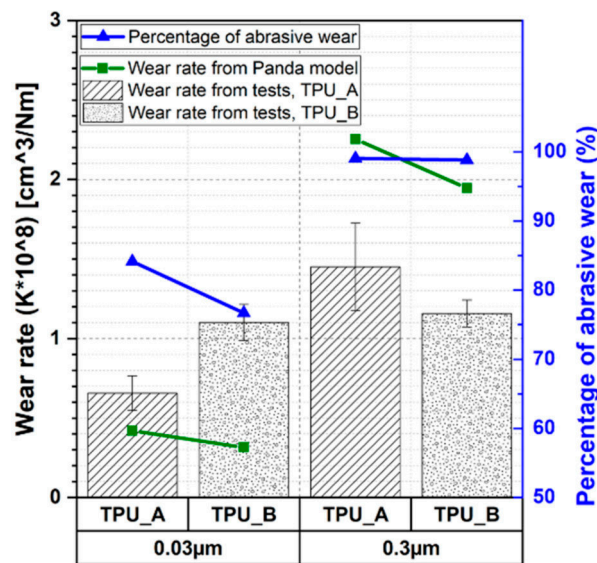
Figure 8. Comparison of wear rates from tests and analytical models.

3.3.2. Atkins Model

With all required parameters, the Atkins model can be used to compare tribological and mechanical fracture wear rates or fatigue cycle numbers, due to the correlation of wear rate $\propto 1/N_f$. The wear rate for the FWPS specimen was calculated in two ways; the first was the inverse value of the fatigue cycle number gained from the crack growth tests, and the second was calculating using the initial crack length, therefore determining a theoretical fatigue cycle number. The first method only includes the fatigue cycles, whereas the second also takes the mechanical fracture values into account. To check if the same trend is given for the dumbbell specimen, their fatigue cycle numbers for medium load levels were taken. In Figure 9, the comparison of the wear rates between the two investigated materials is plotted.
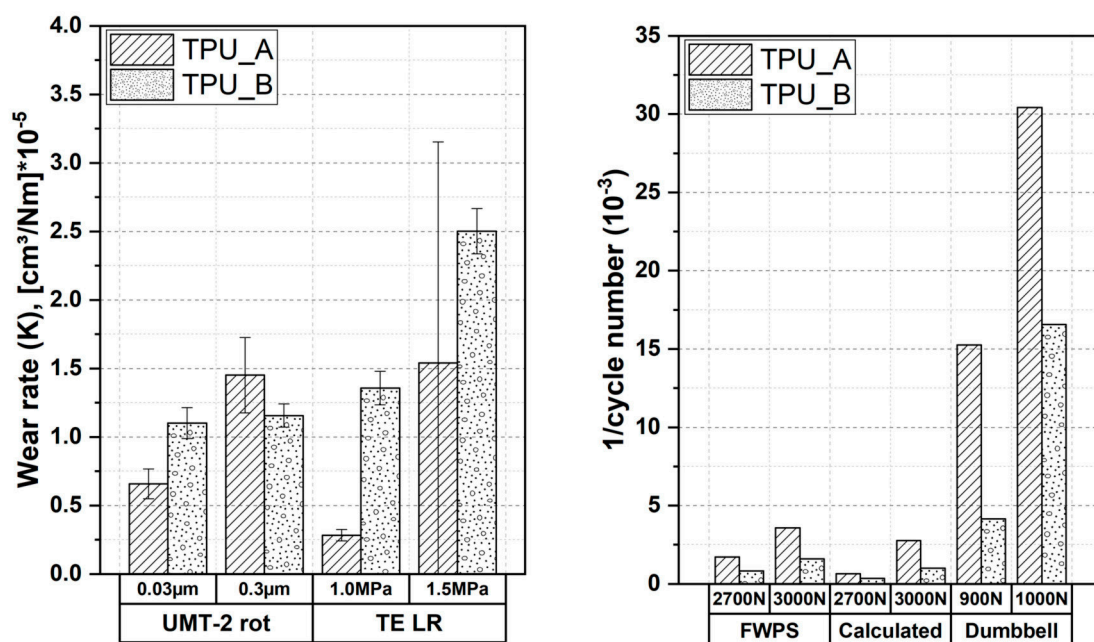
Figure 9. Comparison of the wear rates from the tribological and mechanical fracture tests of TPU_A and TPU_B for selected loads.

The depicted wear rates show a clear trend of higher wear rates for higher loads. Except for TE LR, the wear rate for TPU_A is higher than for TPU_B, the reason being the previously mentioned running-in wear, which is required to develop a transfer film on the counterpart. This fact can also be argued with the required tearing energy of 2400 J/m^2 to see a clear separation in Figure 5. It is possible that for both stressing types, mechanical and tribological, TPU_B needs a certain amount of energy or wear to develop its potential. This might be traced back to the filler, which acts to either stiffen or lubricate, depending on the mode of stressing. Even though TPU_B has a higher wear rate for the load ramp, the factor between the single loads and the counterpart roughness is smaller than for TPU_A. This includes the fact that TPU_B is less affected by higher stressing than the unfilled TPU_A. For mechanical testing, the inverse values of the fatigue cycle numbers were taken. The higher values of the wear rates calculated from the dumbbell specimen are due to the relatively small area of the specimen, which is more affected by higher loading. While the pre-notched area for a dumbbell specimen is around 130 mm^2, the area for a pre-cracked FWPS specimen is over three times higher, with 437.5 mm^2. Furthermore, it has to be mentioned that dumbbell specimens contain different stressing situations compared to the FWPS specimen.

3.3.3. Scope and Comparison of Both Models

Both models seem to cover one specific aspect of the tribological values. Panda's model shows a better fitting for rough surfaces, whereas Atkins' adapted model fits better for the smooth surfaces. This indicates that abrasive wear behavior should be explained using Panda's model, considering the roughness of both bodies. As already mentioned, as soon as a polymer film is developed on the counter surface, the model is no longer valid. On the other hand, a more adhesive wear mechanism can be described with Atkins' model, but only as a trend and not as a precise prediction.

4. Conclusions

In this study, a possible correlation between fatigue and tribological performance of unfilled und filled TPUs was found. This study also provides insight into the influence of filler on the fatigue and tribological properties of TPUs.

(1) Two models were verified to predict wear volume of filled and unfilled TPUs.
(2) The fatigue properties were identified with dumbbell tests. Fillers show a beneficial effect on the fatigue property at both temperatures. However, inverse impacts of temperature on low and high stresses were identified. The crack growth rate was characterized by means of faint waist pure shear tests. Filled TPU shows a better crack growth resistance.
(3) The tribological performance was characterized by various test configurations. An incubation period is necessary to generate a transfer film in the interface. Additionally, the influence of roughness of counterparts was identified.
(4) Similar failure mechanisms were identified in dumbbell, FWPS, and tribological tests.
(5) Panda's model shows a better prediction for the tests with a rough counter surface, while the Atkins model is advantageous to predict the results of the tests with a smooth counter surface. For the tests with a rough counter surface, abrasive wear contributes to more than 96% of the total wear, whereas for a smooth counter surface, abrasive wear is still the primary wear origin, but fatigue wear is about 20% of the total wear. Therefore, for a test, which model is better depends mainly on which wear mechanism is dominant. However, a lot of work still needs to be done to predict the wear precisely. Several factors, e.g., transfer film, temperature, etc., which are essential to wear generation, are not taken into consideration in this study.

Future work should focus on the temperature distribution and its effect on fatigue tests, and tribological tests have yet to be determined.

Conflicts of Interest: The authors declare no conflict of interest.

References

1.　Drobny, J.G. *Handbook of Thermoplastic Elastomers*, 2nd ed.; Elsevier: Amsterdam, The Netherlands, 2014; ISBN 9780323221368.

2.　El-Sonbati, A.Z. *Thermoplastic Elastomers*; InTech: Rijeka, Croatia, 2012; ISBN 978-953-51-0346-2.

3.　Nguyen, D.A.; Lee, Y.R.; Raghu, A.V.; Jeong, H.M.; Shin, C.M.; Kim, B.K. Morphological and physical properties of a thermoplastic polyurethane reinforced with functionalized graphene sheet. *Polym. Int.* **2009**, *58*, 412–417. [CrossRef]

4.　Roy, S.; Srivastava, S.K.; Pionteck, J.; Mittal, V. Mechanically and Thermally Enhanced Multiwalled Carbon Nanotube-Graphene Hybrid filled Thermoplastic Polyurethane Nanocomposites. *Macromol. Mater. Eng.* **2015**, *300*, 346–357. [CrossRef]

5.　Suresha, B. Friction and Dry Slide Wear of Short Glass Fiber Reinforced Thermoplastic Polyurethane Composites. *J. Reinf. Plast. Compos.* **2010**, *29*, 1055–1061. [CrossRef]

6.　Barick, A.K.; Tripathy, D.K. Thermal and dynamic mechanical characterization of thermoplastic polyurethane/ organoclay nanocomposites prepared by melt compounding. *Mater. Sci. Eng. A* **2010**, *527*, 812–823. [CrossRef]

7.　Pinto, U.A.; Visconte, L.L.Y.; Reis Nunes, R.C. Mechanical properties of thermoplastic polyurethane elastomers with mica and aluminum trihydrate. *Eur. Polym. J.* **2001**, *37*, 1935–1937. [CrossRef]

8.　Technical Committee ISO/TC 45 "Rubber and rubber products". *DIN ISO 7619-1:2012-02. Elastomere oder Thermoplastische Elastomere Bestimmung der Eindringhärte Teil_1: Durometer-Verfahren (Shore-Härte) (ISO_7619-1:2010)*; Beuth Verlag GmbH: Berlin, Germany, 2010.

9.　Technical Committee ISO/TC 61/SC 2/WG 1 "Static behavior". *DIN EN ISO 527-2:2012-06. Kunststoffe Bestimmung der Zugeigenschaften Teil_2: Prüfbedingungen für Form-und Extrusionsmassen (ISO_527-2:2012), Deutsche Fassung EN_ISO_527-2:2012*; Beuth Verlag GmbH: Berlin, Germany, 2012.

10.　Panda, S.; Sarangi, M.; Roy Chowdhury, S.K. An Analytical Model of Mechanistic Wear of Polymers. *J. Tribol.* **2018**, *140*, 11609. [CrossRef]

11.　Omar, M.K.; Atkins, A.G.; Lancaster, J.K. The role of crack resistance parameters in polymer wear. *J. Phys. D Appl. Phys.* **1986**, *19*, 177–195. [CrossRef]

12.　Chang, W.R.; Etsion, I.; Bogy, D.B. An Elastic-Plastic Model for the Contact of Rough Surfaces. *J. Tribol.* **1987**, *109*, 257–263. [CrossRef]

13.　Fuller, K.N.G.; Tabor, D. The Effect of Surface Roughness on the Adhesion of Elastic Solids. *Proc. R. Soc. A Math. Phys. Eng. Sci.* **1975**, *345*, 327–342. [CrossRef]

14.　Bahadur, S. The development of transfer layers and their role in polymer tribology. *Wear* **2000**, *245*, 92–99. [CrossRef]

15.　Briscoe, B.J.; Sinha, S.K. Wear of polymers. *Proc. Inst. Mech. Eng. Part J J. Eng. Tribol.* **2002**, *216*, 401–413. [CrossRef]

16.　Rhee, S.H.; Ludema, K.C. Mechanisms of formation of polymeric transfer films. *Wear* **1978**, *46*, 231–240. [CrossRef]

17.　Technical Committee NA 152-03-03 AA "Surfaces". *DIN EN ISO 25178-1:2016-12. Geometrische Produktspezifikation_(GPS)_Oberflächenbeschaffenheit: Flächenhaft_Teil_1: Angabe von Oberflächenbeschaffenheit (ISO_25178-1:2016), Deutsche Fassung EN_ISO_25178-1:2016*; Beuth Verlag GmbH: Berlin, Germany, 2016.

18. Owens, D.K.; Wendt, R.C. Estimation of the surface free energy of polymers. *J. Appl. Polym. Sci.* **1969**, *13*, 1741–1747. [CrossRef]

19. Rabel, W. Einige Aspekte der Benetzungstheorie und ihre Anwendung auf die Untersuchung und Veränderung der Oberflächeneigenschaften von Polymeren. *Farbe und Lack* **1971**, *77*, 997–1005.

20. Kaelble, D.H. Dispersion-Polar Surface Tension Properties of Organic Solids. *J. Adhes.* **1970**, *2*, 66–81. [CrossRef]

21. Schrittesser, B. Performance of Elastomers for High-Pressure Applications. Ph.D. Thesis, University of Leoben, Leoben, Austria, 2014.

22. Stiller, T. InSitutribological and Fracture Mechanical Investigation of Thermoplastic Polyurethanes. Master's Thesis, Montanuniversität Leoben, Leoben, Austria, 2013.

23. Wang, C.H. *Introduction to Fracture Mechanics*; DSTO Aeronautical and Maritime Research Laboratory: Melbourne, Australia, 1996.

24. Joelly, I.A. Assessment of Contact Pressure and Sliding Velocity on the Tribological Performance of TPU SEAL Materials for the Establishment of a Rating System. Master's Thesis, Montanuniversität leoben, Leoben, Austria, 2011.

25. Stachowiak, G.W.; Batchelor, A.W. *Engineering Tribology*; Elsevier: Amsterdam, The Netherlands, 1993; ISBN 0-444-89235-4.

26. Stoček, R. Dynamische Rissausbreitung in Elastomerwerkstoffen. Dissertation, Technische Universität Chemnitz, Chemnitz, Germany, 2011.

27. Gdoutos, E.E.; Daniel, I.M.; Schubel, P. *Fracture Mechanics of Rubbe*; Socirety of Rubber Science and Technology Japan: Tokyo, Japan, 2003.

28. Benthem, J.P.; Koiter, W.T. Asymptotic approximations to crack problems. In *Methods of Analysis and Solutions of Crack Problems*; Sih, G.C., Ed.; Springer: Dordrecht, The Netherlands, 1973; pp. 131–178, ISBN 978-90-481-8246-6.

29. Schieppati, J.; Schrittesser, B.; Wondracek, A.; Robin, S.; Holzner, A.; Pinter, G. Impact of temperature on the fatigue and crack growth behavior of rubbers. *Procedia Struct. Integr.* **2018**, *13*, 642–647. [CrossRef]

30. Schallamach, A. The Load Dependence of Rubber Friction. *Proc. Phys. Soc. B* **1952**, *65*, 657–661. [CrossRef]

31. Grün, F.; Sailer, W.; Gódor, I. Visualization of the processes taking place in the contact zone with in-situ tribometry. *Tribol. Int.* **2012**, *48*, 44–53. [CrossRef]

32. Gódor, I.; Schiffer, J.; Grün, F.; Schwarz, T.; Major, Z. Tribological Behaviour of Unfilled and Filled TPU Materials. In Proceedings of the 14th Nordic Symposium on Tribology, Storforsen, Sweden, 8–11 June 2010; p. 59.

33. Hausberger, A.; Major, Z.; Theiler, G.; Gradt, T. Observation of the adhesive- and deformation- contribution to the friction and wear behaviour of thermoplastic polyurethanes. *Wear* **2018**, *412*, 14–22. [CrossRef]

34. Wang, C.; Hausberger, A.; Nothdurft, P.; Lackner, J.; Schwarz, T. The Potential of Tribological Application of DLC/MoS2 Coated Sealing Materials. *Coatings* **2018**, *8*, 267. [CrossRef]

35. Pampush, J.D.; Daegling, D.J.; Vick, A.E.; McGraw, W.S.; Covey, R.M.; Rapoff, A.J. Technical note: Converting durometer data into elastic modulus in biological materials. *Am. J. Phys. Anthropol.* **2011**, *146*, 650–653. [CrossRef]

Paper 4: Precise Correlation of Friction Force and Contact Area during Stick-Slip by In Situ Microscopy with Microtribometry in An Elastomer-Glass Contact

C. Wang[1], S. Bonyadi[2], F. Grün[3], G. Pinter[4], A. Hausberger[1] and A. C. Dunn[2]

[1] Polymer Competence Center Leoben GmbH,8700 Leoben, Austria

[2] Department of Mechanical Science & Engineering, University of Illinois at Urbana-Champaign, Urbana IL, 61801 USA

[3] Chair of Mechanical Engineering, Montanuniversität Leoben, 8700 Leoben, Austria

[4] Chair of Materials Science and Testing of Plastics, Montanuniversität Leoben, 8700 Leoben, Austria

Authors and relevant contributions to this publication:

- C. Wang: Application and implementation of stick-slip, experimental testing, data evaluation, preparation of the publication
- S. Bonyadi: Data evaluation, review the publication
- F. Grün: Review the publication
- G. Pinter: Review the publication
- A. Hausberger: Discussion of experimental data, review the publication
- A. Dunn: Discussion of experimental data, review the publication

Precise correlation of contact area and forces in the unstable friction between a rough fluoroelastomer surface and borosilicate glass

C. Wang[1], S. Z. Bonyadi[2], F. Grün[3], G. Pinter[4], A. Hausberger[1], A. C. Dunn[2*]

[1]*Polymer Competence Center Leoben GmbH, 8700 Leoben, Austria*

[2]*Department of Mechanical Science & Engineering, University of Illinois at Urbana-Champaign, Urbana IL, 61801 USA*

[3]*Chair of Mechanical Engineering, Montanuniversität Leoben, 8700 Leoben, Austria*

[4]*Chair of Materials Science and Testing of Plastics, Montanuniversität Leoben, 8700 Leoben, Austria*

*Corresponding author: acd@illinois.edu

Address: Department of Mechanical Science & Engineering, University of Illinois at Urbana-Champaign, 1206 W Green St MC 244, Urbana, USA

Tel: +1 217 300-0349

Abstract

Stick-slip friction of elastomers arises due to adhesion, high local strains, surface features, and viscous dissipation. In situ techniques connecting the real contact area to interfacial forces can reveal the contact evolution of a rough elastomer surface leading up to gross slip, as well as provide high-resolution dynamic contact areas for improving current slip models. Samples with rough surfaces were produced by the same manufacturing processes as machined seals. In this work a machined fluoroelastomer (FKM) hemisphere was slid against glass, and the stick-slip behavior was captured optically in situ. The influence of sliding velocity on sliding behavior was studied over a range of speeds from 1 μm/s to 100 μm/s. The real contact area was measured from image sequences thresholded using Otsu's method. The motion of the pinned region was delineated with a machine learning scheme. The first result is that within the macroscale sticking, or pinned phase, local pinned and partial slip regions were observed, and were modeled as a combined contact with contributions to friction by both regions. As a second result, we identified a critical velocity below which the stick-slip motion converted from high frequency with low amplitude to low frequency with high amplitude. This study on the sliding behavior of a viscoelastic machined

elastomer demonstrates a multi-technique approach which reveals precise changes in contact area before and during pinning and slip.

Key words: elastomer stick-slip; In-situ microtribometry; machined seals

1. Introduction

Machined seals are also called customized seals, offering specifically manufacturing according to the demands of end-users. The customizability, time-saving and cost-saving for a small amount enable machined seals a better solution than the traditional molded part. Its market grows fast and will reach a revenue of over USD 2.5 billion by 2021 [1]. Real rough elastomeric surfaces deviate from smooth surfaces in that they could more edges of contact and retain features like asperities or ridges which will deform more readily than a smooth surface. While ideal sliding is smooth, stick-slip problems can be caused by insufficient lubrication at low speeds and high pressures. Stick-slip motion in seals can degrade performance significantly by causing vibrations that lead to cracks and wear [2]. Mitigation of unstable friction includes increasing movement speed or changing the surface roughness and lubricant. However, the motion profiles are typically fixed, and machining marks are inevitable in reducing finishing operations, which minimizes cost. Thus, there is a need to understand stick-slip motions between elastomers and hard surfaces, and especially the effects of surface features on contact area evolution during unstable events.

Stick-slip is generally a dynamic cyclic process where an interface driven in shear dissipates energy in a succession of quick slip events separated by phases of pinning [3]. In the pinned phase, the two surfaces stick together and no gross relative motion occurs; in the slip phase, finite relative motion occurs. Elastomers are particularly susceptible to stick-slip friction due to their compliance and increased surface energy. Under a lateral load, the compliant contacts pin together until internal cohesion reaches its limit, at which time the pinning is released by interfacial slip. The competition between interfacial adhesion and strain energy results in repeated stick and slip events [3, 4]. Elastomers are well-suited as seal materials due to the same compliance and high failure strain, as they can sustain large deformations and conform to mating surface features without fracture or yield.

In elastomer-flat contacts, the contact area is a controlling parameter. In compliant contacts, the real area of contact can approach the real of contact because roughness is small compared to the deformation of the elastomer. Ludema and Tabor proposed that, the rubber friction can be described with contact area and shear strength [4]. They measured the sliding friction between polymers and hard surface at various speeds and temperatures. They suggested that the contact area and shear strength are low

frequency and high frequency process during the deformation process, respectively. In 1971, Schallamach directly observed the contact area between rubber sliders and a hard counter surface, finding that the contact broke not in single large slip events, but rather local slip waves associated with the tangential compressive stress gradient [5]. For actuation of a hard surface against an elastomeric seal, we focus on incipient slip and the low-speed conditions. Bartenev et al [6] found that contact area remained almost constant at low speed, while at high speeds, the slip speeds are faster than the rates of recoil, so rubber properties play a larger role. In the flipped configuration of a hard hemisphere against an elastomer plate using an optical microscope, Barquins [7] defined the movement as a competition between adhesive dragging and relaxation at low speeds. These studies provide the theoretical background for the extreme case of conformal contact, but their application to rough elastomeric surfaces is limited.

Following the foundational work, Arnolds [9] and Roberts [10] included the consideration of roughness and surface energy on rubber friction when conducting experiments between a roughened rubber and a flat glass [8,9]. For roughened rubber, the friction coefficient increased with speed stably. At high speeds, the mechanisms are better understood, such as the stress relief through Schallamach waves relieved stress [10]. Above a critical sliding velocity, the behavior transitions from stick-slip motion to steady sliding [11–13]. Scaling laws and mean field theories [14] have provided guidance for the slip cascades depending upon the description of the interface as shear-weakening or shear-strengthening. From this, we see an open question as to the specific connections between contact area of a rough elastomer against glass and the shear forces as slip is initiated. We hypothesize that contact area changes dynamically under the application of shear forces before slip and during slip, and that modern in situ sliding techniques can capture these dynamic changes. Specifically, based on the theory of junction growth of adhesive asperities [15], we predict that the contact area grows on the application of a shear force. However, there must also be cascading decrease of contact area for gross slip to occur. Thus, we propose it is the competition between adhesive surface forces and cohesive forces which not only predict the speed transition as reported by prior researchers [7-8], but also predicts an increase and decrease in contact area before gross slip occurs.

In this study, we test the hypothesis by systematic slip experiments between a machined elastomeric hemisphere and a glass slide, which are simultaneously observed in bright field microscopy to identify the real area of contact. We mapped the

evolving real contact area upon the application of shear and found that both pinned and slipping regions are present. A machine learning strategy was used in the image analysis to accurately follow the lateral position of the pinned region. The influence of sliding velocity on stick-slip behaviors was studied over a range of speeds from 1 µm/s to 100 µm/s. The correlation between real contact area and friction force, together with the movement of the stick region achieved with machine learning, revealed the stick-slip process of a machined seal material against glass. In addition, we identified a critical velocity threshold between "micro" stick-slip and "macro" stick-slip. Finally, the time evolution of the stick-slip was roughly correlated to the creep relaxation of the rubber. This research provides a more comprehensive understanding of the conditions and modes of stick-slip which can occur during the operation of machined seals, and can benefit the design of elastomeric seal surfaces to prevent unstable friction modes, thereby improving the sealing performance.

2. Materials and Methods

2.1 Microscopy in situ Microtribometry

The in-situ microtribometer consists of two parts, the tribometer and the optical system. With this setup it is possible to perform various tests while observing the contact area, e.g. indentation, creep, and friction tests. Prior groups have primarily used one of two experimental set-ups for optical in-situ tests: sliding a hard, transparent hemisphere against a flat specimen [10,16,17], or, sliding a hard, transparent flat surface against a hemispherical or flat sample [18–22]. The setup for this work is similar to the latter, in that a 1-mm thick microscope slide is slid under an instrumented probe tip.

The entire instrument is located atop the stage of an inverted microscope (Fig. 1). The test specimen is mounted directly to the end of a cantilevered 4-bar flexure. Two capacitance probes mounted orthogonally detect micro-motions of the probe in the normal and lateral orientations, which are then translated to forces through the calibrated flexure stiffness. The flexure assembly is translated downward by a linear piezoelectric stage to establish and maintain contact between the test specimen and the glass slide. The glass countersurface was mounted on and reciprocated by a lateral piezoelectric stage of maximum stroke 1.5 mm. The probe approach, load monitoring,

lateral motion inputs, and data acquisition were done simultaneously through custom software (LabVIEW, National Instruments, Austin TX USA).
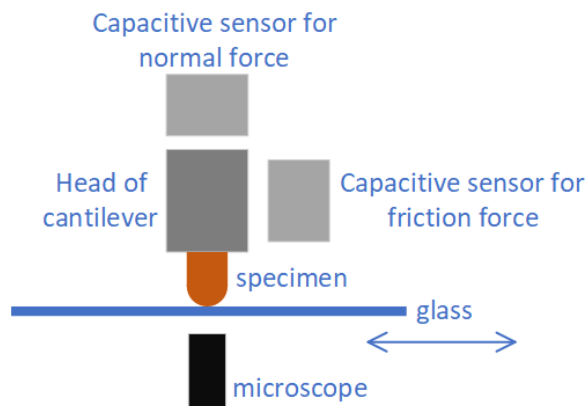
Fig. 1: Sketch of the optical in situ microtribometer

The 4X objective was aligned with the probe specimen. Because the motion of the glass slide was controlled independently between the probe specimen and objective, the contact was maintained in the field of view. The sample contact was illuminated through an LED ring illuminator (64 LEDs). Images were acquired using the microscope camera and software at ~20 frames per second (NIS-Elements 4.0 and TI Eclipse. Nikon, Japan).

2.2 Materials

A fluoroelastomer, specifically FKM (provided by SKF Sealing solutions Austria GmbH, Judenburg, Austria) was selected due to its wide use as a sealing material. The test samples were manufactured through a turning process. The whole sample had a cylindrical form with a length of 5.17 mm. One end of the sample was a hemisphere with a diameter of 4.86 mm. FKM has a shore-A hardness of 84. Prior to the experiment, the topography of the sample was characterized with a three-dimensional focus variation microscope (InfiniteFocus, Alicona, Graz, Austria) and an optical light microscope (Stereo Microscope SZX 12, Olympus, Tokyo, Japan). After manufacturing, turning marks were observed on the sample surface (Fig. 2 A). The surface has an average roughness (Ra) of 1286.0 nm and a mean peak width (RSm) of 104.2 µm. Its waviness (Wa) is 50.2 µm (Fig. 2B-C). The Young's modulus of the glass slide countersurface was over 60 GPa, approximately 4,000 times higher than FKM; because of this, we assumed all deformations occurred in the elastomer specimen. In addition, the countersurface had a roughness less than 2 nm, and as such could be considered flat in comparison to the probe specimen.
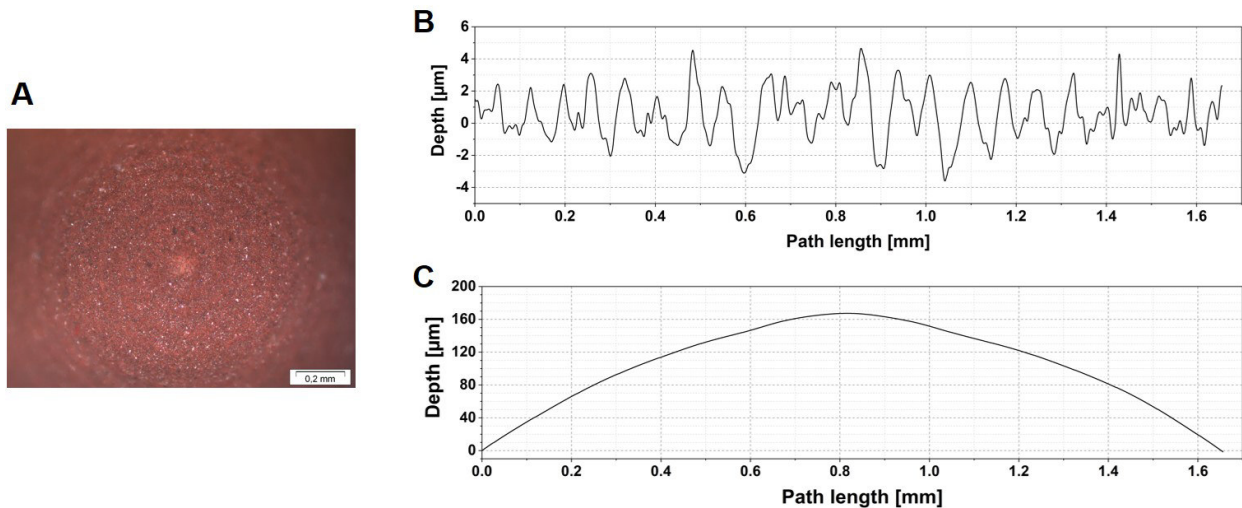
Fig. 2 (a) Micrograph of FKM hemispherical sample texture (b) Roughness and (c) waviness of the topography of FKM probe surface

2.3 Experimental Procedures

For the creep tests, the normal load was kept constant at 800 mN following loading at 50 mN/s. After reaching the target normal force, it was maintained for ~18 minutes. Video of the contact spot was recorded for up to 20 minutes. For the stick-slip tests, the samples were pressed against the glass slide with a normal load of 500 mN and the glass was translated beneath up to a length of 500 µm. Each cycle consisted of two traces in opposite directions, defined here as trace and retrace. In order to investigate the influence of sliding speeds on the stick-slip behavior, four different speeds were selected: 100 µm/s, 20 µm/s, 5 µm/s to 1 µm/s (Table 1). The number of cycles at each speed was limited to the cycles which showed obvious stick-slip; when this behavior ceased, the test was stopped at the end of that reciprocating cycle.

Table 1. Test parameters of stick-slip tests

Test	Speed [µm/s]	Normal load [mN]	Length per trace [µm]	Number of cycles [-]
1	100	500	500	200
2	20	500	500	20
3	5	500	500	30
4	1	500	500	7

2.4 Image Analysis

Each video was converted to stacked images. Then, each frame was cropped to keep the relevant contact region in the frame. Determining the first frame in which the polymer contacts the glass required removing any external light scattering or noise. To accomplish this, the color values of each pixel of a frame in which we knew the polymer

was not contact was subtracted from the rest of the frames. As a result, the frame in which first contact occurred became obvious. The frames prior to contact were irrelevant and would not be considered in the analysis. The following steps are different for creep tests and sliding tests.

For creep tests, the probe pressed into the glass countersurface at 50 µm/s. The contact point was identified with the method outlined earlier. Each frame was thresholded using Otsu's method to compress the greyscale images to binary (black and white) images [23]. After thresholding, the white pixels indicated areas of contact, and conversely, black pixels indicated areas of no contact. To measure the contact area change in time, the area of white pixels was converted to micrometers squared using the dimensions of one pixel, 4.72 µm square.

For sliding stick-slip tests, the subtraction method is not applicable, because the sample deforms with the horizonal movement of the countersurface to some extent. Hence, each frame is directly thresholded using identical value after cropping.

3. Results & discussion

3.1 Creep test

Creep is expected to occur in both normal load and friction tests. It is one of the contributions of contact area increase. The contact area was observed from the beginning of the loading phase. As shown in Fig. 3, after the loading phase, the contact area increased slowly with time from 0.303 mm^2 at the end of loading phase and reached 0.378 mm^2 after 1000 s.
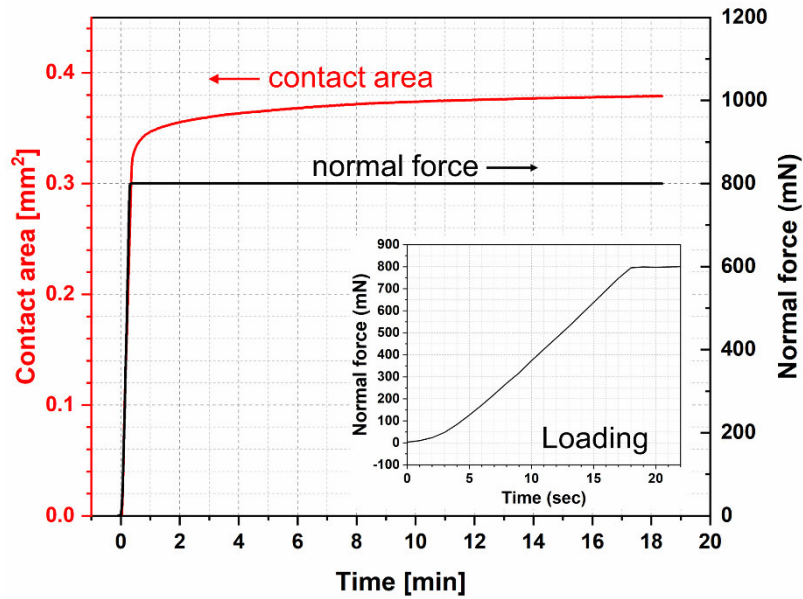
Fig. 3: Force-controlled creep test of FKM fluoroelastomer.

3.2 Stick-slip friction

3.2.1 General description of stick-slip behavior

Stick-slip occurred at all speeds tested, but the character changed over time. Due to the relatively low elasticity of FKM and hemispherical geometry of the specimen, slight changes to contact area are detectable. As can be seen in Fig. 4, as the countersurface moved from one end of the trace (x = -250 μm) to the other end (x = +250 μm), the frictional force (F_f) reached a value of 370 mN during the stick stage just before the first slip occurred. At that moment, the countersurface had already moved about 250 μm. In other words, no slip occurred until 250 μm before it reached its deformation limit.

The duration of stick-slip experienced a decay, lasting fewer cycles at lower sliding speeds. For the tests with 100 μm/s or 20 μm/s sliding speeds, the stick-slip behavior is no longer observed after about 20 cycles (20 mm, 200 s for 100 μm/s, 1000 s for 20 μm/s), while it can still be identified after 30 cycles (30 mm, 6000 s) in the 5 μm/s test. For the test with the lowest sliding speed, the stick-slip behavior disappeared after merely four cycles.
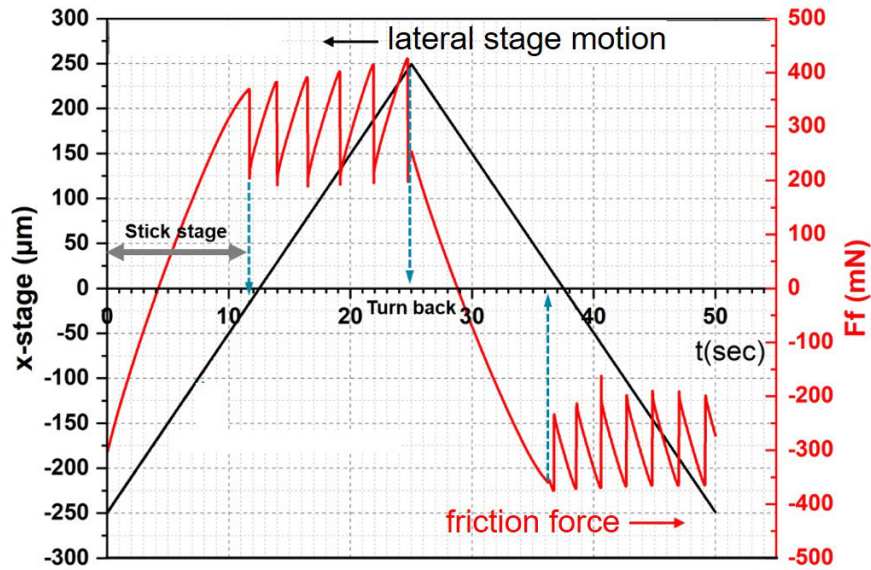
Fig. 4: Input displacement of glass countersurface (black) and resulting friction force (red) during the test at a sliding speed of 20 µm/s.

3.2.2 Comparison of stick-slip behavior of different tests

The influence of sliding speed can be identified with friction force (F_f) and coefficient of friction (COF), in the first cycle in particular (Fig.5). There is a considerable difference between the four test conditions, especially at low speeds. Only focusing on the trace portion, for the tests with decreasing sliding speeds, namely from 100 µm/s to 5 µm/s, 8, 6 and 4 slips took place during the first trace in the tests with 100 µm/s, 20 µm/s, and 5 µm/s, respectively (Fig.5A, 5B, 5C). Therefore, the number of slips reduces with decreasing sliding speeds. However, the test with a sliding speed of 1 µm/s experienced 15 slips in the first trace. At the maximum sliding speed (100 µm/s), a transition from stick-slip to steady sliding was not observed. This result indicates that for an elastomer, there is a critical sliding speed (V_c) above which the stick-slip is "marco" stick-slip. If the speed is lower than V_c, the "macro" stick-slip will become "micro", which has a smaller amplitude but a higher frequency.
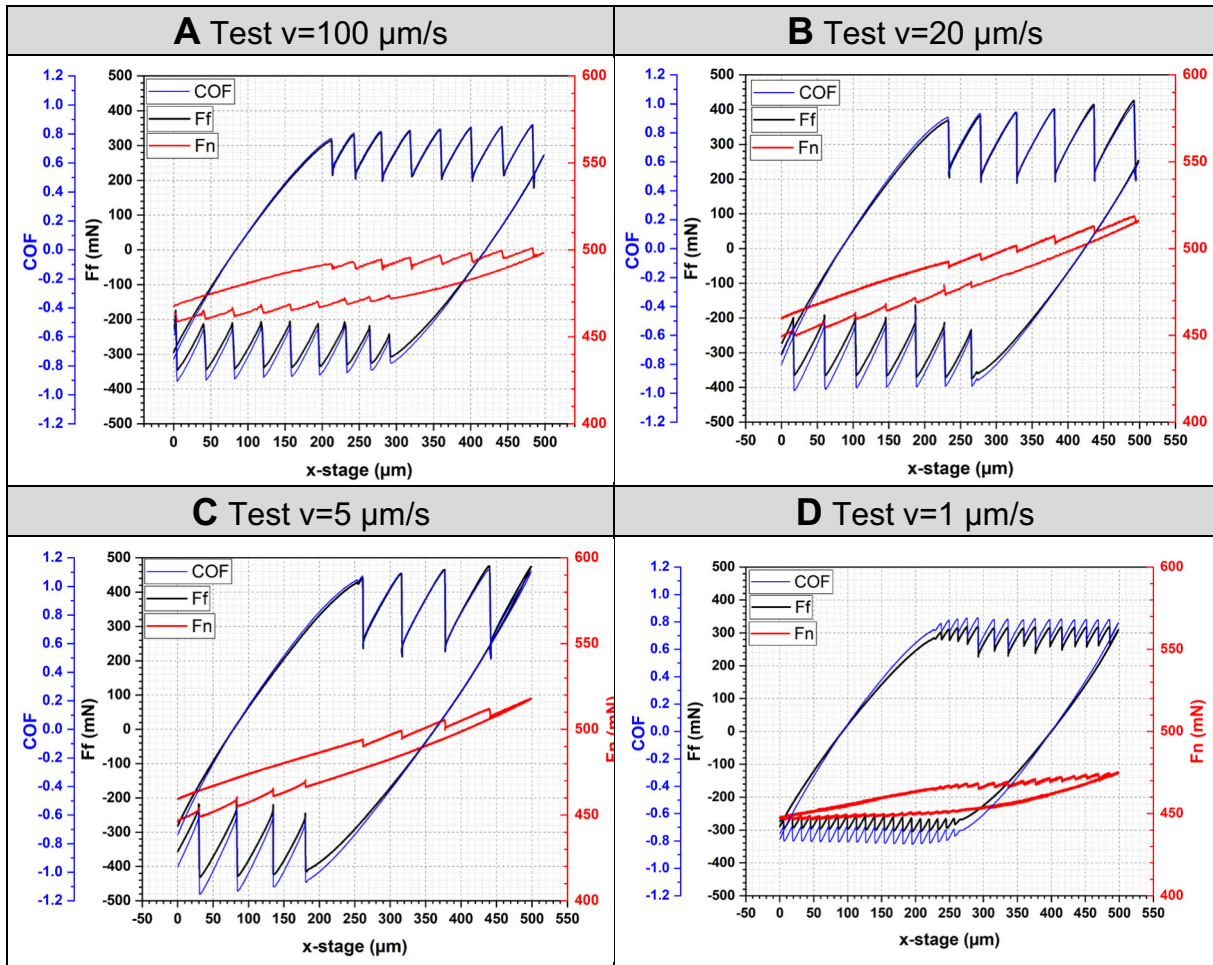
Fig. 5: Comparison of the first cycle in four tests. Data shown is the coefficient of friction (blue), friction force (black), and normal force (red).

This observation is due to the sliding speed being slow enough to allow the elastomeric material time to recover, resulting in the separation of the adhesive bonds at the interface [24]. Therefore, this critical velocity differs from those defined in other studies [11–13], which describe the sliding mode changes from stick-slip to steady sliding. In this study, the critical velocity is found in a low speed regime. The amplitude of stick-slip movement decreases with increasing stick-slip frequency, which is in a good agreement with [25].

The adhesion force plays an important role in stick-slip sliding tests. Generally, for two flat surfaces in contact, the adhesion force increases with increasing test velocity [26,27]. For smooth surfaces, viscous forces have a greater impact than capillary forces on the adhesion forces at the interface[27,28]. Therefore, higher speeds increase the viscous force, which ultimately increases the adhesion force.

For viscoelastic materials, especially elastomers, the tensile strength increases with increasing strain rates. Thus, when the sliding speed is higher, the material behaves stiffer. The results indicate that with increasing speed, adhesion forces increase slower than shear force. However, at 1 μm/s, the adhesion forces remain low enough to be overcome by the low shear forces, even though the material behaves softer at low speeds. This is in good agreement with the velocity dependence of shear stress reported by another group [29].

3.2.3 Normal force response corresponding to stick-slip

During the stick-slip movement, the penetration depth adjusts to the vibration, therefore, the normal force (F_n) changes slightly. This phenomenon is in good agreement with the results from [30]. In terms of reduction of friction force during the slip stage, the largest reduction can be identified in the test with 5 μm/s, which has an average reduction of 245 N in the first trace. The smallest reduction of friction force occurred in the test with 1 μm/s, with an average value of around 50 N, which is almost only one fifth of that in the test with 5 μm/s. For the test with 100 μm/s and 20 μm/s, the friction reduction is 130 N and 210 N, respectively. As shown in Fig. 5, except for the test with 1 μm/s, the reduction of friction force increased slightly during the first trace in all other tests. This phenomenon can be observed in the retrace movement as well.

The first order stick frequency was calculated from the sliding speed and the length of the trace, and there is a trend of more frequent slips at higher speeds (Fig.6A). With the exception of the very low speed regime in which V=1 μm/s, the trend generally follows a power law fit with an exponent of ~ 1.2.
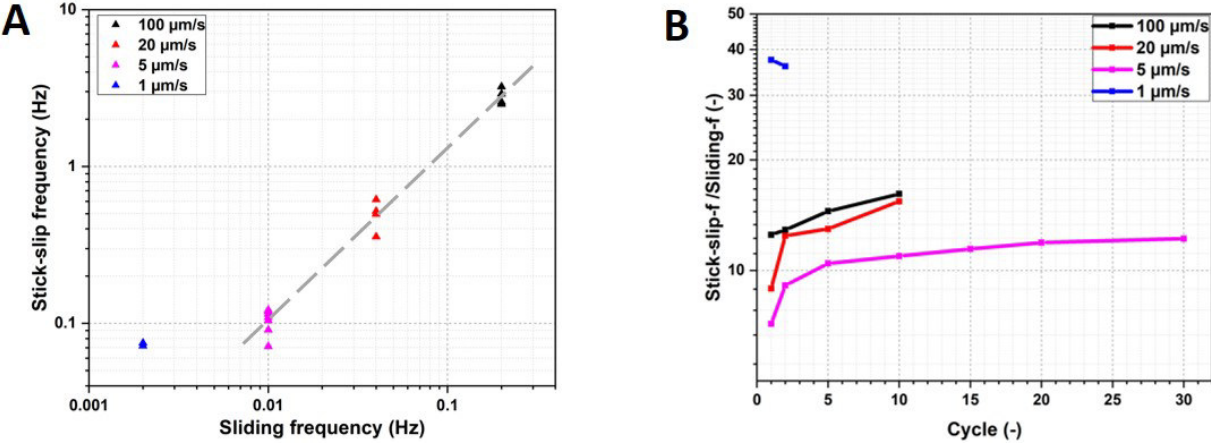
Fig. 6: (A) Relation of stick-slip frequency and sliding frequency in the first trace. (B) Relation of stick-slip frequency/sliding frequency with cycles.

The ratio of stick-slip frequency to sliding frequency of the first cycle is close to 10, with the exception of the test at 1 µm/s. With each additional cycle, the ratio increased. The ratios remained nearly the same after the second cycle for the tests at 100 µm/s and 20 µm/s. For the test with 5 µm/s, the ratio stayed nearly constant after five cycles. The behavior of the very low sliding speed test diverged from the trends of the faster tests, and the ratio began at nearly 40 and did not change significantly. The stick-slip behavior was only observed in the first cycle of the test at 1 µm/s.

3.3 Real contact area results

The area in contact also generally showed a frequency response correlated to the stick-slip as measured by forces alone (Fig. 7). Within a particular cycle, the contact area reached its maximum value when the glass at the turnaround point between forward and reverse strokes. The magnitude of the contact area was slightly reduced in the reverse stroke, but this corresponded to slightly lower friction forces and may be attributable to slight sample misalignment. As the test proceeded from the 1st to the 10th cycle, the contact area increased, though the change of contact area during the stick-slip behavior was considerably smaller between the 10th and 20th cycle than in the 1st and 10th cycles. This may be attributable to the viscoelasticity of material and the evolving surface of the FKM sample due to creep. After 20 cycles (1000 s), the specimen slid smoothly over the countersurface as no stick-slip behavior could be identified. This result is slightly counterintuitive in that an increasing contact area with one surface having identical surface energy should result in more adhesion, and therefore a greater propensity to stick rather than a decreased propensity. This may be explained by the changed contact conditions. The contact area of elastomer was turned (Fig. 2) and its surface was rough. Hence, due to the interfacial tangential force, wear particles were separated from the bulk material. Small particles facilitated the relative movement. Stick-slip was damped. Between the first and 20th cycle, the average friction force is approximately at the same level and the difference of friction between stick and slip was getting smaller (Fig. 7).
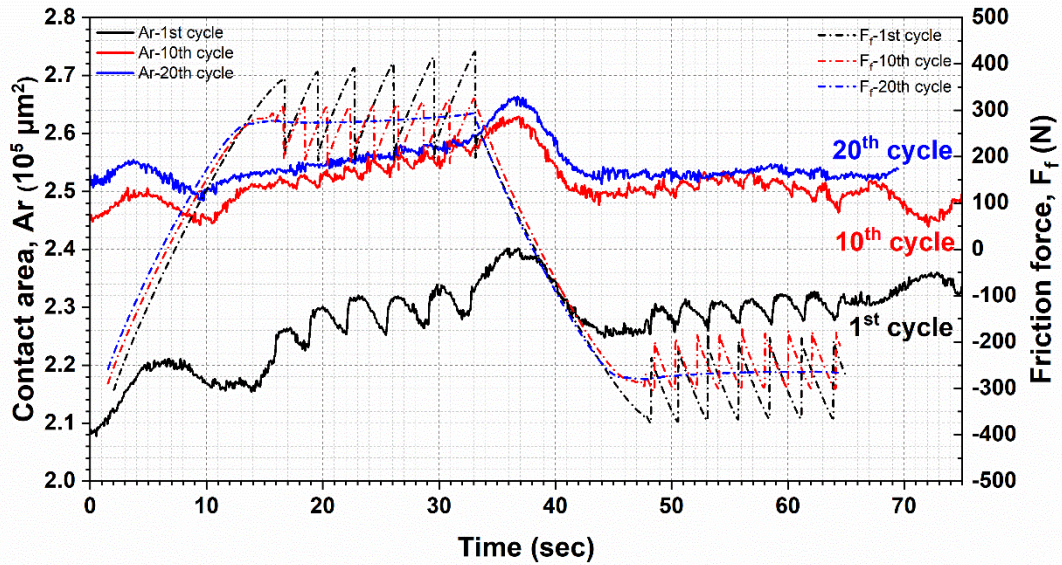
Fig. 7: Change of contact area and friction force with time in the first (black), 10th (red), and 20th (blue) cycle from the test at 20 µm/s.

3.3.1 Stick region in the contact area

Upon close inspection, the entire real contact area exhibited two regions, a completely pinned, or stuck region, and a slipping region. The pinned, central region moves with the countersurface, and the peripheral slipping region has some small relative motion. These regions shift between forward and reverse sliding, and also evolve over the duration of the test. Like the overall contact area, this may be attributed to contact evolution due to plasticity or aging combined with a slight misalignment between the glass surface and the sliding direction.

To calculate the stick region, the countersurface was used as the frame of reference. The pinned region adheres to the countersurface, and they move together. Hence, the pinned region does not experience any relative movement. As can be seen in Fig. 8A, the whole contact region was encompassed by the yellow-dashed circles in the 40th and 1st frames. Before being subtracted by the fortieth frame, the first frame was translated according to the prescribed movement of the glass slide. After subtracting the 1st frame from the 40th frame, we identified the region in which the two frames overlap, which remained pinned during the interim. We indicate this region with a red-dashed oval in Fig.8A.
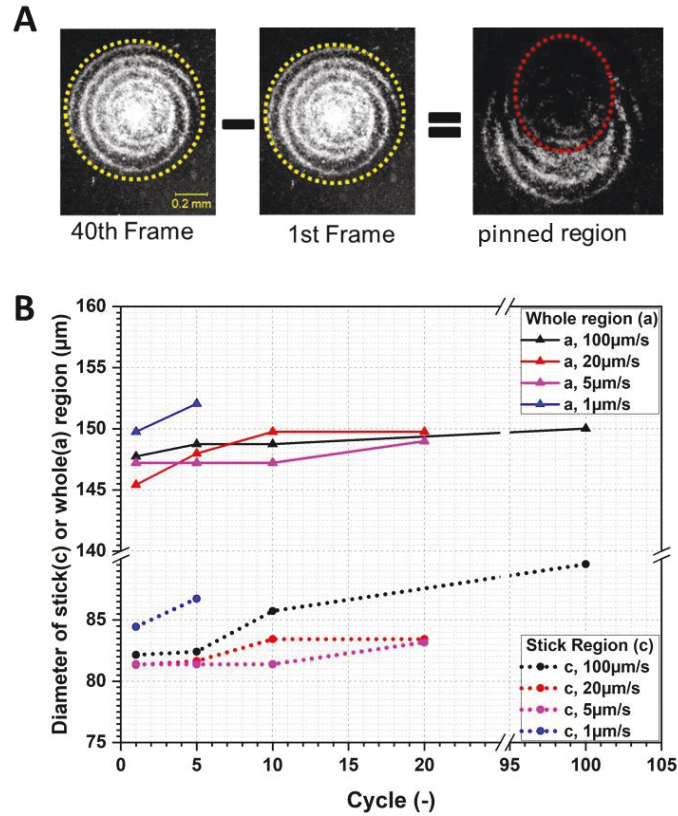
Fig. 8(A) The area of the pinned region was calculated by subtracting the 1st frame from the 40th; identical features are assumed to be pinned to the countersurface. (B) Change of pinned and slipping regions with cycles.

3.3.1.1 Machine learning algorithm for contact area partitioning

The pinned region is a fraction of the whole contact area as shown previously in Fig.8. The complexity of processing this data motivated the use of a machine learning algorithm to understand the movement of the stick region, as exact coordinates of the stick region had to be extracted from the recorded video data. By using the coordinates obtained from manually marking the stick region in about 300 single frames, a convolutional neural network (CNN) was trained to accurately predict the stick region of the remaining 61000 images. The details of the CNN can be found in Supplementary Material.

These ratios for each cycle of the experiment are shown in Fig.8B. The test at 1 μm/s has the largest contact area, and thus also the largest pinned region of all tested speeds. The creep effect must be taken into consideration. With 1 μm/s sliding speed, its cycle time is much longer than other tests. Therefore, the viscoelasticity of the material affects the contact area. In addition, generally for elastomers, the material shows a higher storage modulus with increasing test frequency. For the test with 1

µm/s, the test frequency was 0.002 Hz, which is much lower than the other tests. Meanwhile, its cycle time is much longer than the other tests. Hence, the contact area is slightly larger. For the stick region, the three other tests appear behave similarly during the first cycle. However, after five cycles, the stick region began to increase at different degrees. As to the whole contact area, only a slight difference can be identified among the three tests.

A large composite of the simultaneous stage position pinned region position, friction force, contact area, and shear stress are shown in Fig.9A. The stage position was strongly associated with pinned regions position and friction force. In the stick phase, the pinned region moved with the countersurface at a speed of -5 µm/s. Hence, its position changed proportionally over time. After the stage reversal at t ~ 175 s, the pinned region moved nearly linearly with time, at approximately 5 µm/s.

The movement of the pinned region within one stick phase is shown in Fig. 9 and was identified using the CNN. This pinned region moved with the countersurface until a maximum shear stress was achieved. As shown in Fig.9A, the maximum shear stress was reached just before the slip occurred.
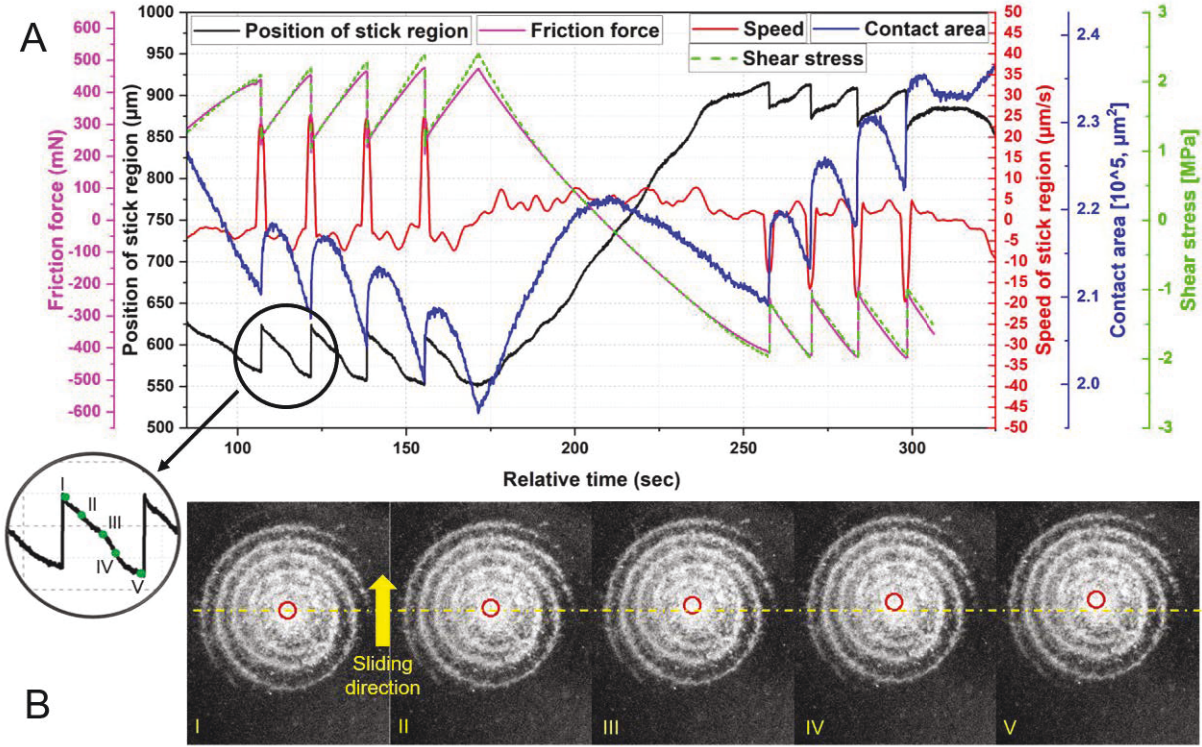
Fig. 9: (A) Relationship of the movement of stick region, friction force, contact area, and shear stress of the first cycle in the 5 µm/s test; (B) Marked stick region within one stick phase (I, II, III, IV, V) using machine learning.

3.3.2 Correlation of friction and real contact area

By observing the contact area during the sliding tests, it is possible to correlate the measured friction force with the contact area, the stick-slip behaviors in particular. The in-situ technique enables a direct correlation of material deformation and the measured forces in real time.

The slope of friction force reduced within a stick phase. As in the bottom graph of Fig. 10, for all tests the static friction increased faster at the beginning of the stick phase than at the end. Interestingly, the changing rate of contact area and friction force behave similarly. It is evident that as the stick region becomes smaller, the frictional force increases more slowly. If no slip occurs in the real contact area, the static friction Q_s can be described by the following equation,

$$Q_s = \sigma_g A_r \qquad\qquad Eq.1$$

where σ_g is the shear strength of static contact and A_r is the real contact area. This equation is also used for static friction in [29,31–33] and for the sliding tests without stick-slip behaviors [4].

$$\frac{dQ_s}{dt} = \underbrace{\sigma_g \frac{dA_r}{dt}}_{Area\ term} + \underbrace{A_r \frac{d\sigma_g}{dt}}_{Strength\ term} \qquad\qquad Eq.2$$

Thus, the change of static friction can be described with two terms (Eq.2). The area term takes the rate of change of the real contact area into consideration. As shown in Fig. 10, its value decreases throughout the stick phase. However, shortly before slip occurs, it begins to increase, but is still negative. Once slip occurs, the rate of change of the real contact area reaches zero and continues to increase. Therefore, the area term is negative prior to slip. The strength term is strongly impacted by sliding speeds. For thermoplastic materials, the strength increases with increasing testing speeds. Generally, the changing rate of strength decreases with increasing strain. It can be concluded from the changing rate of static friction (Fig. 10), that the area term is the dominant term.

However, stick and slip regions can be identified within the contact area during the stick phase. Therefore, the previous assumption is valid at the beginning of the stick phase.

$$Q_s = \sigma_g A_{stick} + \mu F_{nslip}. \qquad\qquad Eq.3$$

$$\frac{dQ_s}{dt} = \underbrace{\underbrace{\sigma_g \frac{dA_{stick}}{dt}}_{Area\ term} + \underbrace{A_{stick} \frac{d\sigma_g}{dt}}_{Strength\ term}}_{Stick\ term} + \underbrace{\underbrace{\mu \frac{dF_{nslip}}{dt}}_{Force\ term} + \underbrace{F_{nslip} \frac{d\mu}{dt}}_{Friction\ term}}_{Slip\ term} \qquad Eq.4$$

The area of the stick region is A_{stick} and the normal load of the slip region is F_{nslip}. The coefficient of friction in the slip region is μ. Regarding the friction force, partial slip part was not mentioned in many studies [4–8,22,34,35]. However, in the partial slip mentioned studies, e.g. [36], the part of slip was not taken into account. As can be seen in Fig. 11, the stick area (marked with a dotted line) decreased from A to E, which correspond to the beginning and end of the stick phase, respectively. At the beginning, due to the low elasticity of FKM, the whole contact area (white area in Fig. 11) moved with the countersurface. Therefore, no slip took place. With further movement, the tangential force increased with increasing deformation of the sample. Consequently, part of the adhesive bonds began to break, and these areas transformed into the slip region. This process began at the outer ring of the left image of Fig. 11, and gradually, changed into the stick area illustrated by the ellipse in the right image of the figure. Because part of the contact surface (upper part of marked areas in Fig. 11C, D, E) was a result of the decreasing shear movement, the area term is negative. The slip region became larger from Fig. 11A to E, which is why the force term of slip is positive. If μ is assumed to be constant, then the slip term is positive. As a result of decreasing stick area, the area term is the only negative term. Therefore, the static friction depends strongly on the stick area.
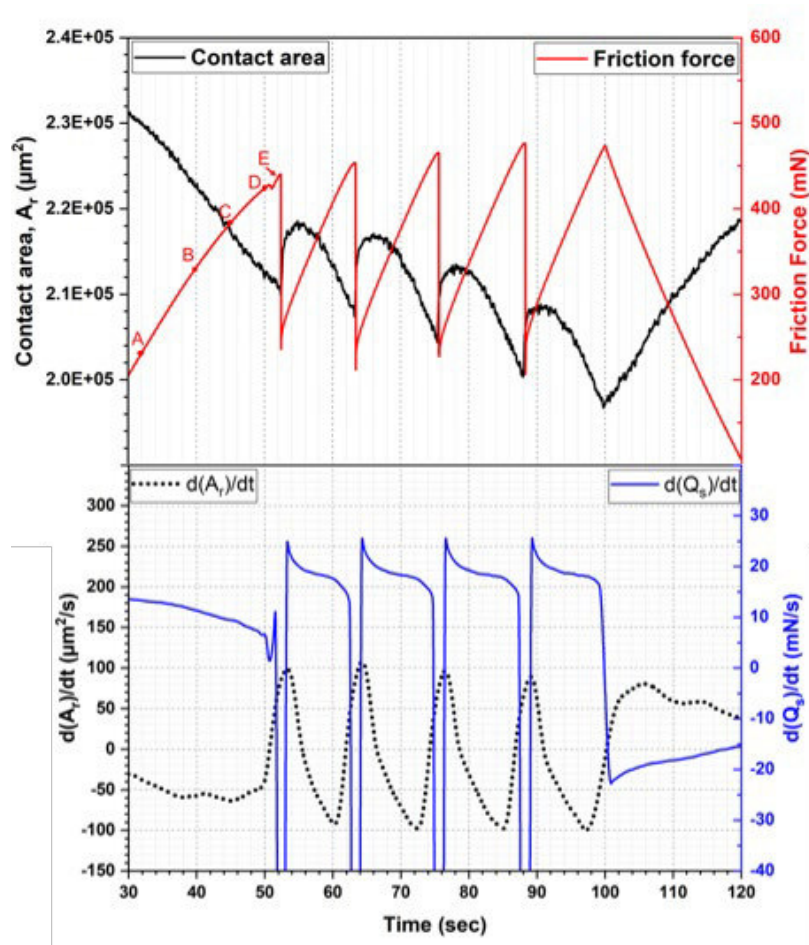
Fig. 10: Upper: Change of contact area and friction force within the stick-slip behavior of the first trace in the 5 μm/s test; Lower: Changing rate of contact area and friction force within the stick-slip behavior of the first trace in the 5 μm/s test.
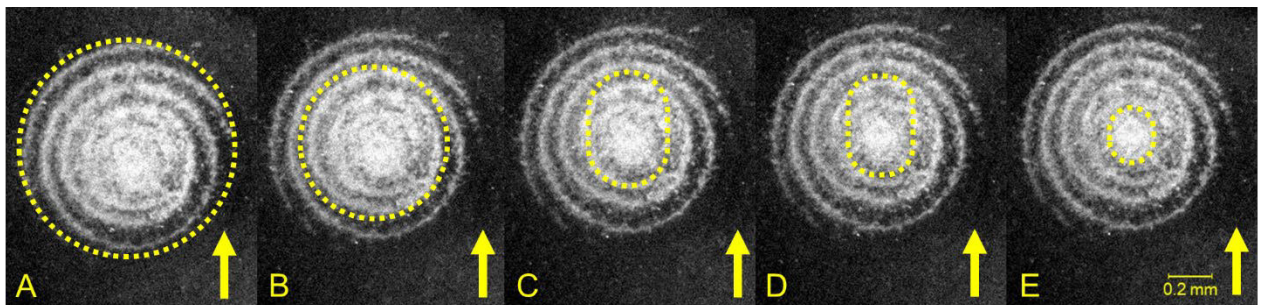
Fig. 11: Change of stick area (dotted line) within stick phase of the 5 μm/s test, arrow shows the movement of counter surface; A, B, C, D, E correspond to Fig. 10upper.

The top graph of Fig. 10 shows the alternating contact area with the corresponding stick-slip behavior. It can be observed that the contact area decreased during the stick phase and increased abruptly with the slip movement of the specimen. It is understood that the whole contact area deformed largely as a consequence of the shear stress. The outer region of the contact area, the slip region in particular, experiences a transition from the contact state to non-contact state. Prior to the first slip, a small drop of friction force can be identified in Fig. 10. This phenomenon has also been identified by other groups [37]. The friction force increased in a nearly linear way until reaching

a peak force. At the peak point, the friction force dropped abruptly from over 400 N to around 200 N. At the same time, the static friction transformed into dynamic friction in about 30 milliseconds. Taking a close look at the loading curve, before reaching the peak force, a small drop (about 1 %) of friction force during the load phase can be seen. This phenomenon only occurs at low speed regimes (5 µm/s and 1 µm/s). Davis et al [38] studied the influence of surface wrinkles on adhesion of elastic materials. She found that for highly cross-linked stiffer materials, adhesive forces affect distances shorter than the wrinkle amplitude, which explains why the adhesion behavior is significantly impacted by wrinkles. The separation stress and debonding energy can be nearly doubled by small wrinkles, while large wrinkles show negative effect. Bennewitz et al [39] found that sliding is preceded by crack-like precursors that cause compressive strain to form along the interface. In addition, the speed of friction force change is shown in Fig. 10. In the stick phase, the speed decreased before the friction force reached its peak. In the slip phase, the speed reached over -6000 mN/s (not shown in Fig. 10). This precursor phenomenon and the previously mentioned "micro" stick-slip at low speeds can be related to the same mechanisms.
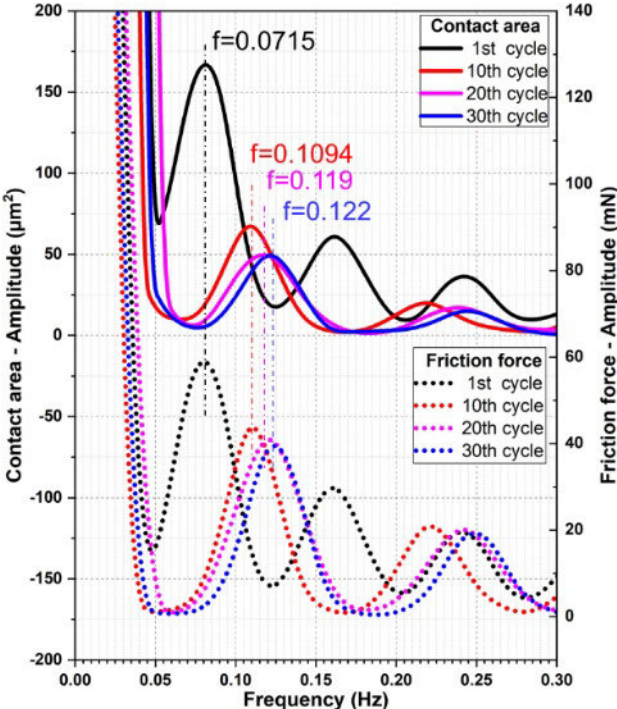
Fig. 12: FFT of contact area and friction force of the test with 5 µm/s.

To attain a clear relationship between the alteration of friction force and contact area, the measured friction force and contact area were transformed from the time domain to the frequency domain using Fast Fourier Transformation (FFT). As shown in Fig. 12, the contact area and friction force changed at the same frequency. Additionally, the

FFT-frequency increased with cycles, from 0.0715 Hz in the first cycle to 0.122 Hz in the 30th cycle.

4. Conclusion

Using the samples with manufacturing marks as machined seals, the real contact area and stick-slip behavior of a hemispheric elastomer sliding on a smooth glass slide were investigated using an in-situ microtribometer. Based on the presented results and discussion, the following conclusions can be drawn:

1) The contact area decreased during the stick phase and increased abruptly with the slip movement of the specimen. The transformation from static friction to dynamic friction took about 30 milliseconds.
2) During each macro stick phase, the contact area increased and then decreased with an asymmetric parabolic shape.
3) The shear strength profile was related to loads and speeds by using machine learning, which resulted in the discovery of the movement of the pinned region within one stick phase.
4) Two mathematical models of time-resolved friction force and shear stress were introduced and offered an understanding of the phanomena, which were observed with microscope and analyzed from the videos.

Future work could focus on the size change of stick region and the temperature alteration in the interface during stick-slip sliding.

References

[1] technavio. Global Machined Seals Market 2017-2021; Available from: https://www.technavio.com/report/global-machined-seals-market.

[2] Alan Hitchcox. Reduce Vibration and Avoid Stiction in Seals; Available from: https://www.hydraulicspneumatics.com/hydraulic-fluids/reduce-vibration-and-avoid-stiction-seals.

[3] Robert M. Gresham. Slip-stick: What's it all about? Tribology & Lubrication Technology 2011;06:32–3.

[4] Ludema KC, Tabor D. The friction and visco-elastic properties of polymeric solids. Wear 1966;9(5):329–48. https://doi.org/10.1016/0043-1648(66)90018-4.

[5] Schallamach A. How does rubber slide? Wear 1971;17(4):301–12. https://doi.org/10.1016/0043-1648(71)90033-0.

[6] Bartenev GM, Lavrentjev VV, Konstantinova NA. The actual contact area and friction properties of elastomers under frictional contact with solid surfaces. Wear 1971;18(6):439–48. https://doi.org/10.1016/0043-1648(71)90168-2.

[7] Barquins M. Sliding friction of rubber and Schallamach waves — A review. Materials Science and Engineering 1985;73:45–63. https://doi.org/10.1016/0025-5416(85)90295-2.

[8] Arnolds SP, Roberts AD, Taylor AD. Rubber friction dependence on roughness and surface energy. 0127-7065 1987.

[9] Roberts AD. A Guide to Estimating the Friction of Rubber. Rubber Chemistry and Technology 1992;65(3):673–86. https://doi.org/10.5254/1.3538633.

[10] Maegawa S, Nakano K. Mechanism of stick-slip associated with Schallamach waves. Wear 2010;268(7-8):924–30. https://doi.org/10.1016/j.wear.2009.12.018.

[11] Robbins MO, Thompson PA. Critical velocity of stick-slip motion. Science 1991;253(5022):916. https://doi.org/10.1126/science.253.5022.916.

[12] Yoshizawa H, McGuiggan P, Israelachvili J. Identification of a second dynamic state during stick-slip motion. Science 1993;259(5099):1305–8. https://doi.org/10.1126/science.259.5099.1305.

[13] Berman AD, Ducker WA, Israelachvili JN. Origin and Characterization of Different Stick−Slip Friction Mechanisms †. Langmuir 1996;12(19):4559–63. https://doi.org/10.1021/la950896z.

[14] Dahmen, Sethna. Hysteresis, avalanches, and disorder-induced critical scaling: A renormalization-group approach. Phys. Rev. B 1996;53(22):14872–905. https://doi.org/10.1103/PhysRevB.53.14872.

[15] Ovcharenko A, Halperin G, Etsion I. In situ and real-time optical investigation of junction growth in spherical elastic–plastic contact. Wear 2008;264(11-12):1043–50. https://doi.org/10.1016/j.wear.2007.08.009.

[16] Chromik RR, Strauss HW, Scharf TW. Materials Phenomena Revealed by In Situ Tribometry. JOM 2012;64(1):35–43. https://doi.org/10.1007/s11837-011-0229-5.

[17] Kim J, Dunn AC. Soft hydrated sliding interfaces as complex fluids. Soft Matter 2016;12(31):6536–46. https://doi.org/10.1039/c6sm00623j.

[18] Grün F, Sailer W, Gódor I. Visualization of the processes taking place in the contact zone with in-situ tribometry. Tribology International 2012;48:44–53. https://doi.org/10.1016/j.triboint.2011.03.026.

[19] Yamaguchi T, Sawae Y, Rubinstein SM. Effects of loading angles on stick–slip dynamics of soft sliders. Extreme Mechanics Letters 2016;9:331–5. https://doi.org/10.1016/j.eml.2016.09.008.

[20] Eguchi M, Shibamiya T, Yamamoto T. Measurement of real contact area and analysis of stick/slip region. Tribology International 2009;42(11-12):1781–91. https://doi.org/10.1016/j.triboint.2009.04.046.

[21] Schulze KD, Bennett AI, Marshall S, Rowe KG, Dunn AC. Real Area of Contact in a Soft Transparent Interface by Particle Exclusion Microscopy. J. Tribol 2016;138(4):41404. https://doi.org/10.1115/1.4032822.

[22] Krick BA, Vail JR, Persson BNJ, Sawyer WG. Optical In Situ Micro Tribometer for Analysis of Real Contact Area for Contact Mechanics, Adhesion, and Sliding

Experiments. Tribol Lett 2012;45(1):185–94. https://doi.org/10.1007/s11249-011-9870-y.

[23] Otsu N. A Threshold Selection Method from Gray-Level Histograms. IEEE Trans. Syst., Man, Cybern. 1979;9(1):62–6. https://doi.org/10.1109/TSMC.1979.4310076.

[24] Sills S, Vorvolakos K, Chaudhury MK, Overney RM. Molecular Origins of Elastomeric Friction. In: Gnecco E, Meyer E, editors. Fundamentals of friction and wear. Berlin, New York: Springer; 2007, p. 659–676.

[25] Liu J, Jiang H, Cheng Q, Wang C. Investigation of nano-scale scratch and stick-slip behaviors of polycarbonate using atomic force microscopy. Tribology International 2018;125:59–65. https://doi.org/10.1016/j.triboint.2018.04.024.

[26] Degrange J-M, Thomine M, Kapsa P, Pelletier JM, Chazeau L, Vigier G et al. Influence of viscoelasticity on the tribological behaviour of carbon black filled nitrile rubber (NBR) for lip seal application. Wear 2005;259(1-6):684–92. https://doi.org/10.1016/j.wear.2005.02.110.

[27] Çolak A, Wormeester H, Zandvliet HJW, Poelsema B. The influence of instrumental parameters on the adhesion force in a flat-on-flat contact geometry. Applied Surface Science 2014;308:106–12. https://doi.org/10.1016 /j.apsusc.2014.04.118.

[28] Cai S, Bhushan B. Meniscus and viscous forces during separation of hydrophilic and hydrophobic surfaces with liquid-mediated contacts. Materials Science and Engineering: R: Reports 2008;61(1-6):78–106. https://doi.org/10.1016/j.mser.2007.03.003.

[29] Persson BNJ, Volokitin AI. Rubber friction on smooth surfaces. Eur Phys J E Soft Matter 2006;21(1):69–80. https://doi.org/10.1140/epje/i2006-10045-9.

[30] Fukahori Y, Gabriel P, Busfield JJC. How does rubber truly slide between Schallamach waves and stick–slip motion? Wear 2010;269(11-12):854–66. https://doi.org/10.1016/j.wear.2010.08.016.

[31] Matsuda K, Hashimoto D, Nakamura K. Real contact area and friction property of rubber with two-dimensional regular wavy surface. Tribology International 2016;93: 523–9. https://doi.org/10.1016/j.triboint.2014.11.011.

[32] Tabor D. Friction—The Present State of Our Understanding. J. Tribol 1981;103 (2):169. https://doi.org/10.1115/1.3251622.

[33] Maegawa S, Itoigawa F, Nakamura T. Dynamics in sliding friction of soft adhesive elastomer: Schallamach waves as a stress-relaxation mechanism. Tribology International 2016;96:23–30. https://doi.org/10.1016/j.triboint.2015.11.034.

[34] Bowden FP, Tabor D. The friction and lubrication of solids. Oxford, New York: Clarendon Press; Oxford University Press; 2001, 1954.

[35] Maegawa S, Nakano K. Dynamic Behaviors of Contact Surfaces in the Sliding Friction of a Soft Material. JAMDSM 2007;1(4):553–61. https://doi.org/10.1299 /jamdsm.1.553.

[36] Deladi EL, Rooij MB de, Schipper DJ. Modelling of static friction in rubber–metal contact. Tribology International 2007;40(4):588–94. https://doi.org/10.1016/j. triboint.2005.11.007.

[37] Rubinstein SM, Cohen G, Fineberg J. Visualizing stick–slip: experimental observations of processes governing the nucleation of frictional sliding. J. Phys. D: Appl. Phys. 2009;42(21):214016. https://doi.org/10.1088/0022-3727/42/21/ 214016.

[38] Davis CS, Martina D, Creton C, Lindner A, Crosby AJ. Enhanced adhesion of elastic materials to small-scale wrinkles. Langmuir 2012;28(42):14899–908. https://doi.org/10.1021/la302314z.

[39] Bennewitz R, David J, Lannoy C-F de, Drevniok B, Hubbard-Davis P, Miura T et al. Dynamic strain measurements in a sliding microstructured contact. J Phys Condens Matter 2008;20(1):15004. https://doi.org/10.1088/0953-8984/20/01/ 015004.

Supplementary Materials for "Precise correlation of contact area and forces in the unstable friction between a rough fluoroelastomer surface and borosilicate glass"

S.1 Details of CNN training for contact area partioning

The CNN takes as input greyscale images resized to 240 × 240 pixels and outputs a two-dimensional vector corresponding to the relative x-, y- coordinates of the predicted centre of the stick region.

The network consists of six convolutional layers, the first having a kernel size of 5 × 5, the other having a kernel size of 3 × 3. The number of feature maps of the convolutional layers are as follows: 1 (input, greyscale) - 4 - 4 - 8 - 8 - 8 - 4. All convolutional layers are equipped with the ReLu (Rectified Linear Unit) activation function, and the first five convolutional layers are each followed by a 2 × 2 max-pooling layer. After the final (sixth) convolutional layer, there is a fully connected layer of size (196 -> 64) equipped with the ReLu activation, followed by the final fully connected layer of size (64 -> 2) equipped with the Sigmoid activation function.

The network was trained over 45 epochs using the Adam Optimizer, minimizing the Mean Squared Error Loss. A batch size of 16 and a learning rate of 0.0005 was used.

Paper 5: The Potential of Tribological Application of DLC/MoS₂ Coated Sealing Materials

C. Wang[1], A. Hausberger[1], P. Nothdurft[2], J. M. Lackner[3], and T. Schwarz[4]

[1] Polymer Competence Center Leoben GmbH,8700 Leoben, Austria

[2] Chair of Chemistry of Polymeric Materials, Montanuniversität Leoben, Leoben, Austria

[3] Institute of Surface Technologies and Photonics, Joanneum Research Forschungsgesellschaft mbH, Niklasdorf, Austria

[4] SKF Sealing Solutions Austria GmbH, 8750 Judenburg, Austria

Authors and relevant contributions to this publication:

- C. Wang: Experimental testing, data evaluation, preparation of the publication
- A. Hausberger: Conceptualization, discussion of experimental data, review the publication
- P. Nothdurft   Chemical characterization
- J. M. Lackner: Conceptualization, coating preparation, surface characterization, review the publication
- T. Schwarz: Specimen production, Review the publication

The Potential of Tribological Application of DLC/MoS₂ Coated Sealing Materials

Chao Wang [1],* [ID], Andreas Hausberger [1], Philipp Nothdurft [2], Jürgen Markus Lackner [3] and Thomas Schwarz [4]

[1] Polymer Competence Center Leoben GmbH, Roseggerstraße 12, 8700 Leoben, Austria; andreas.hausberger@pccl.at

[2] Chair of Chemistry of Polymeric Materials, Montanuniversität Leoben, 8700 Leoben, Austria; philipp.nothdurft@unileoben.ac.at

[3] Institute of Surface Technologies and Photonics, Joanneum Research Forschungsgesellschaft mbH, 8712 Niklasdorf, Austria; juergen.lackner@joanneum.at

[4] SKF Sealing Solutions Austria GmbH, 8750 Judenburg, Austria; Thomas.Schwarz@skf.com

* Correspondence: chao.wang@pccl.at; Tel.: +43-3842-42962-85

Abstract: The potential of the combination of hard and soft coating on elastomers was investigated. Diamond-like carbon (DLC), molybdenum disulfide (MoS₂) and composite coatings of these two materials with various DLC/MoS₂ ratios were deposited on four elastomeric substrates by means of the magnetron sputtering method. The microstructures, surface energy of the coatings, and substrates were characterized by scanning electron microscopy (SEM) and contact angle, respectively. The chemical composition was identified by X-ray Photoelectron Spectroscopy (XPS). A ball on disc configuration was used as the model test, which was performed under dry and lubricated conditions. Based on the results from the model tests, the best coating was selected for each substrate and subsequently verified in component-like test. There is not one coating that is optimal for all substrates. Many factors can affect the coatings performance. The topography and the rigidity of the substrates are the key factors. However, the adhesion between coatings and substrates, and also the coating processes, can impact significantly on the coatings performance.

Keywords: DLC; MoS₂; coating; elastomer; seals

1. Introduction

Coating is one of the approaches that can improve the tribological properties economically. In recent years, the development of the coating methods has opened up new possibilities to enhance the surface properties. Coatings can be generally divided into "soft coatings" and "hard coatings" [1]. Soft coatings, including soft metal (e.g., lead, indium) and lamellar solids (e.g., graphite and molybdenum disulfide (MoS₂)), provide good shearing characteristics and thus result in a reduction of friction. Hard coatings (e.g., diamond-like carbon (DLC), titanium nitride (TiN)) can improve protection against wear and present low wear rates.

The unique properties of elastomers, such as low modulus of elasticity, high Poisson's ratio, and high degree of resilience with low hysteresis, make elastomers very suitable for the application as seals. However, high and erratic friction under dry and starved lubrication conditions could increase the friction and wear rates. As a consequence of surface damage, the lifetime of seals can be shortened greatly [2]. An approach to reduce the friction under dry and starved lubrication conditions is to deposit DLC on rubber. A lot of studies, from deposition techniques to DLC composition on various rubber materials, such as nitrile butadiene rubber (NBR), hydrogenated nitrile butadiene rubber (HNBR),

fluoroelastomer (FKM), and ethylene propylene diene monomer rubber (EPDM), has been done by a Japanese group of Nakahigashi [3,4], Takikawa et al. [5–7], a Dutch group of Pei and Bui et al. [8–12], and other researchers [13,14]. MoS_2 as a solid lubricant is mostly employed with hard surfaces (e.g., metals, ceramics) [15–17]. As to the combination of the two coatings, Wang et al. [18] has deposited MoS_2 on Steels with a supporting DLC film and it showed the MoS_2/DLC compound film reduced the friction force in humid environment. Recently, Zhao et al. [19] has deposited the MoS_2/DLC multilayer coatings on Si wafer and steel in high humidity for aerospace industries and it showed a moderate improvement of the tribological properties. The influence of space irradiation on MoS_2/DLC composite film on Si and steel was investigated by Wu et al. [20]. It showed a reduction of the wear rate after irradiation, which could be related to the increase of hardness. Noshiro et al. [21] has studied the friction properties of sulfide/DLC coating with a nanocomposite or –layered structure on Si wafer, which shows better tribological properties than DLC film. Previous work has focused only on either the composite MoS_2/DLC coating on metals or DLC and MoS_2 separately as coating on elastomers. Therefore, more work is needed to investigate the potential of application of composite coatings on elastomers.

In this research, the tribological properties of DLC, MoS_2, and combined coatings of MoS_2 and DLC were investigated on four elastomers. Coated elastomers were tested in model tests and after that the results were verified in component-like tests. The influence factors of tribological behaviors are discussed. The aim of this study is to investigate the potential of tribological application of composite coatings of MoS_2 and DLC on elastomeric substrates for industrial seals, especially under starved lubrication conditions. In addition, the study provides a guideline to evaluate the coatings.

2. Experimental Details

2.1. Test Materials and Coatings

Four classical sealing materials were tested; i.e., fluoroelastomer (FKM), nitrile butadiene rubber (NBR), hydrogenated nitrile butadiene rubber (HNBR), and thermoplastic polyurethane (TPU). Among these four elastomers, FKM is the softest material, having a shore—a hardness of 84; followed by NBR (85) and HNBR (86). Due to its special chemical composition, TPU is the hardest material with a shore—A hardness of 95. For ball on disc tests, the samples were 20 mm × 20 mm square rubber sheets with a thickness of 2 mm, which were produced by the compression molding process. However, slight differences could be found on the surface under the microscope among TPU, HNBR, and FKM. For TPU a totally different molding die was used and the surface was polished. This is explained in more detail in Section 3.1.1 (microscopic analysis). For ring on disc tests, special samples were used, which are structurally similar to seals [22]. In order to remove contamination on the substrate and also inside the rubber (e.g., plasticizers [23]), all of the samples were cleaned using the standard cleaning procedures [9]. The difference between set and actual values can be explained with sputtering duration (Table 1). As a result of about three times longer sputtering duration time of the DLC 300 nm than the DLC 150 nm, the actual thickness of the DLC 300 nm is over three times thicker. The thickness of MoS_2 coating is proportional to the sputtering time. The thickness varied due to the influence of different sputtering parameters.

Table 2 shows the material and thickness of the investigated coatings. Five different materials (i.e., DLC, MoS_2, and three hybrid combinations of DLC and MoS_2 with various proportions) were deposited as coatings on the substrates. These two materials were not combined as multilayers, but rather in a composite. The proportion of MoS_2 in the composite increases from Hybrid_A to Hybrid_C. Based on our previous work, the set value of 300 nm was selected as the standard thickness for the coatings and the set values of the thickness were defined based on the deposition rate [24]. In order to investigate the influence of the thickness on the tribological properties, 150 nm thick coatings were also obtained through controlling the deposition process time. In order to measure the thickness, several samples were partially covered with tapes during the coating process. After removing the

tapes, the thickness was measured with a contact stylus profilometry (Dektak 150 surface profiler, Veeco, Plainview, NY, USA).

In order to improve the adhesion of the coatings, prior to deposition a pre-treatment process was carried out by using a high vacuum experimentation bell jar system (Leybold Univex 450, Leybold Vacuum GmbH, Cologne, Germany) [25,26]. Substrates were fixed on the rotary table (φ = 560 mm) with a distance of 12 mm to the target.

The cylindrical pulsed laser deposition (PLD) evaporator was used as a target. The pre-treatment was performed at 3 kV DC acceleration voltage with 15 sccm Ar and 5 sccm O_2 gas flow. The chamber pressure was around 8.8×10^{-4} mbar. After pre-treatment, the coatings were deposited by means of the pulsed DC magnetron sputtering method. A graphite target (electrographite, 99.5% purity) was used as a sputtering source for DLC coatings. For MoS_2 its purity is 99.5%. Both targets were purchased from Sindlhauser Material GmbH (Kempten, Germany).

The parameters of the pre-treatment and deposition process are shown in Table 1. For pure DLC film, the ratio of C_2H_2/Ar was 0.19, due to the existence of C_2H_2, a-c: H film was generated [27,28]. For the hybrid coatings, only Ar was used as a source gas [28]. For the hybrid coatings, graphite and MoS_2 were ejected individually from two sputtering sources. Different hybrid variants were generated by varying sputter power. Remarkably, differences of the micro-structures can be observed on the coating when the substrates were deposited at different temperatures [29]. To avoid the thermal influences on substrates and coating processes, the pre-treatment and deposition processes were performed under constant ambient temperature (23 °C). However, due to plasma flow the temperature of the sample surface can increase up to 40 °C. After the deposition process, the samples were stored in Petri dishes in a box.

An optical microscope (Stereo Microscope SZX 12, Olympus, Tokyo, Japan) was employed to analyze the wear scars of the counterparts. The surface roughness was measured in three different regions of each sample with a three-dimensional focus variation microscope (InfiniteFocus, Alicona, Graz, Austria). The surface morphology and wear tracks of coated rubber were characterized with a scanning electron microscope (SEM, VEGA-II, TESCAN, Brno, Czech Republic).

In order to characterize the chemical composition of the coatings, X-ray photoelectron spectroscopy (XPS) analysis were carried out using a Thermo Scientific spectrometer with a micro-focused monochromatic Al Kα source (1486.6 eV, Thermo Fisher Scientific Inc., Waltham, MA, USA). All measurements were conducted with the radiation source operated at 12 kV and a beam current of 1.16 mA in a high vacuum below 10^{-7} mbar. A hemispherical analyzer was applied to detect the accelerated electrons. The electrons were collected from a spot area of 300 μm, which is vertical to the analyzer. To prevent charging and electron charge compensation of the samples, a flood gun was used.

Survey scans were acquired within an energy range of 0–1350 eV using a pass energy of 200 eV, a step size of 1.0 eV, a dwell time of 50 ms, and 2 scans. High resolution scans were obtained using a 50 eV pass energy, 0.1 eV step size, a dwell time of 50 ms, and 8 scans. For C 1s, Mo 3d and S 2p, binding energy ranges and total number of energy steps are as follows: 279–298 eV, 181 steps; 222–240 eV, 181 steps; 157–170 eV, 181 steps; respectively.

The spectra were referenced to the alkyl C 1s photoelectron peak at 284.8 eV, characteristic of the alkyl moieties (C–C/C–H). Peak positions for qualitative analysis are consistent with the corresponding assignment positions found in literature [30].

Spectra were analyzed using the Thermo Avantage software (Version 5932). The ratio of Lorentzian/Gaussian is 0.3. A standard Shirley background is used for the reference samples spectra. The spectra were fitted with Powell algorithm with a convergence of 10^{-6}. The maximum error for peak energy and full width at half maxima (FWHM) is $\pm$0.1 eV. The sensitivity factors (SF) used for calculation are provided by the equipment supplier.

Table 1. Parameters of pre-treatment and deposition process.

Coating	Thickness (nm)	Pre-treatment		Deposition								Frequency (kHz)
		Voltage (V)	Gas flow (sccm)	Sputtering source	Power (W)	Voltage (V)	Current (A)	Gas flow (sccm)	Pressure (mbar)	Rotation (rpm)	Duration (min)	
DLC	300 150	3000	15 Ar + 5 O$_2$ for 5 min, 20 Ar for 25 min	Graphite	3000	577–578 579–582	5.21–5.22 5.22–5.19	42 Ar + 8 C$_2$H$_2$	2.3×10^{-3}	5.00	68 23	80
MoS$_2$	300 150			MoS$_2$	500	462–455 468–461	1.10–1.15 1.10–1.13	50 Ar	2.6×10^{-3}		60 30	
Hybrid_A	300			Graphite + MoS$_2$	C: 3000 MoS$_2$: 54	C: 602–601 MoS$_2$: 270–258	C: 4.95–4.93 MoS$_2$: 0.20–0.19	50 Ar	2.6×10^{-3}		65	
Hybrid_B	300 150				C: 3000 MoS$_2$: 255	C: 604–600 MoS$_2$: 402–403 C: 602–610 MoS$_2$: 405–404	C: 4.98–5.01 MoS$_2$: 0.64–0.66 C: 5.01–4.96 MoS$_2$: 0.65–0.67				54 27	
Hybrid_C	300				C: 3000 MoS$_2$: 440	C: 611–606 MoS$_2$: 467–446	C: 4.95–4.92 MoS$_2$: 0.98–1.04				36	

Table 2. Material and thickness of the coatings.

Material	Thickness (nm)		
	Set Value	Actual Value	Difference
DLC	300	405.0 ± 18.2	35.1%
DLC	150	113.3 ± 5.8	−24.1%
MoS$_2$	300	257.8 ± 19.2	−13.9%
MoS$_2$	150	131.8 ± 7.5	−12.2%
Hybrid_A	300	269.8 ± 14.0	−9.7%
Hybrid_B	300	300.2 ± 8.4	0.4%
	150	116.8 ± 6.0	−22.5%
Hybrid_C	300	246.3 ± 9.5	−17.8%

The determination of surface energy was carried out in a self-developed contact angle device. Distilled water and diiodomethane were applied as liquids to determine the polar and dispersive part of the surface energy, respectively. For each measurement, a drop of 2.5 µL volume was used. Each measurement was repeated three times. Owens et al. [31], Rabel [32] and Kaelble [33] method was applied for calculating the surface energy.

2.2. Test Procedures

The tribological properties were investigated by means of model tests and component-like tests. The model tests were performed on a micro tribometer with a ball on disc configuration (UMT-2, Bruker, Billerica, MA, USA). The development of the sample geometry for the component-like test was reported by Hausberger [22]. The tests were performed on a precision rotary tribometer (TE-93, Phoenix Tribology Ltd., Kingsclere, UK). Each test was repeated three times. All of the tests were conducted at room temperature (22 °C) with a relative humidity of 50% ± 10%. About one month after the coating process, the tribological tests were performed.

2.2.1. Ball on Disc Tests

Commercial 100Cr6 stainless steel balls of 6 mm diameter (HRC 60–62) were used as counterparts. The counter body slid on the elastomer at 100 mm/s with 1 N normal load. The radii of the run tracks were 5 mm and 7.5 mm. The total length of the tracks was 3.143×10^5 m. In order to obtain a better understanding of the function of the coatings, the tests were performed under dry and lubricated conditions. For the lubricated tests, approximately 7 mg Mobil SHC Grease 460WT (Viscosity of Oil, ASTM D 445 [31] cSt @ 40 °C = 460) was smeared equally over the whole surface [32]. The average thickness of the grease can be calculated. Its amount was chosen so that the thickness of the grease layer was approximately 0.02 mm.

2.2.2. Ring on Disc Tests

Ring-shaped counterparts of 34CrNiMo6 were used in the ring on disc test. They possessed an average roughness (R_a) of 0.035 µm. The ring-like sample was so constructed that there was only a line contact between the sample and counterpart [22]. The tests were conducted with 50 N normal load at room temperature (23 °C) and the speed of revolution was 118 rpm. The aim of this research is to improve the tribological properties of seals under starved lubricated conditions. In order to simulate starved lubrication condition in component-like tests, approximately 2 mg Mobil SHC Grease 460WT was smeared on the contact edge of the samples. For uncoated samples the tests lasted 168 h. For the coated samples, the tests were stopped automatically when the abort condition was reached. The abort condition was set according to the coefficient of friction of the uncoated samples. The principle of the ring on disc test is illustrated in Figure 1.
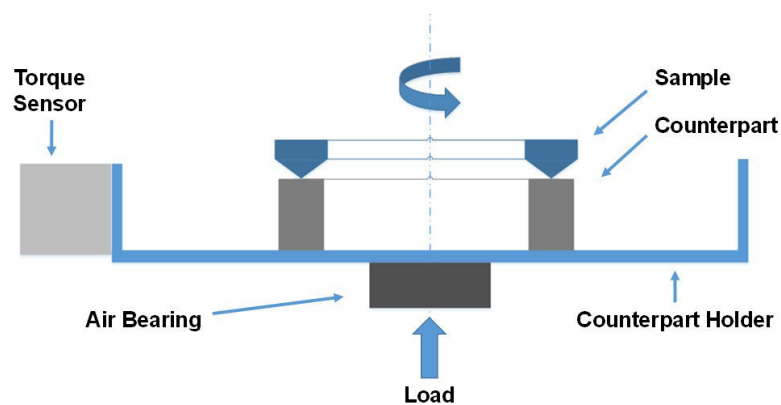

Figure 1. Principle of ring on disc test on TE-93.

The counterpart was fixed on the counterpart holder. The load, which was produced by a pneumatic pump, acted on the sample through the thrust bearing and counterpart. An electric motor was mounted on the top of the machine and drove the sample against the counterpart in a rotational movement. The torque, which was generated through friction, was measured by a torque sensor. Furthermore, the temperature near the contact area and in the middle of the counterpart was also measured during the test.

3. Results and Discussion

3.1. Characteristics of Coatings

After deposition the thickness of coatings was measured. The chemical composition was investigated with XPS measurements. The microstructures of the surfaces were analyzed with roughness and compared among different substrates. Furthermore, the surface energy of the substrates and coatings were identified.

3.1.1. Thickness of the Coatings

For each coating, the thickness was measured at six different positions of the two samples. Table 2 shows the set and actual average thickness. The difference between set and actual values can be explained with sputtering duration (Table 1). As a result of about three times longer sputtering duration time of the DLC 300 nm than the DLC 150 nm, the actual thickness of the DLC 300 nm is over three times thicker. The thickness of the MoS_2 coating is proportional to the sputtering time. The thickness varied due to the influence of different sputtering parameters.

As reported in [7], the application of C_2H_2 accelerates the deposition rate, which leads to a higher thickness than the set value.

3.1.2. Chemical Composition

The chemical composition, the assigned peak energies, full width at half maxima (FWHM), and sensitivity factor (SF) of each peak are given in Table 3 and were obtained with XPS analysis.

Table 3. Spectral fitting parameters.

Elements	Bonds	Peak Energy (eV)	FWHM (eV)	SF Al [34]	Ref.
	C–C/C–H	284.8	1.4		[33]
C 1*s*	C–O	286.0	2.1	1.0	[33]
	–COO	288.4	2.5		[33]
Mo 3*d*	MoS_2	229.0	2.0	5.6	[33,35]
	MoO_3	232.8	1.5		[33,35]
S 2*p*	S^{2-}	162.0	1.4	1.1	[33,36]
	S_2^{2-}	163.6	1.4		[37,38]
S 2*s*	–	226.4	2.2	1.4	[38,39]

In Table 4, the chemical composition of each coating is listed. In order to avoid the influence of the different elastomeric substrates, coatings were deposited on silicon for the XPS analysis.

In both DLC coatings, the portion of C 1*s* is about 90% with no detectable silicon signal corresponding to a homogeneous carbon layer formation. The dominating carbon species are C–C/C–H bonds at 284.8 eV (Figure 2a) which are unambiguous assigned to the atomic structure of the used DLCs. The beneficial properties of DLC in tribology depend mainly on the similar hardness and Young's modulus as diamonds [28,40]. Besides, C–O and –COO signals were also found and are attributed to the surface oxidation during the coating process and storage [41] and is in good agreement with the results obtained in [42].

Table 4. Chemical compositions (C, O, Mo, S, and N) of the coatings.

Sample	Composition (%)							
	C	O	Mo		S	N	MoS$_2$/MoO$_3$	S/Mo
			MoS$_2$	MoO$_3$				
300 nm DLC	90.1	9.9	–	–	–	–	–	–
150 nm DLC	89.5	10.5	–	–	–	–	–	–
300 nm MoS$_2$	22.4	13.6	13.0	3.5	26.5	21.1	3.7	1.6
150 nm MoS$_2$	27.4	15.3	12.1	3.7	24.5	17.0	3.2	1.6
300 nm Hybrid_A	75.2	13.4	1.3	1.3	3.5	5.3	1.0	1.3
300 nm Hybrid_B	60.3	16.5	2.5	2.8	6.7	11.3	0.9	1.3
150 nm Hybrid_B	56.1	17.0	2.5	3.3	6.7	14.5	0.7	1.2
300 nm Hybrid_C	38.4	21.6	2.6	5.7	8.2	23.5	0.5	1.0

In pure MoS$_2$ coatings, the high nitrogen and carbon amounts are attributed to atmospheric contaminations (CO$_2$, hydrocarbons, N$_2$, etc.) during sample transport or storage or manufacturing of the samples. However, the S 2p doublet at 162.0 eV (ΔeV = 1.18) in combination with the doublet at 229.0 eV and 232.1 eV is unambiguous assigned to MoS$_2$ (Figure 1c,d). A second doublet in the Mo 3d spectra is attributed to Mo with environment as in MoO$_3$ [43]. On the subject of oxidation of molybdenum disulfide to molybdenum (VI) oxide, different reports were found [15,44]. In general, the oxidation rate is extremely low at ambient temperature and in the absence of a high concentration of moisture [15]. The oxidized layer at the outmost surface appears to protect the bulk material from further oxidation. However, different oxidation rates at ambient condition were investigated, and it was found the crystallite orientation plays an important role in the oxidation process [45]. Oxidation leads to a higher friction coefficient, enhanced wear rate, and hence a shorter wear life [36,46]. The ratio of MoS$_2$/MoO$_3$ in the reference coatings indicates that oxidation had occurred but the major portion is still MoS$_2$. For the hybrid samples (Figure 2d–f), the amount of MoS$_2$ is increased from Hybrid_A to Hybrid_C. As a result, the ratio of total S/Mo decreases from Hybrid_A (1.3) to Hybrid_C (1.0). The higher the concentration of MoS$_2$, the higher the oxidation rate and as a result the lower the MoS$_2$/MoO$_3$ ratio. It is suggested that the increase of MoS$_2$ amount in the coatings accelerates the oxidation rate and is highest for the Hybrid_C sample.

The S 2p spectrum appears as two overlapping doublets. This means, different types of sulfur ligands, such as bridging terminal S$_2^{2-}$, and bridging S^{2-} species exist in the coating [37]. In addition, our results were in agreement with Benoist et al. observations as a higher oxygen content lead to a decrease in the S^{2-} sulphur component whereas the S$_2^{2-}$ pair increase [43].
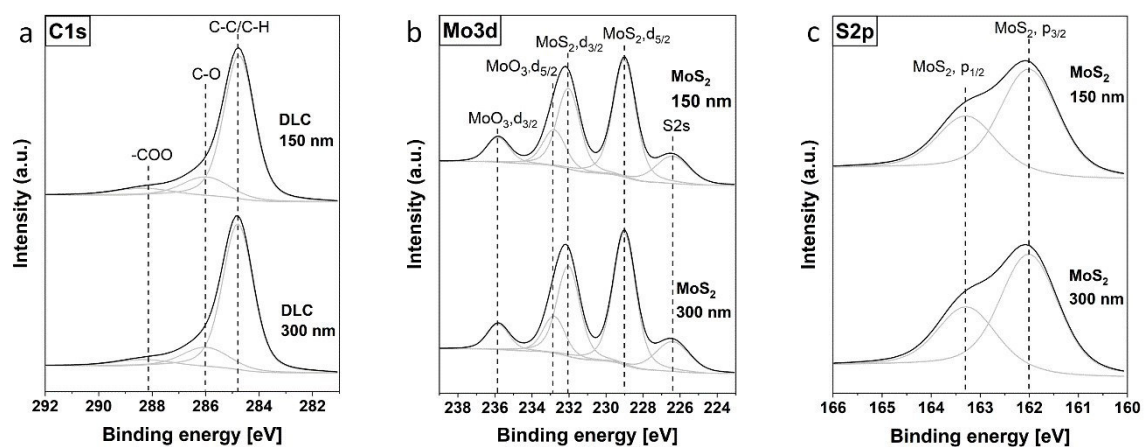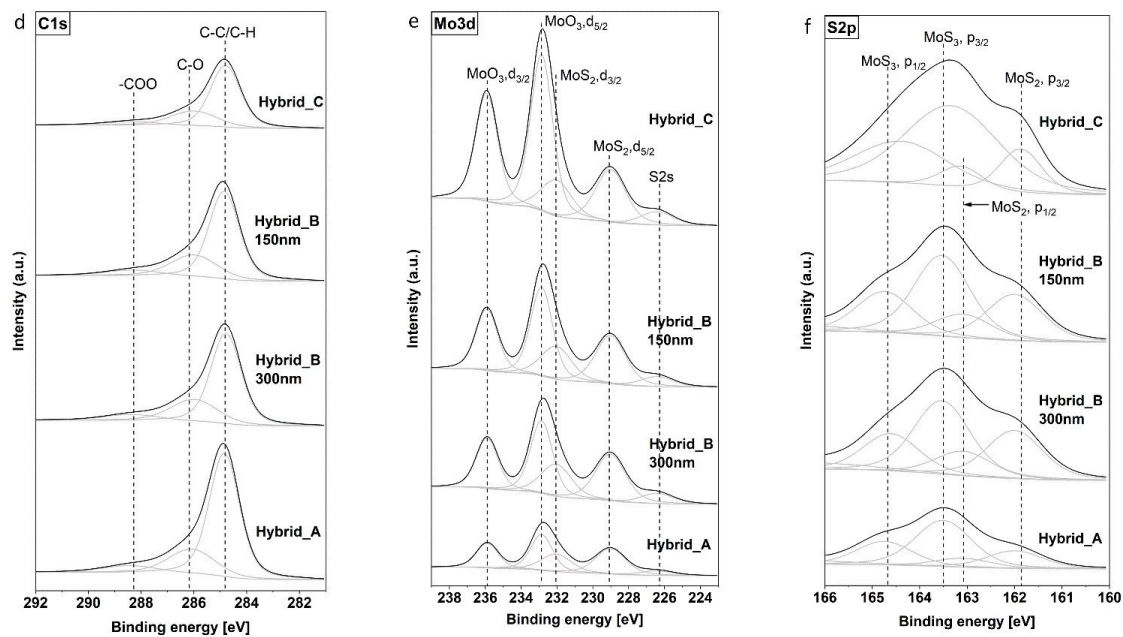

Figure 2. *Cont.*

Figure 2. X-ray photoelectron spectroscopy (XPS) spectra: C 1*s* of diamond-like carbon (DLC) coatings (**a**) and hybrid coatings (**d**); Mo 3*d* of MoS$_2$ coatings (**b**) and hybrid coatings (**e**); S 2*p* of MoS$_2$ coatings (**c**) and hybrid coatings (**f**).

3.1.3. Microscopic Analysis

The uncoated substrates, except HNBR, were analyzed with a microscope and presented in a previous work [24]. Generally, on a macroscopic level the uncoated HNBR, NBR, and FKM possess similar parallel, strip-like structures, whereas TPU presents completely different structures. Due to the different physical properties of elastomers, especially elasticity and viscosity, which can have an effect on the flow properties in the molding process, they behaved differently during the processing [47]. Although uncoated HNBR and FKM show similar macrostructures, on the microscopic level utterly different microstructures can be observed. The surface of uncoated HNBR is relatively smooth but with some small debris. However, the surface of uncoated FKM is much rougher and with dense particles. This can also be explained with R_a and R_z. In spite of the very similar R_a value of uncoated HNBR and FKM, the R_z value of uncoated FKM is more than 30% higher than that of uncoated HNBR (Table 5).

Table 5. The average roughness (R_a), mean roughness depth (R_z) of uncoated samples.

Parameter	FKM	HNBR	NBR	TPU
R_a (μm)	1.00	1.03	0.61	0.44
R_z (μm)	6.74	5.59	3.69	3.98

The surface of uncoated TPU was full of small strips. However, the strips were not as neatly arranged as those of HNBR and FKM. Also, compared to HNBR and FKM, the strips on TPU were much narrower and shallower. Another difference, which must be mentioned, is that, except for the strips, there were almost no small debris or particles on uncoated TPU.

In this section, for each substrate two coatings have been chosen and discussed. The two coatings were so chosen that, regarding the substrate, one of them showed the best tribological performance and the other showed the worst in the dry and lubricated ball on disc tests. In addition, one thin coating for HNBR was chosen to analyze the influence of the thickness.

The strip-like structures on the surface, which can be observed in Figure 3a, were produced because of the compression molding process. Not only can these structures be found in HNBR, but also in FKM and NBR. Figure 3c shows one other position from the same sample as Figure 3a. Not like the rough surface in Figure 3b, flake-like structures with small debris can be observed in Figure 3d. Moreover, cracks can be observed on the surface. As reported by Takikawa and Pei, cracks are typical surface structures of DLC coated rubber [5,12,29].
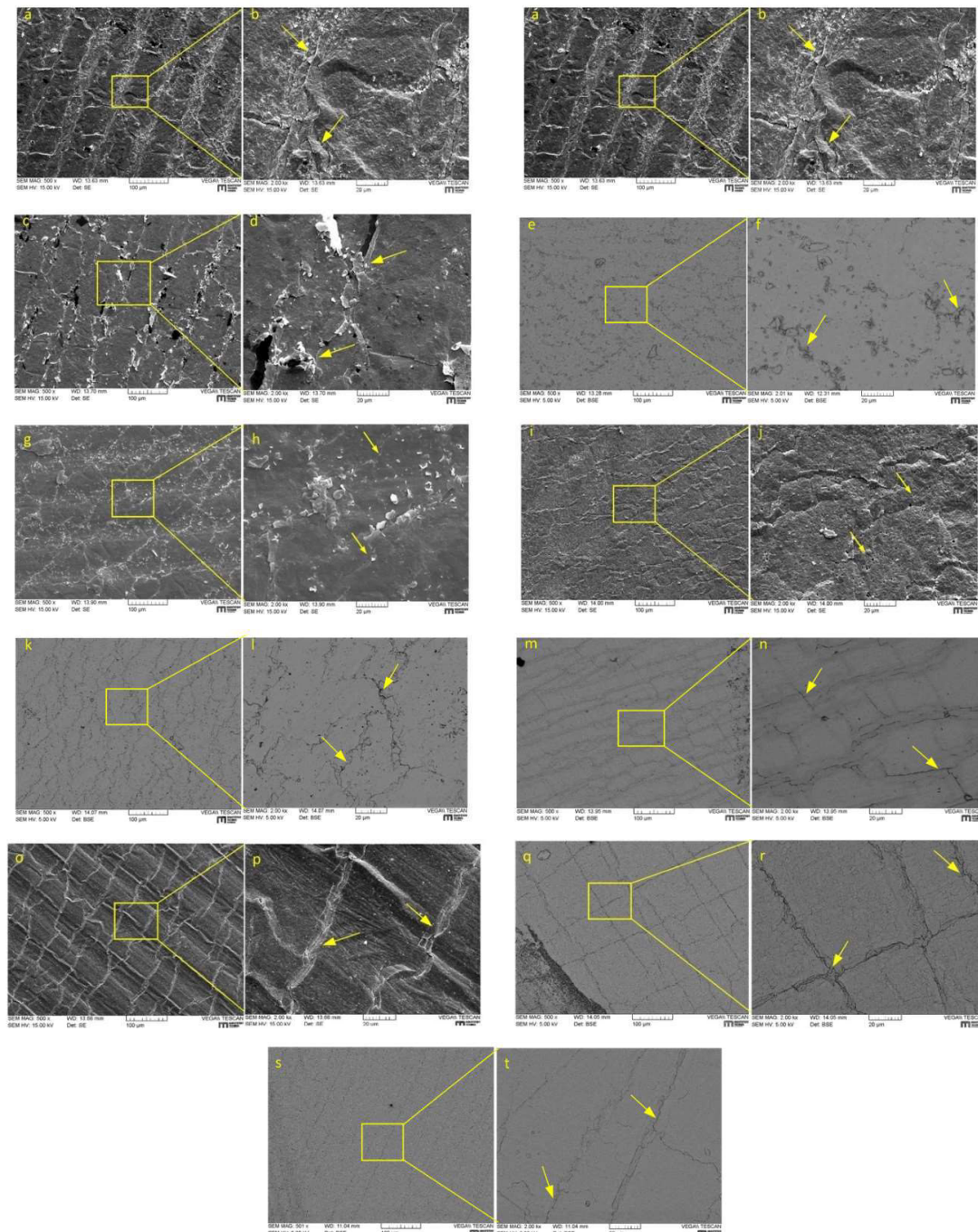
Figure 3. With 300 nm (**a**,**c**) and 150 nm DLC (**e**) coated hydrogenated nitrile butadiene rubber (HNBR); with 300 nm Hybrid_A coated HNBR (**g**), fluoroelastomer (FKM), (**i**) and nitrile butadiene rubber (NBR) (**o**); with 300 nm MoS$_2$ coated FKM (**k**), NBR (**m**) and thermoplastic polyurethane (TPU) (**s**); with 300 nm DLC coated TPU (**q**). High magnification (**b**,**d**,**f**,**h**,**j**,**n**,**p**,**r**,**s**,**t**) are shown to the right side of the respective low magnification (500×).

Compared with the 300 nm DLC coating, the 150 nm DLC coating looks smoother on the whole. However, small particulates can be observed on the surface (Figure 3f). Figure 3g shows the microstructures of 300 nm Hybrid_A on HNBR. Scaly microstructures were observed and they look similar to the DLC coating to some degree (Figure 3b). As previously mentioned, Hybrid_A is a composite coating, which possesses the least MoS_2 among the three hybrid coatings. However, a small amount of MoS_2 changed the microstructures considerably. The gaps between each piece of debris are smaller and the coating is noticeably smoother. This can be attributed to the much lower hardness of MoS_2 compared to DLC [15,48]. It seems that MoS_2 lowered the average hardness. Therefore, the coating can be better suited to the substrates roughness.

Comparing Figure 3h,j shows that the coating roughness was influenced to some extent by the substrate properties. Moreover, under high magnification, small holes can be identified on FKM with a 300 nm Hybrid_A coating (Figure 3j). That means the coating did not totally adhere to the substrate. This can be caused by the lower wettability of FKM compared to HNBR (details in Section 3.1.5). Small holes can also be observed on MoS_2 coated FKM (Figure 3k). However, the coating from MoS_2 looks much finer and smoother than the hybrid coating.

Generally, the surfaces of coated NBR are smoother compared to coated HNBR. Also, it should be emphasized that almost no debris could be found on the surface after coating. Moreover, as can be observed in Figure 3o, cracks which were caused by the removal of the sample from the deposition chamber, are rather neatly arranged on the surface, either parallel or perpendicular to the original microstructure of the substrate.

For TPU samples, they do not have the strip-like, neatly arranged microstructures like other substrates (Figure 3q,s). Because of its shallower and sparser microstructures, the roughness of the TPU substrate is correspondingly lower. Like the previous comparison, MoS_2 coated TPU is also finer and smoother than the DLC coated TPU (Figure 3s).

From the above comparisons, several influence factors that contribute to the coating microstructures were found and discussed. Firstly, the substrate topography is one of the most important influence factors for the coating microstructure. That is because of the smaller thickness (150–300 nm) compared to the roughness of the substrate (Table 5). Secondly, the composition of the coating plays an important role as well. Generally, on DLC or DLC-included coating small debris can be observed. In comparison with DLC, the MoS_2 coating is finer and smoother. Thirdly, the coating microstructures can be influenced by the material properties of the substrates in several ways. Coatings on a substrate like FKM, which has a lower wettability, show a higher possibility that the coating becomes porous and loose. Thermal properties (e.g., thermal expansion coefficient and thermal conductivity), are also influence factors. As shown in Table 6, FKM expands the most among the four materials, when the temperature increases by a given degree. This can lead to the scaly coating, which can be observed in Figure 3i,k.

Table 6. Thermal parameters of used materials.

Parameter	FKM	HNBR	NBR	TPU
Coefficient of thermal expansion (10^{-6}/K)	191	166	165	160
Thermal conductivity (W/(m·K))	0.24	0.15	0.26	0.06

However, the importance of these factors depends to a large extent on the ambient conditions of the coating process. In addition, the microstructure of the coatings is also affected by the deposition condition. For DLC coating, a-c: H was produced by using a plasma of Ar and C_2H_2, while for other coatings, only Ar was used. Generally, the coatings prepared with C_2H_2 look smoother than those without C_2H_2. This is in good agreement with the results in [7].

3.1.4. Surface Roughness

The surface roughness of the coated samples was affected by the substrate surface and also the microstructures of coatings, which can be changed by removing the samples from the deposition chamber (Figure 3o). In addition, the surface microstructure can also affect the adherence of the coating [49]. Generally, a rougher surface can have a better adhesion with coating because more bonding connections can be created. However, the scale of dimensions of the surface microstructures must be less than the film thickness [50]. As can be seen from Figure 4, uncoated substrates have different degrees of roughness. FKM and HNBR possess a similar roughness ($R_a \approx 1.0$ μm), while TPU and NBR have an appreciably lower roughness value. As mentioned previously, two different molding dies were used to produce samples, one for FKM, NBR, and HNBR, the other one for TPU. Moreover, the surface microstructure can be affected by additives, which could come up on the surface.
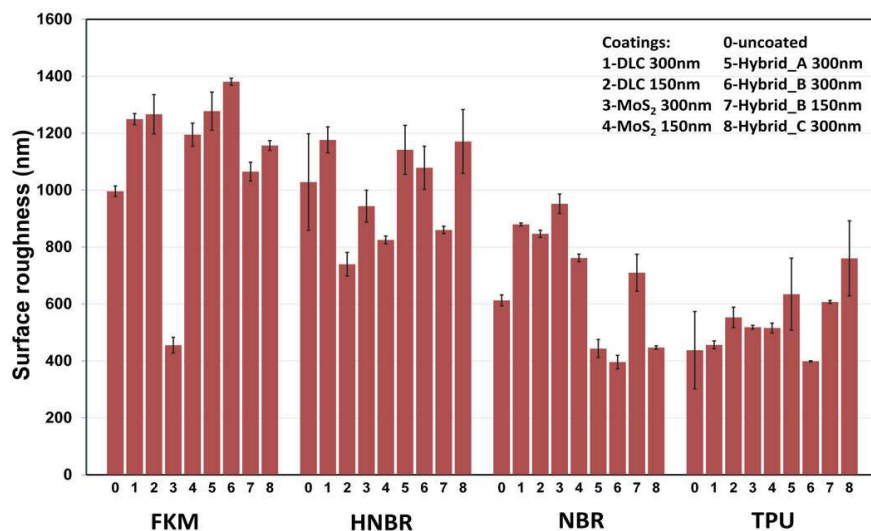

Figure 4. Surface roughness (R_a) of uncoated and coated substrates.

As can be seen from Figure 3a,e, the HNBR with 150 nm DLC is smoother than that with 300 nm DLC. However, for the other three materials with DLC coating, the thickness does not play an important role in the surface roughness. Compared to the uncoated FKM, the roughness of 300 nm MoS$_2$ coated FKM was reduced drastically, whereas the roughness of DLC-containing coatings on FKM was increased to varying degrees. This could be attributed to the larger difference between DLC and substrates in hardness and brittleness [48]. The DLC coatings with a very low thickness could be broken into fractures easily, when the coated samples are removed from the deposition chamber with a small deformation. However, this phenomenon was not found on other materials. For hard material TPU, no obvious differences could be identified in roughness. On the one hand, due to its different processing, its surface is smoother than other materials. On the other hand, higher hardness prevents its deformation by removal.

3.1.5. Surface Energy

One of the conditions for good wetting is that the surface tension of the substrate is higher than that of the still liquid coating material [51]. To eliminate the influences of substrates, coatings were also deposited on silicon. As shown in Figure 5, uncoated Si and coated Si possess higher surface energies than the other four substrates. Surface roughness plays an important role for the surface energy [52]. For four elastomeric substrates, surface energies were increased to varying degrees after coating. On the one hand, through comparison of the microstructures before and after deposition, it can be found that it changed significantly. Although the mean roughness (R_a) of the substrates had not been changed in a very large way, the microstructures were totally modified after the coating process. This leads to a

modification of the surface energy. On the other hand, from the perspective of the material, the surface energy of elastomer substrates [53], DLC and MoS_2 are also different. These two factors together affect the difference of the surface energy after coating.

Compared with an uncoated elastomer, silicon shows a much higher surface energy in both polar and dispersed parts. After coating silicon shows a similar surface energy to the elastomers. Generally, FKM has almost the lowest surface energy in all coatings. Except for the influence of its chemical structure, the surface microstructure of uncoated FKM is different from HNBR and NBR. Comparing to HNBR, which has a similar mean roughness (R_a), FKM is much rougher and dense particles can be seen on the surface [24]. The film thickness has only a limited effect on surface energy.
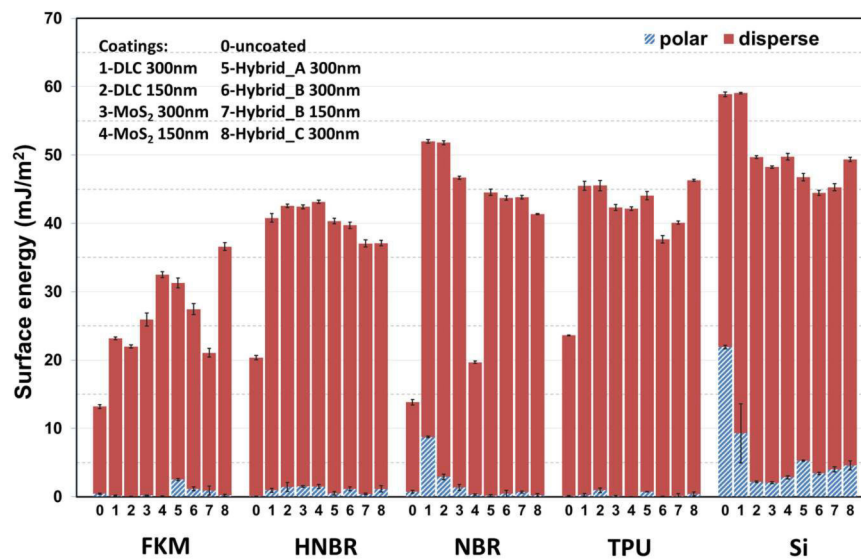

Figure 5. Surface energy of uncoated and coated substrates.

3.2. Tribological Tests

In order to study the potential of DLC/MoS_2 coatings on elastomers for tribological applications, the coatings were firstly tested in the model test under dry and lubricated conditions, so that the coatings could be evaluated comprehensively. Subsequently, the best and worst coatings were selected and investigated under starved lubrication condition in component-like tests.

3.2.1. Coefficient of Friction

The coefficients of friction (COF) for uncoated and coated elastomers in dry and lubricated ball on disc sliding tests are shown in Figure 6. Under dry sliding ambient conditions, almost all of the coatings bring an advantage to the tribological properties. In particular for HNBR, with 300 nm DLC coating, the COF was reduced from 0.99 to 0.18 by 82%. For NBR the frictional reduction, which the 300 nm DLC or Hybrid_A coating brought, was also significant; approximately 74%. For FKM and TPU, the decrease was not so appreciable. What was interesting was that for TPU the COF was slightly brought down by 300 nm Hybrid_B coating. The values of these measurements are in good agreement with the values reported in the literature [3,12,54]. However, when the thickness of the coating was reduced to 150 nm, the COF increased by 11%, compared to the uncoated TPU. This can be explained by microscopic analysis. As can be observed in Figure 7, the 150 nm coating was already severely damaged (Figure 7b) and the elastomeric substrate had direct contact with the counterpart during the test, while the thick variant was still intact (Figure 7a). That means for this coating, the thickness plays an essential role with respect to the tribological properties. However, the thickness cannot bring a significant difference in every case. That depends on several factors, for example, the hardness of the substrate, the coating material, and the adherence of coating material on the counterpart, the

microstructures of the surface, the adherence between coating and substrate, lubrication conditions and so on. Adhesion and deformation are the two most important mechanisms that are responsible for the frictional behaviors of elastomers [55,56]. The high friction of uncoated HNBR and NBR under dry conditions show that not only deformation, which can be related to the relatively low hardness, but also adhesion, which can be seen as a dissipative stick-slip process on molecular level, are influential factors for the dry frictional behaviors [57–60]. This is in good agreement with Rabinowicz's studies, which indicated that low ratios of surface energy/hardness are associated with better surface interactions and also less adhesion [61,62]. Moreover, because of the high friction more dynamic energy would be expected to be transformed into heat, which could lead to an increase of temperature. Based on this conjecture the material's hardness will reduce with a higher temperature so that it could experience a higher wear rate [63].
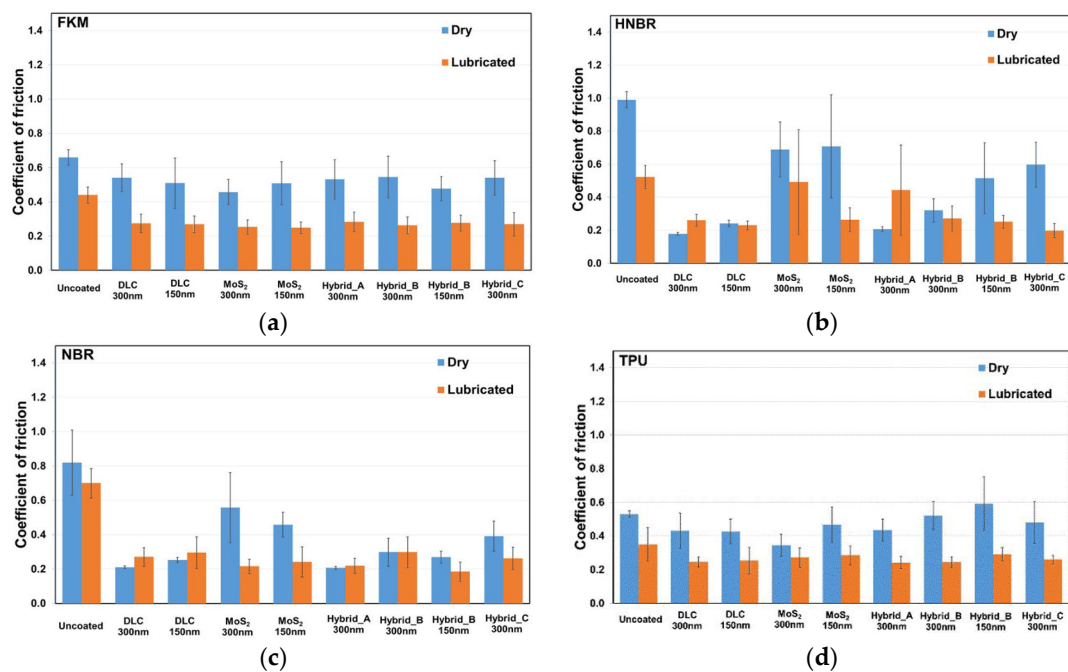

Figure 6. Coefficient of friction of uncoated and coated elastomers in dry and lubricated ball on disc sliding tests: (**a**) FKM; (**b**) HNBR; (**c**) NBR; (**d**) TPU.
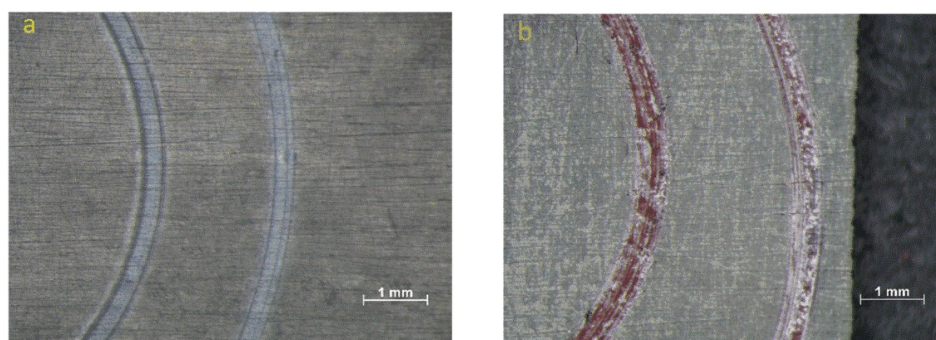

Figure 7. Microscopic images of wear tracks: (**a**) 300 nm Hybrid_B coated TPU; (**b**) 150 nm Hybrid_B coated TPU.

Under lubricated conditions, the differences of COF among various coatings were not as evident as in dry tests. The lubricant has no significant impact on the COF. One reason for this is that lubricants facilitate the stick-slip process on the molecular level to some extent. Therefore, the adhesion part for

friction can be decreased [64]. As to the deformation part, it was assumed to stay on a similar level as under dry conditions in two aspects. One aspect is that the lubricant film is very thin on the contact area hence the stiffness of the film is negligible. The other aspect is that the COF of various coatings is similar.

It should be noted that in some cases the lubricant even brought a slight, negative impact on the tribological properties for DLC coated HNBR and NBR. This can be explained with two main reasons. One important aspect is that because of the high viscosity of the grease used, more energy would be needed to overcome the fluid friction [64,65]. The COF under dry conditions was extremely low. In this case, the benefit of the lubricant was less than its disadvantage. That means more energy was needed to overcome the resistance, which was brought by the lubricant.

Based on the results of the ball on disc tests under dry and lubricated conditions, the best coatings were chosen and verified in the component-like test (ring on disc). For FKM with Hybrid_A coating, its dry COF is slightly lower (2.5%) than Hybrid_B 300 nm. However, its lubricated COF is about 13% higher than Hybrid_B 300 nm. For HNBR with Hybrid_A coating, it is clear that MoS_2 brings a negative effect for the tribological performance. In the dry tests, the coatings with pure MoS_2 or high content of MoS_2 (Hybrid_B and Hybrid_C) were broken after the tests. Therefore, these coatings were not taken into consideration for the selection. In addition, as references, uncoated substrate and the worst coatings were also tested. The best and worst coatings are presented in Table 7. As can be seen from this table, the soft coating MoS_2 provides the best tribological properties for the softest material FKM, whereas the hard coating DLC is the best choice for the hardest material HNBR, only among FKM, NBR, and HNBR. For NBR, which has a middle hardness, a hybrid coating is better than other coatings. Because of its totally different surface structures, TPU was not comparable with the other elastomers.

Table 7. The best and worst coating for each material from ball on disc tests.

Material	Best Coating	Worst Coating
FKM	300 nm MoS_2	300 nm Hybrid_A
NBR	300 nm Hybrid_A	300 nm MoS_2
HNBR	300 nm DLC	300 nm Hybrid_A
TPU	300 nm MoS_2	300 nm DLC

For the ring on disc tests an abort condition was set up so that when the coating was worn or damaged, the test would be stopped immediately. As abort condition, an average COF of the uncoated substrate under stable running conditions was employed. As shown in Figure 8, at the beginning of the tests, for HNBR and TPU the COF of the best and worst coatings were almost at the same level. However, the COF of the uncoated substrate kept at a constant level after the running-in phase with a higher value, while the COF of the worst coating started to increase gradually. After just several hours, the friction was raised to the same level as the uncoated substrate. Compared to the worst coating, the best variant lasted significantly longer until the COF reached the abort condition. This means that the coating failed with increasing test time. Therefore, for HNBR, NBR, and TPU the trends of validation show a good correspondence with the results from the ball on disc tests. However, for FKM with the best coating, after the loading phase, its COF was already slightly over the abort condition, which represents the COF of uncoated FKM. It was found that the coating was already damaged. This implies that the combination of soft coatings like MoS_2 and soft substrate like FKM is inappropriate for this line contact. Because of its low hardness, FKM showed a strong local deformation under line contact. According to Archard's wear law for adhesive wear [66], wear volume is inversely proportional to the hardness of a substrate. By this situation, in which the contact area is relatively small, the soft coating on a soft substrate could be worn quickly.
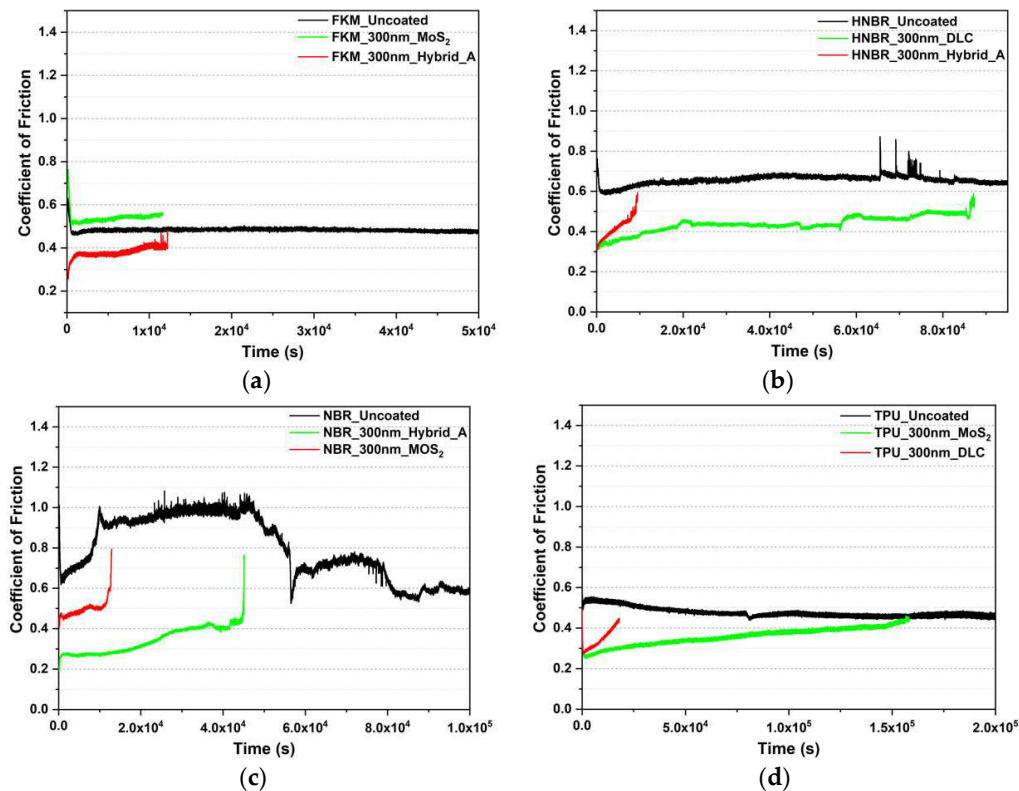
Figure 8. Comparison of the COF: uncoated and coated in Ring on disc test. (**a**) FKM; (**b**) HNBR; (**c**) NBR; (**d**) TPU.

3.2.2. Wear

The SEM images (Figure 9) show the wear track of the 300 nm DLC coated HNBR after a dry ball on disc test. It is evident that in the majority of the run area, the surface got smoother. The DLC coating was slightly pressed down due to the normal load and the microstructures were plastically deformed because of the tangential traction, which was generated by the sliding motion. Some piles of small crystal-like fragments can be found on the run track (Figure 10g). DLC is a very hard material and the thickness of the coating is just 300 nm. That means that when the counter body slid over the surface, both the elastomeric substrate and the coating experienced a deformation. The difference is that the substrate deformed viscoelastically and the coating showed a plastic deformation. Meanwhile, the cracks of the coating can also be ascribed to the enormous difference in hardness between the two materials.

Two positions of the wear track of 300 nm Hybrid_A coated HNBR were shown in Figure 9c,e. Particles can be observed in the troughs, which were located between every two peaks. White particles (Figure 3a,f) can be MoO_3, the oxidation product of MoS_2, which has a negative effect on the performance [15,36]. As shown in Table 4, in hybrid coatings, MoO_3 possesses larger portion than MoS_2. According to [67], when less than 30% of the MoS_2 converted to MoO_3, wear performance is still good. However, when it is greater than 50%, the wear behavior gets poor. As can be seen from Figure 3a,g, a part of the particles were generated during the coating process. Particles were also generated through dynamic motion in crack area. All of these particles were collected during the test in the trough. As can be observed in Figure 9d, some of the particles were pressed on the surface when the ball slid over.

From the same coating and substrate, sheet-like wear particles are visible in Figure 9e,f. This phenomenon can be attributed to surface fatigue [68]. Due to the repeated plastic deformation, sheet-like particles were gradually generated and separated from the coating.
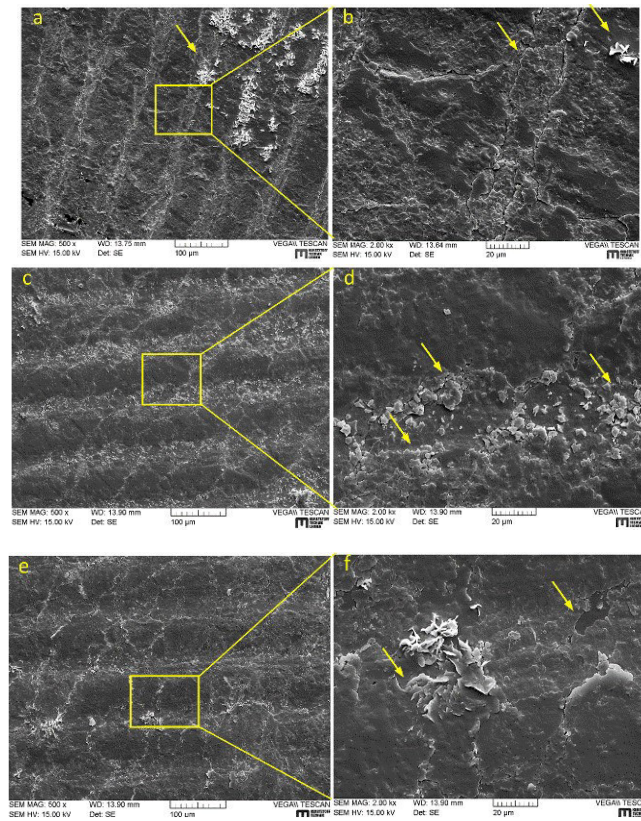
Figure 9. SEM micrographs: wear track of 300 nm DLC coated HNBR (**a**) and 300 nm Hybrid_A coated HNBR (**c**,**e**). Related areas are marked and shown with high magnification (**b**,**d**,**f**).

Compared to the 300 nm Hybrid_A coating on FKM before (Figure 3i) and after (Figure 10a) the test, a great number of cracks was generated during the test. This can be related to the dense particle-like microstructures of uncoated FKM. When the porous and loose coating was pressed by the counter body, it deformed more heavily and easily than other coatings. Besides, due to its lowest hardness among the four elastomers, the deformation of FKM is the largest. These two reasons could explain this phenomenon.
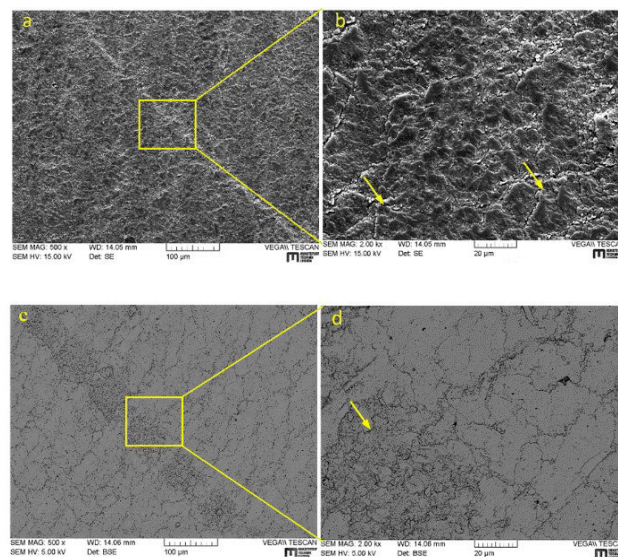

Figure 10. *Cont.*
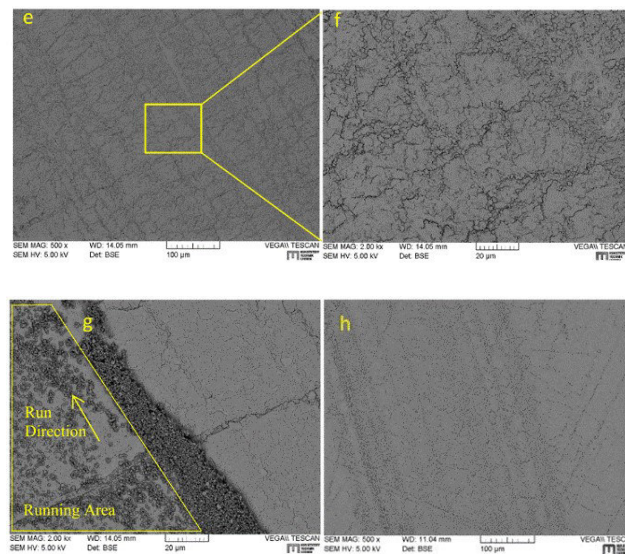
Figure 10. Scanning electron microscope (SEM) micrographs: wear track of 300 nm Hybrid_A coated FKM (**a**), 300 nm MoS$_2$ coated FKM (**c**), 300 nm DLC coated TPU (**e**,**g**), and 300 nm MoS$_2$ coated TPU (**h**). Related areas are marked and shown with high magnification (**b**,**d**,**f**).

Not like the 300 nm Hybrid_A coating, no obvious alteration could be found on the 300 nm MoS$_2$ coating after 10,000 cycles. Only the contact area was pressed and subsequently crushed into small pieces (Figure 10c). This can be attributed to the S–Mo–S sandwich structure of MoS$_2$, which facilitates the sliding motion on its surface [15].

The wear track of 300 nm DLC coated TPU (Figure 10e,f) presented very similar microstructures as MoS$_2$ coated FKM. That means only the DLC coating in the contact area was pressed into small pieces. However, plenty of wear particles, which are around 1 μm, were found close to the edge of the run track (Figure 10g). In some areas, they were piled up together. At the beginning of the test, the DLC coating was pressed into small pieces. However, some of the small particles that were detached from the substrate, rolled down from the sides to the middle of the groove. More and more particles were gathered on the lane with more cycles. At this moment, the particles were pushed out of the lane when the counter body slid over. Still quite a number of particles were found on the track after the test. Apparently, the dynamic movement of these small particles has influenced the tribological behavior to some extent. This can explain why DLC is the best coating for TPU under lubricated conditions but presented worse tribological properties than MoS$_2$ in dry tests. There is a strong possibility that under lubricated conditions the wear particles can be carried out of the track by grease. This is also one of the main functions of a lubricant [69].

Because of its low hardness and good shear characteristics no obvious particles were found on the MoS$_2$ coated TPU. Slight abrasive wear can be observed on the surface (Figure 10h). This is also one of the major wear processes on polymers [70]. Due to its special properties and good adherence on TPU, 300 nm MoS$_2$ shows the best tribological properties in dry tests.

4. Conclusions

The concept of the combination of hard and soft coatings on elastomers has been investigated. In this research, DLC was taken as an example of a hard coating and MoS$_2$ as a soft coating. It was proven that this concept can be used to improve the tribological properties of elastomers, especially under starved lubrication condition. There is not one coating that is optimal for all substrates. For different rubber substrates, the coating should be chosen individually, based on the substrate, coating properties, and their interaction. For a rubber substrate with low rigidity like FKM, soft coatings like MoS$_2$ present better tribological properties than hard coatings like DLC. This is attributed

to the good shear characteristics and good deformation properties of MoS$_2$. Meanwhile, for a substrate with a higher rigidity like HNBR, a hard coating like DLC is a better option. For NBR, whose rigidity is between FKM and HNBR, a hybrid coating is the best choice. It possesses both advantages of hard and soft coatings. For TPU, due to its totally different microstructures, a different wear mechanism was discussed. For a hard substrate with a smooth surface, MoS$_2$ presented a better performance than a hard coating because the small particles of the hard coating can bring disadvantages during sliding motions.

Through the observation of microstructures on uncoated and coated surfaces the influence of the surface roughness and surface energy on tribological properties was investigated. The low surface energy of substrate leads to a porous and loose coating. As a consequence, the tribological properties could be adversely influenced.

The concept of the combination of hard and soft coatings will open new fields for the use of coatings in tribological applications on elastomers. Our data rule out the possibility that the application of DLC/MoS$_2$ as a coating can improve the tribological properties of elastomeric seals, especially under dry or insufficiently lubricated conditions. This finding is promising and should be explored with different combinations of even more than two coatings.

Conflicts of Interest: The authors declare no conflict of interest.

References

1. Holmberg, K.; Matthews, A. *Coatings Tribology. Properties, Mechanisms, Techniques and Applications in Surface Engineering*, 2nd ed.; Elsevier Science: Amsterdam, The Netherlands, 2009.
2. Gawliński, M. Friction and wear of elastomer seals. *Arch. Civ. Mech. Eng.* **2007**, *7*, 57–67. [CrossRef]
3. Nakahigashi, T.; Tanaka, Y.; Miyake, K.; Oohara, H. Properties of flexible DLC film deposited by amplitude-modulated RF P-CVD. *Tribol. Int.* **2004**, *37*, 907–912. [CrossRef]
4. Nakahigashi, T.; Miyake, K.; Murkami, Y. Application of DLC coating to rubber and polymer materials. *J. Jpn. Soc. Tribol.* **2002**, *47*, 833–839.
5. Takikawa, H.; Miyakawa, N.; Minamisawa, S.; Sakakibara, T. Fabrication of diamond-like carbon film on rubber by T-shape filtered-arc-deposition under the influence of various ambient gases. *Thin Solid Films* **2004**, *457*, 143–150. [CrossRef]
6. Takikawa, H.; Miyakawa, N.; Toshifuji, J.; Minamisawa, S.; Matsushita, T.; Takemura, K.; Sakakibara, T. Preparation of elastic DLC film on rubber by T-shape filtered arc deposition. *IEEJ Trans. Fundam. Mater.* **2003**, *123*, 738–743. [CrossRef]
7. Miyakawa, N.; Minamisawa, S.; Takikawa, H.; Sakakibara, T. Physical–chemical hybrid deposition of DLC film on rubber by T-shape filtered-arc-deposition. *Vacuum* **2004**, *73*, 611–617. [CrossRef]
8. Bui, X.; Pei, Y.; de Hosson, J.T.M. Magnetron reactively sputtered Ti-DLC coatings on HNBR rubber: The influence of substrate bias. *Surf. Coat. Technol.* **2008**, *202*, 4939–4944. [CrossRef]
9. Bui, X.L.; Pei, Y.T.; Mulder, E.D.G.; de Hosson, J.T.M. Adhesion improvement of hydrogenated diamond-like carbon thin films by pre-deposition plasma treatment of rubber substrate. *Surf. Coat. Technol.* **2009**, *203*, 1964–1970. [CrossRef]
10. Pei, Y.; Bui, X.; de Hosson, J.T.M. Deposition and characterization of hydrogenated diamond-like carbon thin films on rubber seals. *Thin Solid Films* **2010**, *518*, S42–S45. [CrossRef]

11. Pei, Y.; Martinez-Martinez, D.; van der Pal, J.P.; Bui, X.; Zhou, X.; de Hosson, J.T.M. Flexible diamond-like carbon films on rubber: Friction and the effect of viscoelastic deformation of rubber substrates. *Acta Mater.* **2012**, *60*, 7216–7225. [CrossRef]

12. Pei, Y.; Bui, X.; Zhou, X.; de Hosson, J.T.M. Tribological behavior of W-DLC coated rubber seals. *Surf. Coat. Technol.* **2008**, *202*, 1869–1875. [CrossRef]

13. Lackner, J.M.; Major, R.; Major, L.; Schöberl, T.; Waldhauser, W. RF deposition of soft hydrogenated amorphous carbon coatings for adhesive interfaces on highly elastic polymer materials. *Surf. Coat. Technol.* **2009**, *203*, 2243–2248. [CrossRef]

14. Kahn, M.; Menegazzo, N.; Mizaikoff, B.; Berghauser, R.; Lackner, J.M.; Hufnagel, D.; Waldhauser, W. Properties of DLC and Nitrogen-Doped DLC Films Deposited by DC Magnetron Sputtering. *Plasma Process. Polym.* **2007**, *4*, S200–S204. [CrossRef]

15. Lansdown, A.R. *Molybdenum Disulphide Lubrication*, 1st ed.; Elsevier Science: Amsterdam, The Netherlands, 1999.

16. Bellido-González, V.; Jones, A.H.S.; Hampshire, J.; Allen, T.J.; Witts, J.; Teer, D.G.; Ma, K.J.; Upton, D. Tribological behaviour of high performance MoS_2 coatings produced by magnetron sputtering. *Surf. Coat. Technol.* **1997**, *97*, 687–693. [CrossRef]

17. Donnet, C.; Martin, J.M.; Le Mogne, T.; Belin, M. Super-low friction of MoS_2 coatings in various environments. *Tribol. Int.* **1996**, *29*, 123–128. [CrossRef]

18. Wang, D.; Chang, C.; Ho, W. Microstructure analysis of MoS_2 deposited on diamond-like carbon films for wear improvement. *Surf. Coat. Technol.* **1999**, *111*, 123–127. [CrossRef]

19. Zhao, X.; Lu, Z.; Wu, G.; Zhang, G.; Wang, L.; Xue, Q. Preparation and properties of DLC/MoS_2 multilayer coatings for high humidity tribology. *Mater. Res. Express* **2016**, *3*, 066401. [CrossRef]

20. Wu, Y.; Liu, Y.; Yu, S.; Zhou, B.; Tang, B.; Li, H.; Chen, J. Influences of space irradiations on the structure and properties of MoS_2/DLC lubricant film. *Tribol. Lett.* **2016**, *64*, 24. [CrossRef]

21. Noshiro, J.; Watanabe, S.; Sakurai, T.; Miyake, S. Friction properties of co-sputtered sulfide/DLC solid lubricating films. *Surf. Coat. Technol.* **2006**, *200*, 5849–5854. [CrossRef]

22. Hausberger, A.; Godor, V.; Grün, F.; Pinter, G.; Schwarz, T. Development of ring on disc tests for elastomeric sealing materials. In Proceedings of the International Tribology Conference, Tokyo, Japan, 16–20 September 2015.

23. Rodgers, B.; Waddell, W. The science of rubber compounding. In *Science and Technology of Rubber*, 4th ed.; Mark, J.E., Erman, B., Roland, C.M., Eds.; Academic Press: Cambridge, MA, USA, 2013; pp. 417–471.

24. Thirumalai, S.; Hausberger, A.; Lackner, J.M.; Waldhauser, W.; Schwarz, T. Effect of the type of elastomeric substrate on the microstructural, surface and tribological characteristics of diamond-like carbon (DLC) coatings. *Surf. Coat. Technol.* **2016**, *302*, 244–254. [CrossRef]

25. Lackner, J.M.; Waldhauser, W.; Schwarz, M.; Mahoney, L.; Major, L.; Major, B. Polymer pre-treatment by linear anode layer source plasma for adhesion improvement of sputtered TiN coatings. *Vacuum* **2008**, *83*, 302–307. [CrossRef]

26. Assender, H.; Bliznyuk, V.; Porfyrakis, K. How surface topography relates to materials' properties. *Science* **2002**, *297*, 973–976. [CrossRef] [PubMed]

27. Cho, N.-H.; Krishnan, K.M.; Veirs, D.K.; Rubin, M.D.; Hopper, C.B.; Bhushan, B.; Bogy, D.B. Chemical structure and physical properties of diamond-like amorphous carbon films prepared by magnetron sputtering. *J. Mater. Res.* **1990**, *5*, 2543–2554. [CrossRef]

28. Robertson, J. Diamond-like amorphous carbon. *Mater. Sci. Eng. R Rep.* **2002**, *37*, 129–281. [CrossRef]

29. Martinez-Martinez, D.; de Hosson, J.T.M. On the deposition and properties of DLC protective coatings on elastomers: A critical review. *Surf. Coat. Technol.* **2014**, *258*, 677–690. [CrossRef]

30. Moulder, J.F. *Handbook of X-ray Photoelectron Spectroscopy. A Reference Book of Standard Spectra for Identification and Interpretation of XPS Data*; Perkin-Elmer: Eden Prairie, MN, USA, 1992.

31. *ASTM D445-17a Test Method for Kinematic Viscosity of Transparent and Opaque Liquids (and Calculation of Dynamic Viscosity)*; ASTM International: West Conshohocken, PA, USA, 2017.

32. *Data Sheet of Mobil SHC™ Grease 460 WT*; Exxon Mobil Corporation: Irving, TX, USA, 2016.

33. *NIST X-ray Photoelectron Spectroscopy Database*; Version 4.1; National Institute of Standards and Technology: Gaithersburg, MD, USA. Available online: https://srdata.nist.gov/xps/Default.aspx (accessed on 13 June 2018).

34. Scofield, J.H. Hartree-slater subshell photoionization cross-sections at 1254 and 1487 eV. *J. Electron Spectrosc. Relat. Phenom.* **1976**, *8*, 129–137. [CrossRef]

35. Xu, Y.; Zheng, C.; Wang, S.; Hou, Y. 3D arrays of molybdenum sulphide nanosheets on Mo meshes: Efficient electrocatalysts for hydrogen evolution reaction. *Electrochim. Acta* **2015**, *174*, 653–659. [CrossRef]

36. Fleischauer, P.D.; Lince, J.R. A comparison of oxidation and oxygen substitution in MoS_2 solid film lubricants. *Tribol. Int.* **1999**, *32*, 627–636. [CrossRef]

37. Weber, T.; Muijsers, J.C.; Niemantsverdriet, J.W. Structure of Amorphous MoS_3. *J. Phys. Chem.* **1995**, *99*, 9194–9200. [CrossRef]

38. Baker, M.A.; Gilmore, R.; Lenardi, C.; Gissler, W. XPS investigation of preferential sputtering of S from MoS_2 and determination of MoS_x stoichiometry from Mo and S peak positions. *Appl. Surf. Sci.* **1999**, *150*, 255–262. [CrossRef]

39. Qiu, L.; Xu, G. Peak overlaps and corresponding solutions in the X-ray photoelectron spectroscopic study of hydrodesulfurization catalysts. *Appl. Surf. Sci.* **2010**, *256*, 3413–3417. [CrossRef]

40. Robertson, J. Classification of diamond-like carbons. In *Tribology of Diamond-Like Carbon Films: Fundamentals and Applications*; Donnet, C., Ed.; Springer: Boston, MA, USA, 2008; pp. 13–24.

41. Paik, N. Raman and XPS studies of DLC films prepared by a magnetron sputter-type negative ion source. *Surf. Coat. Technol.* **2005**, *200*, 2170–2174. [CrossRef]

42. Leung, T.Y.; Man, W.F.; Lim, P.K.; Chan, W.C.; Gaspari, F.; Zukotynski, S. Determination of the sp^3/sp^2 ratio of a-C: H by XPS and XAES. *J. Non-Cryst. Solids* **1999**, *254*, 156–160. [CrossRef]

43. Benoist, L.; Gonbeau, D.; Pfister-Guillouzo, G.; Schmidt, E.; Meunier, G.; Levasseur, A. XPS analysis of lithium intercalation in thin films of molybdenum oxysulphides. *Surf. Interface Anal.* **1994**, *22*, 206–210. [CrossRef]

44. Martincová, J.; Otyepka, M.; Lazar, P. Is single layer MoS_2 stable in the air? *Chemistry* **2017**, *23*, 13233–13239. [CrossRef] [PubMed]

45. Fleischauer, P.D. Effects of crystallite orientation on environmental stability and lubrication properties of sputtered MoS_2 thin films. *ASLE Trans.* **2008**, *27*, 82–88. [CrossRef]

46. Fleischauer, P.D.; Bauer, R. Chemical and structural effects on the lubrication properties of sputtered MoS_2 films. *Tribol. Trans.* **1988**, *31*, 239–250. [CrossRef]

47. Theilade, U.A.; Hansen, H.N. Surface microstructure replication in injection molding. *Int. J. Adv. Manuf. Technol.* **2007**, *33*, 157–166. [CrossRef]

48. Donnet, C.; Erdemir, A. *Tribology of Diamond-Like Carbon Films. Fundamentals and Applications*; Springer: Boston, MA, USA, 2008.

49. Neuville, S.; Matthews, A. A perspective on the optimisation of hard carbon and related coatings for engineering applications. *Thin Solid Films* **2007**, *515*, 6619–6653. [CrossRef]

50. Baglin, J.E.E. Interface design for thin film adhesion. In *Fundamentals of Adhesion*; Lee, L.-H., Ed.; Springer: Boston, MA, USA, 2014; pp. 363–382.

51. Goldschmidt, A.; Streitberger, H.-J. *BASF Handbook on Basics of Coating Technology*, 2nd ed.; Vincentz Network: Hannover, Germany, 2007.

52. Quéré, D. Wetting and Roughness. *Annu. Rev. Mater. Res.* **2008**, *38*, 71–99. [CrossRef]

53. Martínez, L.; Nevshupa, R.; Álvarez, L.; Huttel, Y.; Méndez, J.; Román, E.; Mozas, E.; Valdés, J.R.; Jimenez, M.A.; Gachon, Y.; et al. Application of diamond-like carbon coatings to elastomers frictional surfaces. *Tribol. Int.* **2009**, *42*, 584–590. [CrossRef]

54. Van der Pal, J.P.; Martinez-Martinez, D.; Pei, Y.T.; Rudolf, P.; de Hosson, J.T.M. Microstructure and tribological performance of diamond-like carbon films deposited on hydrogenated rubber. *Thin Solid Films* **2012**, *524*, 218–223. [CrossRef]

55. Grosch, K.A. The relation between the friction and visco-elastic properties of rubber. *Proc. R. Soc. A Math. Phys. Eng. Sci.* **1963**, *274*, 21–39. [CrossRef]

56. Zhang, S.-W. *Tribology of Elastomers*, 1st ed.; Elsevier: Amsterdam, The Netherlands, 2004.

57. Fuller, K.N.G.; Tabor, D. The effect of surface roughness on the adhesion of elastic solids. *Proc. R. Soc. A* **1975**, *345*, 327–342. [CrossRef]

58. Persson, B.N.J. On the theory of rubber friction. *Surf. Sci.* **1998**, *401*, 445–454. [CrossRef]

59. Mofidi, M.; Prakash, B. Influence of counterface topography on sliding friction and wear of some elastomers under dry sliding conditions. *Proc. Inst. Mech. Eng. Part J J. Eng. Tribol.* **2008**, *222*, 667–673. [CrossRef]

60. Glaeser, W.A.; Brundle, C.R.; Evans, C.A. *Characterization of Tribological Materials*, 2nd ed.; Momentum Press: New York, NY, USA, 2012.

61. Rabinowicz, E. Influence of surface energy on friction and wear phenomena. *J. Appl. Phys.* **1961**, *32*, 1440–1444. [CrossRef]

62. Rabinowicz, E. *Friction and Wear of Materials*, 2nd ed.; Wiley: New York, NY, USA, 1995.

63. Friedrich, K. *Friction and Wear of Polymer Composites*; North Holland Publishing Co.: Amsterdam, The Netherlands, 1986.

64. Bowden, F.P.; Tabor, D. *The Friction and Lubrication of Solids*; Oxford University Press: London, UK, 1963.

65. Okrent, E.H. The effect of lubricant viscosity and composition on engine friction and bearing wear. *ASLE Trans.* **1961**, *4*, 97–108. [CrossRef]

66. Archard, J.F. Contact and rubbing of flat surfaces. *J. Appl. Phys.* **1953**, *24*, 981–988. [CrossRef]

67. Lince, J.R.; Frantz, P.P. Anisotropic oxidation of MoS_2 crystallites studied by angle-resolved X-ray photoelectron spectroscopy. *Tribol. Lett.* **2001**, *9*, 211–218. [CrossRef]

68. Booser, E.R. *CRC Handbook of Lubrication. (Theory and Practice of Tribology). Theory and Design*; CRC Press: Boca Raton, FL, USA, 1983.

69. Pirro, D.M.; Daschner, E. *Lubrication Fundamentals*, 3rd ed.; Wessol, A.A., Ed.; CRC Press: Boca Raton, FL, USA, 2016.

70. Zum Gahr, K.-H. *Microstructure and Wear of Materials*; North Holland Publishing Co.: Amsterdam, The Netherlands, 1987.